CAVERN ROOF STABILITY FOR NATURAL GAS STORAGE IN BEDDED SALT

FINAL REPORT
26 September 2002–31 March 2005

by

Kerry L. DeVries
Kirby D. Mellegard
Gary D. Callahan
William M. Goodman

June 2005

RESPEC
P.O. Box 725
Rapid City, South Dakota 57709

CAVERN ROOF STABILITY FOR NATURAL GAS STORAGE IN BEDDED SALT

Topical Report RSI-1829
DE-FG26-02NT41651

by

Kerry L. DeVries
Kirby D. Mellegard
Gary D. Callahan
William M. Goodman

RESPEC
P.O. Box 725
Rapid City, South Dakota 57709

prepared for

June 2005

ABSTRACT

This report documents research performed to develop a new stress-based criterion for predicting the onset of damage in salt formations surrounding natural gas storage caverns. Laboratory tests were conducted to investigate the effects of shear stress, mean stress, pore pressure, temperature, and Lode angle on the strength and creep characteristics of salt. The laboratory test data were used in the development of the new criterion. The laboratory results indicate that the strength of salt strongly depends on the mean stress and Lode angle. The strength of the salt does not appear to be sensitive to temperature. Pore pressure effects were not readily apparent until a significant level of damage was induced and the permeability was increased to allow penetration of the liquid permeant.

Utilizing the new criterion, numerical simulations were used to estimate the minimum allowable gas pressure for hypothetical storage caverns located in a bedded salt formation. The simulations performed illustrate the influence that cavern roof span, depth, roof salt thickness, shale thickness, and shale stiffness have on the allowable operating pressure range. Interestingly, comparison of predictions using the new criterion with that of a commonly used criterion indicate that lower minimum gas pressures may be allowed for caverns at shallow depths. However, as cavern depth is increased, less conservative estimates for minimum gas pressure were determined by the new criterion.

EXECUTIVE SUMMARY

The main objective of the research discussed in this report is to improve the predictive technology used to evaluate the structural stability of natural gas storage caverns in bedded salt deposits. The structural stability of caverns in bedded salt depends on many interrelated factors, including local hydrology, local geology and rock properties, cavern operating conditions, cavern depth, cavern geometry, and cavern location with respect to other caverns. Cavern design entails avoidance of conditions known to be adverse for cavern stability. For caverns sited in salt deposits, integrity of the salt is crucial for long-term cavern stability. Rock salt is a viscoplastic material that is difficult to fail under moderate levels of confining pressure, which is one of the reasons salt is a favored storage medium. To maintain the integrity of a host salt formation, cavern design philosophy involves circumventing states of stress that cause the salt to dilate. Dilation manifests as a volumetric expansion resulting from microfracturing of the material. Therefore, structural stability is maintained by avoiding or limiting microfracturing in the salt.

This study focuses primarily on the strength and deformation characteristics of the salt and nonsalt beds surrounding and overlying the cavern. Even with complete knowledge of these material properties, problems may still arise because all of the geological features will never be known and the state-of-the-art in salt mechanics has not advanced to the point of establishing a full understanding of salt response at all possible states of stress. This is important for salt storage caverns because varying states of stress exist around the caverns. Rock is typically weaker in triaxial extension than in triaxial compression. Because triaxial extension states of stress exist in the roofs of bedded salt caverns, it is important to understand the creep and strength characteristics of salt under this state of stress. Therefore, use of current strength and damage criteria based on triaxial compression laboratory tests may indicate that failure of the roof salt will not occur; whereas, a failure criterion based on stress states other than triaxial compression may indicate failure. Design criteria that describe the dilation limit for states of stress ranging from triaxial compression to triaxial extension are necessary to address some of the shortcomings of existing dilation criteria for salt and are the primary topic of this study.

Three major work efforts were included in this project: (1) laboratory testing, (2) constitutive model development, and (3) numerical analyses. Laboratory testing was performed to characterize the strength and deformation behavior of bedded salt formations in the northeastern United States for evaluating cavern performance and predicting cavern stability. A new salt dilation criterion was developed based on the results of the laboratory tests. The new criterion includes Lode angle dependency to account for the lower strength exhibited by rock salt under triaxial extension states of stress compared to triaxial compression states of stress. This feature is not included in many of the existing dilation criteria and is an important aspect in evaluating the potential for salt damage. Finite element analyses were performed

that simulate hypothetical natural gas storage caverns to illustrate the use of the new criterion under a wide range of conditions that are expected to exist in the Appalachian Basin.

LABORATORY TESTING

The purpose of the laboratory testing task was (1) to investigate the behavior of salt under load paths and states of stress that simulate those found in the field and (2) to acquire data that can be used to define the constitutive models used to assess accurately the stability of the roof salt. All testing was performed on Cayuta salt recovered from the Bale No. 1 Well, located approximately 1 mile southwest of Cayuta in Schuyler County, New York. RESPEC conducted the tests at its facility in Rapid City, South Dakota.

A total of 34 successful laboratory tests were performed: 4 constant strain rate strength tests, 23 constant mean stress tests, and 7 constant stress creep tests. Tests performed were subjected to triaxial extension and triaxial compression states of stress. The confined compression tests provided data for determining: (1) compressive strength, (2) Young's modulus of elasticity, and (3) Poisson's ratio. These strength and deformation properties are used directly in modeling underground structures, in comparing rock types, and in examining variations in rock properties from one location to another. The constant mean stress dilation tests provide data used exclusively for determining the stress conditions that produce dilation (volume expansion as a result of microfracturing) in the salt. The creep tests were performed to assess the time-dependent deformation properties of the salt. The following general conclusions were determined from the laboratory testing of Cayuta salt:

1. The dilation limit is about 30 percent lower in extension than in compression.

2. The steady-state strain rates are equal in extension and compression.

3. Cycling between compression and extension produces a transient strain response each time the load is cycled under constant shear stress conditions.

4. Fluid pressure effects do not have a significant affect on the dilation limit.

5. A nonlinear relationship exists between mean stress and the dilation limit.

NEW DILATION CRITERION

A salt dilation criterion based on a Mohr-Coulomb-type model was developed using experimental evidence obtained from testing of Cayuta salt under triaxial compression and triaxial extension states of stress. The new criterion, which is named the RD criterion, assumes that the dilation limit of salt is a function of three stress invariants: (1) the first invariant of the Cauchy stress tensor (I_1), (2) the second invariant of the deviatoric stress tensor (J_2), and (3) the Lode angle (ψ). The RD criterion provides a nonlinear relationship

between dilation strength and mean stress and includes a nonzero value when mean stress is zero. Based on a comparison of measured strength results obtained in this and other studies, pore or fluid pressure and temperature were not found to have a significant impact on the dilation limit of salt. Although bedding plane orientation is expected to have a significant impact on the dilation limit, oriented salt core was not available for constitutive model development. However, the triaxial extension tests performed should provide the lowest possible dilation limit for bedded salt because the maximum compressive stress in these tests was oriented parallel to the bedding plane.

NUMERICAL ANALYSES

A stratigraphic sequence and a hypothetical solution-mined cavern geometry were selected as the base model for the numerical evaluation of natural gas storage caverns in the Appalachian Basin. A total of 160 finite element analyses were performed to assess the stability of natural gas storage in the representative bedded salt formation. The analyses were performed to assess the effects of various cavern design parameters on the stability of the cavern using the newly developed RD criterion for predicting the potential for salt dilation. Cavern design parameters that were investigated include:

- Three cavern roof salt thicknesses (3, 9.1, and 27.4 meters).

- Four cavern depths (300, 600, 900, and 1,200 meters).

- Four cavern roof spans (18.3, 58.3, 138.3, and 218.3 meters).

- Three overlying shale bed thicknesses (3, 6.1, and 12.2 meters).

- Three interbedded shale unit stiffnesses (Young's modulus of 1.5, 10, and 70 GPa).

- Two natural gas storage cycles (a single rapid withdrawal cycle and a 10-year annual gas service cycle).

Collectively, the range of cavern design parameters in the analyses represents a diverse collection of natural gas storage cavern designs in several possible formation depths. Although efforts were taken to provide reasonable cavern designs within the Appalachian Basin, the analyses are not intended for design purposes. They were used to investigate cavern response over an extremely large range of possible salt bed depths that exist within the Appalachian Basin.

The following findings were determined from the numerical analyses and application of the RD criterion:

1. The thickness of the cavern roof salt does not have a significant affect on the minimum allowable gas pressure necessary to prevent salt surrounding the cavern from dilating.

2. The thickness of the first nonsalt bed overlying the cavern has very little affect on the potential for salt surrounding the cavern to dilate provided failure does not occur in the nonsalt bed.

3. The stiffness of the first nonsalt bed overlying the cavern is an important factor controlling the minimum gas pressure for the caverns investigated. Lower minimum gas pressures were predicted for increasingly greater values specified for Young's modulus of the shale bed above the cavern. This finding is based on analyses having a roof salt thickness of 10 meters. The influence of the nonsalt material stiffness is expected to be a function of distance from the cavern.

4. Based on the RD criterion, the percentage of overburden that must be supported by cushion gas to maintain cavern stability increases with depth (i.e., the minimum gas pressure gradient increases with depth).

5. Although lower minimum gas pressures can be realized for caverns that have extremely stiff overlying nonsalt beds, the stiffer beds modeled were more likely to fail than softer nonsalt beds.

CONCLUSIONS

The Michigan and Appalachian Basins contain multiple salt beds suitable for natural gas storage. Because of variability in the salt-bearing formations and overlying roof shales and carbonates throughout the basins, site-specific reconnaissance would be required before specific storage cavern designs are considered. In general, the geologic analysis shows a range of salt bed thicknesses, depths, and overlying rock types available as storage sites. The laboratory testing showed that the steady-state strain rate for salt is the same for triaxial extension and triaxial compression states of stress. However, the laboratory tests also revealed that the transient behavior of salt exhibits an anisotropic hardening or deformation induced anisotropy when the Lode angle is changed (i.e., cycled between triaxial extension and triaxial compression). The laboratory testing also demonstrated that salt dilates much easier under triaxial extension states of stress than triaxial compression states of stress, which amplifies the need for a dilation criterion that accommodates these changes as the state of stress changes. Based on the laboratory tests, a new dilation criterion (RD criterion) was developed that improves the predictive ability of dilation around salt caverns. The RD criterion was used to evaluate the influence of design parameters on the stability of underground caverns. Based on these analyses, cavern roof span and competency of the overlying nonsalt strata were found to be the most important mechanical design considerations.

Based on the operating pressure range and size of existing natural gas storage caverns in bedded salt, the RD criterion appears to provide reasonable estimates for the minimum allowable gas pressure necessary to maintain stability under most of the conditions simulated. One area of concern is the predicted results at very shallow depths. Analyses of caverns at a depth of 300 meters indicate that minimum pressures less than those typically used by storage operators are possible without causing damage to the salt. As a result, caverns with large roof spans were predicted to be permissible while only requiring a moderate amount of cushion gas pressure to maintain stability. Although the state of stress in the salt surrounding the cavern at a depth of 300 meters is within the range of that tested in the laboratory, the extremely low minimum gas pressures predicted for caverns with large roof spans produces some doubt about the results at low mean stress. However, the RD criterion was applied in these analyses with no inherent factor of safety. In actual design situations, the RD criterion material constants should be adjusted so that a factor of safety is maintained with respect to the dilation boundary.

The new RD criterion provides an improved method for evaluating cavern designs and avoiding dilatant states of stress that would be detrimental to the long-term stability of the cavern. Although the criterion was applied to the assessment of natural gas storage caverns in bedded salt, it is also applicable to caverns in domal salt.

TABLE OF CONTENTS

TABLE OF CONTENTS
(Continued)

TABLE OF CONTENTS
(Continued)

LIST OF TABLES

LIST OF FIGURES

LIST OF FIGURES
(Continued)

LIST OF FIGURES
(Continued)

LIST OF FIGURES
(Continued)

1.0 INTRODUCTION

Cavern stability is a crucial consideration for the design and development of storage caverns. Cavern stability issues limit cavern size, spacing, and operating pressure range in salt formations. An acceptable operating pressure range for a salt cavern is generally determined from a geomechanics evaluation that typically requires that the cavern response satisfies various design constraints. These constraints are intended to ensure containment of the gas, cavern stability, and safe operation of the storage cavern. Application of current methods for evaluating structural stability has not been completely successful in predicting known roof failures and surface spalls in storage caverns located in bedded and domal salt formations throughout North America. Better failure criteria and predictive technologies are needed to accurately predict the failure of salt. This report documents the research that was performed under Department of Energy Contract DE-FG26-02NT41651 to advance the current technology used to assess the stability of natural gas storage in bedded salt formations.

1.1 BACKGROUND

Bedded salt formations occur in varying thicknesses, and other interbedded sedimentary rock types are always present. The relatively thin nature of the salt beds and the local presence of interbedded nonsalt strata present problems unique to bedded salt storage that can typically be avoided in a cavern located in a salt dome.

Salt domes provide massive quantities of salt real estate, which provides significant cavern design flexibility. In salt domes, storage caverns are typically cylindrically shaped and significantly taller than they are wide. Controlled solution-mining results in a nicely domed roof, which is favorable from a mechanical stability standpoint. Furthermore, the cavern can be positioned such that a significant amount of salt is present between the cavern roof and the caprock in the dome. However, the height of a bedded salt cavern depends on the thickness of the salt bed(s) and is usually much less than the height of a domal salt cavern. This forces the diameter of a bedded salt cavern to be much greater than its height to obtain sufficient storage volume. The bedded salt cavern configuration is less desirable from a rock mechanics standpoint because of the potentially large roof spans that must be supported by the geologic formation. In addition, because of the relatively thin nature of the salt beds, the favorable domed roof present in salt dome caverns is impossible to obtain, as is the massive layer of salt between the cavern roof and the next adjacent structurally significant stratigraphic layer.

Another characteristic complicating the design of caverns in bedded salts is the in situ stress state. In a salt dome, the in situ principal stresses are nearly equal in magnitude. This is not usually the case in bedded salts. In the northeastern United States, the maximum horizontal principal stress can be significantly higher than the minimum horizontal principal stress. Further complicating this issue is the fact that multiple-well leaching is often used in bedded

salts to increase the efficiency of the leaching process, resulting in horizontally elongated caverns. In such cases, orientation of the cavern will also have an affect on cavern stability.

The structural stability of caverns in bedded salt depends on the strength and deformation characteristics of the salt and nonsalt beds surrounding and overlying the cavern. Even with complete knowledge of this information, problems may still arise because the state-of-the-art in salt mechanics has not advanced to the point of establishing a full understanding of salt response at all possible states of stress. This is important for salt storage caverns because varying states of stress exist around the caverns. Rock is typically weaker in triaxial extension than in triaxial compression. Because triaxial extension states of stress exist in the roofs of bedded salt caverns, it is important to understand the creep and strength characteristics of salt under this state of stress. Therefore, use of current strength and damage criteria based on triaxial compression laboratory tests may indicate that failure of the roof salt will not occur; whereas, a failure criterion based on stress states other than triaxial compression may indicate failure. Design criteria that describe the dilation limit for states of stress ranging from triaxial compression to triaxial extension are necessary to address some of the shortcomings of previous dilation criteria for salt and are the primary topic of this study.

1.2 PROJECT SCOPE

The scope of work performed includes geologic analysis, laboratory testing, theoretical development, and numerical analysis. A brief description of the project scope is listed below.

- Establish a representative lithology for the Appalachian Basin along with characteristic rock properties and in situ conditions.

- Conduct laboratory tests on core from the Appalachian Basin. The matrix of laboratory tests includes special tests to provide data at the states of stress prevalent in salt forming the cavern roof.

- Develop a new failure criterion for the roof salt in bedded salt caverns based on the prevalent states of stresses in the salt.

- Develop representative numerical simulation models of natural gas storage caverns based on the characteristics of the Appalachian Basin.

- Evaluate the effect of basic design parameters on cavern roof salt stability using representative models, together with the newly developed failure criterion. Design parameters to evaluate include: (1) cavern roof salt thickness, (2) cavern depth, (3) cavern roof span, (4) overlying nonsalt thickness, (5) overlying nonsalt stiffness, and (6) cavern operating pressures.

- Use the results of the numerical analyses to recommend guidelines that enable potential bedded salt cavern gas storage developers to recognize favorable and unfavorable geologic settings for cavern development.

1.3 REPORT ORGANIZATION

This report contains eight chapters, including this introduction. Chapter 2.0 describes the geological analysis of the Appalachian Basin. The laboratory testing program is described in Chapter 3.0 along with a brief discussion of the elastic, strength, and creep properties of Cayuta salt. The material model used to describe the creep of Cayuta is also provided in Chapter 3.0. The new design criterion developed for assessing salt failure is given in Chapter 4.0. Chapter 5.0 presents the technical approach and describes the numerical analyses and results used to assess cavern stability. Chapter 6.0 provides a detailed summary of the numerical analyses, and conclusions are given in Chapter 7.0. A list of cited references is given in Chapter 8.0, followed by appendices containing supporting documentation.

2.0 GEOLOGICAL ANALYSIS OF THE APPALACHIAN BASIN

Natural gas is often stored in caverns solution mined in domal or bedded salt formations. Salt caverns are an effective means of providing flexible gas storage services that ease dependence on pipeline supply. Figure 2-1 shows the major salt deposits in the United States (after Johnson and Gonzales [1978]). As shown in the figure, most of the bedded salt deposits are located in the central portion of the United States with most salt domes located along the Gulf Coast, but much of the projected growth in natural gas demand is in the northeastern United States. A few natural gas storage caverns in salt formations have been developed within the Michigan and Appalachian Basins (see Figure 2-1); however, only about 4 billion standard cubic feet (Bcf) of salt cavern storage currently exists in these regions [Energy Information Administration, 2001]. The Appalachian and Michigan Basins are near major gas markets in the Northeast, making gas storage in these bedded salts very desirable. However, technical issues have hindered development of solution-mined salt caverns for natural gas storage in this region, as well as in the Midwest. It is understood that, for purposes of developing storage caverns, thick salt sections are considered the best targets. Three major salt-bearing zones exist within the salt-bearing Silurian Salina Group in the Appalachian Basin. These zones are further defined below and their stratigraphic and structural patterns are described for the New York, Pennsylvania, and Ohio regions with the goal of identifying attractive regions for cavern development. General geologic conditions, such as salt bed thicknesses and salt bed elevations, are presented as well as a representative stratigraphic column used during the numerical analysis portion of this project.

2.1 GENERAL STRATIGRAPHIC SETTING AND BASIC BASIN CONFIGURATION

The salt beds of the Upper Silurian Salina Group occur within a stratified sequence of shales, dolomites, and evaporites that infilled the Appalachian Foreland Basin. The depositional trough of the basin extended across parts of New York, Pennsylvania, West Virginia, Maryland, Ohio, and Ontario (Figure 2-2). In general, the Appalachian Basin salts range from the horizontal, interbedded halite and anhydrite stringers in Ohio; to the severely folded and faulted salts with irregular flow banding and large, steeply dipping rafts of nonsalt strata in central New York; to the extremely brecciated, tectonically homogenized salt sequences of south-central New York. The maximum thickness of the Salina Group is on the order of 760 meters in the subsurface of north-central Pennsylvania [Rickard, 1969]. The aggregate salt thickness exceeds 275 meters in this same area (see Figure 2-2).

The salt beds are not exposed in the outcrop belts that define the contemporary Appalachian Basin margins. Instead, the salts are mainly preserved in the axial trough of the basin. The depocenter (i.e., the area of maximum thickness of salt) did not remain stationary over time [Rickard, 1969; Mesolella, 1978]. The thickest zone of each of the three major salt-bearing
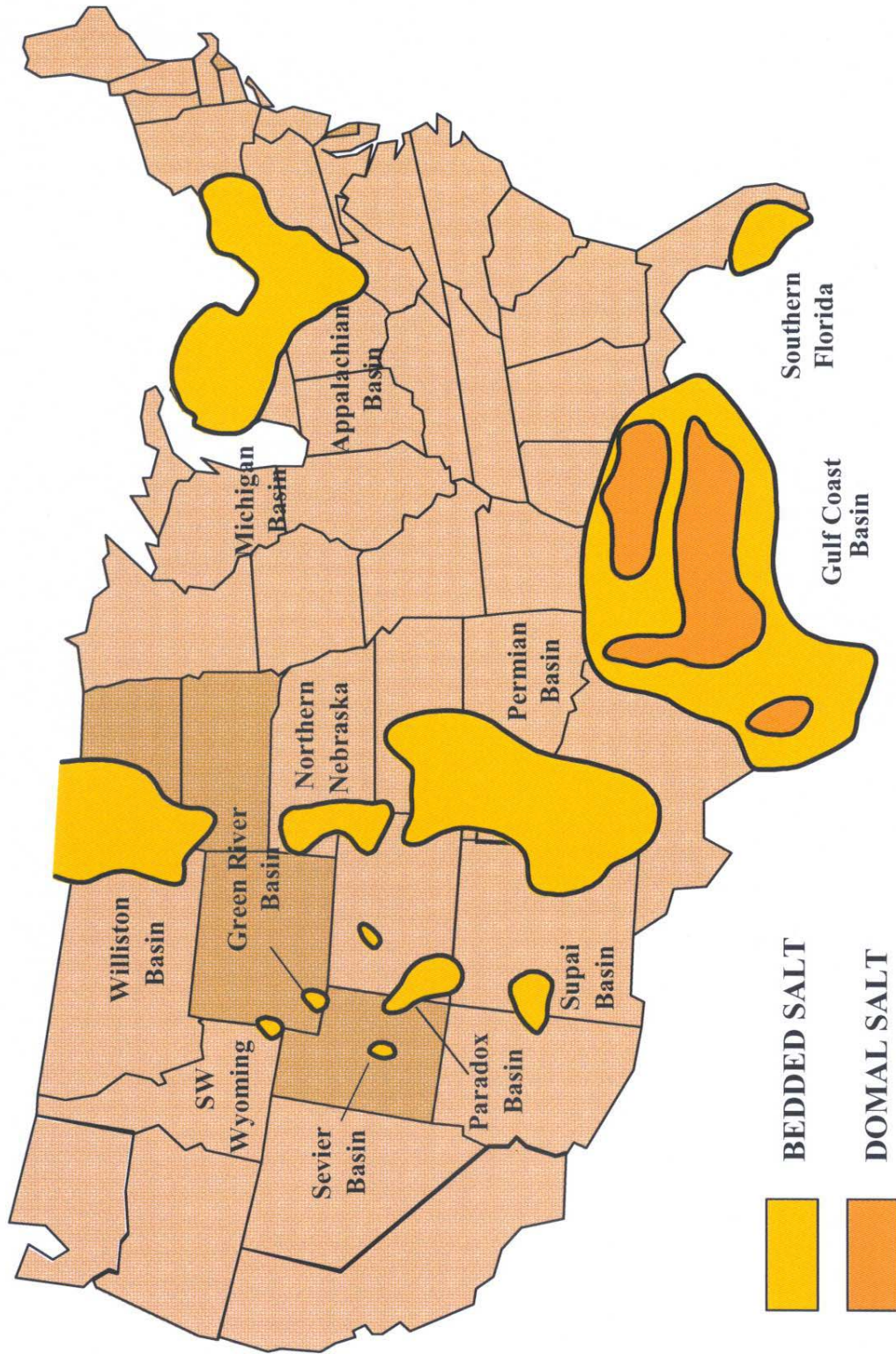
Figure 2-1. Major Salt Deposits in the United States.

BEDDED SALT

DOMAL SALT

Southern Florida

Gulf Coast Basin

Appalachian Basin

Michigan Basin

Permian Basin

Northern Nebraska

Green River Basin

Williston Basin

SW Wyoming

Sevier Basin

Paradox Basin

Supai Basin
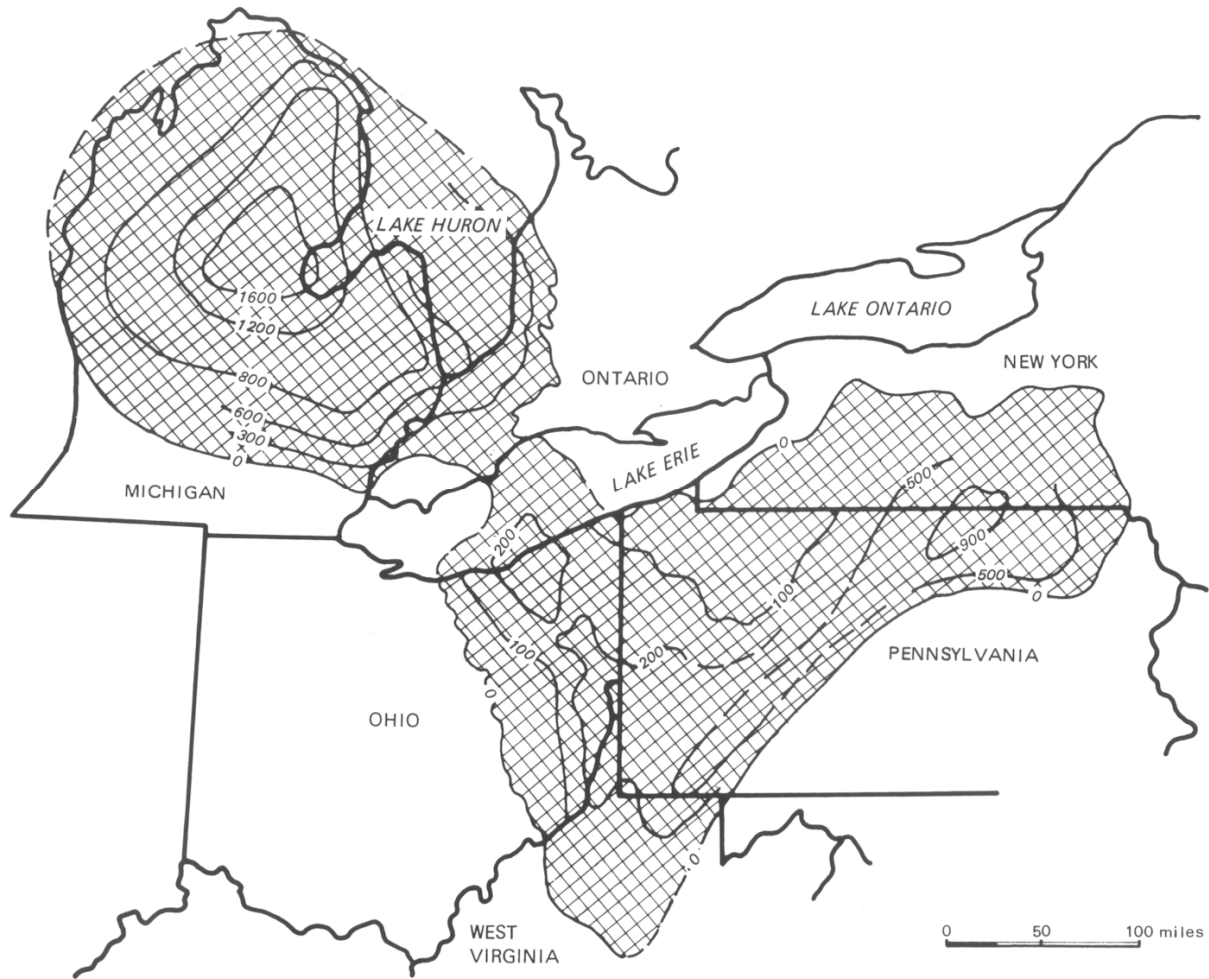
Figure 2-2. Generalized Boundaries and Salt Thickness of the Appalachian Basin (From Clifford [1973]).

units (lower, middle, and upper Salina Group) appears to have shifted southeastward over time (Figure 2-3). This type of depocenter migration is typical of foreland basins that owe their formation to differential loading of the lithosphere by thrust sheets. The Appalachian Basin suffered multiple episodes of compressional tectonism during the Paleozoic Era. As a consequence of the multiple cycles of thrust sheet emplacement (i.e., mountain building) and erosional unloading of its tectonically active eastern margin, the Appalachian Basin sedimentary fill is riddled with unconformities, and its formation thickness variations record a remarkable history of lateral basin axis shift [Goodman and Brett, 1994]. The stratigraphy of the Salina Group salts records a significant part of this dynamic basin history, as discussed in the next section.

2.2 STRATIGRAPHIC NOMENCLATURE

The Salina Group evaporite sequence of the Appalachian Basin connects with, and extends into, the Michigan Basin via the Chatham Sag, a narrow structural low on the Findlay-Algonquin Arch system that separates the two basins (see Figure 2-2). The Chatham Sag was probably controlled by basement-related block faults that were periodically reactivated over Phanerozoic time [Sanford et al., 1985].

The stratigraphic nomenclature most commonly applied to the Salina Group of the Appalachian Basin is that of Landes [1945] who actually established his labeling system for the correlative Michigan Basin sequence. He divided the Salina Group into seven vertically stacked units, designated A through G, with the A unit occurring at the base of the sequence and the G unit at its top.

Ulteig [1964], Rickard [1969], Jacoby [1969], and Clifford [1973] have demonstrated that Landes' nomenclatural scheme works well for the Appalachian Basin deposits. It is preferred over the local lithostratigraphic terms (such as the Vernon, Syracuse, and Camillus Formations of New York), because Landes' nomenclature facilitates correlations across both geopolitical and basin boundaries.

As illustrated in Figure 2-4, the salt beds of the Salina Group are predominantly concentrated in three zones (B, D, and F units). The intervening A, C, E, and G units are predominantly shale, anhydrite, and/or dolomite. There is a thin salt bed in the Salina E unit within the New York sections, but it is too thin to be considered a viable target for cavern development. However, this bed thickens to become a more viable target beneath southeastern Ohio and adjacent Pennsylvania and West Virginia. The E-Salt was mapped in Ohio in combination with the D-Salts by Clifford [1973].

In the following sections of this chapter, the stratigraphy of each of the three major salt-bearing zones is discussed with an emphasis on identification of thick zones for each salt.
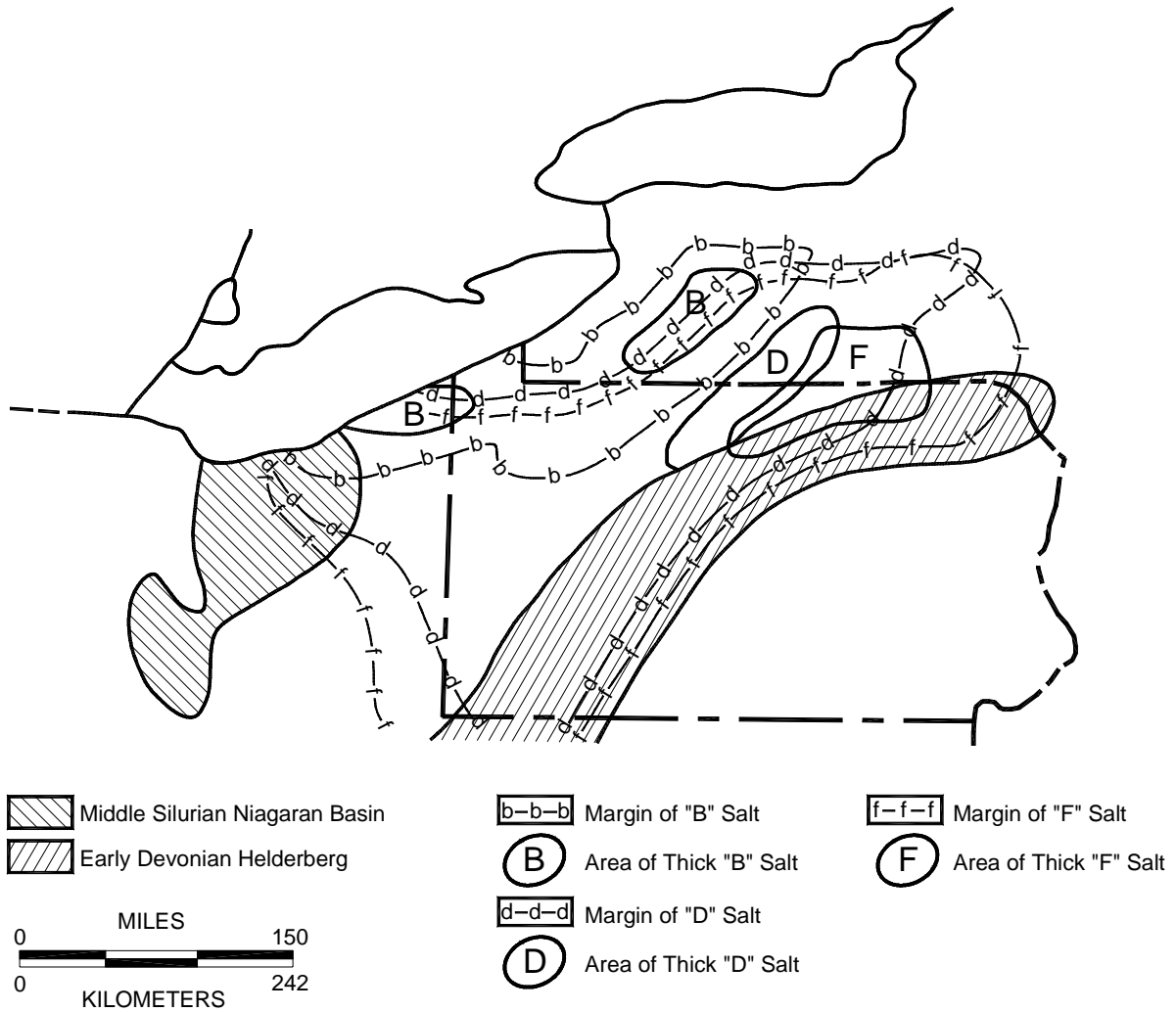
Figure 2-3. Progressive Southward Shift in the Position of the Salina B-, D-, and F-Salts (Modified From Mesolella [1978]).

8
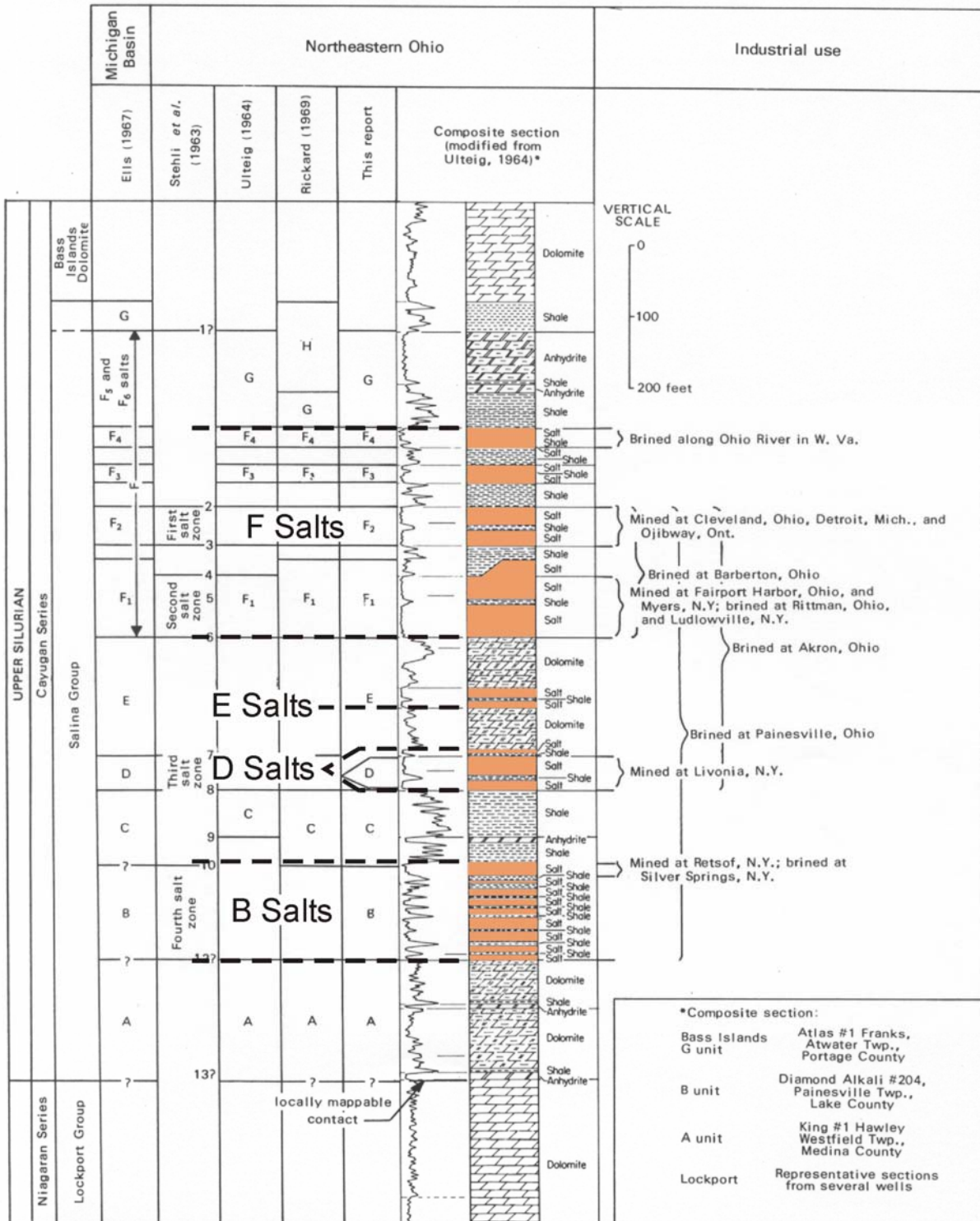
Figure 2-4. Representative Stratigraphic Column and Historic Use (Modified From Clifford [1973]).

2.2.1 Salina B-Salt Trends

The B-Salts are situated within a v-shaped trough whose axis trends southwestward from Livingston County, New York, to Venango County, Pennsylvania (Figure 2-5). The trough extends northwestward from Venango County into northeastern Ohio. Near its northern limits in Livingston County, New York, the top of the B-Salt sequence resides at a subsurface elevation of about 33 meters above mean sea level (drilling depth of about 213 meters). Near its southern limits in Pennsylvania, the B-Salts decline in elevation to –1,650 meters mean sea level (msl) (drilling depth of about 2,100 meters).

Near its northern boundary in Lake County, Ohio, the B-Salts reside at subsurface elevations just below –457 meters msl (with a drilling depth of 700 to 731 meters). Near its southern limit in Portage County, Ohio, the top of the B-Salts declines in elevation to about –762 to –914 meters msl (with a drilling depth of about 1,100 meters).

According to Rickard [1969], the B-Salts are thickest near the northeast and northwest extremities of its subcrop belt. The thickest zone (over 33 meters in aggregate salt bed thickness) occurs beneath eastern Lake County and western Ashtabula County, Ohio. In this area, six discrete salt beds, ranging in thickness between 1.5 and 6 meters, comprise the Salina B-Salts. The nonsalt interbeds range in thickness between 1 and 4.6 meters (Clifford [1973], Plate 1). This thick zone extends northwestward beneath Lake Erie where the B-Salts of northern Ohio connect with the correlative B unit salts of the Michigan Basin.

The region of thick B-Salts within the Ohio Subbasin is rimmed by a zone within which Rickard [1969] depicts aggregate salt thicknesses to range between 15 and 30.5 meters. Comparable thicknesses are reported in New York along the axis of the depositional trough that extends southwesterly from Livingston County into northwestern Allegany County and eastern Cattaraugus County (see Figure 2-5). In the vicinity of the now flooded Retsof Mine in Livingston County (where the B-Salt stratigraphy is well studied), the aggregate salt thickness is 23 meters. There are six major B-Salt beds, the thickest of which (the Retsof Bed) occurs at the top of the sequence and attains a thickness of 4.6 to 6.1 meters [Rickard, 1969; Jacoby, 1969]. Nonsalt interbeds within the Salina B-Salt sequence range in thickness from less than 3 meters to about 10.7 meters. The thickest nonsalt interbed separates the Retsof Bed from the remainder of the underlying B-Salt sequence.

2.2.2 Salina D-Salt Trends

Separating the B-Salts from the stratigraphically higher D-Salts is a 15- to 122-meter-thick sequence of nonsalt-bearing dolomites, anhydrites, and shales assigned to the Salina C. The Salina C is thickest in north-central Pennsylvania and is thinnest is southern Ontario [Rickard, 1969].
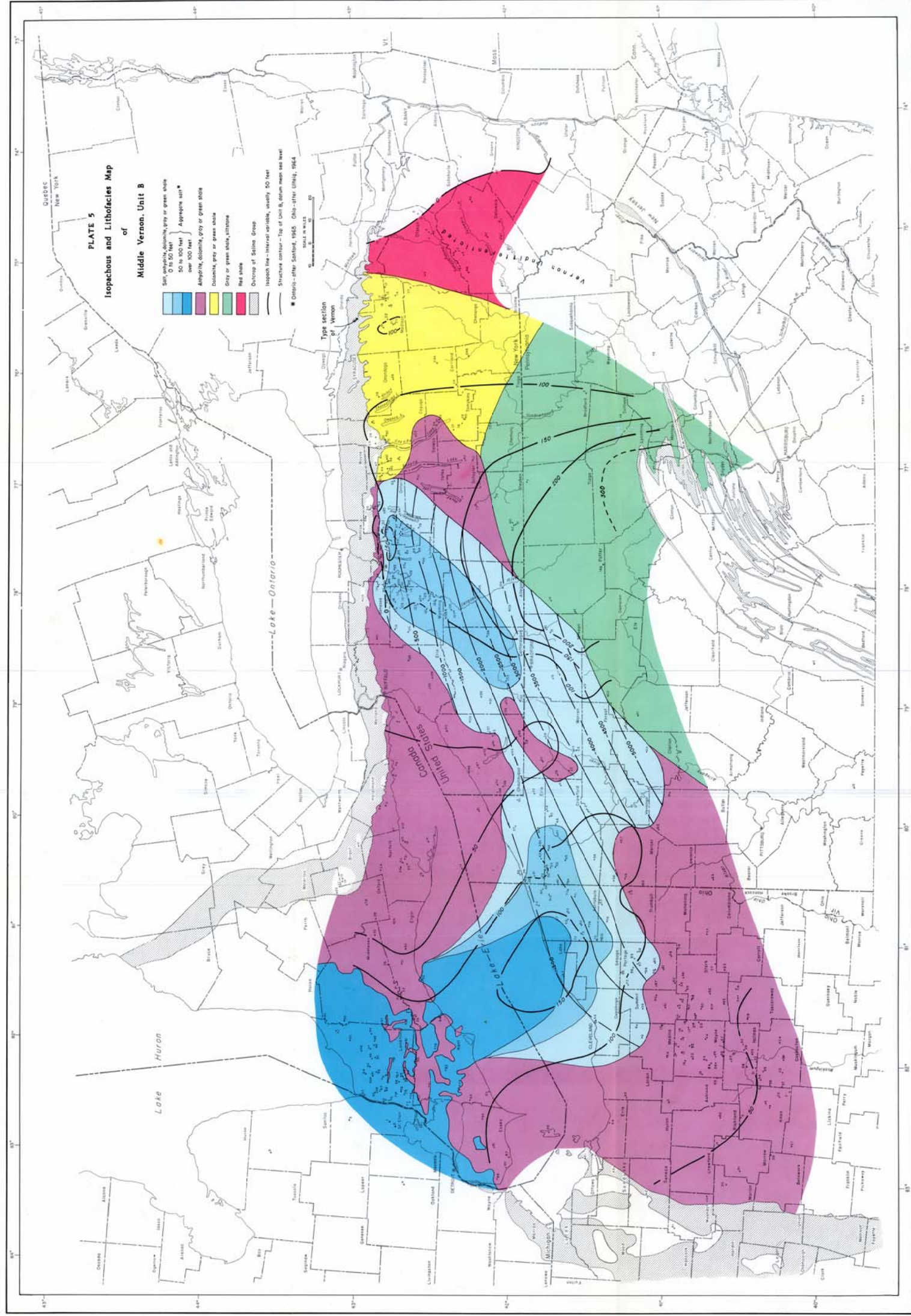
Figure 2-5. Isopachous and Lithofacies Map of Middle Vernon, Unit B (From Rickard [1969]).

11

Spatial differences between the B-Salt and D-Salt subcrop belts record the formerly dynamic nature of the Appalachian Foreland Basin. Between the times that the B-Salts and D-Salts accumulated, the depositional trough of the basin appears to have shifted approximately 80 kilometers to the southeast (see Figure 2-3). In addition, the Ohio Subbasin appears to have flexed upward; thus, eliminating the westerly salt depocenter that had previously existed for the B-Salts (Figure 2-6). The gentle upward flexure of the Ohio Subbasin also resulted in decoupling of the D-Salts of the Appalachian Basin from those of the adjacent Michigan Basin.

Near its northern limits in Ontario County, New York, the top of the D-Salt sequence resides at a subsurface elevation of about –122 meters msl (with a drilling depth 457 meters). It is noteworthy that the top of the D-Salt sequence is about 150 meters lower than the top of the B-Salt sequence even though it is a stratigraphically higher unit. This peculiar relationship was illustrated by Jacoby [1969] (Figure 2). Jacoby's Figure 2 is included in this report as Figure 2-7. The downlapping relationship between the Salina C and Salina D salt beds along the northern margin of the basin appears to be primarily the result of tectonic flexure as opposed to sea-level fluctuation.

Near its southern limits in north-central Pennsylvania, the Salina D resides at a subsurface elevation of about –2,100 meters msl with a drilling depth of 2,650–2,680 meters in Potter County. In northern Ohio, the D-Salts reside at a subsurface elevation of about –457 meters msl (see Figure 2-6). This elevation translates to drilling depths of about 640 to 730 meters across Cuyahoga, Lake, and Ashtabula Counties.

According to Rickard [1969], the D-Salts are thickest in a southwesterly trending region that extends from Schuyler County, New York, to Cameron County, Pennsylvania (see Figure 2-6). Within this 160-kilometer-long by 45-kilometer-wide region, Rickard [1969] reports D-Salt aggregate thicknesses in excess of 24 meters. Surrounding the D-Salt depocenter is a broad region where aggregate D-Salt thicknesses reportedly range between 12 and 24 meters.

Two to three salt beds comprise the D-Salt sequence. Although they are relatively thin, the D-Salts are pure and laterally persistent. In New York, discrete D-Salt bed thicknesses generally do not exceed 10.7 meters. Comparable maximum bed thicknesses are reported by Clifford [1973] for the individual salt beds in the subsurface of eastern Ohio.

Separating the D-Salts from the stratigraphically higher F-Salts is a 20- to 167-meter-thick sequence of dolomites, shales, and evaporites assigned to the Salina E. Much of this sequence across the northernmost regions of the basin is nonsalt-bearing. There is, however, at least one salt zone in the Salina E that attains a mappable thickness in the subsurface of southern New York, Pennsylvania, West Virginia, and Ohio. Rickard [1969] depicted the boundaries of the E-Salt in his isopachous and lithofacies map of the Lower Syracuse Formation, Units D and E (Figure 2-6 of this report). Clifford [1973] mapped the E-Salt in combination with the D-Salt sequence in southeastern Ohio. His isopach map is provided in Figure 2-8.
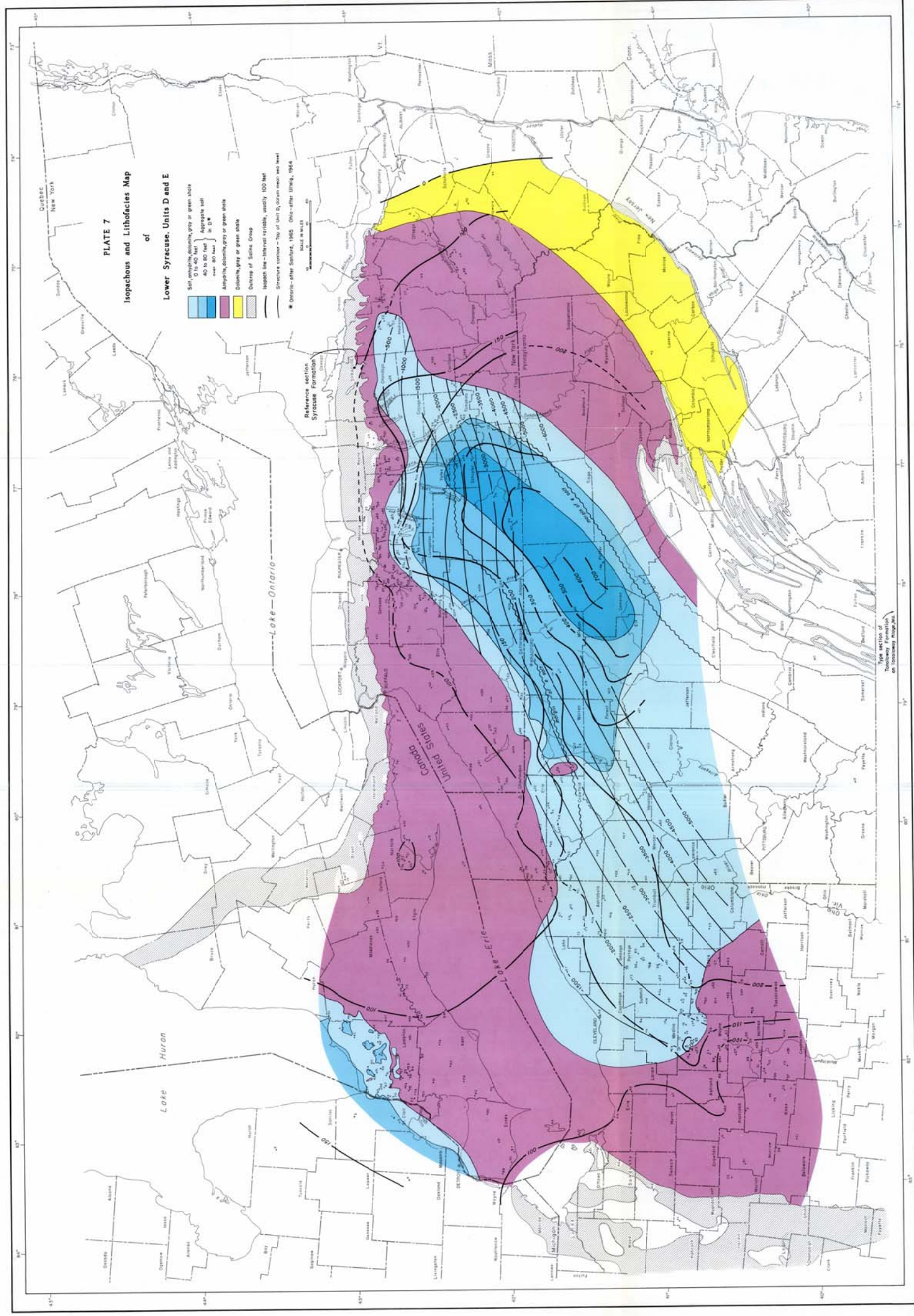
Figure 2-6. Isopachous and Lithofacies Map of Lower Syracuse, Units D and E (From Rickard [1969]).

13
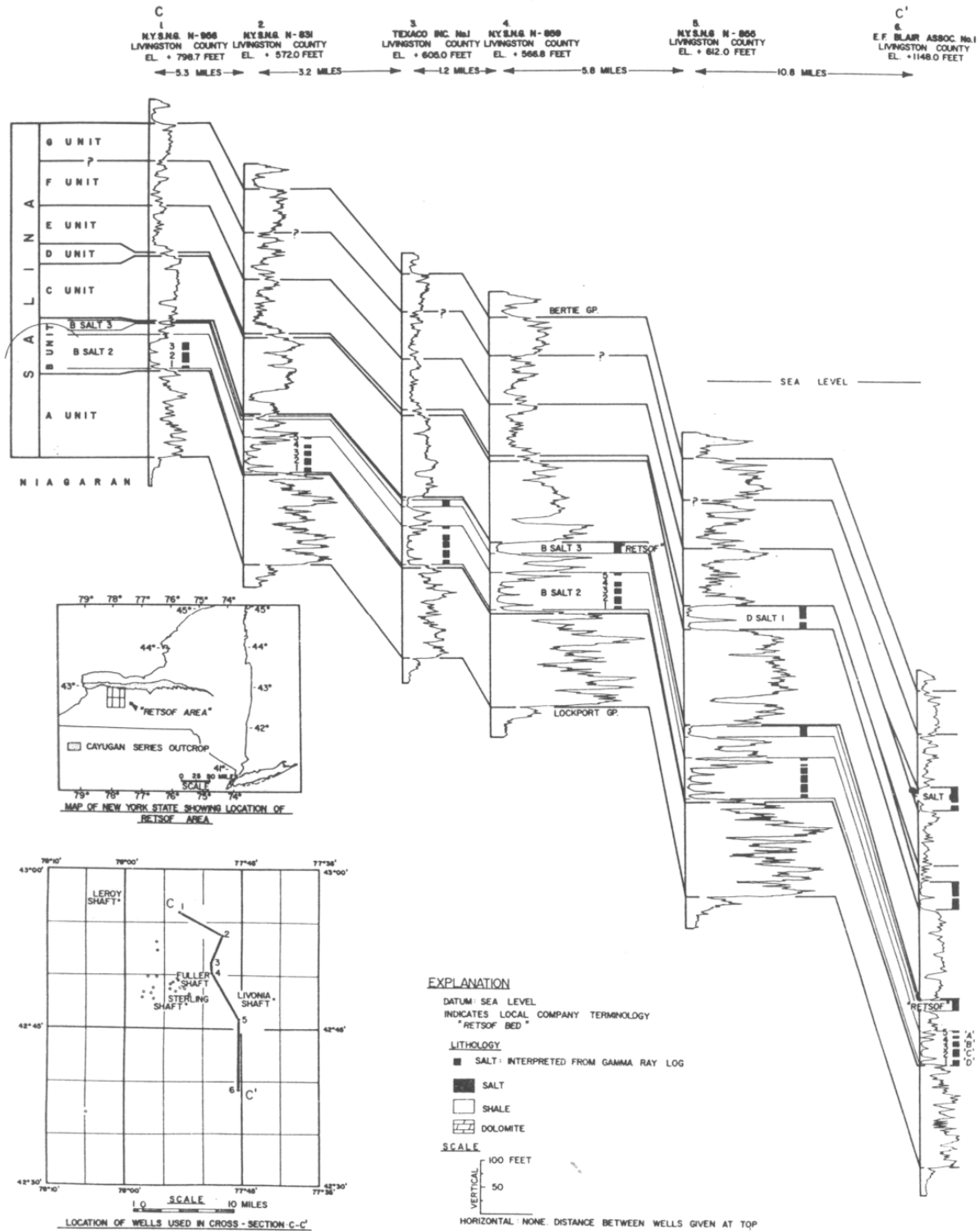
Figure 2-7. Correlated Gamma Ray Logs, Retsof Area, Livingston County, New York (From Jacoby [1969]).

14

E SALT (D AND E COMBINED SOUTH OF LINE)

Figure 2-8. Isopach Map of Combined D- and E-Salts Beneath Eastern Ohio (From Clifford [1973]).

15

2.2.3 Salina F-Salt Trends

The F-Salt sequence is, by far, the thickest salt-bearing zone of the three in the Salina Group. The F salts range in elevation from a high near Syracuse in Onondaga County of 20 meters above mean sea level. They occur as deep as about –785 meters msl in Sullivan County, Pennsylvania. It is, however, also the most structurally complex; it appears to have borne the brunt of much of the compressional tectonic forces imposed on Appalachian Basin strata during the late Paleozoic Alleghenian Orogeny. The New York, Pennsylvania, and West Virginia sections of the F-Salt sequence are intensely folded and faulted. Locally, the salt beds are also brecciated.

Rickard [1969] depicts a zone of F-Salt aggregate thickness in excess of 152 meters centered on Chemung and Tioga Counties in New York and Bradford County, Pennsylvania (Figure 2-9). Because of the substantial thicknesses attained by the F-Salts, the contour interval (250 feet) used by Rickard [1969] is large compared to the contour intervals used for the B-Salts (50 feet) and the D-Salts (40 feet). Although the salt beds commonly split locally into thinner discrete beds, and secondary structure complicates the stratigraphic sections in north-central Pennsylvania and central New York, four major salt beds are generally recognized [Rickard, 1969; Clifford, 1973]. In ascending order, these salt beds are designated F1 through F4.

Given the large contour interval used by Rickard [1969] for the F-Salts, little detail is provided in his contour map for the Ohio region. Additional detail is, however, provided by Clifford [1973] who published contour maps for each of the four discrete salt beds that comprise the F-Salt sequence in that region.

The relatively undeformed F-Salt sections of the Ohio Subbasin generally exhibit an upward bed thinning pattern. At their thickest in the depositional trough of the subbasin, the maximum thicknesses of the F1 through F4 beds are on the order of 33.5, 21, 7.6, and 4.6 meters, respectively (Clifford [1973], Plate 1).

The only region where there is an apparent exception to the upward bed-thinning trend is in southeastern Ohio near the West Virginia border. It is suspected that this region exhibits the more intense folding and faulting that is characteristic of the Pennsylvania and south-central New York sections. In this area, the F4 beds are considerably thicker (maximum of about 35.5 meters in Monroe County). This thickening pattern is likely to be tectonic as opposed to a primary depositional trend.

Because of structural deformation, it is difficult to reconstruct original stratigraphic patterns for the F-Salt sequence in south-central New York and Pennsylvania. Bed-by-bed correlation across even a single fold in south-central New York can be difficult because of the degree of folding and faulting. Primary depositional bedding has been completely obliterated [Goodman and Plumeau, 2004], and large rafts of the nonsalt interbeds can be observed in drill cores to be standing on end.

16

Figure 2-9. Salina Unit F-Salt Isopachous and Lithofacies Map (From Rickard [1969]).

17

2.3 REPRESENTATIVE STRATIGRAPHIC MODEL OF THE APPALACHIAN BASIN

As discussed above, the depth to the lowermost salt sequence (Salina B-Salt) varies significantly within the Appalachian Basin. The uppermost salt sequence (Salina F-Salt) is generally the thickest of the three major salt layers comprising the Salina Group. F-Salt subsurface depths vary from about 250 meters to more than 2,700 meters within the Appalachian Basin. The F-Salt trends are structurally complex and are intensely folded and faulted. As a result, the local stratigraphy at one location may not resemble the stratigraphy at another relatively close location. Because of variability in the formations throughout the Appalachian Basin, a single representative stratigraphic model of this formation cannot be clearly identified. However, the geologic analysis does provide a range for formation thicknesses, depths, and rock type which can be synthesized into a representative model of the Appalachian Basin for the purposes of this study.

Salt beds in the Appalachian Basin that are extremely shallow and those that are extremely deep are not well suited for natural gas storage. Assuming ground conditions are suitable for developing caverns at relatively shallow depths, the pressure range at which gas can be cycled in shallow caverns is relatively small since the maximum pressure must remain safely below the overburden pressure. As a result, extremely large caverns or a large number of caverns would be required to obtain any significant storage volume. Conversely, a large pressure range is possible for relatively deep caverns; however, the cost of wellbore casing and surface compression equipment make development of extremely deep caverns less economical. For this project, depths between 300 and 1,200 meters are proposed for the numerical evaluations of caverns in bedded salt. These depths fall within the possible range for top-of-salt depths that exist in the Appalachian Basin.

Although the total thickness reported for the F-Salt beds exceeds 150 meters in some areas, the reported thicknesses are the aggregate thickness of the salt and nonsalt interbeds. Figure 2-10 illustrates the cored portion of the Bale No. 1 Well, located 1 mile southwest of Cayuta in Schuyler County, New York. As shown in Figure 2-10, the salt beds at this location vary from less than 1 meter to about 40 meters in thickness. Similar thicknesses are also found for the nonsalt beds in this borehole. Relatively thick nonsalt beds within the cavern horizon can create problems during cavern development. Whereas thinner shale beds are likely to fall to the bottom of the cavern as small masses during solution mining, relatively thick nonsalt members are less prone to breaking apart and falling harmlessly into the cavern sump. As a result, relatively thick nonsalt beds are more likely to have deleterious affects on the leaching process and may even prevent the upward development of the cavern. For this project, the aggregate thickness of the salt formation was assumed to be less than 150 meters thick and is comprised of salt and shale beds less than 40 meters in thickness. The Salina Group salt and shale bed thicknesses of 40 meters or less is a reasonable assumption based on the geologic description of the Appalachian Basin at potential gas storage locations.
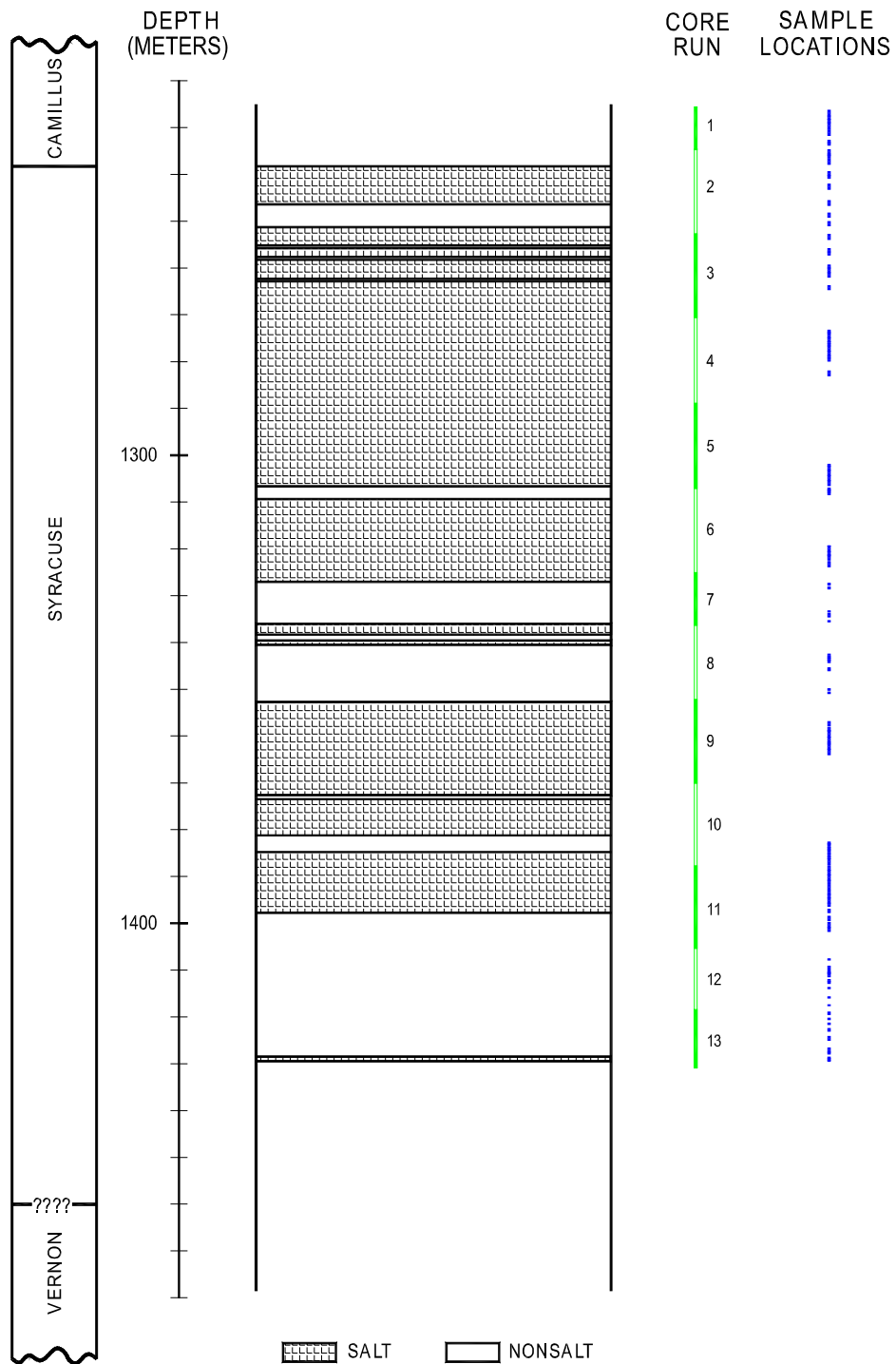
Figure 2-10. Bale Well No. 1 Stratigraphy and Core Intervals.

19

Figure 2-11 shows the proposed representative stratigraphic model of the Appalachian Basin for use during the numerical analysis task of this project. The proposed stratigraphy is comprised of three major sections. The uppermost section represents the bedded formation overlying the Salina Group and does not include any salt. This region is designated as being 213.4 meters thick; however, the top of this region does not necessarily correspond with ground surface. No differentiation is provided for this region in terms of the lithology because all the beds have been grouped into a single material to represent the "average" or combined response of the units overlying the Salina Group. Combining the sedimentary formations in this region simplifies the model; however, this simplification is not expected to have a significant impact on the modeling results. The effects of this region on the modeling results are diminished by the averaging of material properties and the remoteness of this region from the cavern horizon.

The middle section of the proposed stratigraphy represents a salt-bearing interval of the Salina Group. This section is composed of six salt beds having thicknesses varying from 9.1 to 38.1 meters and five shale beds ranging from 1.2 to 22.9 meters in thickness. Shale beds less than 1 meter thick do not provide significant structural support and are commonly assigned properties of the predominate joining lithology during numerical analyses of salt caverns. The combined thickness of the middle section of the representative stratigraphy is about 152 meters.

The bottom section of the model represents the "basement" formation underling the salt-bearing portion of the Salina Group. This region extends 243.8 meters below the salt section and does not contain salt. This region was simplified by grouping the different beds that comprise the Vernon Formation into a single material, similar to the upper section of the representative model. The combined extent of the three sections is 609.6 meters. The proposed representative model illustrated in Figure 2-11 provides a baseline stratigraphy from which modest changes can be specified for the comparative analyses performed in this study.
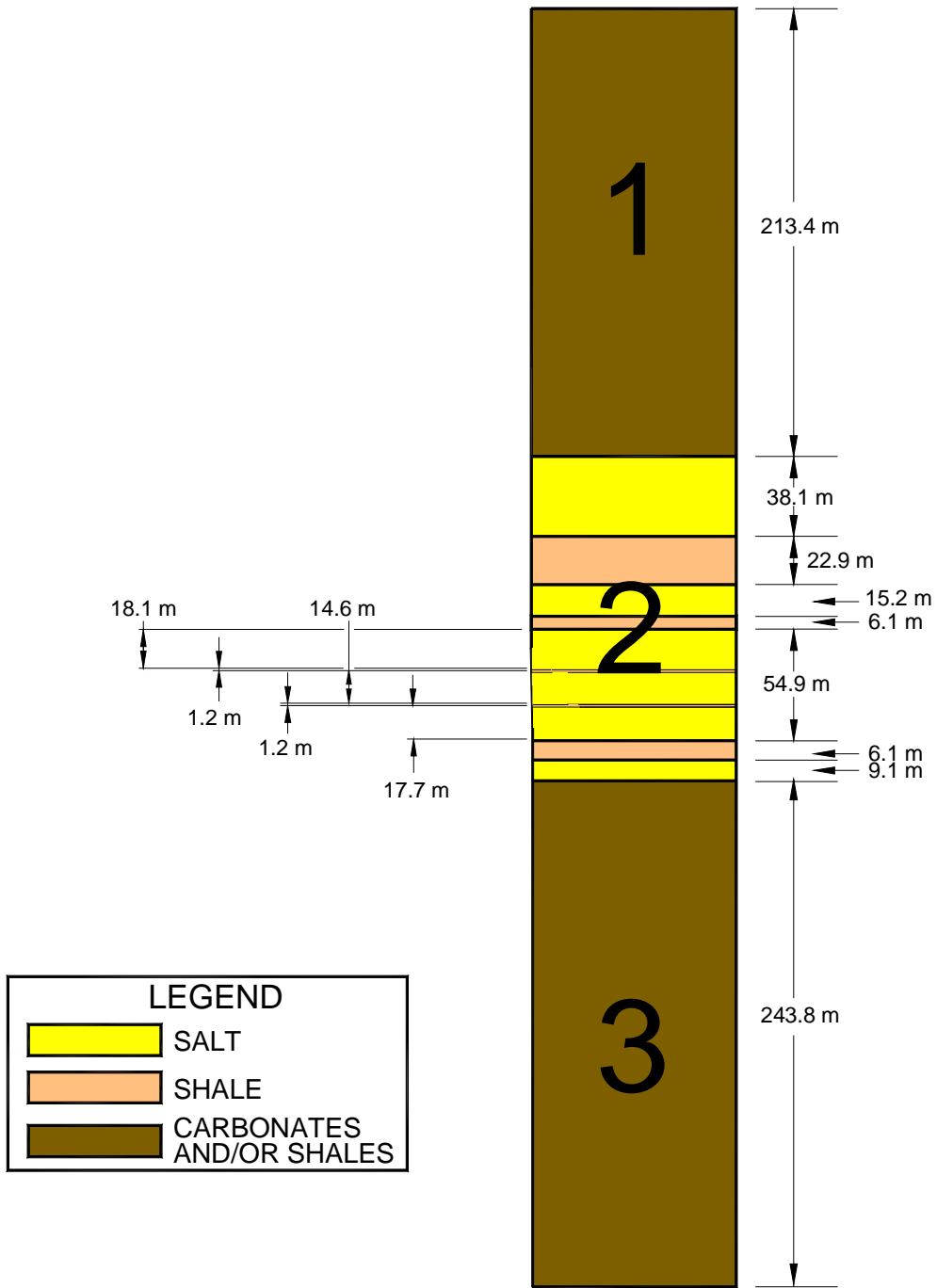
Figure 2-11. Representative Stratigraphy of Appalachian Basin.

3.0 LABORATORY TESTING AND ROCK PROPERTIES

The purpose of the laboratory testing effort is (1) to investigate the behavior of salt under load paths and states of stress that simulate those found in the field and (2) to acquire data for defining the constitutive models used to assess accurately the stability of the roof salt. All testing was performed on Cayuta salt recovered from Bale No. 1 Well [Nieland et al., 2001]. Bale No. 1 Well is located approximately 1 mile southwest of Cayuta in Schuyler County, New York. RESPEC conducted the tests at its facility in Rapid City, South Dakota. A description of specimen preparation, testing procedures, and machine calibration procedures is provided in Appendix A.

Three types of tests were performed for this study to collect data for defining the material behavior of bedded salt in the Appalachian Basin. The types of tests performed were:

- Confined constant strain rate (CSR) tests.

- Confined constant mean stress (CMS) dilation tests.

- Confined creep tests.

A total of 34 laboratory tests were performed: 4 constant strain rate strength tests, 23 constant mean stress tests, and 7 constant stress creep tests. This test data was combined with that of Brazilian, unconfined compressive, and creep tests obtained from other testing programs performed on Cayuta salt [Nieland et al., 2001]. Tests performed were subjected to triaxial extension and triaxial compression states of stress. The confined compression tests provided data for determining: (1) compressive strength, (2) Young's modulus of elasticity, and (3) Poisson's ratio. These strength and deformation properties are used directly in modeling of underground structures, in comparisons between rock types, and in examining variations in rock properties from one location to another. The constant mean stress dilation tests provide data used exclusively for determining the stress conditions that produce dilation (volume expansion as a result of microfracturing) in the salt. The creep tests were performed to assess the time-dependent deformation properties of the salt. The laboratory testing information and data are presented with the sign convention that compression is positive. Each of these tests types and results is discussed separately below.

3.1 CONSTANT MEAN STRESS TESTS

Twenty-three successful constant mean stress tests were conducted. These tests include: ten jacketed triaxial compression, seven jacketed triaxial extension, and six unjacketed triaxial compression tests. Jacketed specimens are isolated from the confining pressure fluid; whereas, the confining fluid is free to penetrate unjacketed specimens. Eighteen of the 23 test specimens were tested in their virgin condition following specimen preparation via machining. The

remaining five specimens were preconditioned either at a hydrostatic stress of 13.8 MPa or under a small shear load to reduce any initial damage that may have occurred to the salt core. The term *preconditioned* is used to describe specimens that are held under a hydrostatic stress (or some other conditioning state of stress) for a period of time to reduce or eliminate specimen damage that may have occurred during core drilling and handling or specimen preparation.

The dilation limit for each test was determined as the difference between axial and lateral stress at the point where the volumetric strain reached its maximum compaction value. The volumetric strain was calculated as the sum of the axial strain plus twice the lateral strain. The complete test matrix and results are summarized in Table 3-1, where σ_m is the mean stress and $\Delta\sigma_{dil} = \sigma_1 - \sigma_3$ is the stress difference where dilation initiates with σ_i, i = 1, 2, 3 representing the principal stresses. Other terms in Table 3-1 include the first invariant of the stress tensor $\left(I_1 = 3\sigma_m\right)$, the second invariant of the deviatoric stress $\left(J_2 = \frac{1}{2}s_{ij}s_{ji}\right.$ where $s_{ij} = \sigma_{ij} - \sigma_m\delta_{ij}$), and ψ (see Appendix F) is the Lode angle. Additional details on the test conditions and interpretation of results are given in the following sections and Appendix B.

3.1.1 <u>Mean Stress Effects</u>

Mean stress is known to suppress brittle deformation in most rocks, including salt. Ten jacketed constant mean stress tests were performed under triaxial compression states of stress and a loading rate of 0.02 MPa/s to determine the mean stress dependency of Cayuta bedded salt. These tests are referred to here as "CMC" tests and were performed on specimens that were not preconditioned. The mean stress specified for the tests ranged from 6.8 to 20.7 MPa. The dilation limits determined from these tests are provided in Table 3-1. Figure 3-1 provides a graphical illustration of the dilation limit dependency on mean stress. The linear dilation boundary determined by Ratigan et al. [1991] for Avery Island and Waste Isolation Pilot Plant (WIPP) salt is provided in Figure 3-1 for comparison. The results show that the dependency of the dilation limit on mean stress is nonlinear with respect to shear stress. Further, a nonzero intercept appears appropriate for Cayuta salt. The data define a distinct boundary with some variation at low mean stress. Close agreement was determined for the tests repeated at a mean stress of 13.8 MPa.

3.1.2 <u>Lode Angle Effects</u>

Typically, laboratory test data are collected from triaxial compression tests as illustrated in Figure 3-2. In a triaxial compression test, the magnitude of the compressive confining pressure is less than the magnitude of the compressive axial stress. Figure 3-2 also illustrates the triaxial extension test (referred to here as "CMX" tests) where the magnitude of the compressive confining pressure is greater than the magnitude of the compressive axial stress.

Table 3-1. Summary of Constant Mean Stress Dilation Testing

Specimen I.D.	Test Type	σ_m (MPa)	$\Delta\sigma_{dil}$ (MPa)	Dilation Stress State			Jacket? (Y/N)	Preconditioning N = none H = hydrostatic S = creep shear
				I_1 (MPa)	$\sqrt{J_2}$ (MPa)	ψ (deg)		
Triaxial Extension Tests on Virgin Specimens								
BAL1/151/4	CMX	5.20	7.50	15.60	4.33	−30	Y	N
BAL1/152/5	CMX	7.10	8.00	21.30	4.62	−30	Y	N
BAL1/124/4	CMX	10.60	9.50	31.80	5.48	−30	Y	N
BAL1/152/3	CMX	14.20	12.50	42.60	7.22	−30	Y	N
BAL1/124/1	CMX	17.70	14.50	53.10	8.37	−30	Y	N
BAL1/152/1	CMX	21.20	15.50	63.60	8.95	−30	Y	N
BAL1/151/1[a]	CMX	10.60	9.00	31.80	5.20	−30	Y	N
Triaxial Compression Tests on Virgin Specimens								
BAL1/151/5	CMC	6.80	12.00	20.40	6.93	30	Y	N
BAL1/124/5	CMC	10.30	15.00	30.90	8.66	30	Y	N
BAL1/229/3	CMC	10.33	12.50	30.99	7.22	30	Y	N
BAL1/151/2	CMC	13.80	16.00	41.40	9.24	30	Y	N
BAL1/125/4	CMC	13.80	16.50	41.40	9.53	30	Y	N
BAL1/126/3	CMC	13.80	15.00	41.40	8.66	30	Y	N
BAL1/124/3	CMC	17.20	20.00	51.60	11.55	30	Y	N
BAL1/152/2	CMC	20.70	22.00	62.10	12.70	30	Y	N
BAL1/152/4[a]	CMC	13.80	15.50	41.40	8.95	30	Y	N
BAL1/64/1	CMC	13.80	11.50	41.40	6.64	30	N	N
BAL1/126/1	CMC	13.80	7.50	41.40	4.33	30	N	N
Triaxial Compression Tests on Pretreated Specimens								
BAL1/186/1	CMC	13.80	20.50	41.40	11.84	30	Y	H
BAL1/126/5	CMC	13.80	9.50	41.40	5.48	30	N	H
BAL1/183/4	CMC	13.80	14.00	41.40	8.08	30	N	H
BAL1/182/1	CMC	13.80	26.00	41.40	15.01	30	N	S
BAL1/125/1	CMC	13.80	25.50	41.40	14.72	30	N	S

(a) Loading rate of 0.002 MPa/s with all other tests at 0.02 MPa/s.

While these two types of tests do not look substantially different, the results from these two types of tests can be dramatically different if the behavior of the material being tested depends on the intermediate principal stress. Rock salt is typically weaker in triaxial extension than triaxial compression states of stress. The six triaxial extension constant mean stress tests listed in Table 3-1 having a loading rate of 0.02 MPa/s were performed to address the Lode
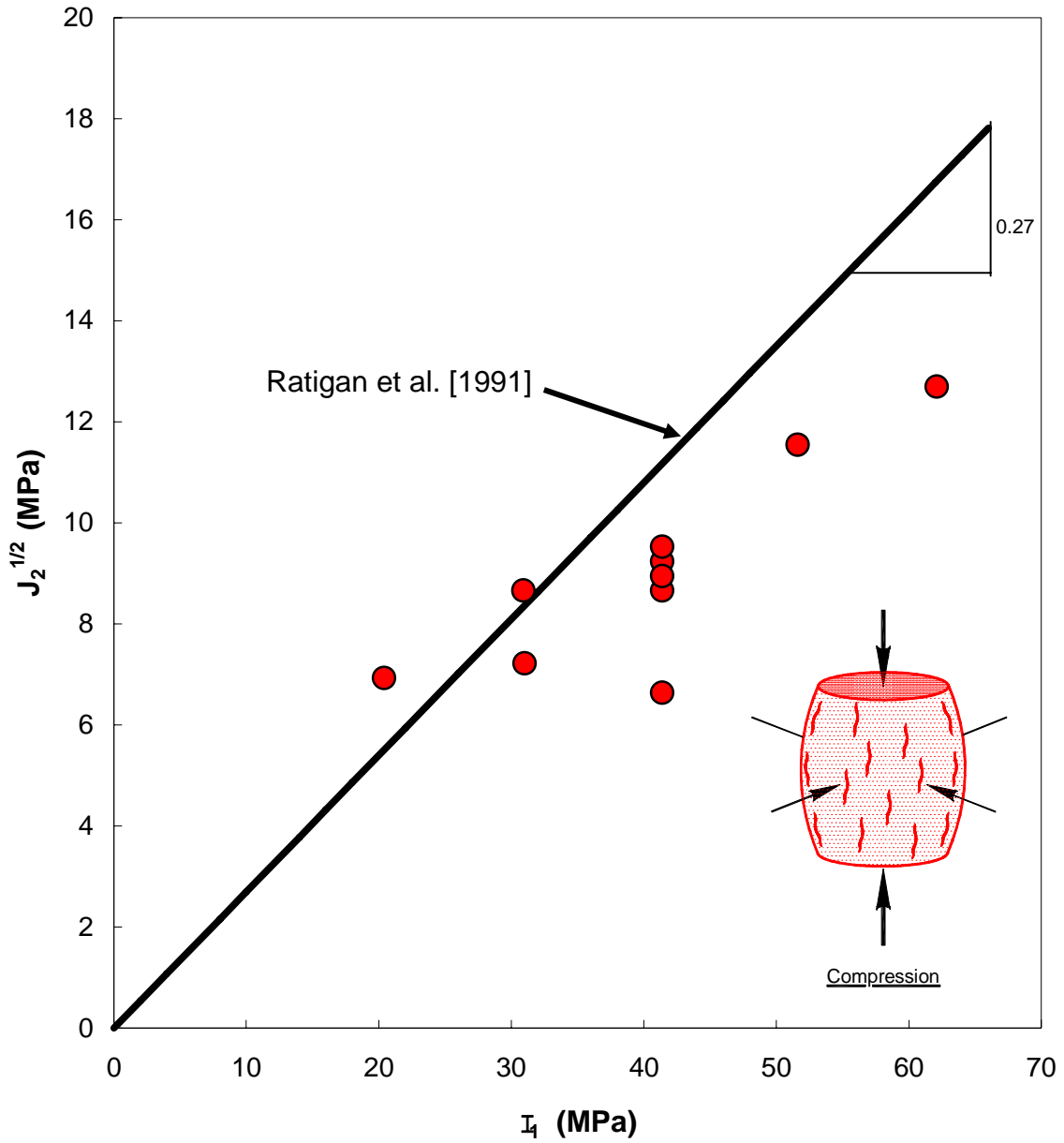
Figure 3-1. Dilational Stress States Determined From Jacketed Triaxial Compression Constant Mean Stress Tests on Virgin Salt Specimens.

Triaxial Compression

Triaxial Extension

$$\sigma_1 > \sigma_2 = \sigma_3 \qquad\qquad \sigma_1 = \sigma_2 > \sigma_3$$
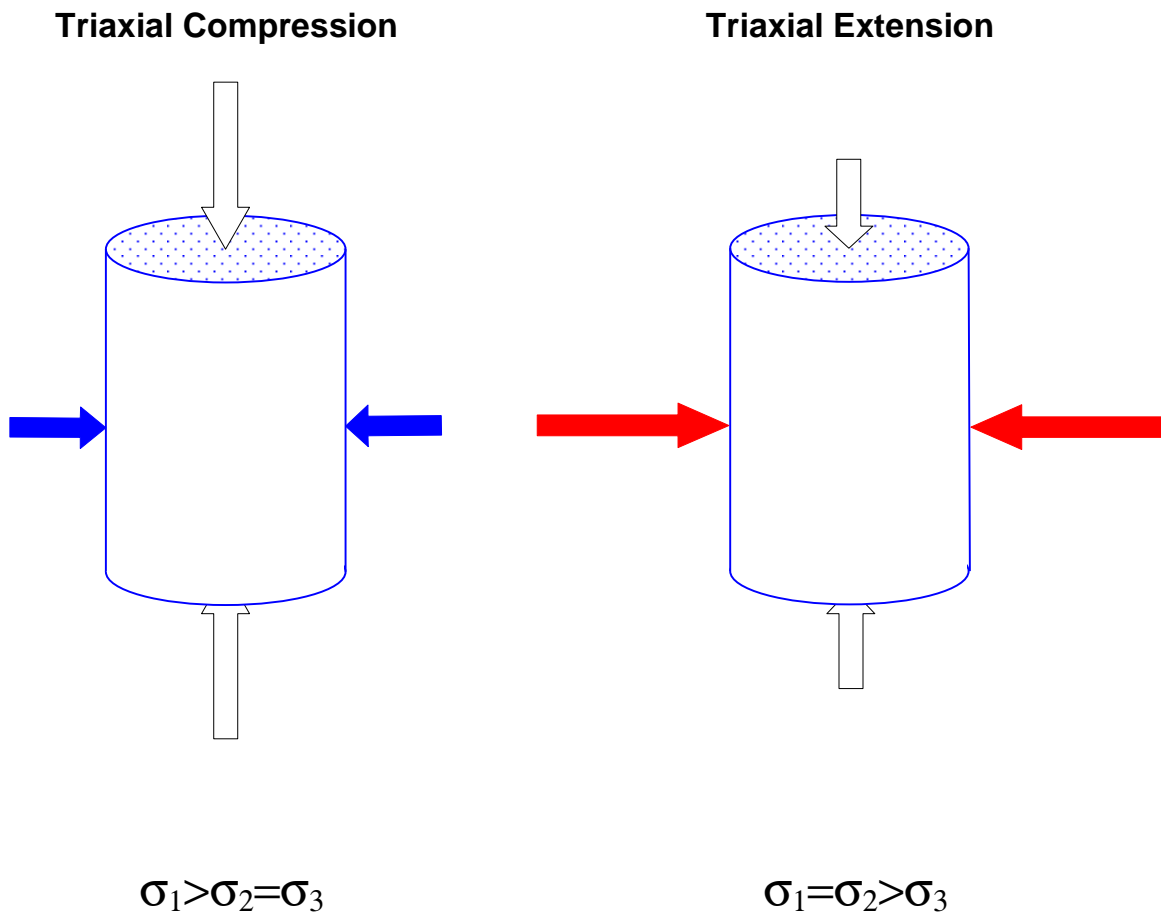
Figure 3-2. Illustration of Triaxial Compression and Triaxial Extension Tests Performed on Circular Cylindrical Specimens.

angle issue. The triaxial extension dilation limits determined from these tests are plotted as green triangles in Figure 3-3 for comparison with the triaxial compression results (plotted as red circles). The triaxial extension results indicate a nearly identical trend for the dilation limit dependency on mean stress; however, the dilation limit is approximately 30 percent lower than the results obtained at triaxial compression.

3.1.3 Rate Effects

The rate at which the axial load and confining pressure are changed remains constant throughout the duration of a constant mean stress test. All previous constant mean stress testing performed in the RESPEC laboratory were done using an axial loading rate of 0.02 MPa/s. At this loading rate, a typical constant mean stress test is completed in a few minutes. To investigate the possibility that the onset of dilation may be a function of the loading rate, one triaxial compression and one triaxial extension constant mean stress test were performed using an axial loading rate an order of magnitude slower than that typically used (0.002 MPa/s). The triaxial extension test (see Table 3-1, BAL/151/1) was performed at a mean stress of 10.6 MPa, and the triaxial compression test (BAL/152/4) was performed at a mean stress of 13.8 MPa. As shown in Figure 3-3, the dilation stress determined for these two tests do not differ significantly from the other tests performed at the same mean stress but at a higher loading rate.

3.1.4 Fluid Pressure Effects

To investigate the behavior of fluid pressure, the unjacketed triaxial compression constant mean stress tests listed in Table 3-1 were performed. The tests were performed on both virgin and preconditioned specimens at a common mean stress of 13.8 MPa. The introduction of the preconditioning variable provided data for investigating the presence (or absence) of preexisting damage in the so-called "virgin" specimens. The preconditioning treatments varied with some specimens simply held at a hydrostatic pressure while others were subjected to nondilational shear stresses imposed during creep tests. Five specimens listed in Table 3-1 were considered "preconditioned." Those five tests are listed again in Table 3-2, where additional details of their preconditioning treatments are given, and the dilation stress state results are repeated from Table 3-1. The preconditioning had significant effects, as will be discussed next.

All of the tests used to investigate fluid pressure effects were performed under a triaxial compression state of stress and at a mean stress of 13.8 MPa. All of these test results are shown in Figure 3-4 to give an overall comparison. Figure 3-4 plots axial stress difference (axial stress minus confining pressure) as a function of volumetric strain. The volumetric strain scale was expanded in Figure 3-4 to better illustrate the region where the specimens begin to dilate. The complete test curves show much larger volumetric strains (> 0.01 in some cases) than appear in Figure 3-4. As shown in Figure 3-4, the results vary considerably despite the same test conditions. These differences are believed to be attributable to the condition of the specimen at the time of testing.
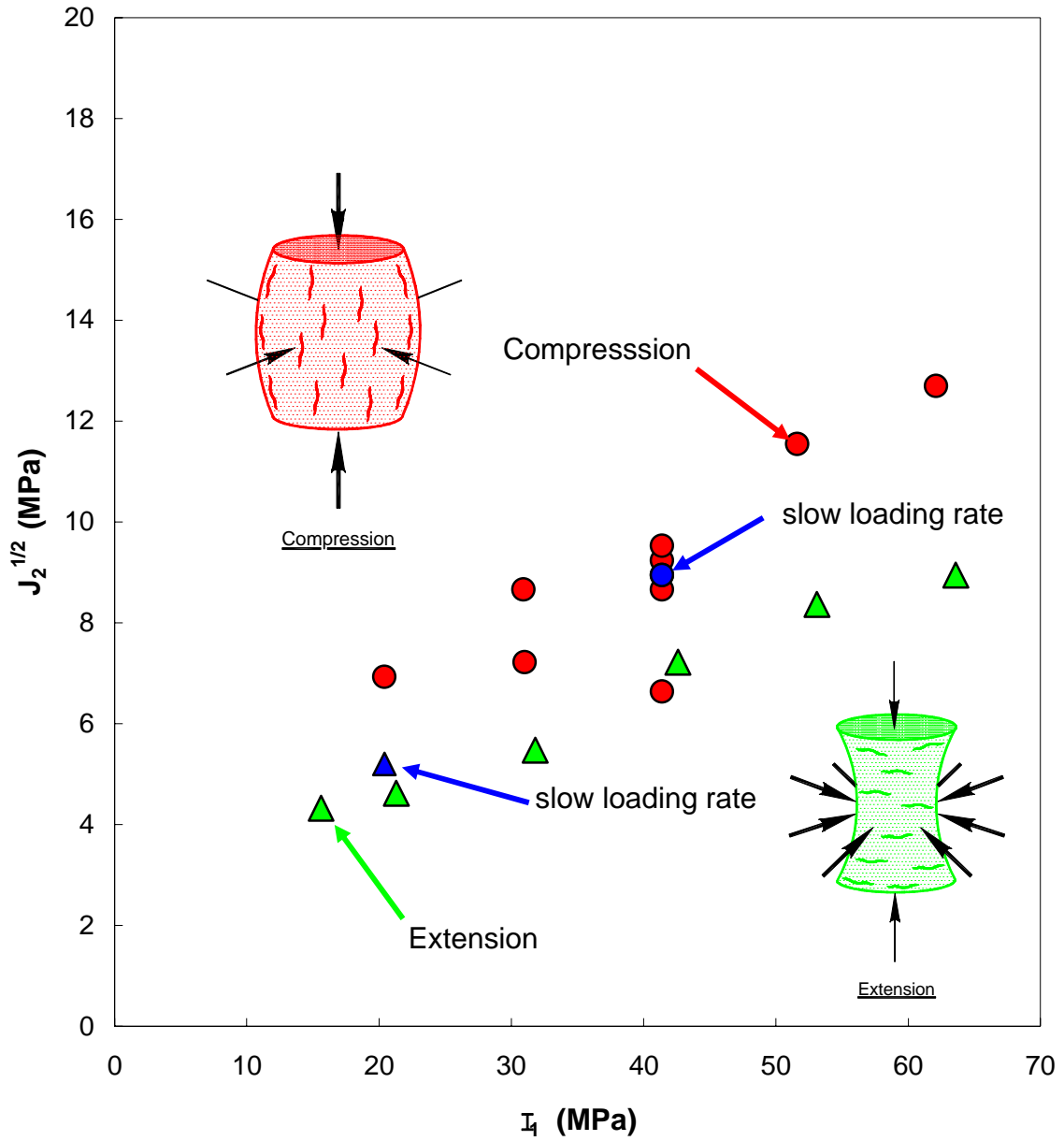
Figure 3-3. Comparison of Dilational Stresses Under Triaxial Compression and Triaxial Extension States of Stress.

Table 3-2. Preconditioning Treatments of Five Triaxial Compression Tests

Specimen I.D.	Dilation Stress State			Jacket? (Y/N)	Preconditioning Treatment (Specimens Jacketed During Preconditioning)
	I_1 (MPa)	$\sqrt{J_2}$ (MPa)	ψ (deg)		
BAL1/186/1	41.40	11.84	30	Y	1 stage of hydrostatic compaction at 20°C: (P = 27.6 MPa, 9 days)
BAL1/126/5	41.40	5.48	30	N	5 stages of hydrostatic compaction at 20°C: (P = 13.8 MPa, 20 hrs), (P = 27.6 MPa, 6 hrs), (P = 27.6 MPa, 18 hrs), (P = 13.8 MPa, 3 hrs), (P = 13.8 MPa, 1.5 hrs, jacket leak in final stage)
BAL1/183/4	41.40	8.08	30	N	1 stage of hydrostatic compaction at 55°C: (P = 27.6 MPa, 13 days)
BAL1/182/1	41.40	15.01	30	N	1 stage of shear compaction (creep) at 40°C: ($\sigma_a - \sigma_c$ = 20.7 MPa, σ_c = 27.6 MPa, 13 days)
BAL1/125/1	41.40	14.72	30	N	3 stages of shear compaction (creep) at 40°C: ($\sigma_a - \sigma_c$ = 20.7 MPa, σ_c = 27.6 MPa, 61 days), ($\sigma_a - \sigma_c$ = –20.7 MPa, σ_c = 27.6 MPa, 63 days), ($\sigma_a - \sigma_c$ = –20.7 MPa, σ_c = 34.5 MPa, 56 days)

The effect of the specimen jacket can be seen by comparing the results from jacketed and unjacketed virgin specimens, as shown in Figure 3-5. As seen in the figure, the unjacketed virgin specimens display a somewhat lower dilation stress followed by an equally reduced ability to support additional stress difference as straining continues.

The apparent "jacket effect" illustrated in Figure 3-5 was believed not to really exist and that it was likely a surrogate for preexisting damage. The preexisting damage in the specimens is assumed to be induced by one or all of the processes involved in obtaining a virgin laboratory test specimen; i.e., field coring, transport to the laboratory, or machining of the core to prepare the specimen. This preexisting damage idea was investigated by comparing the unjacketed virgin specimens with the unjacketed specimens that had received some preconditioning treatment that could eliminate or at least reduce the amount of preexisting damage. The comparison of these tests is shown in Figure 3-6, and the comparison indicates that the hypothesis is correct. That is, the jacket effect seen in Figure 3-5 is really just a manifestation of whether or not the specimen being tested is damaged sufficiently to allow the penetration of the confining fluid. This conclusion is reinforced in Figure 3-6, which shows the results obtained from jacketed virgin specimens and unjacketed specimens that received pre-conditioning. The results in Figure 3-6 are reasonably comparable, indicating that the "healing" treatment of the unjacketed specimens had reduced their permeability to the point where the confining fluid could not penetrate the specimen until the stress difference reached a point where brittle damage could begin again.
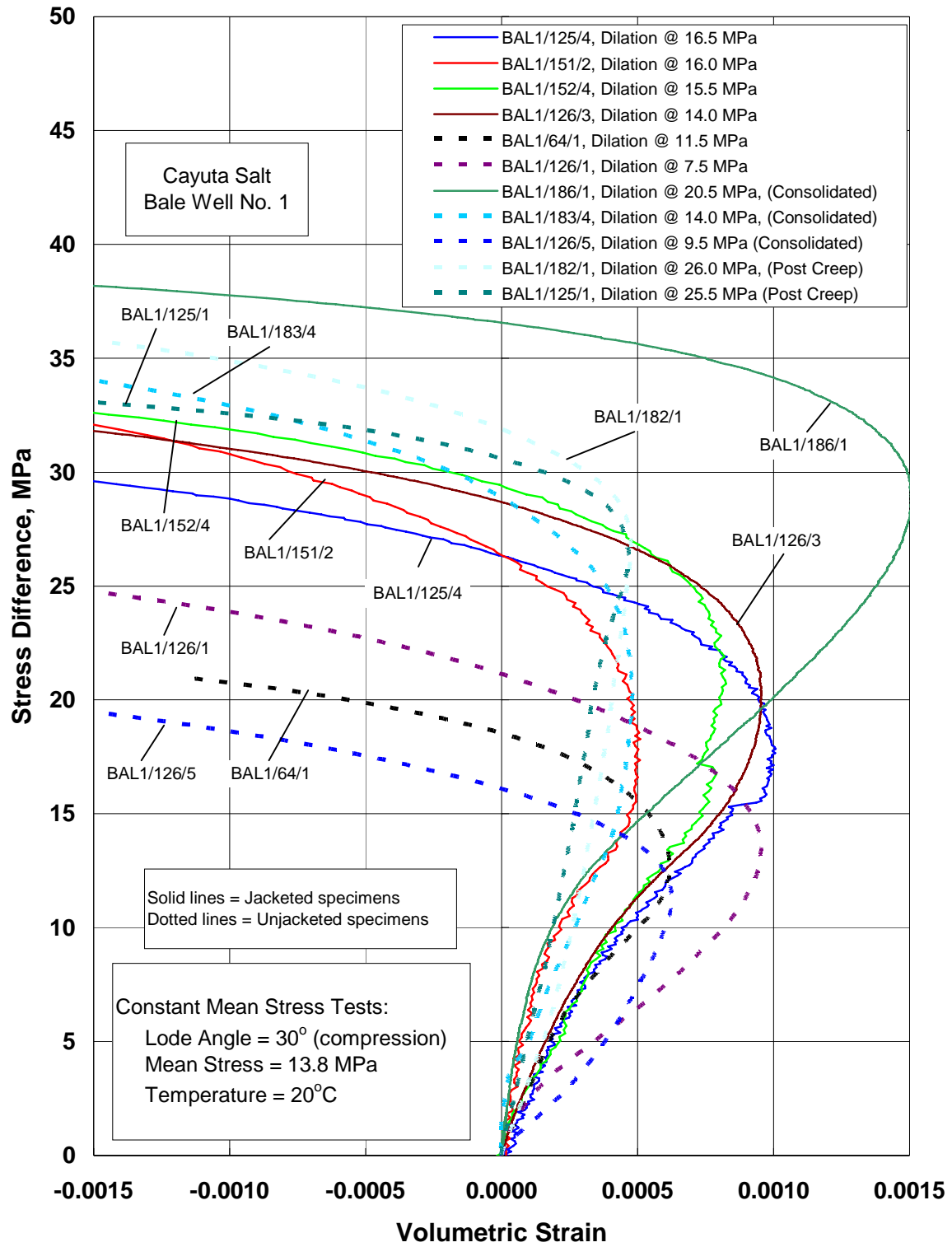
Figure 3-4. Comparison of Stress Difference as a Function of Volumetric Strain for all 13.8 MPa Constant Mean Stress Tests.
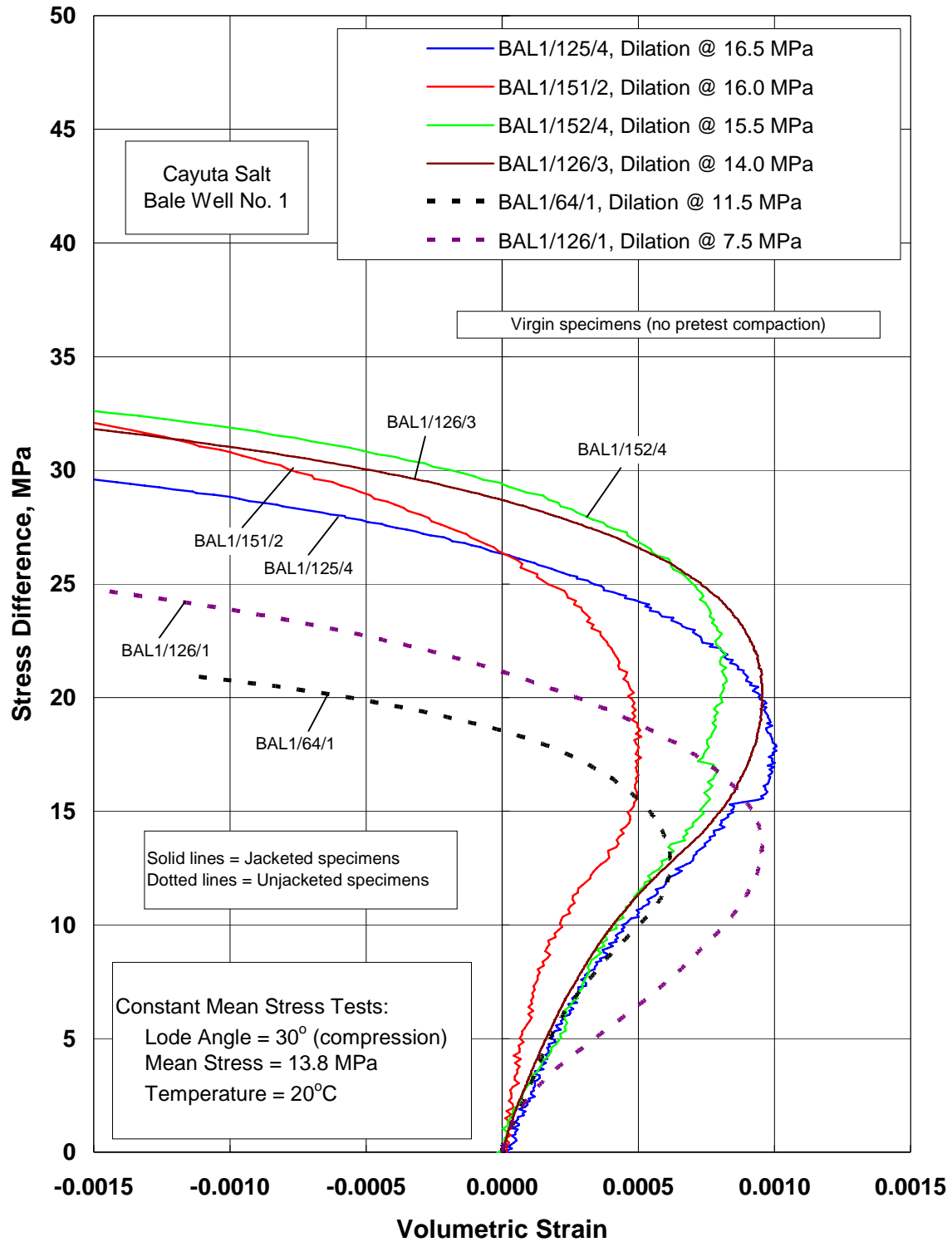
Figure 3-5. Comparison of Constant Mean Stress Tests Performed on Jacketed and Unjacketed Virgin Specimens.

31
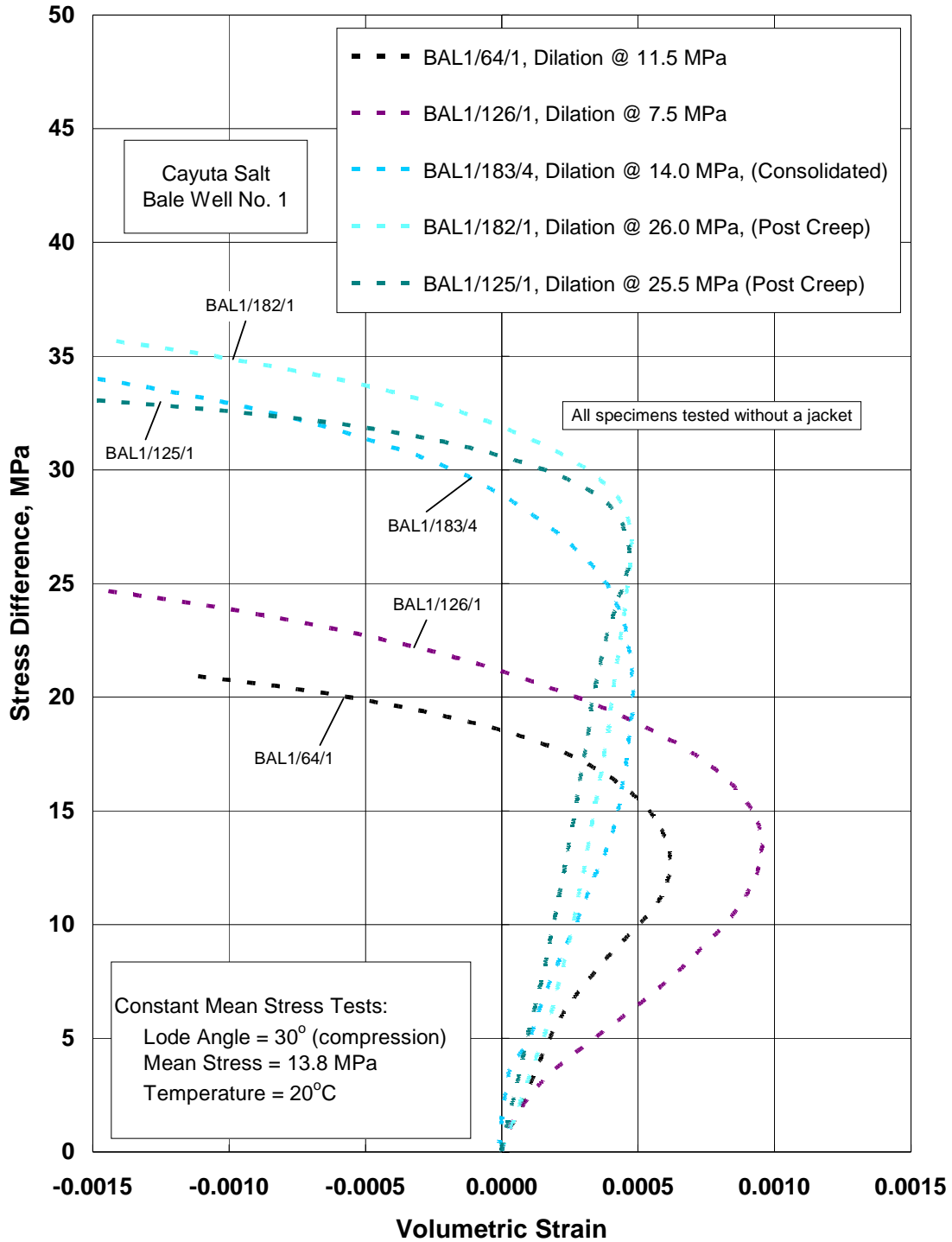
Figure 3-6. Comparison of Constant Mean Stress Tests Performed on Virgin and Preconditioned Unjacketed Specimens.

An interesting byproduct of the testing performed to create Figures 3-5 and 3-6 is the comparison of the effect that different preconditioning treatments can have. The authors and other researchers have noted that some shear-enhanced compaction often occurs when testing virgin specimens and that same observation is valid here, even on the specimens that were preconditioned with a sizeable hydrostatic pressure. To the contrary, the two specimens that were preconditioned with shear stress (by virtue of the fact that they were used for performing creep tests before the dilation tests were performed) exhibited much less shear-enhanced compaction. Apparently, the application of a shear stress that is still lower than the dilation limit aids in reducing the pore space in the salt and may be beneficial to the reduction of preexisting damage, which enhances the salt's ability to resist dilation. However, the data also indicate that once dilation has begun, the salt quickly exhibits a fairly uniform ability to support additional stress beyond the dilation limit.

The final conclusion drawn from the testing performed to investigate fluid effects is that the dilation limits established by RESPEC for triaxial compression tests in the past are probably conservative. The dilation data have typically been obtained from tests on jacketed, virgin specimens where the dilation stress for an individual test has been defined as the point where the curve begins to deviate from the nearly linear volumetric compaction region that occurs just before the maximum compressive volumetric strain is reached. The current data indicate that if any other measure of dilation stress or specimen treatment were used, the estimates of the dilation stress would be higher than traditionally measured. Additional discussion on the use of the constant mean stress test results to define the parameters of the material models that predict the dilation strength of salt is provided in Chapter 4.0.

3.2 CONSTANT STRAIN RATE TEST

Four constant strain rate tests were performed at a temperature of 20°C (68°F) on the Cayuta salt at an axial strain rate of $10^{-4}\,s^{-1}$. These tests were performed to further investigate the effects of fluid pressure and to provide strength and elastic constants (Young's modulus and Poisson's ratio). Three of the tests were performed on unjacketed specimens under confining pressures of 0.69, 1.38, and 3.44 MPa. The fourth test was performed on a jacketed specimen with a confining pressure of 1.38 MPa. The results of these four tests were compared with those obtained from a previous laboratory study using jacketed specimens on Cayuta salt (reported by Nieland et al. [2001]). The tests from the previous study were also run at 20°C and an axial strain rate of $10^{-4}\,s^{-1}$.

In all tests, an unload/reload cycle was performed to generate data for estimating values of the elastic moduli. The axial loading was then resumed and continued until the axial strain transducer reached its limit of about 7.5 percent strain or the specimen failed. The test results for the four tests performed for this study are included in Appendix C in figures that plot axial stress difference versus axial and radial strain. The strength and elastic properties measured

are summarized in Table 3-3. The strength reported in Table 3-3 is the maximum axial stress difference applied to the specimen. Results are provided for the jacketed specimens reported by Nieland et al. [2001] as well as those obtained from this study with and without jacketing the specimens.

Table 3-3. Summary of Constant Strain Rate Test Results

Nieland et al. [2001] Results				
Specimen I.D.	Confining Pressure (MPa)	Jacketed Specimen		
		Strength σ_{max} (GPa)	Young's Modulus (GPa)	Poisson's Ratio
BAL1/1/82/1	0.69	24.54	23.7	(a)
BAL1/1/86-1/2	0.70	29.48	25.0	0.49
BAL1/1/82/2	1.38	41.57	28.1	0.50
BAL1/1/86-1/2	1.38	>35.86	28.5	0.33
BAL1/1/85/1	3.45	48.44	30.3	0.30
BAL1/1/86-2/1	3.45	46.92	27.8	0.30
Current Project Results				
Jacketed Specimen				
BAL1/1/180/3	1.38	28.9	23.3	0.17
Unjacketed Specimen				
BAL1/1/183/1	0.70	28.2	23.1	0.12
BAL1/1/183/3	1.38	32.8	24.9	0.15
BAL1/1/182/4	3.45	29.5	19.2	0.25

(a) Poisson's ratio greater than 0.5.

As shown in Table 3-3, Young's modulus varies from 23.3 to 30.3 GPa for the jacketed specimens, with an average value of 26.7 GPa. The value of Young's modulus determined from the unjacketed specimens varied from 19.2 to 24.9 GPa, with an average value of 22.4 GPa. The average values determined for Poisson's ratio for the jacketed and unjacketed specimens were 0.35 and 0.17, respectively. Thus smaller values were obtained for Poisson's ratio for the unjacketed tests compared to the jacketed tests. Two of the three values for Young's modulus obtained from the unjacketed tests fall within the range of those for the jacketed specimens. The third result is slightly lower than the range obtained for the jacketed specimens.

As shown in Table 3-3, the strength determined for the unjacketed specimens at confining pressures of 0.69 and 1.38 MPa fall within the range of those tests performed on jacketed specimens at the same confining pressure. The strength determined for the test performed on the unjacketed specimen using a confining pressure of 3.48 MPa was 29.5 GPa. This value is considerably lower than the strength results of the two tests performed at the same condition on jacketed specimens (48.44 and 46.92 GPa). Although no explanation can be given for the lower strength observed for the unjacketed specimen performed with a confining pressure of 3.48 MPa, the other results suggest that fluid pressure does not influence the ultimate strength of salt for the range of pressures examined in these tests.

3.3 CONSTANT STRESS CREEP TESTS

3.3.1 <u>Creep Test Results</u>

Seven constant stress creep tests were performed to help characterize the time-dependent behavior of Cayuta salt under triaxial compression and extension states of stress. Two tests were performed at a temperature of 40°C (104°F) and five tests were performed at a temperature of 55°C (131°F). The initial plan was to perform all the tests at the same temperature (40°C) until near steady-state conditions were achieved. However, the slow creep rate that Cayuta salt exhibits at this temperature indicated that an extremely long time would be required to complete the desired test matrix. Because the time to reach steady-state is typically shorter at higher temperatures, the duration of each test could be reduced if the temperature was increased. For this reason, the test matrix was modified to include the five tests at the elevated temperature of 55°C. Table 3-4 identifies the conditions at which each creep test was performed. The test conditions given in the table are presented in two formats: (1) in terms of confining pressure, σ_{conf}, and axial stress difference, $\Delta\sigma$ (axial stress minus confining pressure); and (2) in terms of the stress invariants I_1, $\sqrt{J_2}$, and ψ.

As shown in Table 3-4, all but one of the tests included multiple stages. Multiple stages were used to determine the effects of Lode angle on the creep response of Cayuta salt. Using the same specimen to investigate the potential effect of Lode angle makes assessment of the results straightforward because specimen-to-specimen variability does not have to be considered. Thus if differences are noted in the responses under compression and extension, these differences are not attributable to variations in the specimens (e.g., grain size, impurity content, or different load history).

The specimens were initially hydrostatically loaded to the confining pressure level specified for the first stage, then the stress difference was applied to the specimen. When the stage was complete, the stress difference was removed and the hydrostatic state was adjusted to the confining pressure needed for the next stage. The stress difference was then reapplied and the new stage was begun. For a stage performed at a triaxial compression state of stress, the axial

Table 3-4. Creep Test Matrix

Test No.	Specimen I.D.	Test Stage	I_1 (MPa)	$\sqrt{J_2}$ (MPa)	Temperature (°C)	Confining Pressure (MPa)	Stress Difference[a] (MPa)	Steady-State Strain Rate (s^{-1})
1	BAL1/48/4	1	69	8	40	27.58	–13.79	$-1.85(10^{-10})$
		2	69	8	40	18.39	13.79	$1.18(10^{-10})$
		3	69	8	40	27.58	–13.79	$-1.46(10^{-10})$
		4			40	A series of short duration compression/extension cycles		
2	BAL1/125/1	1	103	12	40	27.58	20.69	$7.30(10^{-10})$
		2	62	12	40	27.58	–20.69	$-6.48(10^{-10})$
3	BAL1/179/1	1	69	8	55	27.58	–13.79	$-1.04(10^{-9})$
		2	69	8	55	18.39	13.79	$8.87(10^{-10})$
		3			55	A series of short duration compression/extension cycles		
4	BAL1/180/2	1	69	8	55	18.39	13.79	$1.96(10^{-9})$
		2	69	8	55	27.58	–13.79	$-2.06(10^{-9})$
		3	69	8	55	18.39	13.79	$2.10(10^{-9})$
		4	69	8	55	27.58	–13.79	$-2.20(10^{-9})$
5	BAL1/179/2	1	69	10	55	17.24	17.24	$2.28(10^{-9})$
		2	69	10	55	28.73	–17.24	$-2.90(10^{-9})$
		3			55	A series of short duration compression/extension cycles		
6	BAL1/179/4	1	69	10	55	28.73	–17.24	$-2.18(10^{-9})$
		2	69	10	55	17.24	17.24	$-2.09(10^{-9})$
		3			55	A series of short duration compression/extension cycles		
7	BAL1/182/2	1	69	14	55	31.03	–24.13	(b)

(a) Stress difference is defined as axial stress minus confining pressure; therefore, all triaxial extension tests are negative.

(b) This test was terminated because of machine limitations before obtaining a nearly steady-state strain rate.

stress was increased while holding the confining pressure constant. For a stage performed at a triaxial extension state of stress, the axial stress was decreased while the confining pressure was held constant. Also given in Table 3-4 are the steady-state axial strain rates observed in each long-term stage. The steady-state strain rate was estimated from the final 2 days of data collected at the end of each stage.

The data in Table 3-4 provide strong evidence that Lode angle does not affect the steady-state strain rate of Cayuta salt, at least for the stresses and temperature investigated. This is evident because the steady-state strain rates at different Lode angles for any single test have nearly identical magnitudes and only the sign changes. The fact that the strain rates vary somewhat among the tests is attributed to specimen-to-specimen variation. The test records for each of the specimens listed in Table 3-4 are contained in Appendix D where plots of strain-versus-time are presented for each specimen. The loading conditions are also contained in the plots. The strain measure used in the plots is total strain. Total strain includes not only the creep strain accumulated while stress is held constant, but also the elastic and inelastic strains induced during changes in stress.

Figures 3-7 and 3-8 provide the axial strain versus time response for the two multistage compression/extension creep tests (BAL1/179/1 and BAL1/180/2) performed at 55°C with a stress difference of 13.8 MPa ($\Delta\sigma = \sqrt{3J_2}$). Within each test, all stages were completed at the same mean stress and stress difference magnitude with only the Lode angle changing between stages. These two tests are typical of the results obtained for the entire suite of creep tests and exemplify the behavior of salt creep under triaxial extension and compression states of stress. As seen in Figures 3-7 and 3-8, each time the Lode angle was changed, a significant transient response was observed. A possible explanation for this behavior is that the hardening of salt is anisotropic; however, an explanation for this behavior could not be concluded from this study.

At the end of the tests performed on specimens BAL1/48/4, BAL1/179/1, BAL1/179/2, and BAL1/179/4, a relatively rapid cyclical load path was imposed that alternated between triaxial compression and extension while holding I_1 and J_2 constant to investigate how the transient behavior of the salt changes with Lode angle. Additional insight into the transient behavior of the salt is provided in Figures 3-9 and 3-10. These figures present the results during the third stage of the tests performed on BAL1/179/1 and BAL1/179/2 listed in Table 3-4.

In Figure 3-9, the Lode angle was cycled between −30° (extension) and 30° (compression) at equal intervals of time (1 week). Throughout the cycling stage, the mean stress and stress difference were held constant at the values used in the first two stages (I_1 = 69 MPa, $\sqrt{J_2}$ = 8 MPa). After the first cycle, the behavior settled into a pattern where the extensional deformation over a 1-week period exceeded the compressive deformation from the previous 1-week period. This result indicates that the magnitude of the transient strain rate is somewhat dependent on Lode angle; i.e., strain rate magnitudes are larger at the extension Lode angle of −30° than they are at the compression Lode angle of 30°. In Figure 3-10, the Lode
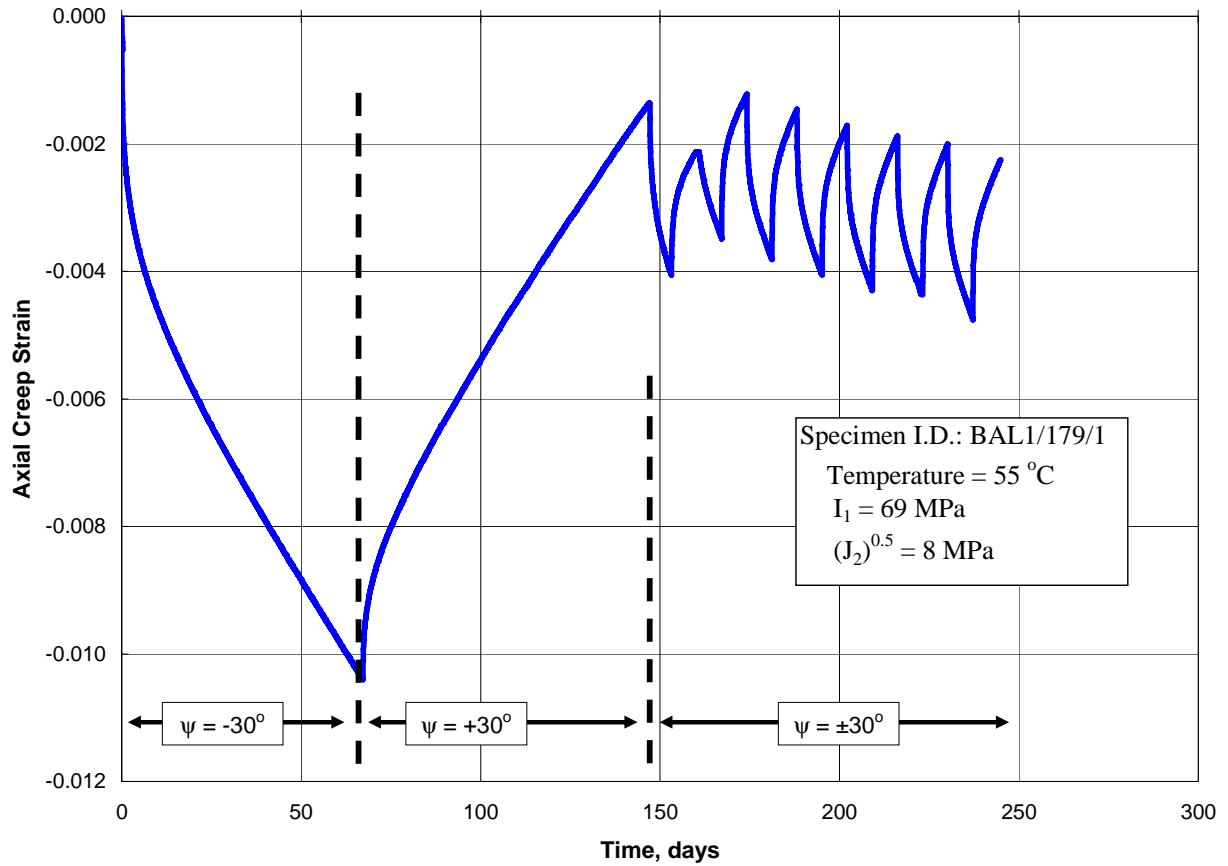
Figure 3-7. Compression/Extension Creep of BAL1/179/1 at 55°C and a Stress Difference of ±13.8 MPa ($\sqrt{J_2}$ = 8 MPa).
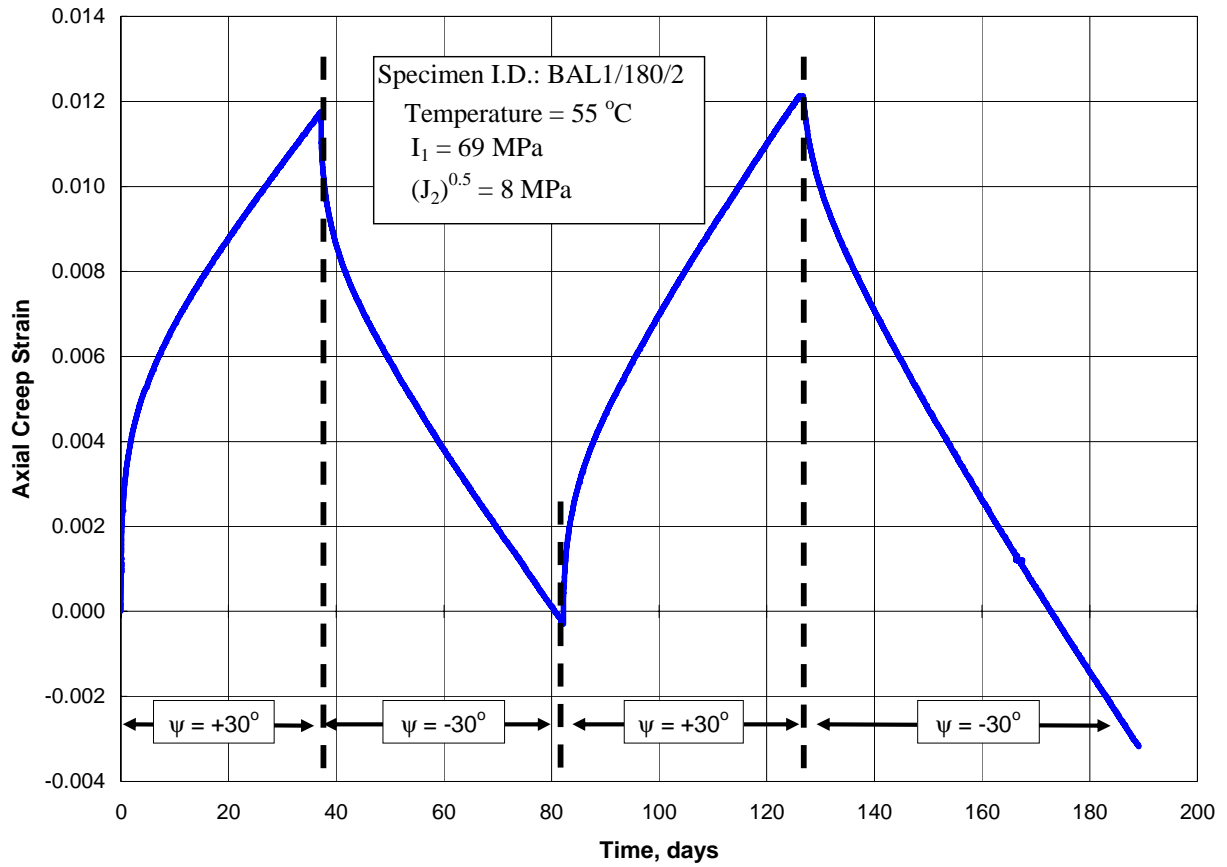
Figure 3-8. Compression/Extension Creep of BAL1/180/2 at 55°C and a Stress Difference of ±13.8 MPa ($\sqrt{J_2}$ = 8 MPa).
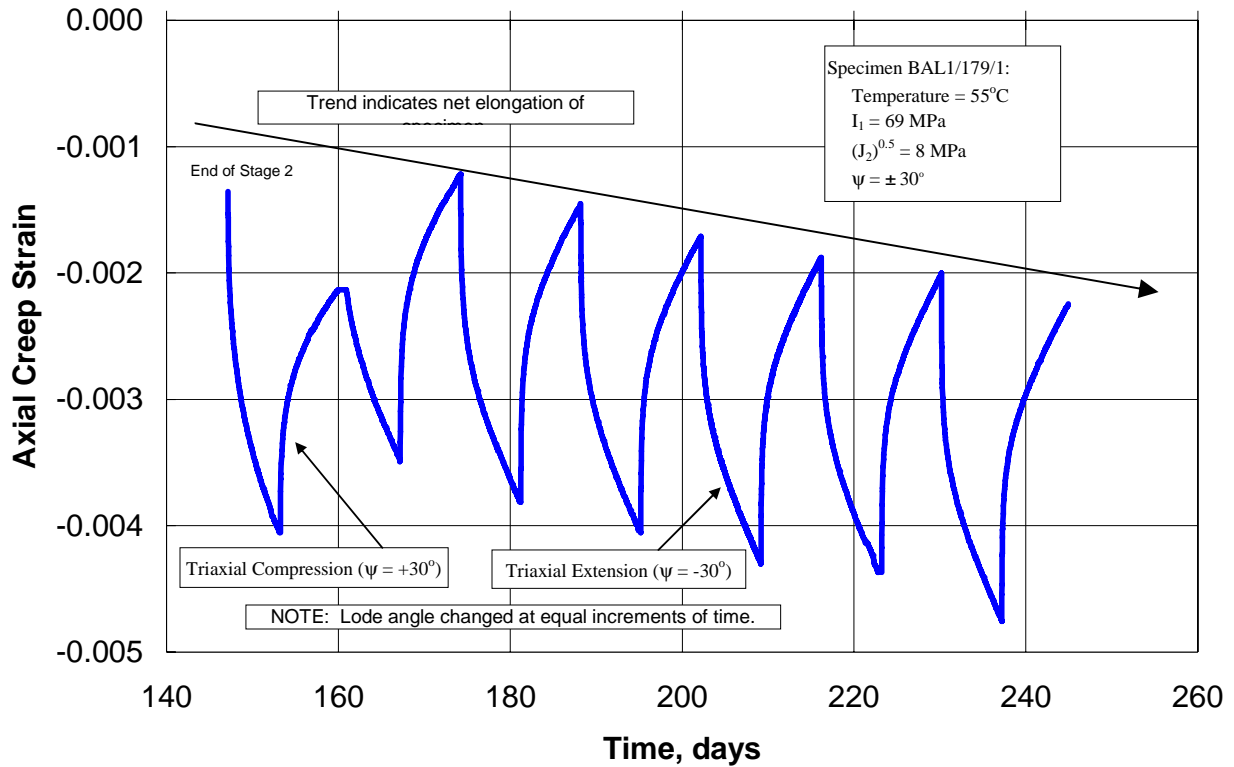
Figure 3-9. Strain-Controlled Cyclic Loading of BAL1/179/1 at 55°C and a Stress Difference of ±13.8 MPa ($\sqrt{J_2}$ = 8 MPa).
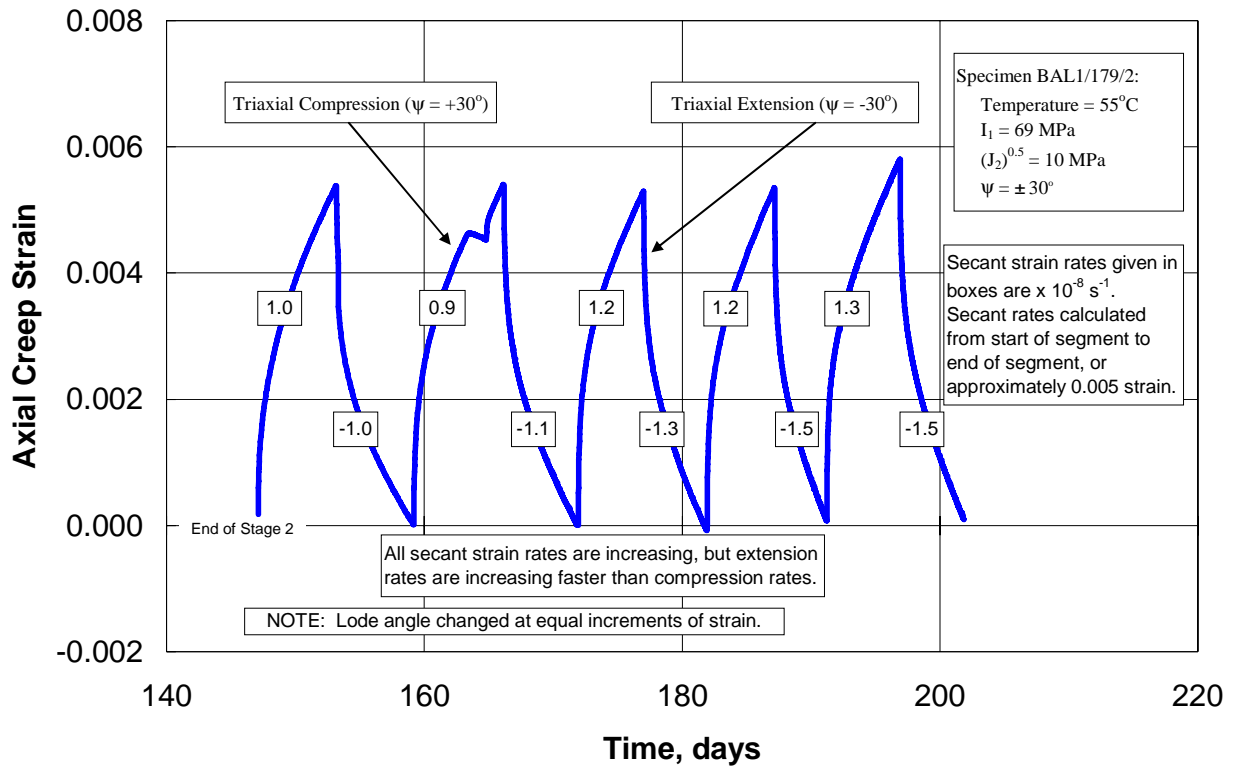
Figure 3-10. Time-Controlled Cyclic Loading of BAL1/179/2 at 55°C and a Stress Difference of ±17.2 MPa ($\sqrt{J_2}$ = 10 MPa).

41

angle was cycled between –30° (extension) and 30° (compression) at equal intervals of strain (~0.005).   As with the previous cyclic test, the mean stress and stress difference were held constant at the values used in the first two stages (I_1 = 69 MPa, $\sqrt{J_2}$ = 10 MPa).

At first glance, Figure 3-10 would appear to contradict the trend identified in Figure 3-9 because it appears that the net elongation of the specimen has disappeared. This difference between the two figures occurs because the loading conditions are different. In Figure 3-9, the Lode angle was cycled at equal intervals of time to affect a time-controlled test where strain is the response variable. In Figure 3-10, the Lode angle was cycled at equal intervals of strain to affect a strain-controlled test where the material response is reflected in the length of the time interval between cycles.

A secant strain rate for each of the equal strain segments in Figure 3-10 was calculated using the beginning and ending data points from each segment. Those secant strain rates are shown in the boxes superposed over each segment in the figure.   The secant strain rates indicate that the average transient strain rate is gradually increasing as cycling proceeds and this leads to the apparent decrease in time interval between peaks (an increase in cycle frequency).   Moreover, the transient strain rates at a Lode angle of –30° (extension) are increasing faster than the transient strain rates exhibited during triaxial compression. The fact that the extensional strain rates are outpacing the compression strain rates means that the specimen would exhibit a net elongation if the Lode angle were cycled at equal intervals of time instead of equal intervals of strain. This result agrees with the net elongation identified in Figure 3-9, and the two tests are actually leading to the same conclusion that the magnitude of transient strain rate depends upon the value of the Lode angle with the larger strain rate magnitudes occurring under a state of triaxial extension.

3.3.2 M-D Model for Salt Creep

The creep model used in this study is based on the M-D model originally proposed by Munson et al. [1989] but updated by DeVries et al. [2002]. The M-D constitutive model has been found to perform reasonably well in fitting data from laboratory constant-stress tests and in predicting the response of laboratory, field, and bench-scale tests performed on salt from the WIPP site in New Mexico. The M-D model is capable of predicting both the primary (transient) and secondary (steady-state) creep of rock salt. When pressure conditions in a storage cavern are changed, the transient nature of the M-D model can be an important factor in the response of the cavern. The transient recovery term of the M-D model was modified by DeVries et al. [2002] to predict more accurately the creep rate of salt when the deviatoric stress has decreased (i.e., the gas pressure in the cavern is significantly greater than the minimum gas pressure). Although much of the closure that occurs for a storage cavern occurs when the cavern is at or near minimum pressure, the creep response of hardened salt when the gas pressure is greater than the minimum pressure was found to have a significant impact on the annual closure rate

of the caverns. The updated recovery term was also found to have some impact on the predicted state of stress in the salt surrounding the storage cavern.

The model described by DeVries et al. [2002] includes terms to predict shear- and tensile-induced damage. This model is referred to as the Multimechanism Deformation Creep Fracture (MDCF) model and was originally developed by Chan et al. [1992] and updated as proposed by Chan [1993; 1996] and Chan et al. [1995a; 1996a; 1996b]. The MDCF model was developed using the M-D model as the foundation for describing isochoric creep. If the damage terms are omitted from the MDCF model, the original M-D model proposed by Munson et al. [1989] is retained. The damage terms were not included in the form of the model used here to predict the creep behavior of salt; however, the revision to the recovery term proposed by DeVries et al. [2002] was adopted. The three-dimensional form of the M-D model used for this study is given in Appendix E.

3.3.3 Salt Creep Test Data and Model Fits

The creep data reported in Section 3.3.1 was combined with that determined from testing of Cayuta salt under other testing programs [Nieland et al., 2001] to define the parameter estimates for the creep constitutive model. The M-D model has 17 parameters that must be determined experimentally or estimated empirically (see Appendix E). The parameter values used to represent Cayuta salt were determined by fitting the model to the data obtained from ten triaxial compression creep tests performed on salt from Bale Well No. 1 using a combination of linear and nonlinear, least-squares procedures. The seven creep tests identified in Section 3.3.1 (Table 3-4) were used along with three creep tests documented by Nieland et al. [2001] (see Table 3-5) during the fitting procedure.

Table 3-5. Creep Test Matrix for Bale Well No. 1 Upper Horizon Salt (From Nieland et al. [2001])[a]

Test No.	Specimen I.D.	Axial Stress Difference (MPa)	Confining Pressure (MPa)	Duration (days)
8	BAL1/87/1	10.34	27.58	17.0
9	BAL1/87/2	15.50	27.58	13.9
10	BAL1/89/1	20.68	27.58	13.9

(a) All tests performed at a temperature of 40°C.

As discussed in Section 3.3.1, the multistage creep tests exhibited a transient response each time the stress state on the specimens was changed from triaxial compression to triaxial extension. This behavior cannot be described by models that include only isotropic hardening such as the M-D model. Therefore, accurate predictions of the creep strain versus time response of the multistage laboratory tests is not possible with the M-D model. For this reason,

only the first stage of each test and the steady-state strain rates of the subsequent stages were used to evaluate the parameter estimates of the M-D model.

Because of the limited number of creep tests performed on the Cayuta salt, not all of the M-D parameters can be uniquely determined. Several M-D model parameter values were assumed to be the same as those determined from an extensive study of long-term creep tests on the bedded salt at the WIPP in New Mexico. The M-D model includes three steady-state mechanisms: (1) a low-stress, high-temperature mechanism (dislocation climb); (2) an undefined, low-temperature, low-stress mechanism; and (3) a high-stress mechanism (dislocation glide). The first and third steady-state mechanisms do not have a significant impact on the predicted response of a compressed natural gas storage cavern because salt storage caverns are usually operated at conditions under which the aforementioned mechanisms are inactive or do not contribute significantly to the total deformation rate. Several of the parameters that describe the first and third mechanism were taken to be the same as WIPP salt; specifically, the parameters Q_1, n_1, q, σ_o, α_r, and β_r. In addition, an assumption was made that dictated that the relative contribution of each of the three steady-state strain rates to the total steady-state strain rate is the same as that of WIPP salt at 40°C. This assumption provided a unique relationship between the leading coefficients A_1, A_2, B_1, and B_2 in the expressions for the steady-state strain rate. This has no meaningful impact on the predicted creep rates because the second mechanism dominates over the range of stress and temperature of interest.

The fitting effort produced the parameter estimates for the M-D model provided in Table 3-6. The impurity content and crystalline structure of bedded salt formations can vary significantly with depth and laterally across the formation. These variations influence the deformational behavior of the salt making the laboratory test results less reproducible. The reproducibility of Cayuta salt can be viewed by comparing the creep test results performed at the same stress difference and temperature conditions. Despite specimen-to-specimen variability, the M-D model was able to provide a reasonable prediction for the suite of creep tests.

Figures 3-11 and 3-12 provide a comparison of the measured axial strain data from the creep tests performed on Cayuta salt and the strains predicted by the M-D model at 40°C and 55°C, respectively. These figures show the prediction of axial strain as positive for extension and negative for compression. Three of the triaxial compression tests identified in Figure 3-11 were obtained from Nieland et al. [2001] (see Table 3-5). The remaining two tests include a redundant test in compression at a stress difference of 10 MPa and one in extension at the same stress difference (see Tests 1 and 2 in Table 3-4). The two compression tests at a stress difference of 10 MPa shown in Figure 3-11 illustrate the reproducibility of Cayuta salt. Test conditions are not repeated for any of the four 55°C tests illustrated in Figure 3-12. However, these tests, combined with the 40°C creep tests, provide sufficient information to define the temperature dependency of Cayuta salt over a limited temperature range typical of that expected around salt storage caverns in the Appalachian Basin.

Table 3-6. Munson-Dawson Parameters Used to Model the Creep of the Cayuta Salt

Parameter	Units	Value	Basis for Value
A_1	day^{-1}	3.13(10^{20})	Cayuta Salt
A_2	day^{-1}	5.14(10^{21})	Cayuta Salt
B_1	day^{-1}	2.27(10^{4})	Cayuta Salt
B_2	day^{-1}	1.13(10^{-4})	Cayuta Salt
K_0	—	11.3	Cayuta Salt
m	—	2.82	Cayuta Salt
α_w	—	9.07	Cayuta Salt
β_w	—	0.795	Cayuta Salt
q	—	5,335	WIPP Salt
Q_1/R	K	12,580	WIPP Salt
Q_2/R	K	12,830	Cayuta Salt
n_1	—	5.5	WIPP Salt
n_2	—	4.68	Cayuta Salt
σ_0	MPa	20.57	WIPP Salt
c	K^{-1}	0.036	Cayuta Salt
α_r	—	0.58	WIPP Salt
β_r	—	0.0	WIPP Salt

Because the Lode angle is not included in the M-D model formulation, the strain magnitudes predicted by the model are equal for triaxial extension and compression states of stress. This does not appear to be an issue because the creep behavior exhibited by salt is similar under both states of stress. As discussed in Section 3.3.1, the steady-state creep rates are nearly the same for compression and extension states of stress with slightly greater transient strains measured under triaxial extension states of stress compared to triaxial compression. The M-D model and corresponding parameter estimates determined for Cayuta salt are believed adequate for the evaluations proposed in this study. Refinement of the model to predict the transient response observed when the loading condition is sequentially changed between compression and extension is beyond the scope of this project and is left as a topic for future research.
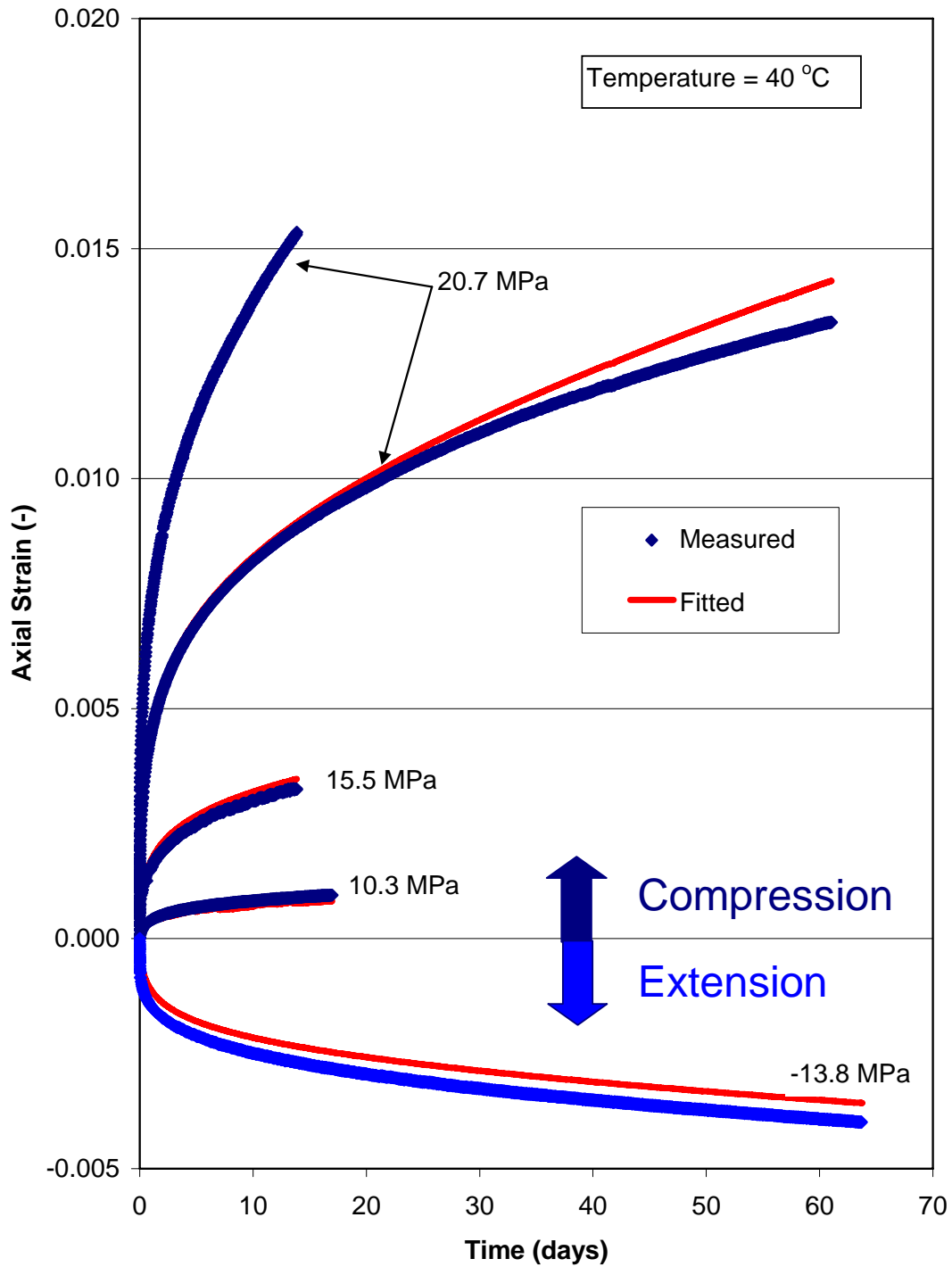
Figure 3-11. Comparison of Measured and Predicted Axial Strains Using the M-D Model of the Cayuta Salt Creep Tests Performed at 40°C.
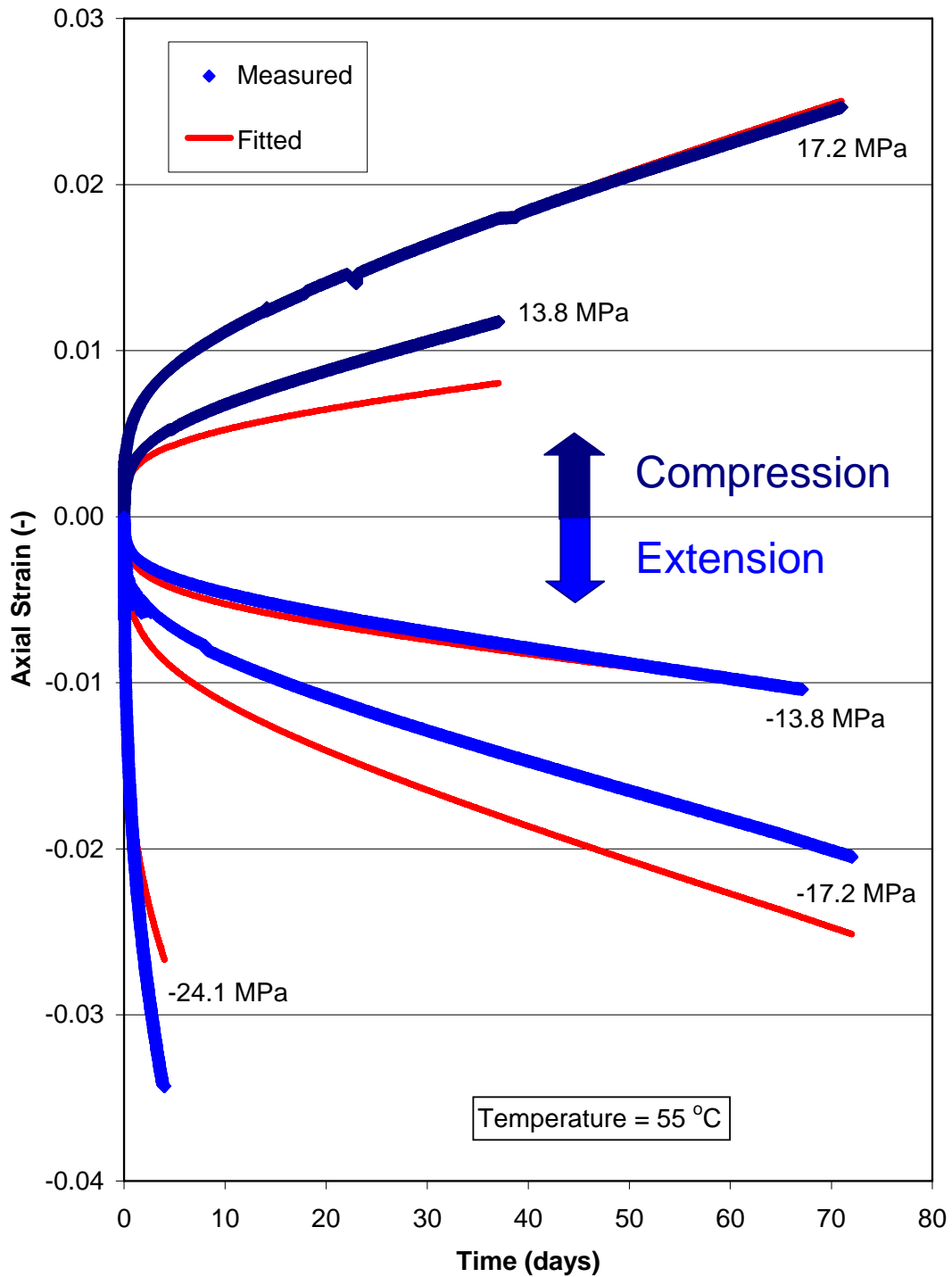
Figure 3-12. Comparison of Measured and Predicted Axial Strains Using the M-D Model of the Cayuta Salt Creep Tests Performed at 55°C.

47

4.0 DESIGN CRITERION DEVELOPMENT

The objective of this chapter is to present a design criterion useful for storage caverns situated in arbitrary stress fields. The chapter includes four subsections. The first two sections provide an overview of salt behavior and give examples of existing salt dilation criterion developed by other researchers. The next section briefly discusses important aspects of salt behavior that are necessary to accurately characterize the dilation boundary for rock salt. The final section presents the salt dilation criterion developed by this project.

4.1 BACKGROUND

Caverns in salt progressively close because salt deforms continuously (creeps) when subjected to shear stress. The shear stresses around a storage cavern are induced by the difference between the cavern pressure acting on the walls of the cavern and the in situ stress in the surrounding salt. The shear stresses increase as the cavern pressure decreases. In turn, the rate of creep closure increases nonlinearly as a power function of the shear stress.

Creep deformation alone is a constant volume process in salt. That is, salt changes shape in response to shear stress, but its volume remains constant. However, if the pressure in a cavern is decreased too far, the shear stresses in the surrounding salt can exceed the strength of the salt. The salt then will microfracture or dilate, creating additional porosity in the salt, and its volume will increase during creep deformation. Microfracturing, which is referred to as *damage,* causes the creep rate of salt to increase because the salt is weakened and its resistance to shear stress is reduced.

Like creep, damage is a progressive process and will accumulate as long as the shear stress exceeds the strength of the salt. Hence, if damaging states of stress are maintained for extended periods or are induced frequently around a storage cavern because the pressure is cycled too low, the resultant microfracturing can coalesce and slabs of salt can spall from the roof and walls. Progressive microfracturing and spalling can potentially damage the casing seat and hanging string. Stress-based dilatancy criteria are routinely used to identify states of stress that will result in the accumulation of damage around caverns solution mined in salt (e.g., Van Sambeek et al. [1993]; Thoms et al. [1999]; Chabannes et al. [1999]; Ehgartner and Sobolik [2002]; Nieland et al. [2001]).

4.2 EXISTING DILATION BOUNDARY MODELS

To be useful, a dilatancy criterion must be able to determine the potential for dilatant behavior in rock salt surrounding openings. To accomplish this, the stress conditions can be calculated using, for instance, finite element or finite difference methods and appropriate

material properties. Dilatancy surfaces (damage surfaces defined by the onset of volumetric expansion under compressive loading) have been derived by research programs both in the United States and internationally. Several models for the dilatancy boundary of rock salt have been published recently (e.g., Spiers et al. [1988]; Stormont et al. [1992]; Ratigan et al. [1991]; Hunsche [1993]; Thorel et al. [1996]; Hatzor and Heyman [1997]).

Dilatancy criteria are typically expressed in terms of stress invariants and empirical fitting parameters. Four selected dilation criteria are described briefly below. A comparison of the four dilation boundaries or criteria is shown in Figure 4-1. The criteria discussed below do not include the effects of loading history as they are developed from only one stress path. Loading history and its impact on damage are addressed by more advanced constitutive models developed to track the evolution of damage leading to creep rupture (e.g., Aubertin et al. [1993]; Chan et al. [1995b]; Lux et al. [1998]; Schulz et al. [1998]; DeVries et al. [2002]; Nieland et al. [1999]).

4.2.1 Salt Dilation Criterion After Spiers et al. [1988]

Spiers et al. [1988] used the results of constant strain rate tests on core taken from the Asse Salt Mine in Germany to develop their dilation criterion for salt. The constant strain rate tests were performed on cylindrical specimens under triaxial compression states of stress. The dilatancy criterion developed by Spiers et al. [1988] has the form:

$$\Delta\sigma = 2.74P + 6.4 \tag{4-1}$$

where P is the confining pressure and $\Delta\sigma$ is the difference between the axial stress and the confining pressure with stress given in units of MPa. The above expression produces a linear relationship when expressed in terms of the second invariant of the deviatoric stress tensor (J_2) and the first invariant of the stress tensor (I_1) with a nonzero intercept; viz,

$$\sqrt{J_2} = 0.27 I_1 + 1.9 \tag{4-2}$$

4.2.2 Salt Dilation Criterion After Ratigan et al. [1991]

Ratigan et al. [1991] developed a criterion that characterizes the potential for damage of salt from WIPP near Carlsbad, New Mexico. The criterion was developed from evaluation of volumetric strain rates for WIPP and Avery Island, Louisiana, domal salt creep tests performed at room temperature. Those tests that resulted in a measured negative volumetric strain were identified as "nondilating" and those specimens that experienced a positive volumetric strain rate were identified as "dilating." Using the dilating and nondilating identification, the results of 84 creep tests were plotted in the $I_1 - \sqrt{J_2}$ stress space. The approximate mathematical limit surface separating the dilating and nondilating WIPP salt tests is stated mathematically as:

$$\sqrt{J_2} = 0.27 I_1 \tag{4-3}$$
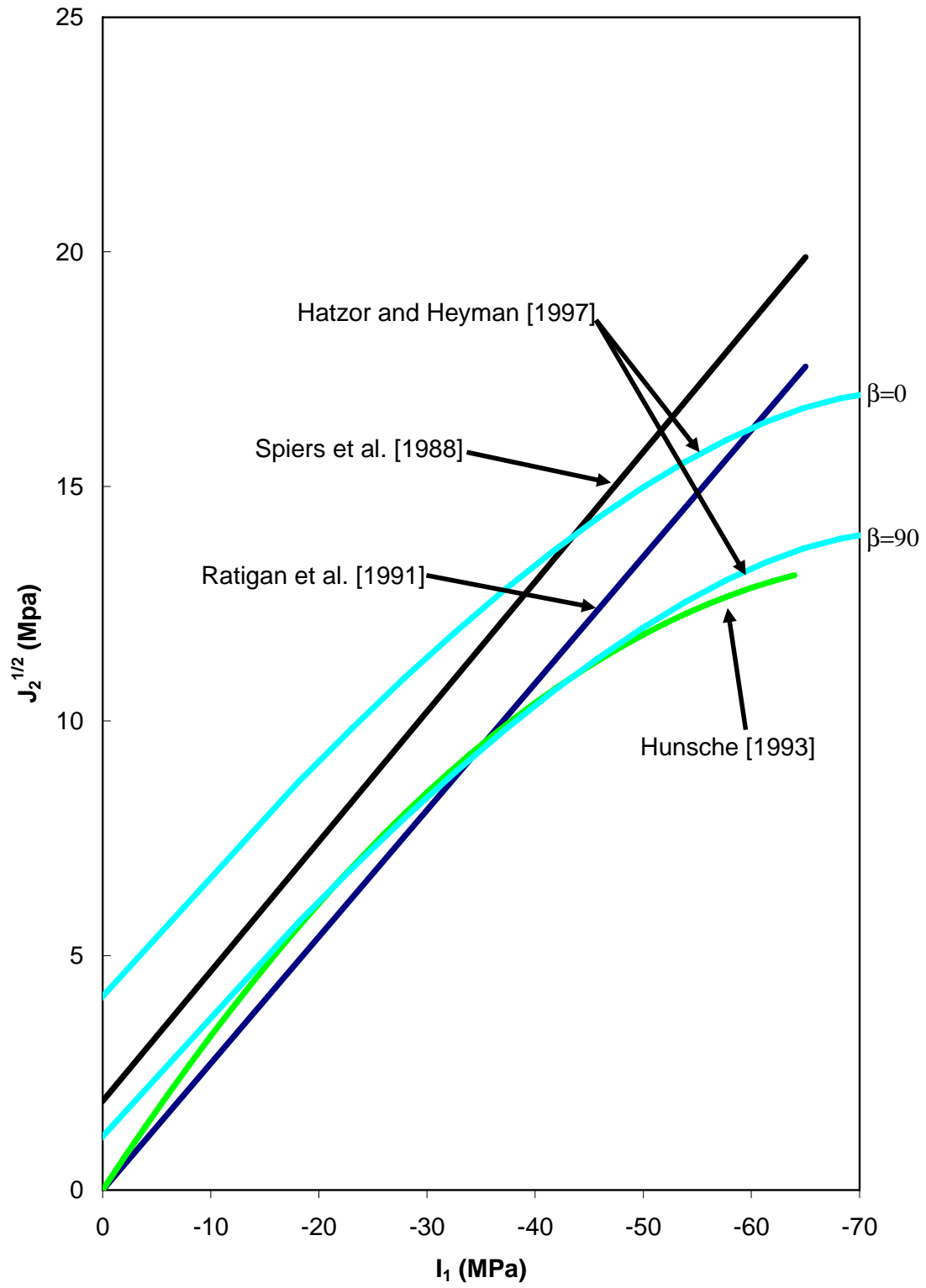
Figure 4-1. Comparison Salt Dilation Boundaries of Different Research Organizations.

50

This criterion is essentially identical to that of Spiers et al. [1988] with the exception of the intercept.

4.2.3 Salt Dilation Criterion After Hunsche [1993]

Hunsche [1993] used the results of 14 true triaxial tests on cubic specimens of salt from the Asse Salt Mine to develop a compressibility/dilatancy boundary. The boundary was identified using volumetric strain measurements together with acoustic emission rates as the basis for determining the compressibility/dilatancy boundary of Asse salt. Hunsche [1993] states that the specimens either exhibit a volume increase (dilatancy) or decrease (compression) because of microcrack opening or closing thus, the term compressibility/dilatancy. However, Hunsche [1993] also admits that the determination of volume change in the true triaxial tests is very difficult. Calculations used to compute volumetric strain had to take into account the deformation of the platens and pistons, as well as the small amount of salt which is squeezed out between the platens at the edges of the cubic samples.

The mathematical expression for the compressibility/dilatancy boundary at triaxial compression states of stress is given by:

$$\tau_{oct} = f_1\,\sigma_m^2 + f_2\,\sigma_m \qquad\qquad (4\text{-}4)$$

where τ_{oct} is the octahedral shear stress and σ_m is the mean or octahedral normal stress with the constants f_1 and f_2 assigned values of –0.0168 MPa^{-1} and 0.86, respectively, for an octahedral stress unit of MPa. An expression for the dilatancy boundary for triaxial extension was not given in Hunsche [1993]; however, the results of failure strength tests in extension exhibited the lowest strengths, averaging about 30 percent less than the compression tests. Equation 4-4 can be cast in terms of the first invariant of the Cauchy stress tensor and the second invariant of the deviatoric stress tensor as follows:

$$\sqrt{J_2} = \sqrt{\frac{3}{2}}\left(f_1\frac{I_1^2}{9} + f_2\frac{I_1}{3} \right) \qquad\qquad (4\text{-}5)$$

4.2.4 Salt Dilation Criterion After Hatzor and Heyman [1997]

Hatzor and Heyman [1997] used constant strain rate tests performed on cylindrical specimens from the Mount Sedom Diaper, Israel, to develop a salt dilatancy criterion. The Mount Sedom Diaper comprises a sequence of bedded salt layers that are nearly vertically inclined at the surface, with the inclination decreasing with depth. Hatzor and Heyman's [1997] work is unique because their dilation criterion includes the effect of bedding plane orientation on the onset of dilation, a feature ignored by other salt dilation criteria models. Hatzor and Heyman [1997] conclude that salt is weaker when the specimens are loaded such that the most compressive principal stress (σ_1) is parallel to the bedding plane orientation. They define their dilation criterion using principles stresses $(\sigma_1$ and $\sigma_3)$ and bedding plane

orientation (β). A total of 24 tests were performed: 10 on samples loaded normal to the bedding plane ($\beta = 0°$), 10 on samples loaded parallel to bedding ($\beta = 90°$), and 4 on samples loaded at oblique angles to bedding. Their empirical model for the compression/dilatancy boundary for anisotropic rock salt has the form:

$$\sigma_1 = k_1 e^{k_2 \beta} \tag{4-6}$$

where k_1 is a function of σ_3 given by a second-order polynomial having units of MPa:

$$k_1 = -0.0743\sigma_3^2 + 3.2223\sigma_3 + 12.9 \tag{4-7}$$

The value of k_2 is estimated to be –0.0057 and was determined from regression analyses along with the constants defining k_1 given by Equation 4-7. Because Hatzor and Heyman's [1997] formulation is for an anisotropic material, isotropy in stress space is lost, and their equation cannot be cast in terms of the stress invariants and compared with the other dilation criteria presented here. Thus a triaxial compression test is assumed with the bedding plane assumed to be perpendicular and parallel to the minimum principal stress and the results plotted as given in Figure 4-1.

4.3 DILATION CRITERION CONSIDERATIONS

The discussion above provides a brief orientation to the types of dilation criteria developed for salt and the variables that have been found to be important in defining the onset of dilation. Variables that have been identified as having an influence, or possibly having an influence, on the propensity for salt to microcrack include:

- Mean stress
- Lode angle
- Temperature
- Pore pressure (fluid pressure)
- Bedding plane orientation.

4.3.1 <u>Mean Stress</u>

Mean stress is known to suppress brittle deformation in most rocks, including salt. A vast majority of the laboratory tests performed by researchers to determine the strength and propensity for salt to microcrack address the influence of mean stress. Because of its significance, it is essential that dilation criteria for salt include mean stress dependency. The constant mean stress test results presented in Chapter 3.0 show that the dependency of the dilation limit on mean stress is nonlinear with respect to shear stress. Furthermore, a nonzero

intercept appears to be appropriate for Cayuta salt. The dilation criterion developed for Cayuta salt and discussed later in this chapter includes these aspects of material behavior.

4.3.2 Lode Angle

To date, limited research has been conducted to study the effect of intermediate stress (Lode angle) on the dilation limit and strength of salt. Hunsche [1993] reported results of true triaxial tests that indicate the failure strength of salt is about 30 percent less for tests subjected to triaxial extension stress states compared with triaxial compression stress states. Similar results were reported by Schmidt and Staudtmeister [1989]. The results of the laboratory testing discussed in Chapter 3.0 confirm the significance of Lode angle on rock salt strength. An important aspect of the new dilation criterion for Cayuta salt is to include the effects of this variable.

4.3.3 Temperature

As temperature increases, salt deformation becomes more ductile as crystalline plasticity (creep) dominates intercrystalline microcracking. However, few data are available that show the influence of temperature on failure or the dilatancy boundary for salt. Laboratory tests were performed on Cayuta salt by Nieland et al. [2001] specifically to address this issue. Based on the results of constant strain rate and constant mean stress tests, Nieland et al. [2001] concluded "…*salt dilation is not significantly affected as the temperature is decreased from 20°C to –30°C (68°F to 22°F)."* Schmidt and Staudtmeister [1989] reported that the short-term strength of rock salt is reduced about 5 to 10 percent when the temperature of laboratory tests is increased from 22°C to 60°C (72°F to 140°F). Because of a lack of experimental data and an indication of a minor influence of temperature on salt dilation, temperature dependency was not considered during the development of a salt dilation criteria for Cayuta salt.

4.3.4 Pore Pressure

Traditionally, the effect of the pore fluid pressure on the mechanical and hydrologic properties of salt has been ignored because rock salt has such a low permeability that it is commonly assumed to be impermeable. In other RESPEC laboratory projects, salt specimens have been exposed to high brine pressures (7 MPa) for several weeks in an effort to measure the permeability of undamaged salt. Efforts to push brine through these salt specimens resulted in the brine penetrating into the specimen less than 10 millimeters. Therefore, it is postulated that unless the permeability of the salt is enhanced by damage as indicated by dilation, pore pressure should not have any affect on the dilation limit of salt. After the dilation limit is exceeded, the microcracks that develop will enhance the permeability and accelerate the damage evolution process.

Fokker et al. [1993] examined the effect of pore pressure on the confined strength and permeability of salt and showed that strength decreases and permeability increases with

increases in pore pressure. Furthermore, the confined compressive strength of salt was shown to be approximately equivalent to its unconfined strength when the pore pressure and confining pressure were equal. Based on these results, Fokker et al. [1993] suggested the use of the well-known Terzaghi effective stress concept for characterizing salt strength. Unjacketed specimens were also tested by Thorel et al. [1996] and Cosenza and Ghoreychi [1998] to investigate the effects of high pore fluid pressure on salt. They determined that unjacketed specimens were weaker than jacketed specimens. This conclusion contradicts the idea that salt is impermeable and that fluid pressure can be regarded as simply a mechanical pressure applied to the surface.

The results of Fokker et al. [1993] were reviewed by Popp et al. [1999] who suggested that a possible explanation for the apparent Terzaghi behavior is that specimens contained preexisting damage before testing commenced. Damage can occur to salt specimens during coring operations, packing, shipping, and specimen preparation. Damaged salt would provide flow paths for the brine to penetrate into the specimen, thereby influencing the strength and mechanical behavior. Popp et al. [1999] completed dilation tests on damaged and undamaged specimens and concluded that pore fluid effects did not appear until a significant level of damage was induced and permeability was increased to allow penetration of the fluid.

Unjacketed triaxial compression constant means stress tests were performed as described in Chapter 3.0 to further investigate this issue. An assessment of these tests is provided in Chapter 3.0 and by DeVries et al. [2003]. The conclusion drawn from this assessment is that fluid pressure effects are inconsequential for undamaged salt. Fluid pressure effects become apparent when damage is present because damage enhances the permeability of salt. The objective of the present work is to describe the onset of dilation. While fluid pressures are important when preexisting damage exists, the existing evidence shows that the role of fluid pressure is minimal in creating damage in virgin rock salt. Therefore, pore pressure effects were not included during the development of a dilatancy criterion for this project.

4.3.5 Bedding Plane Orientation

Bedding plane orientation, shear plane orientation, and other anisotropic features have been largely overlooked during development of dilatancy criteria. Hatzor and Heyman [1997] recognize that salt is inherently anisotropic on all scales as exhibited by the preferred orientation of halite crystals and well-developed bedding planes in bedded salt deposits. However, anisotropy is not as well pronounced or easily distinguished in many salt domes. Hatzor and Heyman [1997] contend that the dilation processes nucleate inside available discontinuities and that the work required to initiate dilation is a function of the angle between the major principal stress (σ_1) and the outward normal of the discontinuity; in their case, the discontinuities are associated with the bedding plane.

The influence of bedding plane orientation was not investigated by the laboratory testing program performed for this project. Tests of this nature require core drilled at different

orientations with respect to the predominately horizontal stratigraphy, which is not available for Cayuta salt (all core was recovered from a vertical borehole). However, it should be noted that the orientation of the major principal stress with respect to the bedding plane orientation differs for the triaxial compression and triaxial extension tests performed. As a result, a lower limit for the dilation boundary is observed for the triaxial extension tests. However, any distinction between the effects of Lode angle and bedding orientation cannot be separated based on the available test data. Because data are not available, development of a criterion to include bedding plane orientation effects has been postponed until more definite results are obtained.

4.4 SALT DILATION CRITERION DEVELOPMENT

The remainder of this chapter presents some of the theoretical considerations and derivation process for developing a new dilatancy criterion for salt. To facilitate the reader, Appendix E discusses the representation of states of stress in principal stress space for ease of visualizing; presenting; and discussing yield, potential, and fracture criteria used as constitutive models.

4.4.1 <u>Mohr-Coulomb Type of Salt Dilation Criterion</u>

RESPEC pioneered the use of a stress-based dilation criterion [Ratigan et al., 1991; Van Sambeek et al., 1993] for salt cavern design that compares the computed states of stress around a cavern with the stress state that initiates dilation or microfracturing as determined through laboratory tests. The use of this criterion to assess the potential for microcracking around salt caverns is referred to as the Damage Potential (DP) Method. Shortcomings identified for the DP criterion are that this criterion does not include: (1) a nonzero intercept, (2) a nonlinear relation for the dilatancy boundary in the $I_1 - \sqrt{J_2}$ stress space, and (3) the effects of Lode angle.

A vivid two-dimensional illustration of the original criterion (DP) yield (potential) surface is achieved by projecting stresses into the π-plane or Haigh-Westergaard stress space (e.g., Chen and Han [1988]). The π-plane is a plane perpendicular to the hydrostatic axis $(\sigma_1 = \sigma_2 = \sigma_3)$ where the mean stress $(\sigma_m = (\sigma_1 + \sigma_2 + \sigma_3)/3)$ is zero, and Haigh-Westergaard stress space is similar to the π-plane but includes those planes where the mean stress is a nonzero constant. For simplicity, these representations will be referred to as the π-plane, recognizing the shortcomings in nomenclature as stated above. Equation 4-3 is plotted in the π-plane in Figure 4-2 using the coordinate systems developed in Appendix F and appears as a circle. Coincidence with the Mohr-Coulomb criterion (described later) at triaxial compression is arbitrary. Figure 4-2 shows that the original stress-based dilation criterion is constant with respect to the Lode angle. Equation 4-3 cannot describe a material's strength that varies with the intermediate principal stress. Therefore, a comprehensive dilation limit will be developed based on a Mohr-Coulomb type of failure criterion that eliminates this inherent weakness in the original salt dilation criterion.
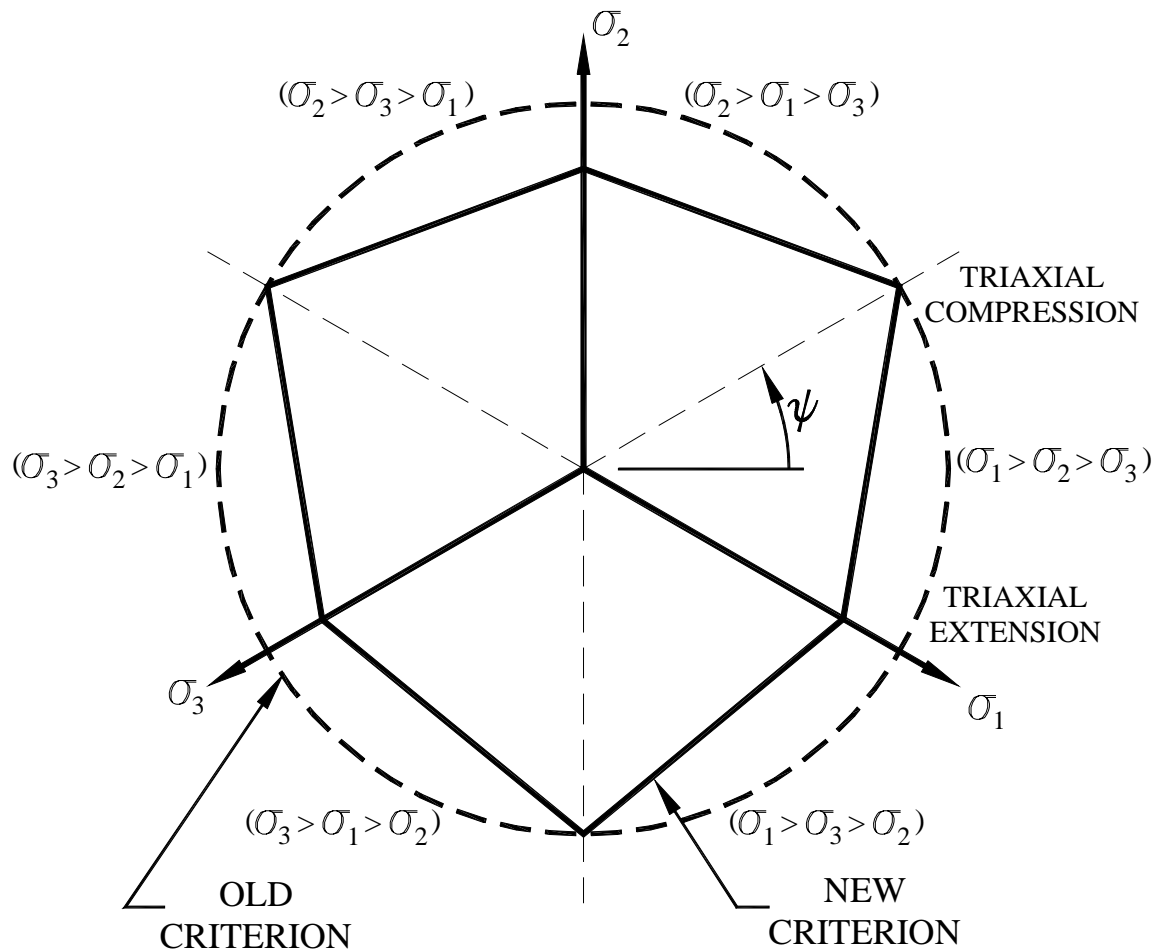
Figure 4-2. Illustration of the Original Stress-Based Dilation Criterion and the New Mohr-Coulomb Criterion Plotted in Principal Stress Space.

The Mohr-Coulomb criterion is typically written in its familiar linear form as:

$$|\tau| = S_0 - \sigma_n \tan\phi \tag{4-8}$$

where τ is the shear stress along the failure plane, σ_n is the normal stress on the plane, ϕ is the angle of internal friction, and S_0 is the material cohesion. When the Mohr-Coulomb criterion is written in invariant form using the invariants σ_m, J_2, and ψ, it becomes:

$$\sqrt{J_2}\left(\cos\psi - \frac{1}{\sqrt{3}}\sin\psi\,\sin\phi\right) + \sigma_m\sin\phi - S_0\cos\phi = 0 \tag{4-9}$$

Figure 4-2 illustrates the Mohr-Coulomb criterion plotted along with the original criterion. Stress lines of interest (triaxial compression and triaxial extension) are labeled along with the ordering of the principal stresses in the sextants. Figure 4-2 shows the ability of the Mohr-Coulomb criterion to predict differences in material strength at triaxial compression and triaxial extension stress conditions. The strength is less in triaxial extension and a continuous linear variation is observed between triaxial extension and compression.

After rearranging, Equation 4-9 may be written as:

$$\sqrt{J_2} = \frac{S_0\cos\phi - \sigma_m\sin\phi}{\left(\cos\psi - \dfrac{1}{\sqrt{3}}\sin\psi\,\sin\phi\right)} \tag{4-10}$$

If Equation 4-10 is reduced to triaxial compression $\left(\psi = 30°\right)$ and triaxial extension $\left(\psi = -30°\right)$ conditions, the material strength differences in triaxial compression and triaxial extension may be examined. Performing these reductions for triaxial compression, the equation becomes:

$$\sqrt{J_2} = \frac{S_0\cos\phi - \sigma_m\sin\phi}{\dfrac{\sqrt{3}}{2}\left(1 - \dfrac{\sin\phi}{3}\right)} \tag{4-11}$$

and for triaxial extension, the equation becomes:

$$\sqrt{J_2} = \frac{S_0\cos\phi - \sigma_m\sin\phi}{\dfrac{\sqrt{3}}{2}\left(1 + \dfrac{\sin\phi}{3}\right)} \tag{4-12}$$

Equations 4-11 and 4-12 illustrate the reduction in strength of a Mohr-Coulomb material (see Figure 4-2) as the state of stress changes from one of triaxial compression to one of triaxial extension.

If a conservative assumption is made that the angle of internal friction is zero (i.e., $\phi = 0$), Equations 4-11 and 4-12 are seen to be equal and may be written as:

$$\sqrt{J_2} = \frac{2\,S_0}{\sqrt{3}} \tag{4-13}$$

From the Mohr diagram, the cohesion can be related to the unconfined tensile strength (T_0) as:

$$S_0 = \frac{T_0(1+\sin\phi)}{2\cos\phi} \tag{4-14}$$

Using the $\phi = 0$ assumption and substituting Equation 4-14 into Equation 4-13 produces:

$$\sqrt{J_2} = \frac{T_0}{\sqrt{3}} \tag{4-15}$$

For the normal range of angles of internal friction, using $\phi = 0$ produces the minimum value for S_0 in Equation 4-14. Thus Equation 4-15 is a conservative estimate for a stress-based dilation criterion at a mean stress of zero (i.e., the intercept on the stress difference or $\sqrt{J_2}$ axis).

Equation 4-10 gives the strength for all states of stress (any value of Lode angle). Thus a general stress-based dilation criterion for salt is expected to have a similar form, which may be stated as:

$$\sqrt{J_2} = \frac{C_1\,I_1 + C_2}{\left(\cos\psi - \dfrac{1}{\sqrt{3}}\sin\psi\,D_2\right)} \tag{4-16}$$

where C_1, C_2, and D_2 are material constants to be evaluated from laboratory test data. Accepting the assumptions inherent in Equation 4-15, Equation 4-16 may be written as:

$$\sqrt{J_2} = \frac{C_3\,I_1 + T_0}{\left(\sqrt{3}\cos\psi - D_2\,\sin\psi\right)} \tag{4-17}$$

where C_3 is a material constant. In terms of the octahedral shear stress $\left(\tau_0 = \sqrt{2\,J_2/3}\right)$ and mean stress, Equation 4-17 may be written as:

$$\tau_0 = \frac{K\;\sigma_m + \sqrt{2}\,T_0}{\left(3\cos\psi - L\,\sin\psi\right)} \tag{4-18}$$

where $K\left(K = 3\sqrt{2}\,C_3\right)$ and $L\left(L = \sqrt{3}\,D_2\right)$ are material constants.

As discussed earlier, the dilation limit may be better represented by a nonlinear function than the linear relationship given in Equation 4-17. Therefore, Equation 4-17 is rewritten as:

$$\sqrt{J_2} = \frac{D_1 \left(\dfrac{I_1}{\operatorname{sgn}(I_1)\sigma_0} \right)^n + T_0}{\left(\sqrt{3}\cos\psi - D_2 \sin\psi \right)} \tag{4-19}$$

where n is a power less than or equal to one and σ_0 is a dimensional constant with the same units as I_1. When $n = 1$, Equation 4-19 is identical to Equation 4-17, reproducing the linear form. The plotted form of Equation 4-19 appears identical to the Mohr-Coulomb criterion plotted in Figure 4-2 because the plane in Figure 4-2 is for a constant mean stress. However, the nonlinearity of Equation 4-19 changes the three-dimensional view and magnitude of the new dilation criterion at varying mean stress values.

The ratio of triaxial extension dilation to triaxial compression dilation (SR) can be determined from Equation 4-19 to be:

$$SR = \frac{3 - D_2}{3 + D_2} \tag{4-20}$$

4.4.2 RD Criterion

The formulation given by Equation 4-19 represents the new dilation criterion for salt developed by this project, referred to hereafter as the RESPEC Dilation criterion (RD criterion). The proposed criterion is based on a Mohr-Coulomb-type of failure criterion to represent salt failure as a function of shear stress, mean stress, and Lode angle.

Figure 4-3 plots the dilation criterion given by Equation 4-19 with the constant mean stress test data (see Section 3.1) using the fitted parameter values determined for Cayuta salt ($n = 0.693$, $D_1 = 0.773$, $D_2 = 0.524$, and $T_0 = 1.95$). The original stress-based criterion given by Ratigan et al. [1991] with a proportionality constant of 0.18 (Equation 4-3) and frequently used by RESPEC is also provided in Figure 4-3. Keep in mind that the original criterion does not distinguish between triaxial extension and triaxial compression. However, provision for the different stress states (triaxial compression and triaxial extension) is inherent in the new criterion represented by Equation 4-19.

Figure 4-3 shows that the new dilation criterion fits both the triaxial compression and triaxial extension data quite well. Figure 4-3 also shows that the new dilation criterion provides a significant improvement over the linear dilation criterion in its ability to represent the test data. Another significant change from the original criterion is the intercept on the $\sqrt{J_2}$ axis. The original criterion shows an intercept of zero, which is unreasonable. The new

59
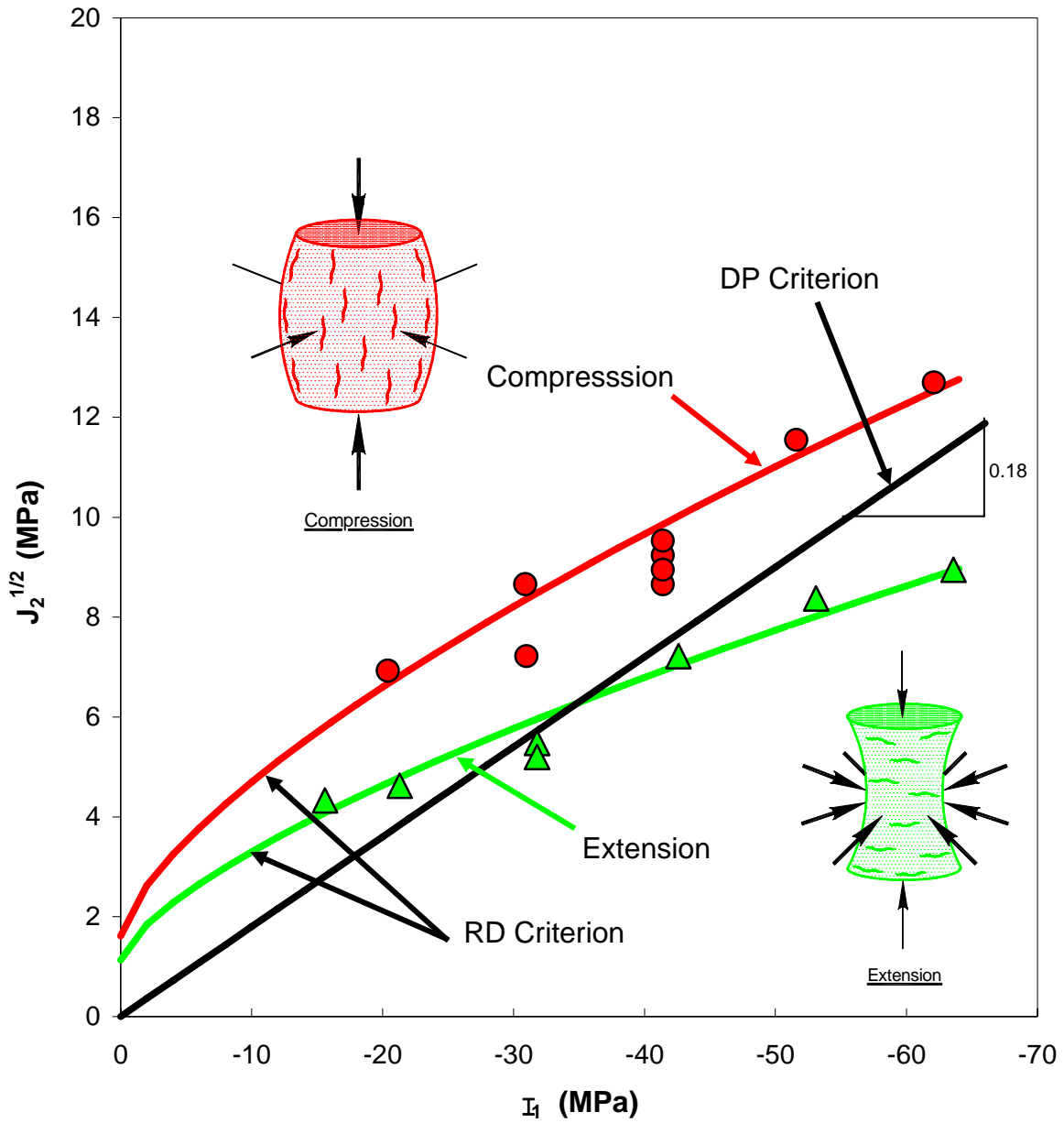
Figure 4-3. Comparison of the Original and Newly Developed Dilation Criteria With Laboratory Test Data.

criterion has a nonzero intercept based on the material's tensile strength, which is believed to be a reasonable, conservative assumption. The triaxial extension dilation limit predicted by the new criterion is about 30 percent less than the triaxial compression dilation limit for Cayuta salt (Equation 4-20).

5.0 NUMERICAL ANALYSIS

Geomechanical analyses are often used to assess the operating pressure range of natural gas storage caverns in salt that will ensure the structural stability of the salt and nonsalt strata surrounding the cavern and the gas containment capability of the cavern. The operating pressures for natural gas storage are typically established while considering the following criteria:

- The recommended maximum and minimum operating pressures will not result in connectivity with adjacent caverns caused by tensile failure or hydraulic fracturing.

- The recommended minimum operating pressure will not result in dilation (micro-fracturing) of the salt or shear failure of the nonsalt units that could lead to spalling of the roof and/or walls of the cavern and subsequent damage to the well or hanging string.

- The recommended minimum operating pressure and the operating pressure cycle will not yield excessive cavern closure that could produce excessive subsidence and/or damage to adjacent caverns and well casings.

Only the minimum operating pressure that will not result in dilation of the salt or shear failure of the nonsalt units is considered in this study. Although the other aforementioned items must be considered during a detailed geomechanical evaluation, the impetus of the numerical analyses performed for this study was to evaluate the RD criterion under conditions representative of the Appalachian Basin bedded salt lithology.

This chapter provides a complete description of the numerical analyses that were used to assess the effects of various cavern design parameters on cavern stability within a bedded salt formation. A total of 160 axisymmetric finite element simulations were performed during the course of this work. Again, cavern stability is defined here as a condition that does not result in dilation of the salt or shear/tensile failure of the nonsalt units. Cavern design parameters that were investigated include: (1) cavern roof salt thickness, (2) cavern depth, (3) cavern roof span, (4) overlying nonsalt thickness, (5) overlying nonsalt stiffness, and (6) cavern operating pressure cycle.

This chapter begins with a description of the technical approach used to evaluate cavern stability. Following the technical approach, a section is provided that identifies the cavern design parameters used for each of the numerical analyses that was performed. Results of the analyses are provided at the end of this chapter.

5.1 TECHNICAL APPROACH

The technical approach for assessing the effects of different cavern design parameters relies on axisymmetric finite element analyses that closely simulate conditions similar to those that would be expected for a natural gas storage cavern sited in the Appalachian Basin. Material properties for the salt were determined from the current and previous laboratory testing of rock samples collected from the Appalachian Basin, as discussed in Chapters 3.0 and 4.0. Cavern stability was then evaluated by comparing stress states predicted by the simulations to criteria developed from laboratory testing of the salt and nonsalt rocks. States of stress in the host formation were monitored during depressurization and repressurization of the cavern to determine the pressure that would initiate salt dilatation and/or tensile stress development. Similarly, the factors of safety were evaluated in the nonsalt units above the cavern to determine the cavern pressure that causes shear failure in the nonsalt beds. The lowest cavern pressure that caused none of these adverse conditions was identified as the minimum allowable pressure necessary to maintain cavern stability.

An overview of the technical approach, software programs, stratigraphy, finite element meshes, rock properties, in situ conditions, well fluid properties, and cavern operating scenarios are discussed below.

5.2 OVERVIEW OF THE TECHNICAL APPROACH

As discussed in Chapter 2.0, it would be overwhelming to simulate caverns sited in multiple geologic settings. Therefore, a single representative stratigraphic model was selected from which variations in formation thickness, elevation, and material properties could be considered. The modeled region selected extends 610 meters vertically and is composed of three distinct regions, as shown in Figure 5-1. The top section of the model represents the shale and carbonate sequence overlying the salt-bearing portion of the Salina Group. The center section of the model represents the salt-bearing formation and includes six salt beds separated by shale layers of thicknesses varying from less than 1 meter to about 38 meters. The bottom section of the model represents a predominately nonsalt region about 244 meters thick. The response of a cavern within this representative model provides the basis for assessing the effects of various cavern design parameters on cavern stability using the newly developed RD criterion.

Figure 5-1 illustrates the local stratigraphy and geometry of a typical cavern simulated in this study. As shown in Figure 5-1, two nonsalt beds are within the cavern interval. These nonsalt (shale) beds intersect the cavern approximately 11 and 27 meters below the roof. The cavern radius modeled is enlarged near the lower shale bed and reduced at the upper shale bed. Both of these features are common for solution-mined caverns in bedded deposits and provide a realistic cavern shape for evaluation.

SHALE BED THICKNESSES
(3, 6.1, OR 12.2 m)

ROOF SALT THICKNESSES
(3, 9.1, OR 27.4 m)

9.15 m

1.2 m

14.6 m

37.1 m

1.2 m

17.7 m

6.1 m

1

213.4 m

38.1 m

22.9 m

15.2 m

6.1 m

2

152.4 m

6.1 m

9.1 m

3

243.8 m

LEGEND

SALT

SHALE

CARBONATES
AND/OR SHALES
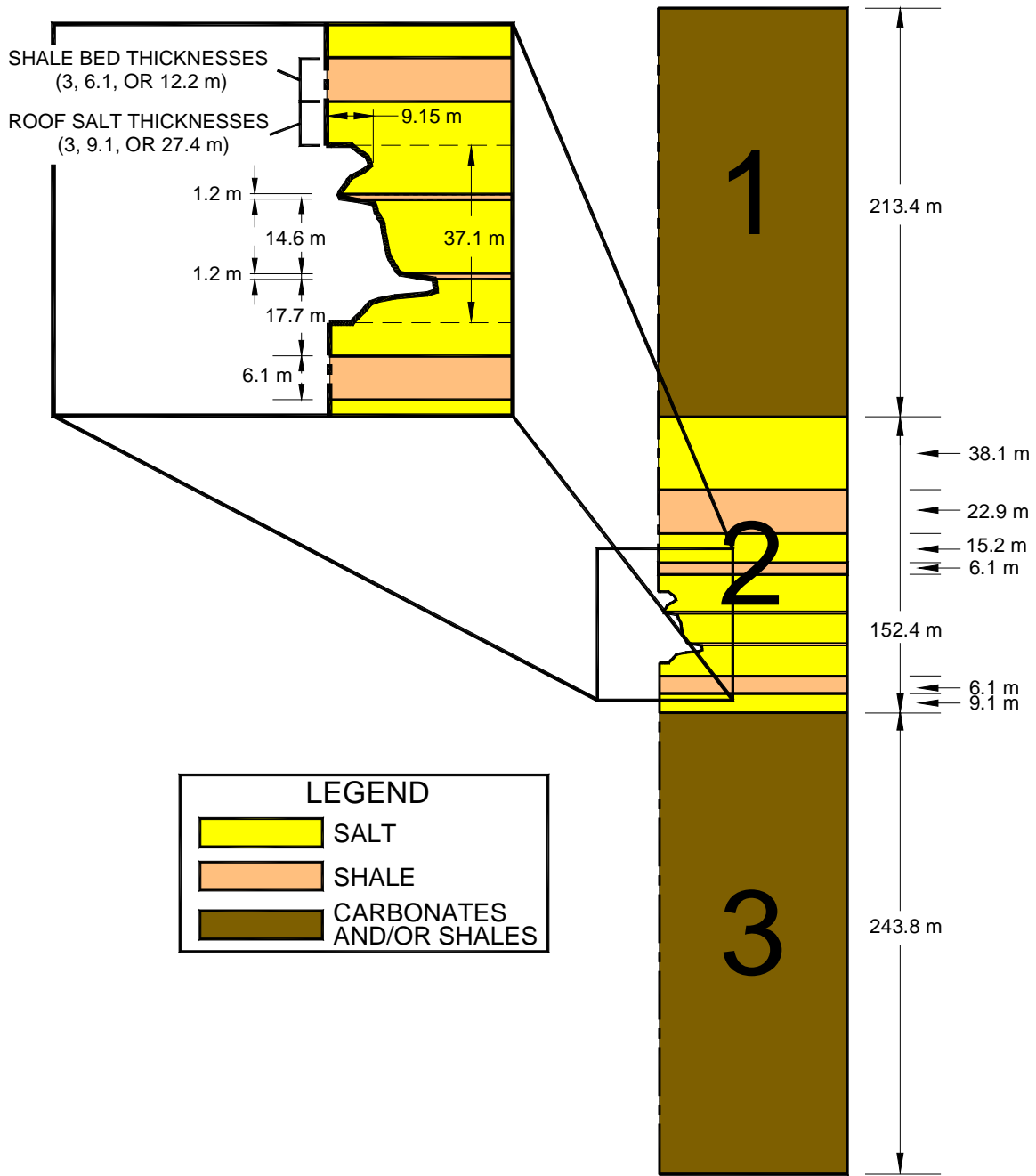
Figure 5-1. Local Stratigraphy and Geometry of a Typical Cavern Modeled.

Position of the cavern with respect to the shale bed below the cavern, cavern height, and irregular geometry of the cavern sidewall was the same for all the simulations performed. For those simulations used to investigate the influence of cavern roof span, the horizontal flat sections of the roof and floor were extended by the specified distance while maintaining a constant cavern height of about 37 meters. Roof spans of about 18.3, 58.3, 138.3, and 218.3 meters were investigated in this study. Using the same aforementioned features for all simulations provide a consistent framework for investigating the effects of the other cavern design parameters in this comparative study. Specific combinations of these modeling parameters are discussed in subsequent sections.

The following stages of cavern development and operation were simulated:

- Cavern excavation by solutioning

- Cavern dewatering

- Natural gas service cycles.

The first stages of each cavern analysis simulated leaching, dewatering, and filling the cavern with natural gas. This was followed by simulations of either rapid gas withdrawal or a 10-year gas service cycle. The purpose of simulating the leaching and dewatering of the cavern was to obtain the stress distribution before converting the facility to natural gas storage. At the start of each simulation, the cavern was instantaneously excavated and a normal traction equal to the brine pressure head was applied inside the cavern. The cavern was then allowed to creep for 1.5 years, which is an estimate for the time required to leach the cavern. This was followed by the dewatering period in which the gas was injected at maximum gas pressure. Maximum pressure used in this study is expressed in terms of depth to the casing shoe. A maximum pressure of 0.0204 MPa/m depth at the casing shoe was specified for the simulations. Temperature perturbations from the in situ temperature distribution were neglected during the simulations.

After dewatering the cavern, simulations of gas injection and withdrawal were performed to determine the minimum allowable pressure necessary to prevent salt dilation or failure of the nonsalt beds above the cavern. Failure of the shale beds in the sidewall or below the floor of the cavern is not expected to result in cavern instability. Thus failure of the shale in these zones was not considered a design constraint in this investigation. However, a detailed geomechanics investigation of an actual cavern should not ignore these failures because they could result in pathways for gas transport.

5.2.1 Software Program

Numerical modeling has proven to be a valuable tool in predictive and comparative analyses of solution-mined caverns. SPECTROM-32 [Callahan et al., 1989] is a thermomechanical finite element program developed by RESPEC for the solution of rock mechanics problems and was

used to perform the numerical analyses identified in this study. The program was designed specifically for the simulation of underground openings and structures. SPECTROM-32 not only has the capability to model the elastic-plastic response that is commonly associated with brittle rock types, but it also has the capability to simulate the viscoplastic behavior that is observed in rock salt. The features and capabilities of SPECTROM-32 required specifically for this analysis include:

- Option for modeling two-dimensional and axisymmetric geometries

- Kinematic and traction boundary conditions

- M-D constitutive model for viscoplastic behavior of salt

- Capability to represent arbitrary in situ stress and temperature fields.

5.2.2 <u>Stratigraphic Models</u>

Variations in the geologic column of the representative model were specified to determine the effects of roof salt thickness and the thickness of the shale bed immediately above the cavern on cavern stability. Figure 5-2 illustrates the five geologic columns that were used in this study. The vertical distance between the bottom of the shale bed immediately above the cavern and the roof of the cavern is referred to as roof salt thickness in this report. Figure 5-2 illustrates roof salt thicknesses of 9.1, 3.0, and 27.4 meters for Models 1, 2, and 3, respectively. The thickness of the shale bed immediately above the roof salt for these three models is 6.1 meters. Models 4 and 5 are similar to Model 1 except for the thickness of the shale bed immediately above the cavern. The shale bed thickness specified for Model 4 is about 3 meters; whereas, the thickness of this bed is 12.2 meters in Model 5. To accommodate the different thicknesses for the roof salt and shale bed, the thickness of the top nonsalt region was adjusted accordingly to maintain a constant vertical extent for the representative models. These five stratigraphic models were used for the numerical simulations performed in this study.

5.2.3 <u>Finite Element Meshes</u>

A total of 80 finite element meshes were developed to complete this project. Eighty different meshes were necessary to simulate the desired combinations of cavern depth, cavern roof spans, roof salt thickness, and shale bed thickness. The axisymmetric models developed represent single isolated caverns; consequently, no affects of other caverns are considered by these models. The right radial boundaries of the meshes are approximately 914 meters from the cavern. The top and bottom boundaries are approximately 300 meters above and below the cavern. These boundaries were selected to approximate far-field conditions where the boundaries are far enough removed to prevent them from having a significant influence on the cavern results.

66
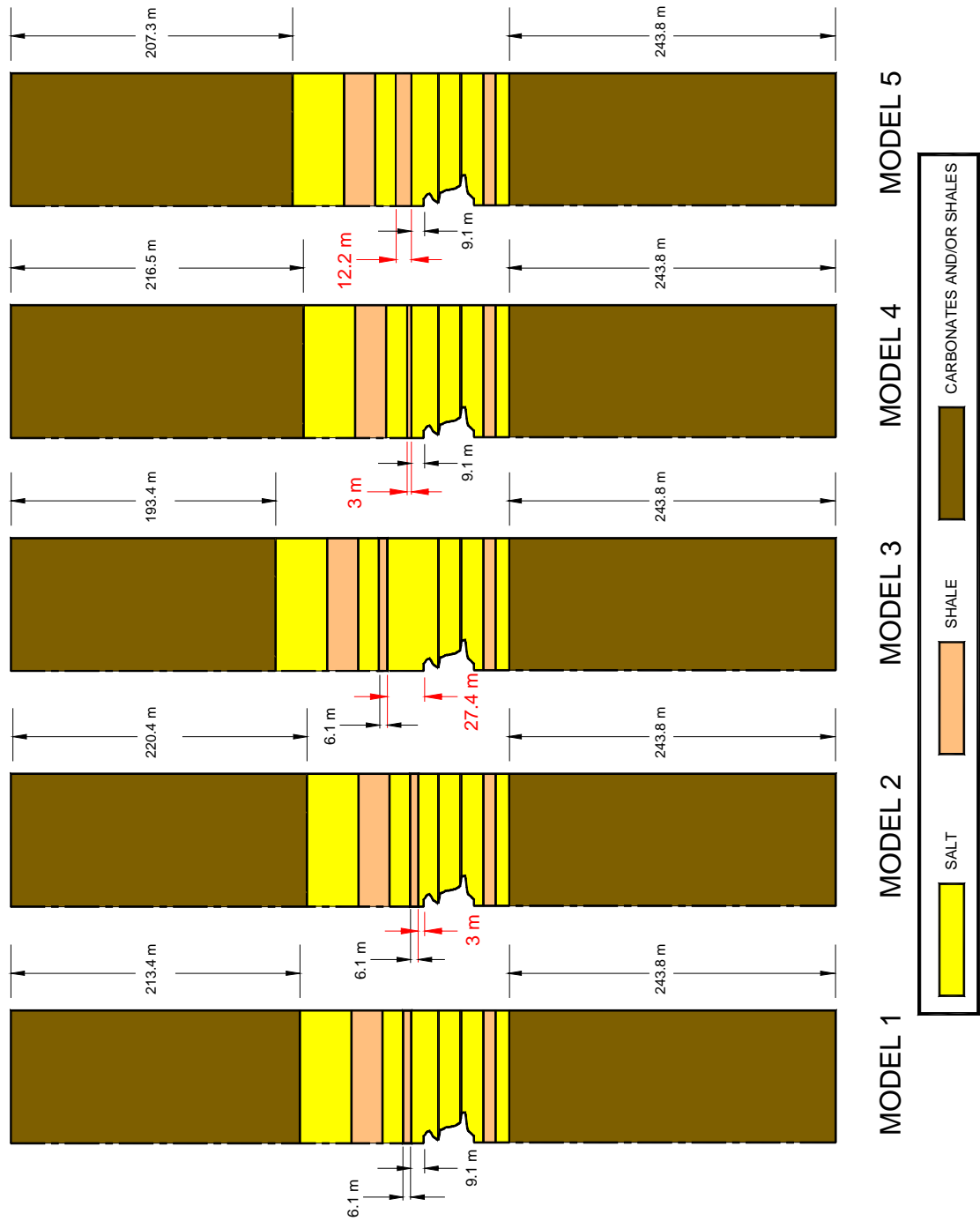
Figure 5-2. Five Stratigraphic Models Used for the Numerical Simulations.

The finite element meshes contained between 3,600 and 5,700 eight-noded quadrilateral elements. The area immediately outside of the cavern is very finely subdivided to accurately represent the high-stress gradients that are anticipated near the cavern. Tractions are applied along the top of the models to represent the overburden at the specified depth under consideration. An example of the finite element meshes generated is provided in Figure 5-3. Figure 5-3 illustrates the finite element mesh generated for a cavern at a depth of about 300 meters with a roof span of approximately 18.3 meters. Figure 5-4 provides a graphic illustration of four finite element meshes in the vicinity of the cavern with roof spans of 18.3, 58.3, 138.3, and 218.3 meters used in this study. Figure 5-5 provides a graphic illustration of three finite element meshes depicting roof salt thicknesses of 3.0, 9.1, and 27.4 meters. Figure 5-6 is similar to Figure 5-5 except this figure provides a comparison of the models having roof shale thicknesses of 3.0, 6.1, and 12.2 meters.

The kinematic boundary conditions specified along the sides of the axisymmetric models were:

- No radial displacement along the centerline.

- No radial displacement along the outer radius.

- No vertical displacement along the bottom surface.

The upper surface of the model is free to move in both the radial and vertical directions. After excavation of the salt was simulated, normal tractions were specified along the surface of the cavern to simulate the fluid pressure inside the cavern. The magnitudes of these tractions were equal to the hydrostatic pressure based on the densities of the fluids in the cavern plus the pressure specified at the wellhead.

5.2.4 Rock Properties

Quantification of significant rock mass properties, such as strength and deformability, is one of the most important aspects of site characterization. The representative models include massive nonsalt layers and salt layers containing interbedded shales. The creep and strength properties specified for the salt are given in Chapters 3.0 and 4.0. The nonsalt and interbedded shale beds were modeled as elastic materials in this study. The actual strength and elastic properties of the nonsalt beds in the Appalachian Basin will be site specific and are expected to vary considerably over the range of depth and extent of the basin. For this reason, elastic constants were selected to provide a broad range in the possible formation properties that may exist.

Three values were selected for Young's modulus of the shale beds to represent extremely weak, extremely strong, and a reasonable expectation for the material stiffness of the shale beds. Elastic properties for the massive nonsalt layers above and below the interbedded salt and shale of the representative model of the Appalachian Basin have less impact on the model
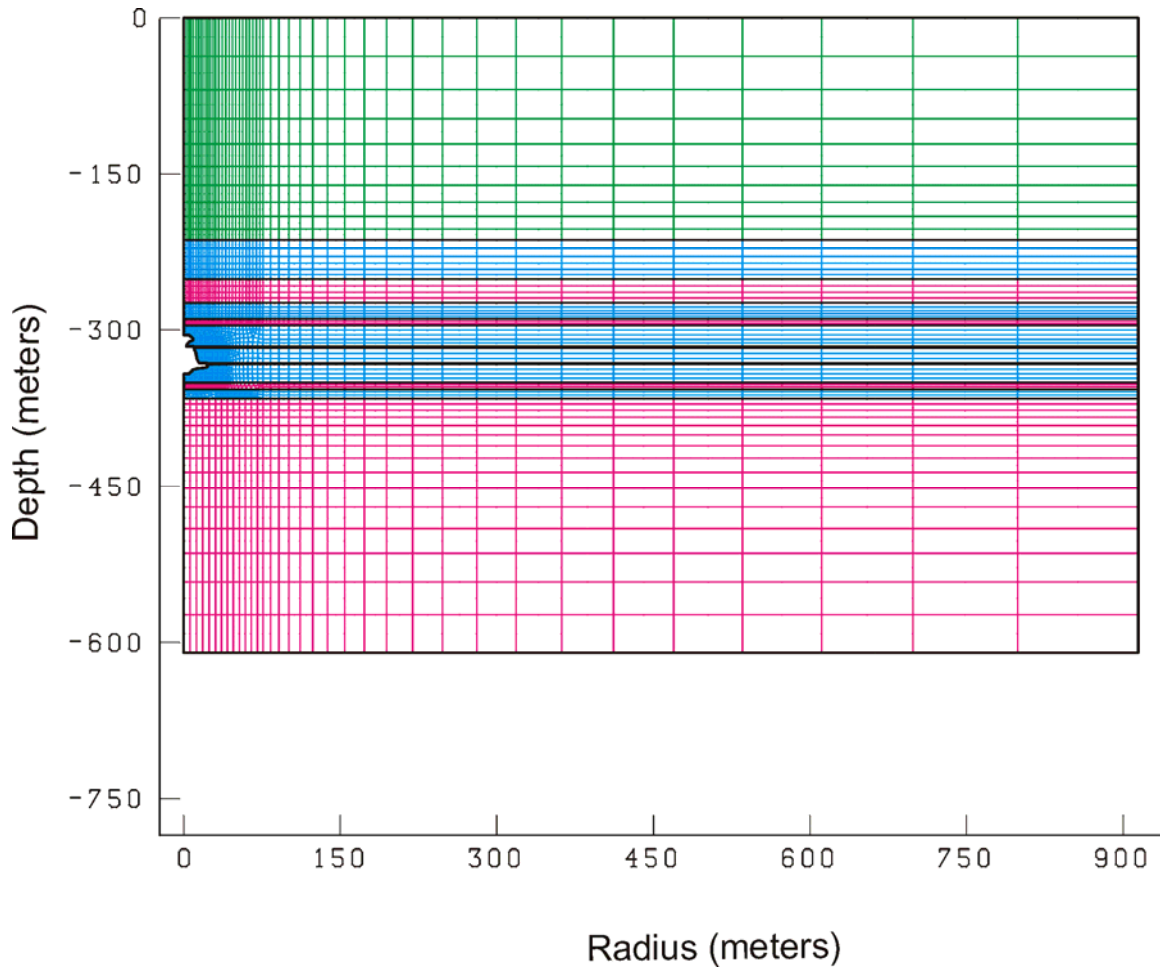
Figure 5-3. Example Finite Element Mesh With an 18.3-Meter Roof Span, 9.1-Meter-Thick Roof Salt, and 6.1-Meter-Thick Overlying Shale Bed (Baseline Model).
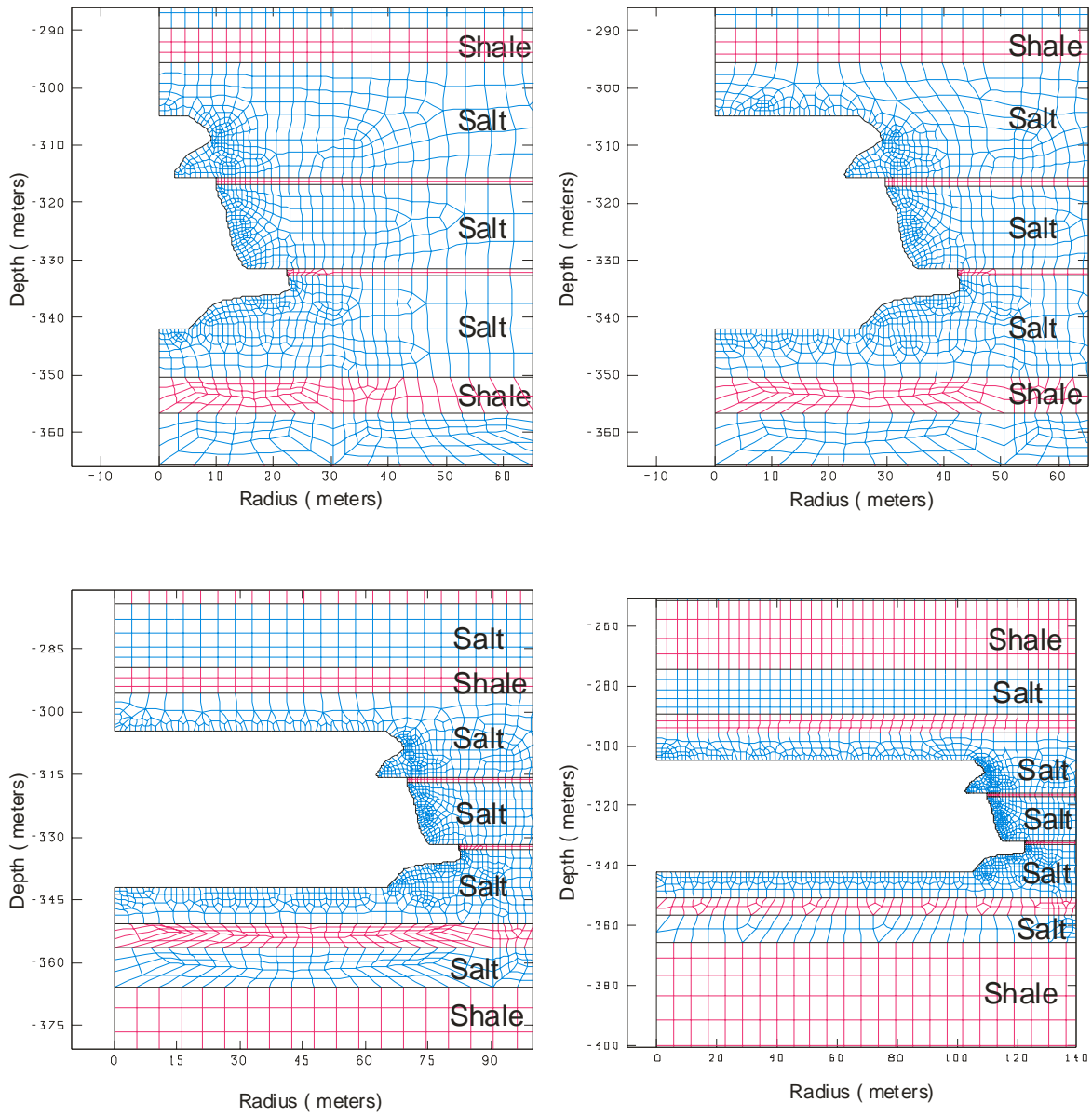
Figure 5-4. Comparison of Finite Element Meshes With Roof Spans of 18.3, 58.3, 138.3, and 218.3 Meters (Partial Views).

70
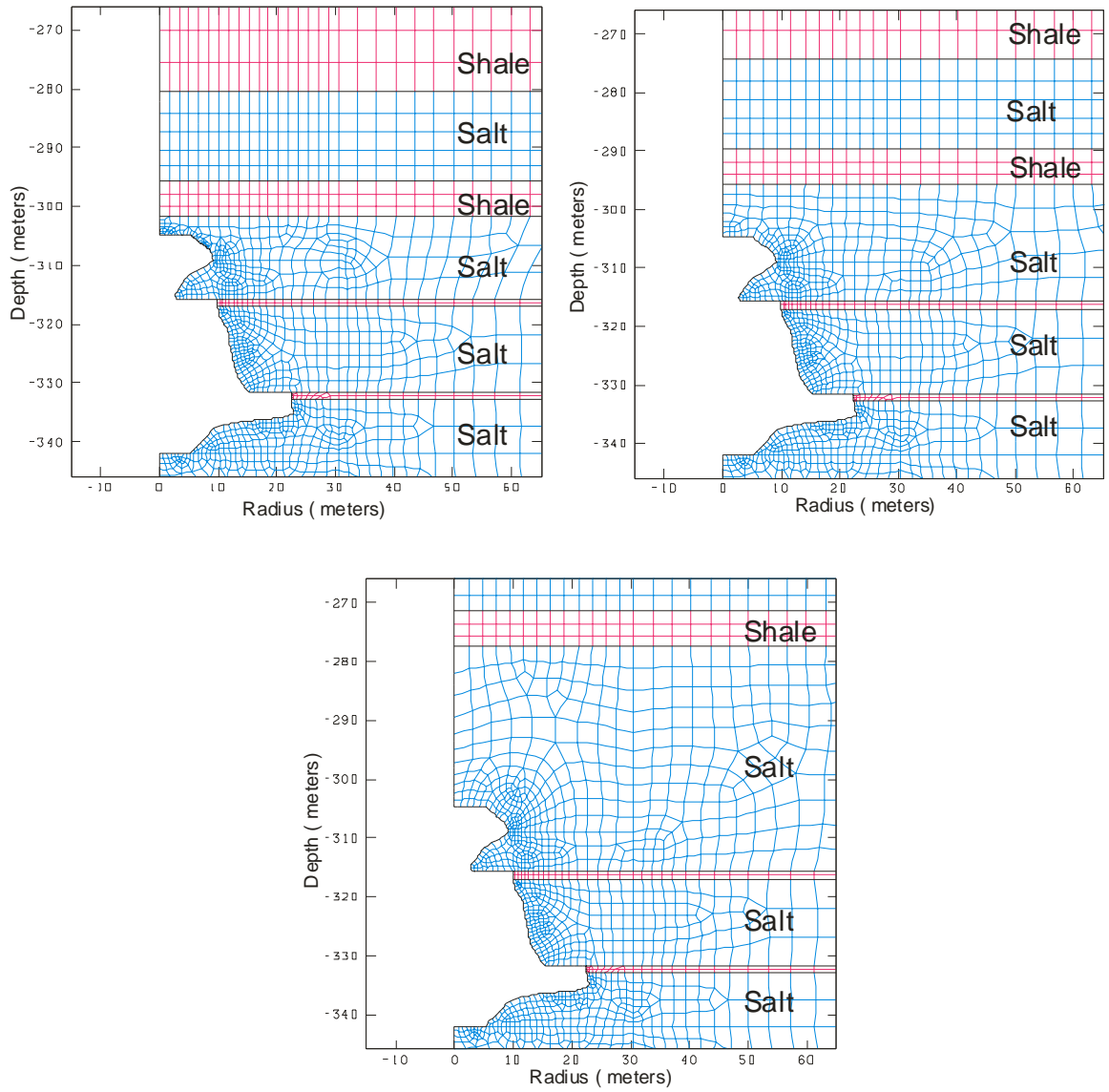
Figure 5-5. Comparison of Finite Element Meshes With Roof Salt Thicknesses of 3, 9.1, and 27.4 Meters (Partial Views).

71
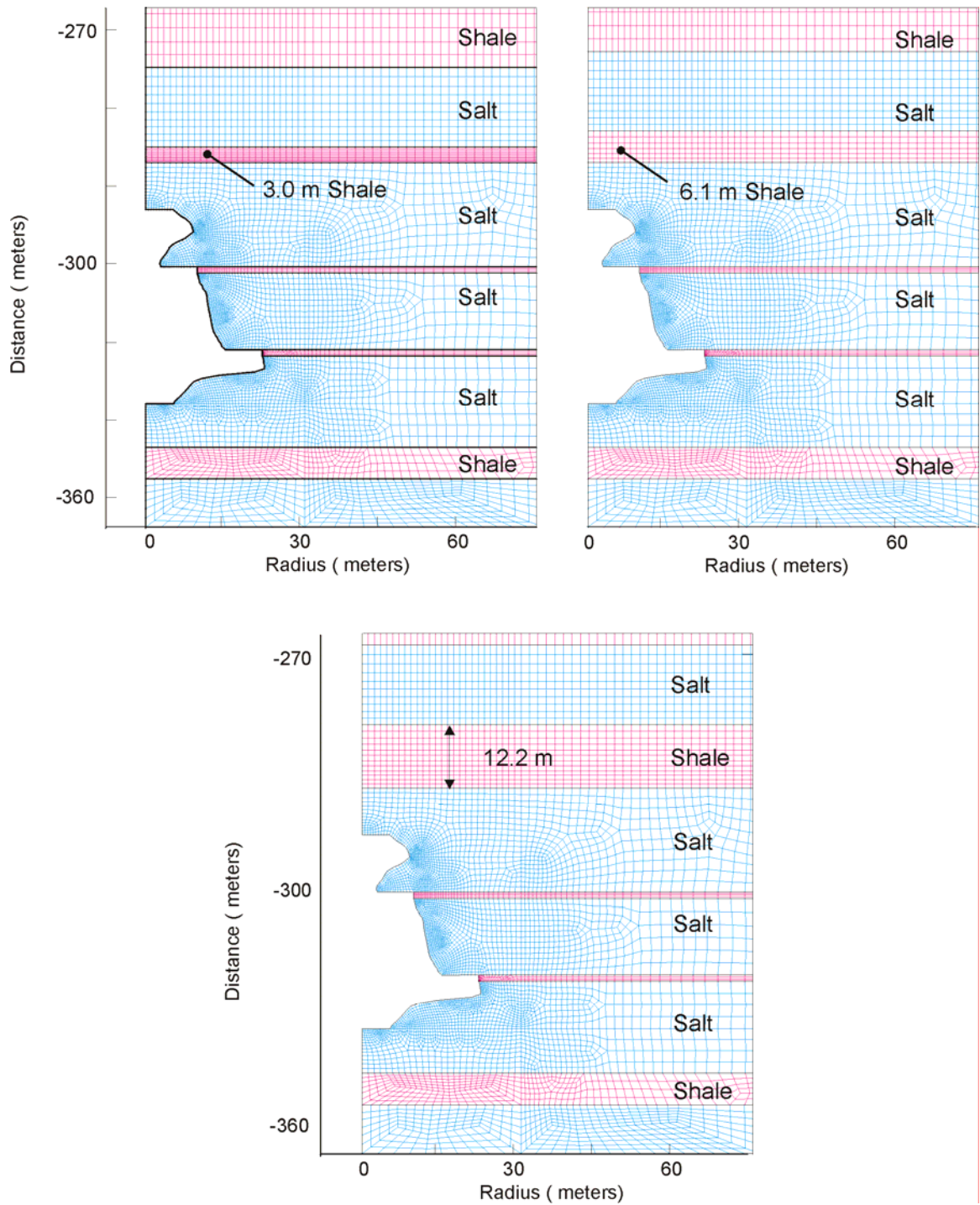
Figure 5-6. Comparison of Finite Element Meshes With Overlying Shale Thicknesses of 3, 6.1, and 12.2 Meters (Partial Views).

results than those of the salt and interbedded shales because of their greater distance from the cavern. For this study, a single set of elastic constants was specified for the two massive nonsalt units comprising the upper and lower portions of the models. The effect that Poisson's ratio has on the results was not considered in this study. Table 5-1 provides the elastic properties for the geologic units modeled in this study.

Table 5-1. Elastic Properties Used to Represent the Geologic Units in the Representative Model

Geologic Unit	Young's Modulus (GPa)	Young's Modulus (10^6 psi)	Poisson's Ratio[a] (–)	Density (g/cm^3)	Density (lb/ft^3)
Overlying Shale and Carbonate Sequence	34.5	5.00	0.20	2.4	150
Salina Group Salts	23.8	3.45	0.29	2.1	131
Underlying Vernon Shale and Nonsalt Formations	34.5	5.00	0.20	2.4	150
Salina Group Shale Beds (Weak Estimate)	1.5	0.22	0.20	2.4	150
Salina Group Shale Beds (Strong Estimate)	70.0	10.15	0.20	2.4	150
Salina Group Shale Beds (Baseline Estimate)	10.0	1.45	0.20	2.4	150

5.2.5 In Situ Conditions

The integrity of the walls and roof of a storage cavern is directly related to the deviatoric stress state resulting from the in situ stress and the forces exerted on the cavern walls by the fluid in the cavern. Therefore, it is important to model in situ stresses which are representative of those in the vicinity of the storage cavern. Accurate representation of the in situ temperatures is also important because the creep rate of the salt, and thus the closure of the cavern, is dependent upon both stress and temperature.

5.2.5.1 In Situ Stress Distribution

Principal in situ stresses are generally assumed to be aligned with a coordinate system that is vertical and horizontal. The magnitude of the vertical principal stress is typically assumed to be equal to the weight of the overburden. This assumption was made in this study using the densities listed in Table 5-1 for the geologic units in the representative stratigraphic model.

The tractions applied to the top of the representative models were based on an average overburden density of 2.4 g/cm^3.

In some locations, the differences in the magnitudes of the principal stresses are relatively low. For example, the in situ principal stresses in a salt dome are typically assumed to be equal. However, in most nonsalt locations in North America, the magnitudes of the principal stresses are not equal. The inequality of the principal stresses in most regions is reflected in the regional faulting or active tectonics. The faulting in the Appalachian Basin suggests that the in situ stresses are not equal in magnitude.

The assessment of failure for the shale beds is strongly influenced by the initial state of stress. The numerical modeling performed could not accurately reflect the in situ state of stress of the nonsalt units for two reasons: (1) the axisymmetric representation requires equality of both horizontal principal stresses, and (2) the horizontal principal stresses are expected to vary throughout the Appalachian Basin. Simulations were performed assuming an isotropic initial state of stress. Simulations assuming an isotropic in situ stress distribution are not conservative but selection of anything other than an isotropic initial state of stress would be arbitrary.

5.2.5.2 Geothermal Temperature Profile

The assumed initial in situ temperature gradient is based on thermal gradients measured in Pennsylvania [Clark, 1966]. A surface temperature of 10°C (50°F) was assumed. The resulting initial in situ temperature as a function of depth is described by the following equation:

$$T = 10 + 0.0273 \times D \qquad (5\text{-}1)$$

where T is in degrees Celsius and D is the depth in meters.

The circulation of brine during filling of the cavern with natural gas and the subsequent natural gas movements will perturb the ambient temperature distribution in the immediate vicinity of the cavern. These perturbations were assumed to have little affect on the mechanical behavior of the salt in the vicinity of the cavern and were not modeled.

5.2.6 Properties of Cavern Fluids

The mechanical response of a cavern depends not only on the material properties of the salt and nonsalt surrounding the cavern but also on the material properties of the fluids inside the cavern. The cavern is assumed to be filled with saturated brine before being dewatered. During dewatering, the cavern is filled with natural gas. In the simulations, these fluids are represented by equivalent pressures applied as tractions normal to the surfaces of the cavern walls. The fluids are assumed to be essentially stagnant, so at a given depth, the vertical pressure gradient is computed from the fluid's density at that depth. In the following two

subsections, the resultant vertical pressure gradients are presented for natural gas and saturated brine.

5.2.6.1 Natural Gas Properties

The gas pressure, P, in a cavern can be described as:

$$P = P_0 + \int_0^z \rho g dz \qquad (5\text{-}2)$$

where:

$$P_0 = \text{wellhead pressure}$$
$$\rho = \text{density of the gas}$$
$$g = \text{gravitational acceleration}$$
$$z = \text{depth below wellhead.}$$

The density of natural gas is dependent on pressure and temperature, both of which change with depth. A compressibility equation for natural gas described by Coker [1993] was used to calculate the density as a function of pressure and temperature. Equation 5-2 was integrated numerically to determine the pressure-versus-depth data, which can be approximated by a linear pressure gradient in the gas at the various pressures considered in this study.

5.2.6.2 Brine Properties

Because of the very small compressibility of brine, approximately 2.8×10^{-4}/MPa, the increase in brine density associated with the hydrostatic pressure increases over the height of the cavern is negligible. Consequently, the brine density was assumed to remain a constant 1.2 g/cm^3, resulting in a vertical pressure gradient of 0.0118 MPa/m.

5.2.7 Cavern Operating Scenarios

The numerical calculations performed during this study simulated cavern creation by solution mining, cavern dewatering, and natural gas operation. When dewatering was complete, the caverns were full of natural gas at a pressure equal to 0.0204 MPa/meter depth at the casing shoe (0.9 psi/foot). Operation of the cavern was assumed to commence immediately following dewatering of the cavern. Injection and withdrawal of gas was modeled as cavern pressure changes by incrementally increasing or decreasing the tractions specified on the elemental surfaces of the cavern.

To evaluate the stability of the caverns during gas storage, two gas storage scenarios were examined, including rapid and complete withdrawal of gas from the cavern (see Cycle 1 in Figure 5-7). This type of gas storage scenario is typically used to aid in the determination of
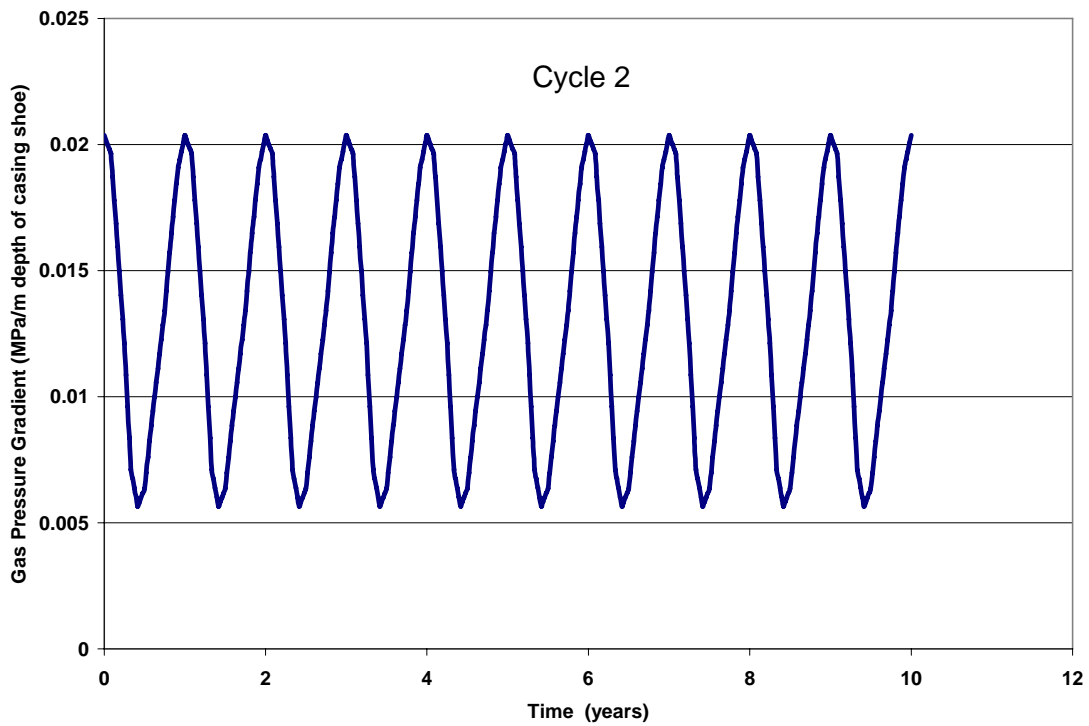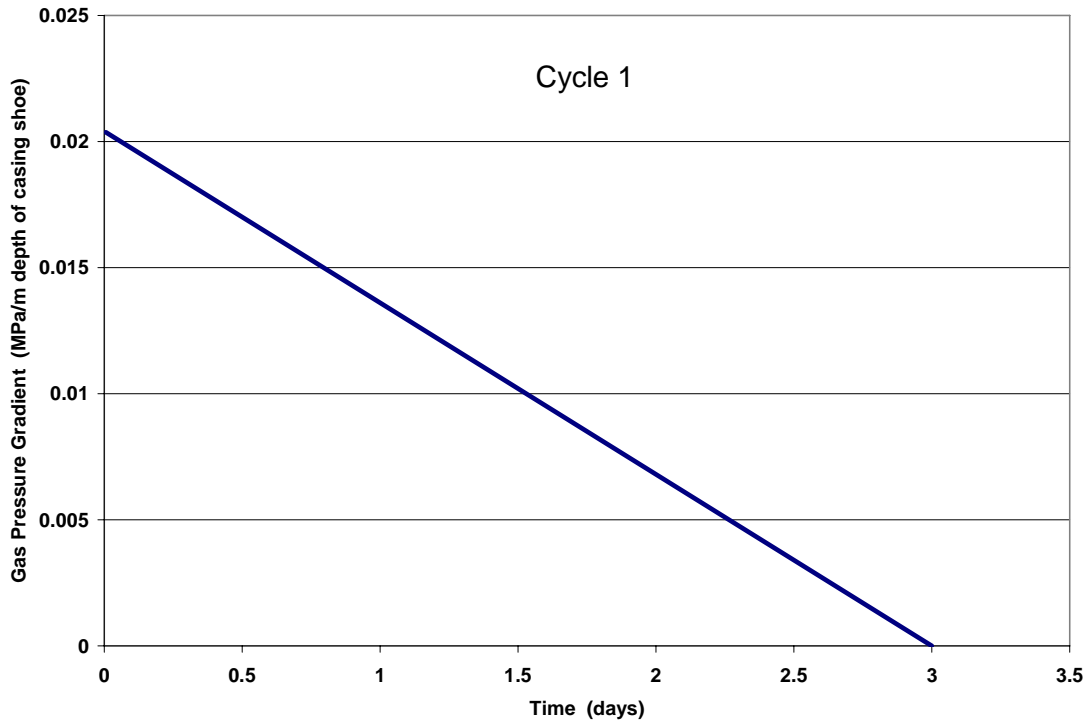
Figure 5-7. Simulated Natural Gas Storage Cycles: (a) Rapid Withdrawal (Cycle 1) and (b) 10-Year Service Cycle (Cycle 2).

minimum gas pressure based on the criterion for salt damage. Simulation of this storage pressure cycle is believed to provide the worst-case scenario for potentially generating salt damage because of the minimal amount of time available for the salt to redistribute the load by creep. The salt immediately surrounding the cavern must support the load previously supported by the gas pressure in the cavern. With time, creep of salt will redistribute this load farther away from the cavern, thereby reducing the shear stress in the salt very near the cavern surface. For the analyses performed using Cycle 1 in this study, the gas pressure at the casing shoe was reduced from 0.0204 MPa/meter depth at the casing shoe (0.9 psi/foot) to zero in 3 days.

Salt creep will result in continued deformation of the rock mass surrounding the cavern. This time-dependent deformation will add to the deflection (bending) of the shale beds, potentially reducing the factors of safety with time. The annual gas service cycle identified as Cycle 2 in Figure 5-7 was repeated ten times to determine if the caverns will remain stable or degrade with time for several of the analyses performed in this study. As used here, degradation means an evolution of the stress field with continued service cycles that produces less favorable conditions. As shown in Figure 5-7, the gas pressure was assumed to vary between 0.0204 and 0.0057 MPa/meter depth at the casing shoe (0.9 and 0.25 psi/foot). The minimum and maximum pressures were arbitrarily chosen to provide consistent reference pressures relative to the cavern depth (overburden pressure) for comparative purposes. In some cases, this pressure range may be outside the range necessary to maintain cavern stability. Regardless, the service cycle provides a reasonable expectation for the effects of time on the cavern stability criteria evaluated.

5.3 NUMERICAL ANALYSES

A total of 160 finite element analyses were performed to assess the stability of natural gas storage in bedded salt formations. The analyses were performed to assess the effects of various cavern design parameters on the stability of the cavern based on the newly developed RD criterion for predicting the potential for salt dilation. Cavern design parameters investigated include:

- Three cavern roof salt thicknesses (3.0, 9.1, and 27.4 meters).

- Four cavern depths (300, 600, 900, and 1,200 meters).

- Four cavern roof spans (18.3, 58.3, 138.3, and 218.3 meters).

- Three overlying shale bed thicknesses (3, 6.1, and 12.2 meters).

- Three interbedded shale stiffnesses (Young's modulus of 1.5, 10, and 70 GPa).

- Two natural gas storage cycles (a single rapid withdrawal cycle (Cycle 1) and a 10-year annual gas service cycle (Cycle 2).

All possible permutations of the design parameters were not evaluated in this study, which would have required 1,152 finite element analyses. The combinations of design parameters used for each of the analyses are identified in Table 5-2. As shown in Table 5-2, a total of 112 analyses were performed using the natural gas service cycle identified as Cycle 1. A total of 48 analyses were performed using the 10-year annual gas service cycle (Cycle 2). These 48 analyses are identified using the "Cycle 1 & 2" designation in the last column of Table 5-2. Thus each of the 48 analyses performed using the Cycle 2 annual service cycle were also performed using the Cycle 1 gas storage cycle. Taken collectively, the analyses represent a vast range of diversity for natural gas storage cavern designs in a bedded salt formation.

5.4 NUMERICAL ANALYSIS RESULTS

Finite element modeling was used to predict the minimum gas pressure that prevents a significant volume of salt from exceeding a state of stress that would result in dilation. Two dilation criteria were used in the assessment: (1) the original Damage Potential (DP) criterion pioneered by RESPEC based on the results of laboratory testing of Avery Island domal salt and WIPP bedded salt and (2) the newly developed RESPEC Dilation (RD) criterion based on the laboratory testing performed under this project on salt from the Appalachian Basin.

For the DP criterion, a DP ratio of 0.18 was assumed to be the limiting value for the salt. A value of 0.18 for the $\sqrt{J_2}/I_1$ stress ratio provides a reasonable approximation for the dilation limit of Cayuga salt based on the triaxial extension tests. However, because of model limitations, it is not possible to predict accurately the measured response over all possible states of stress expected in the salt surrounding the caverns. Based on the laboratory constant mean stress test results, a value of 0.18 is likely to underpredict the onset of dilation at mean stresses more compressive than –11 MPa and overpredict the dilation limit at mean stress states greater than –11 MPa (see Figure 4-3). The DP criterion used in this study has the form given in Equation 4-3.

For the RD criterion (Equation 4-19), parameter values determined for Cayuta salt (n = 0.693, D_1 = 0.773, D_2 = 0.524, and T_o = 1.95) were used assuming the state of stress in the salt is not allowed to exceed that predicted by the criterion. This approach is equivalent to a minimum factor of safety of 1.0. The results determined using the RD criterion are not considered conservative because the RD criterion parameter estimates were determined from a least-squares fit to the data. This fitting procedure resulted in a dilation boundary that is greater than the dilation limit observed during some of the laboratory tests. It would be prudent to incorporate a factor of safety during geomechanical assessments of actual storage caverns if the criterion results are based on a least-squares fit to laboratory data, as was done here.

Table 5-2. Description of Bedded Salt Cavern Numerical Analyses (Page 1 of 4)

Run ID	Depth (m)	Roof Span (m)	Roof Thickness (m)	Shale Thickness (m)	Shale Stiffness (MPa)	Gas Service Cycle
1	300	18.3	9.1	6.1	10,000	Cycle 1 & 2
2	600	18.3	9.1	6.1	10,000	Cycle 1 & 2
3	900	18.3	9.1	6.1	10,000	Cycle 1 & 2
4	1,200	18.3	9.1	6.1	10,000	Cycle 1 & 2
5	300	58.3	9.1	6.1	10,000	Cycle 1 & 2
6	600	58.3	9.1	6.1	10,000	Cycle 1 & 2
7	900	58.3	9.1	6.1	10,000	Cycle 1 & 2
8	1,200	58.3	9.1	6.1	10,000	Cycle 1 & 2
9	300	138.3	9.1	6.1	10,000	Cycle 1 & 2
10	600	138.3	9.1	6.1	10,000	Cycle 1 & 2
11	900	138.3	9.1	6.1	10,000	Cycle 1 & 2
12	1,200	138.3	9.1	6.1	10,000	Cycle 1 & 2
13	300	218.3	9.1	6.1	10,000	Cycle 1 & 2
14	600	218.3	9.1	6.1	10,000	Cycle 1 & 2
15	900	218.3	9.1	6.1	10,000	Cycle 1 & 2
16	1,200	218.3	9.1	6.1	10,000	Cycle 1 & 2
17	300	18.3	3.0	6.1	10,000	Cycle 1
18	600	18.3	3.0	6.1	10,000	Cycle 1
19	900	18.3	3.0	6.1	10,000	Cycle 1
20	1,200	18.3	3.0	6.1	10,000	Cycle 1
21	300	58.3	3.0	6.1	10,000	Cycle 1
22	600	58.3	3.0	6.1	10,000	Cycle 1
23	900	58.3	3.0	6.1	10,000	Cycle 1
24	1,200	58.3	3.0	6.1	10,000	Cycle 1
25	300	138.3	3.0	6.1	10,000	Cycle 1
26	600	138.3	3.0	6.1	10,000	Cycle 1
27	900	138.3	3.0	6.1	10,000	Cycle 1
28	1,200	138.3	3.0	6.1	10,000	Cycle 1

Table 5-2. Description of Bedded Salt Cavern Numerical Analyses (Page 2 of 4)

Run ID	Depth (m)	Roof Span (m)	Roof Thickness (m)	Shale Thickness (m)	Shale Stiffness (MPa)	Gas Service Cycle
29	300	218.3	3.0	6.1	10,000	Cycle 1
30	600	218.3	3.0	6.1	10,000	Cycle 1
31	900	218.3	3.0	6.1	10,000	Cycle 1
32	1,200	218.3	3.0	6.1	10,000	Cycle 1
33	300	18.3	27.4	6.1	10,000	Cycle 1
34	600	18.3	27.4	6.1	10,000	Cycle 1
35	900	18.3	27.4	6.1	10,000	Cycle 1
36	1,200	18.3	27.4	6.1	10,000	Cycle 1
37	300	58.3	27.4	6.1	10,000	Cycle 1
38	600	58.3	27.4	6.1	10,000	Cycle 1
39	900	58.3	27.4	6.1	10,000	Cycle 1
40	1,200	58.3	27.4	6.1	10,000	Cycle 1
41	300	138.3	27.4	6.1	10,000	Cycle 1
42	600	138.3	27.4	6.1	10,000	Cycle 1
43	900	138.3	27.4	6.1	10,000	Cycle 1
44	1,200	138.3	27.4	6.1	10,000	Cycle 1
45	300	218.3	27.4	6.1	10,000	Cycle 1
46	600	218.3	27.4	6.1	10,000	Cycle 1
47	900	218.3	27.4	6.1	10,000	Cycle 1
48	1,200	218.3	27.4	6.1	10,000	Cycle 1
49	300	18.3	9.1	6.1	1,500	Cycle 1 & 2
50	600	18.3	9.1	6.1	1,500	Cycle 1 & 2
51	900	18.3	9.1	6.1	1,500	Cycle 1 & 2
52	1,200	18.3	9.1	6.1	1,500	Cycle 1 & 2
53	300	58.3	9.1	6.1	1,500	Cycle 1 & 2
54	600	58.3	9.1	6.1	1,500	Cycle 1 & 2
55	900	58.3	9.1	6.1	1,500	Cycle 1 & 2
56	1,200	58.3	9.1	6.1	1,500	Cycle 1 & 2

Table 5-2. Description of Bedded Salt Cavern Numerical Analyses (Page 3 of 4)

Run ID	Depth (m)	Roof Span (m)	Roof Thickness (m)	Shale Thickness (m)	Shale Stiffness (MPa)	Gas Service Cycle
57	300	138.3	9.1	6.1	1,500	Cycle 1 & 2
58	600	138.3	9.1	6.1	1,500	Cycle 1 & 2
59	900	138.3	9.1	6.1	1,500	Cycle 1 & 2
60	1,200	138.3	9.1	6.1	1,500	Cycle 1 & 2
61	300	218.3	9.1	6.1	1,500	Cycle 1 & 2
62	600	218.3	9.1	6.1	1,500	Cycle 1 & 2
63	900	218.3	9.1	6.1	1,500	Cycle 1 & 2
64	1,200	218.3	9.1	6.1	1,500	Cycle 1 & 2
65	300	18.3	9.1	6.1	70,000	Cycle 1 & 2
66	600	18.3	9.1	6.1	70,000	Cycle 1 & 2
67	900	18.3	9.1	6.1	70,000	Cycle 1 & 2
68	1,200	18.3	9.1	6.1	70,000	Cycle 1 & 2
69	300	58.3	9.1	6.1	70,000	Cycle 1 & 2
70	600	58.3	9.1	6.1	70,000	Cycle 1 & 2
71	900	58.3	9.1	6.1	70,000	Cycle 1 & 2
72	1,200	58.3	9.1	6.1	70,000	Cycle 1 & 2
73	300	138.3	9.1	6.1	70,000	Cycle 1 & 2
74	600	138.3	9.1	6.1	70,000	Cycle 1 & 2
75	900	138.3	9.1	6.1	70,000	Cycle 1 & 2
76	1,200	138.3	9.1	6.1	70,000	Cycle 1 & 2
77	300	218.3	9.1	6.1	70,000	Cycle 1 & 2
78	600	218.3	9.1	6.1	70,000	Cycle 1 & 2
79	900	218.3	9.1	6.1	70,000	Cycle 1 & 2
80	1,200	218.3	9.1	6.1	70,000	Cycle 1 & 2
81	300	18.3	9.1	12.2	10,000	Cycle 1
82	600	18.3	9.1	12.2	10,000	Cycle 1
83	900	18.3	9.1	12.2	10,000	Cycle 1
84	1,200	18.3	9.1	12.2	10,000	Cycle 1

Table 5-2. Description of Bedded Salt Cavern Numerical Analyses (Page 4 of 4)

Run ID	Depth (m)	Roof Span (m)	Roof Thickness (m)	Shale Thickness (m)	Shale Stiffness (MPa)	Gas Service Cycle
85	300	58.3	9.1	12.2	10,000	Cycle 1
86	600	58.3	9.1	12.2	10,000	Cycle 1
87	900	58.3	9.1	12.2	10,000	Cycle 1
88	1,200	58.3	9.1	12.2	10,000	Cycle 1
89	300	138.3	9.1	12.2	10,000	Cycle 1
90	600	138.3	9.1	12.2	10,000	Cycle 1
91	900	138.3	9.1	12.2	10,000	Cycle 1
92	1,200	138.3	9.1	12.2	10,000	Cycle 1
93	300	218.3	9.1	12.2	10,000	Cycle 1
94	600	218.3	9.1	12.2	10,000	Cycle 1
95	900	218.3	9.1	12.2	10,000	Cycle 1
96	1,200	218.3	9.1	12.2	10,000	Cycle 1
97	300	18.3	9.1	3.0	10,000	Cycle 1
98	600	18.3	9.1	3.0	10,000	Cycle 1
99	900	18.3	9.1	3.0	10,000	Cycle 1
100	1,200	18.3	9.1	3.0	10,000	Cycle 1
101	300	58.3	9.1	3.0	10,000	Cycle 1
102	600	58.3	9.1	3.0	10,000	Cycle 1
103	900	58.3	9.1	3.0	10,000	Cycle 1
104	1,200	58.3	9.1	3.0	10,000	Cycle 1
105	300	138.3	9.1	3.0	10,000	Cycle 1
106	600	138.3	9.1	3.0	10,000	Cycle 1
107	900	138.3	9.1	3.0	10,000	Cycle 1
108	1,200	138.3	9.1	3.0	10,000	Cycle 1
109	300	218.3	9.1	3.0	10,000	Cycle 1
110	600	218.3	9.1	3.0	10,000	Cycle 1
111	900	218.3	9.1	3.0	10,000	Cycle 1
112	1,200	218.3	9.1	3.0	10,000	Cycle 1

The minimum pressure was identified as the pressure applied to the cavern surfaces at the time when 40 m^2 of the two-dimensional axisymmetric model exceeded the dilation limit. During cavern development, it is not uncommon for cavern protrusions and small areas of high-stress concentrations to slough off the cavern wall and form a rubble zone at the bottom of the cavern. Therefore, some of the salt was allowed to exceed the dilation limit to account for these localized failures, which are inconsequential to the overall cavern stability. Stress concentrations in the finite element models used in this study are induced by the irregular geometry of the cavern simulated. In reality, zones of high-stress concentration would either not be created during brining of the cavern or would slough off, producing a more stable geometry free of high-stress concentrations and protuberances. The 40 m^2 cross-sectional area appears to account for these cavern development aspects and to provide reasonable estimates for minimum gas pressure for the modeled caverns.

In the United States, the pressure limits of a cavern are often stated as the ratio of the gas pressure in psi divided by the casing shoe depth in feet. A 1 psi/foot pressure gradient is equivalent to an average overburden density of 144 lb/ft^3, a reasonable approximation for the depth range of interest in many rock formations. The maximum allowable gas pressure for many natural gas storage caverns is limited by regulation to less than 85 percent of the overburden pressure. Thus if the cavern is at maximum pressure, a pressure gradient of 0.85 is used to express the gas pressure in the cavern. Similarly, a pressure gradient of 0.30 is equivalent to 30 percent of the overburden stress at the casing shoe. This method for expressing the gas pressure in the cavern is used in this study versus expressing absolute pressure or gauge pressure; however, the pressure gradients are converted to SI units. An advantage of expressing the pressure in terms of a gradient is that it provides a quantitative measure for comparing gas pressures for caverns at different depths.

Minimum gas pressures were determined for each of the analyses identified in Table 5-2. The results presented in the next two subsections were determined for the gas service cycle that assumes a maximum withdrawal rate equivalent to removing all the gas from the cavern in 3 days (Cycle 1). As shown in Table 5-2, a total of 48 numerical analyses were performed using Cycle 2. This gas service cycle is much longer in duration but more moderate in terms of gas injection and withdrawal rates (1 turn per year for 10 years) compared to Cycle 1. Results obtained using the Cycle 2 gas service cycle show that the factors of safety are lowest in the salt during the first cycle. Subsequent gas cycles resulted in greater factors of safety for the salt because some of the load that was originally carried by the salt near the cavern had been transferred to the overlying nonsalt beds and to the rock farther removed from the cavern. Therefore, the simulations of rapid gas withdrawal following dewatering of the caverns (Cycle 1) were used to determine the minimum allowable gas pressure necessary to prevent salt failure because it is believed that this cycle represents the worst-case scenario for most gas storage caverns. However, it is possible that long-term stress redistribution and creep deformation can lead to additional loads within the nonsalt beds. This aspect of salt cavern storage was investigated by the 48 simulations that simulated the Cycle 2 annual gas service

cycle. Estimates for the potential failure of the shale bed overlying the cavern are provided following the discussion of minimum gas pressures necessary to prevent salt dilation using the DP and RD criteria.

5.4.1 <u>Minimum Pressure Determined Using DP Criterion</u>

Table 5-3 provides the approximate allowable minimum gas pressure based on the DP criterion for the analyses using the Cycle 1 gas service cycle. As a visual aid, red numbers are used to identify minimum gas pressure gradients greater than 0.00837 MPa/m depth to the casing shoe in Table 5-3. The 0.00837 MPa/m value was selected arbitrarily but indicates caverns that require relatively high minimum gas pressures to maintain cavern stability. High minimum gas pressures have a negative impact on the economics of gas storage in salt caverns and could prevent the construction of the gas storage facility. Results provided in Table 5-3 are grouped into three sections for comparison. The top grouping compares the results of the analyses used to investigate the effects of cavern roof span, depth, and roof salt thickness. Roof salt thicknesses of 3.0, 9.1, and 27.4 meters are presented in this grouping for four different cavern roof spans and four different depths. A reasonable stiffness for the shale beds (Young's modulus of 10,000 MPa) within the salt formation was specified for each of these 36 analyses. The shale bed immediately above the caverns was modeled as being 6.1 meters thick for this grouping. Therefore, the central column values under each depth do not change from grouping to grouping.

The second or middle group of results shown in Table 5-3 illustrate the effect that shale stiffness has on determining the minimum allowable gas pressure. The results provided in this second grouping were determined assuming three different values for Young's modulus (1,500, 10,000, and 70,000 MPa) for the shale beds within the salt sections of the model. The shale bed immediately above the cavern roof was assumed to be 6.1 meters thick for the analyses comprising this second grouping. The material properties of the massive nonsalt beds comprising the upper and lower portions of the model were not changed for any of the analyses.

The third and final group of results presented in Table 5-3 illustrates the importance of the thickness of the shale bed immediately above the cavern roof. Results determined from the analyses that specified thicknesses of 3.0, 6.1, and 12.2 meters for this shale bed are provided in the third grouping. Young's modulus of the shale and the roof salt thickness specified for the analyses presented in this grouping was 10,000 MPa and 9.1 meters, respectively.

Table 5-3 shows that the minimum gas pressure determined using the DP criterion is fairly insensitive to all three variables examined (roof salt thickness, overlying shale thickness, and overlying shale stiffness), but it is least sensitive to the overlying shale thickness.

Table 5-3. Minimum Gas Pressure Gradients (MPa/m) Determined Using the DP Criterion

Roof Span (m)	300-Meter-Depth Roof Salt Thickness			600-Meter-Depth Roof Salt Thickness			900-Meter-Depth Roof Salt Thickness			1,200-Meter-Depth Roof Salt Thickness		
	3 (m)	9.1 (m)	27.4 (m)	3 (m)	9.1 (m)	27.4 (m)	3 (m)	9.1 (m)	27.4 (m)	3 (m)	9.1 (m)	27.4 (m)
18.3	0.0085	0.0085	0.0085	0.0078	0.0077	0.0078	0.0072	0.0072	0.0071	0.0066	0.0066	0.0064
58.3	0.0092	0.0092	0.0092	0.0083	0.0083	0.0083	0.0076	0.0077	0.0076	0.0069	0.0070	0.0069
138.3	0.0101	0.0101	0.0101	0.0087	0.0085	0.0085	0.0076	0.0077	0.0076	0.0069	0.0069	0.0069
218.3	0.0114	0.0114	0.0114	0.0094	0.0094	0.0094	0.0083	0.0083	0.0083	0.0073	0.0073	0.0073

Roof Span (m)	300-Meter-Depth Shale Stiffness			600-Meter-Depth Shale Stiffness			900-Meter-Depth Shale Stiffness			1,200-Meter-Depth Shale Stiffness		
	1,500 (MPa)	10,000 (MPa)	70,000 (MPa)	1,500 (MPa)	10,000 (MPa)	70,000 (MPa)	1,500 (MPa)	10,000 (MPa)	70,000 (MPa)	1,500 (MPa)	10,000 (MPa)	70,000 (MPa)
18.3	0.0089	0.0085	0.0083	0.0080	0.0077	0.0076	0.0072	0.0072	0.0067	0.0066	0.0066	0.0060
58.3	0.0121	0.0092	0.0085	0.0101	0.0083	0.0076	0.0087	0.0077	0.0069	0.0078	0.0070	0.0064
138.3	0.0153	0.0101	0.0085	0.0132	0.0085	0.0076	0.0110	0.0077	0.0069	0.0110	0.0069	0.0064
218.3	0.0168	0.0114	0.0085	0.0141	0.0094	0.0076	0.0128	0.0083	0.0069	0.0125	0.0073	0.0064

Roof Span (m)	300-Meter-Depth Shale Thickness			600-Meter-Depth Shale Thickness			900-Meter-Depth Shale Thickness			1,200-Meter-Depth Shale Thickness		
	3 (m)	6.1 (m)	12.2 (m)	3 (m)	6.1 (m)	12.2 (m)	3 (m)	6.1 (m)	12.2 (m)	3 (m)	6.1 (m)	12.2 (m)
18.3	0.0085	0.0085	0.0085	0.0076	0.0077	0.0076	0.0071	0.0072	0.0071	0.0064	0.0066	0.0064
58.3	0.0092	0.0092	0.0089	0.0083	0.0083	0.0083	0.0076	0.0077	0.0076	0.0069	0.0070	0.0069
138.3	0.0101	0.0101	0.0101	0.0085	0.0085	0.0085	0.0076	0.0077	0.0076	0.0069	0.0069	0.0069
218.3	0.0115	0.0116	0.0115	0.0094	0.0094	0.0094	0.0083	0.0083	0.0083	0.0073	0.0073	0.0073

5.4.2 Minimum Pressure Determined Using RD Criterion

The minimum gas pressures determined based on the RD criterion for each of the analyses using the Cycle 1 gas service cycle are presented in Table 5-4. The layout of Table 5-4 is identical to that of Table 5-3 discussed above. Results are provided for four depths, four cavern roof spans, three roof salt thicknesses, three shale bed thicknesses, and three different values for Young's modulus of the shale. As in Table 5-3, the red numbers are used in Table 5-4 to identify minimum gas pressure gradients greater than 0.00837 MPa/m depth to the casing shoe.

Table 5-4 shows that the minimum gas pressure determined using the RD criterion is more sensitive to the variables examined (roof salt thickness, overlying shale thickness, and overlying shale stiffness) than the DP criterion, but it is still least sensitive to the overlying shale thickness. Comparing Tables 5-3 and 5-4 to plotted criteria in Figure 4-3, the data trends are what one would expect. That is, the RD criterion has fewer minimum gas pressures greater than the arbitrary 0.00837 MPa/m value at shallower depths than the DP criterion and has more minimum gas pressures greater than the arbitrary 0.00837 MPa/m value at the greater depths than the DP criterion.

5.4.3 Potential Failure of the Shale Beds

The results provided in Tables 5-3 and 5-4 show that lower minimum gas pressures can be specified for caverns located below the shale beds having a higher stiffness. These results are based on a single rapid gas service withdrawal cycle and do not indicate the factor of safety within the shale bed. It is possible that the shale above the roof of the cavern could fail, causing a major roof collapse. Further, the potential for failure of the shale is directly related to the magnitude of deformation. Because of salt creep, the shale bed above the cavern is expected to continually deform with each gas cycle. Forty-eight analyses that simulate long-term annual gas service cycles were performed to investigate the potential for failure of the shale beds and to see if the factors of safety in the shale decreases with time. The analyses simulate four cavern depths, four cavern roof spans, and three stiffnesses for the shale bed. These analyses are identified as those using the Cycle 2 gas service cycle in Table 5-2.

For comparative purposes, it was assumed that the maximum and minimum gas pressures during the annual service cycles varied between 0.0204 and 0.0057 MPa/m depth at the casing shoe. In some cases, the minimum pressure necessary to prevent salt dilation is greater than 0.0057 MPa/m depth at the casing shoe (see Table 5-4). Nonetheless, a direct comparison of the factors of safety for the shale would not be meaningful without maintaining a consistent pressure range.

Table 5-4. Minimum Gas Pressure Gradients (MPa/m) Determined Using the RD Criterion

Roof Span (m)	300-Meter-Depth Roof Salt Thickness 3 (m)	9.1 (m)	27.4 (m)	600-Meter-Depth Roof Salt Thickness 3 (m)	9.1 (m)	27.4 (m)	900-Meter-Depth Roof Salt Thickness 3 (m)	9.1 (m)	27.4 (m)	1,200-Meter-Depth Roof Salt Thickness 3 (m)	9.1 (m)	27.4 (m)
18.3	0.0022	0.0022	0.0019	0.0064	0.0066	0.0062	0.0075	0.0075	0.0074	0.0077	0.0077	0.0074
58.3	0.0037	0.0035	0.0035	0.0074	0.0074	0.0074	0.0080	0.0080	0.0080	0.0080	0.0080	0.0080
138.3	0.0071	0.0069	0.0069	0.0094	0.0094	0.0094	0.0094	0.0094	0.0094	0.0094	0.0094	0.0094
218.3	0.0087	0.0087	0.0087	0.0103	0.0101	0.0103	0.0101	0.0101	0.0101	0.0105	0.0105	0.0105

Roof Span (m)	300-Meter-Depth Shale Stiffness 1,500 (MPa)	10,000 (MPa)	70,000 (MPa)	600-Meter-Depth Shale Stiffness 1,500 (MPa)	10,000 (MPa)	70,000 (MPa)	900-Meter-Depth Shale Stiffness 1,500 (MPa)	10,000 (MPa)	70,000 (MPa)	1,200-Meter-Depth Shale Stiffness 1,500 (MPa)	10,000 (MPa)	70,000 (MPa)
18.3	0.0035	0.0022	0.0012	0.0077	0.0066	0.0055	0.0086	0.0075	0.0064	0.0086	0.0077	0.0067
58.3	0.0094	0.0035	0.0012	0.0107	0.0074	0.0055	0.0103	0.0080	0.0064	0.0107	0.0080	0.0067
138.3	0.0132	0.0069	0.0028	0.0123	0.0094	0.0069	0.0123	0.0094	0.0076	0.0132	0.0094	0.0076
218.3	0.0146	0.0087	0.0044	0.0130	0.0101	0.0078	0.0139	0.0101	0.0083	0.0148	0.0105	0.0083

Roof Span (m)	300-Meter-Depth Shale Thickness 3 (m)	6.1 (m)	12.2 (m)	600-Meter-Depth Shale Thickness 3 (m)	6.1 (m)	12.2 (m)	900-Meter-Depth Shale Thickness 3 (m)	6.1 (m)	12.2 (m)	1,200-Meter-Depth Shale Thickness 3 (m)	6.1 (m)	12.2 (m)
18.3	0.0022	0.0022	0.0022	0.0064	0.0066	0.0064	0.0074	0.0075	0.0074	0.0076	0.0077	0.0076
58.3	0.0035	0.0035	0.0035	0.0074	0.0074	0.0074	0.0080	0.0080	0.0080	0.0080	0.0080	0.0080
138.3	0.0071	0.0069	0.0071	0.0094	0.0094	0.0094	0.0094	0.0094	0.0094	0.0094	0.0094	0.0094
218.3	0.0087	0.0087	0.0087	0.0101	0.0101	0.0101	0.0101	0.0101	0.0101	0.0105	0.0105	0.0105

Table 5-5 presents the minimum factors of safety in the shale bed above the cavern for each of the 48 analyses performed using the Cycle 2 gas service cycle. Mohr-Coulomb factors of safety were determined assuming the cohesion and friction angle of shale are 3.5 MPa and 25 degrees, respectively. The Mohr-Coulomb factor of safety is defined as the strength of the material given by Equation 4-10 divided by the stress at a point in the material. Selection of the Mohr-Coulomb properties was somewhat arbitrary and was not a function of the material stiffness. The properties chosen represent reasonable values for deteriorated and fractured rock.

Figure 5-8 illustrates the minimum factors of safety in the shale bed above the cavern having an 18.3-meter roof span as a function of time for depths of 300, 600, 900, and 1,200 meters. The factors of safety increase when the pressure in the cavern is rising and decrease when gas is being withdrawn from the cavern. Figure 5-8 shows that the minimum factors of safety decrease slightly with each gas service cycle. This figure also shows that the factors of safety for the shale are reduced as the depth increases. The results of these analyses indicate that the factors of safety in the shale do not decrease significantly with time as a result of stress redistribution.

Figure 5-9 is similar to Figure 5-8 except factor-of-safety results are given for different cavern roof spans. The results presented in Figure 5-9 are for caverns at a depth of 600 meters; however, similar trends were predicted at the other simulated cavern depths. Interestingly, the factors of safety are not significantly different for roof spans of 58.3, 138.3, and 218.3 meters at this depth.

Table 5-5. **Minimum Mohr-Coulomb Factor of Safety in the Shale Bed Overlying the Caverns During the Cycle 2 Gas Service Cycle**

Roof Span (m)	300-Meter-Depth Shale Stiffness			600-Meter-Depth Shale Stiffness			900-Meter-Depth Shale Stiffness			1,200-Meter-Depth Shale Stiffness		
	1,500 (MPa)	10,000 (MPa)	70,000 (MPa)	1,500 (MPa)	10,000 (MPa)	70,000 (MPa)	1,500 (MPa)	10,000 (MPa)	70,000 (MPa)	1,500 (MPa)	10,000 (MPa)	70,000 (MPa)
18.3	16.04	7.23	3.89	7.11	3.71	2.38	2.84	2.09	1.65	1.97	1.21	1.16
58.3	2.48	2.18	1.43	1.53	1.30	0.99	1.28	0.98	0.78	1.05	0.79	0.68
138.3	1.98	1.72	1.36	1.33	1.05	0.92	1.13	0.88	0.76	0.98	0.78	0.67
218.3	1.93	1.63	1.26	1.31	1.01	0.88	1.13	0.85	0.74	0.97	0.77	0.62
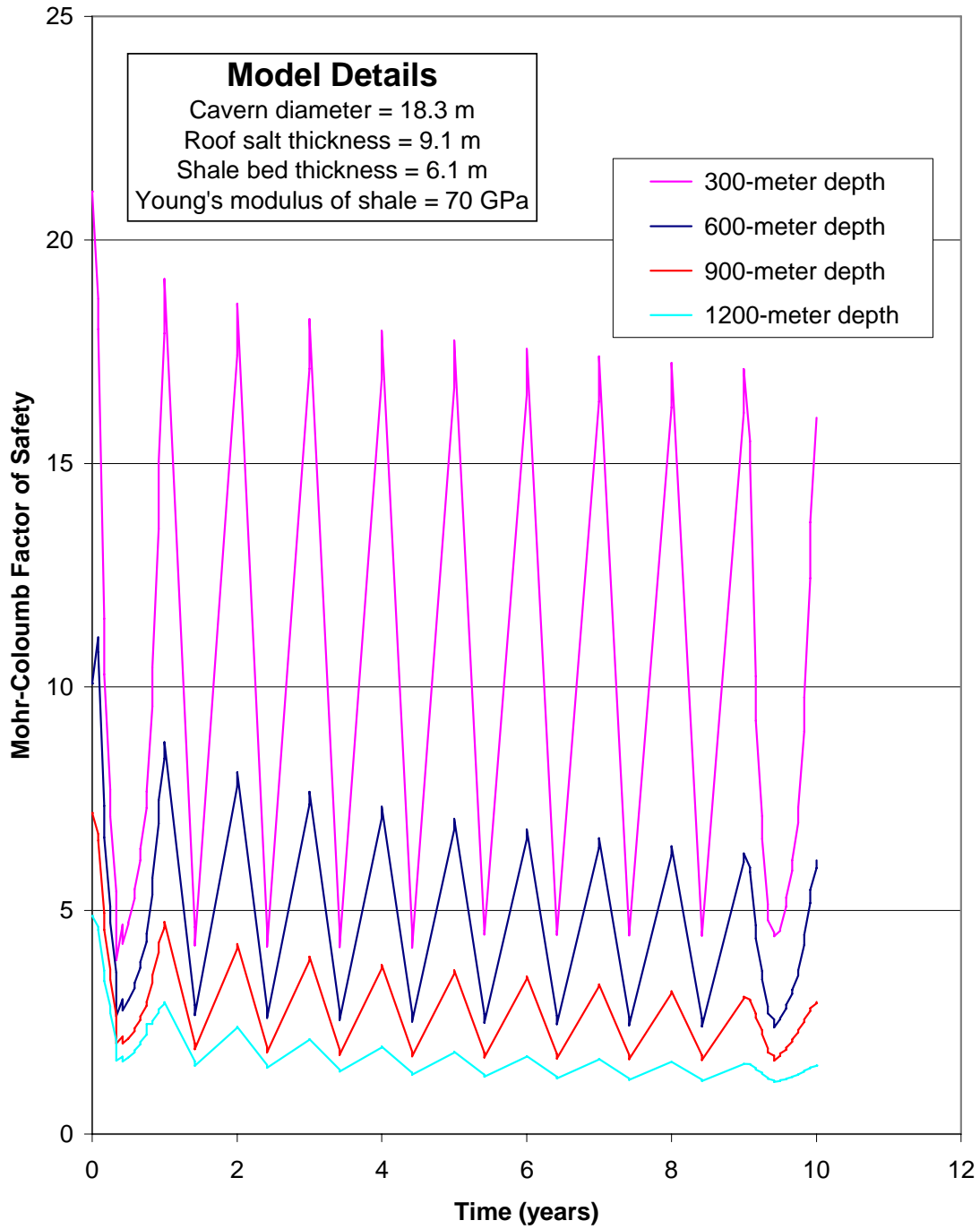
Figure 5-8. Minimum Mohr-Coulomb Factors of Safety in a 6.1-Meter Shale Bed Overlying a Cavern With an 18.3-Meter Roof Span at Depths of 300, 600, 900, and 1,200 Meters.

90
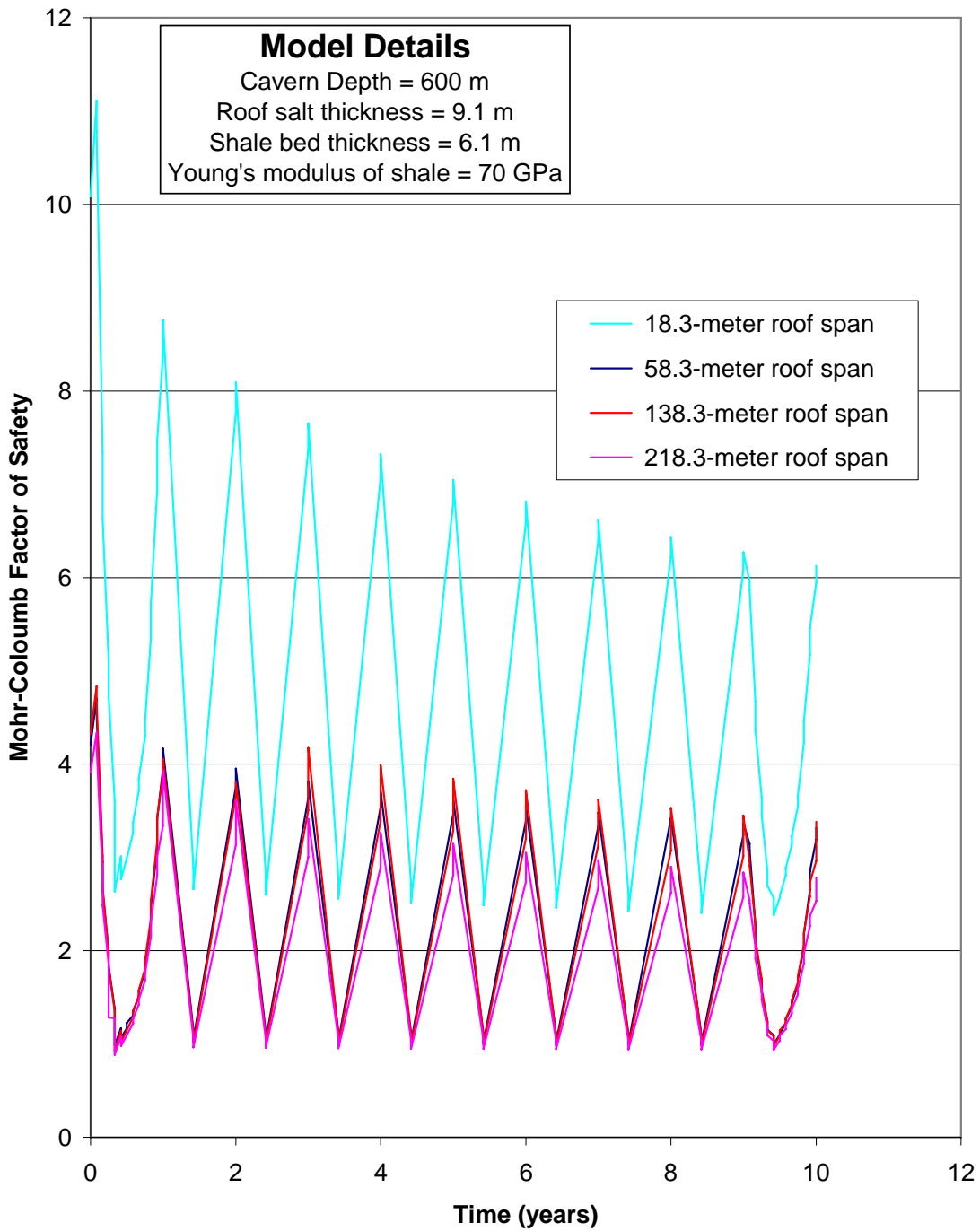
Figure 5-9. Minimum Mohr-Coulomb Factors of Safety in a 6.1-Meter-Thick Shale Bed Overlying Caverns Having Roof Spans of 18.3, 58.3, 138.3, and 218.3 Meters at a Depth of 600 Meters.

6.0 DISCUSSION OF RESULTS

The purpose of the numerical modeling effort was to illustrate the use of the dilation criterion developed in this study and to provide some guidance in defining acceptable cavern designs in bedded salt. The scope of the modeling effort was limited to defining minimum gas pressures necessary to maintain cavern stability based on the new dilation criterion developed under this project. The new criterion provides a better description for strength of salt than existing criteria because it accounts for some of the shortcomings of existing dilatancy boundary models. The effects of design parameters investigated during the numerical modeling effort are discussed in this chapter.

6.1 EFFECTS OF CAVERN DESIGN PARAMETERS

Minimum gas pressures necessary to prevent salt dilation using the criterion developed by this project (RD criterion) were presented in Chapter 5.0 for each of the 112 numerical analyses performed in this study using a 3-day withdrawal cycle. For comparison, determination of minimum gas pressures using an existing dilation criterion (DP criterion) were also computed and presented in Chapter 5.0. Design parameters investigated include cavern depth, cavern roof span, roof salt thickness, overlying shale thickness, overlying shale stiffness, and cavern operating scenarios. Each of these issues is discussed separately below.

6.1.1 <u>Cavern Depth</u>

In bedded salt formations, cavern depth is usually dictated by the elevation and thickness of the salt beds that can be solution mined. To prevent hydraulic fracturing of the salt, the maximum pressure is limited to pressures less than the overburden stress. In addition to controlling the maximum allowable gas pressure, cavern depth is also a key element in determining the minimum allowable gas pressure necessary to maintain stability. The effects of cavern depth on the minimum allowable gas pressure were assessed using the DP and RD criteria. Recall that the DP and RD criteria describe the stress conditions below which microfracturing of the salt should not occur.

Figure 6-1 provides an example illustration of the effects of cavern depth on the minimum allowable gas pressure gradient determined using the RD criterion. The results shown in Figure 6-1 were obtained from the simulations of the caverns having roof spans of 18.3, 58.3, 128.3, and 218.3 meters with accompanying stratigraphic details identified in the figure. Although not shown, similar trends were predicted by the simulations that modeled different thicknesses for the roof salt and shale beds and different stiffnesses for the shale beds. As shown in Figure 6-1, lower gas pressure gradients can be realized in very shallow caverns compared to caverns at great depth. However, keep in mind that, despite the similar gas
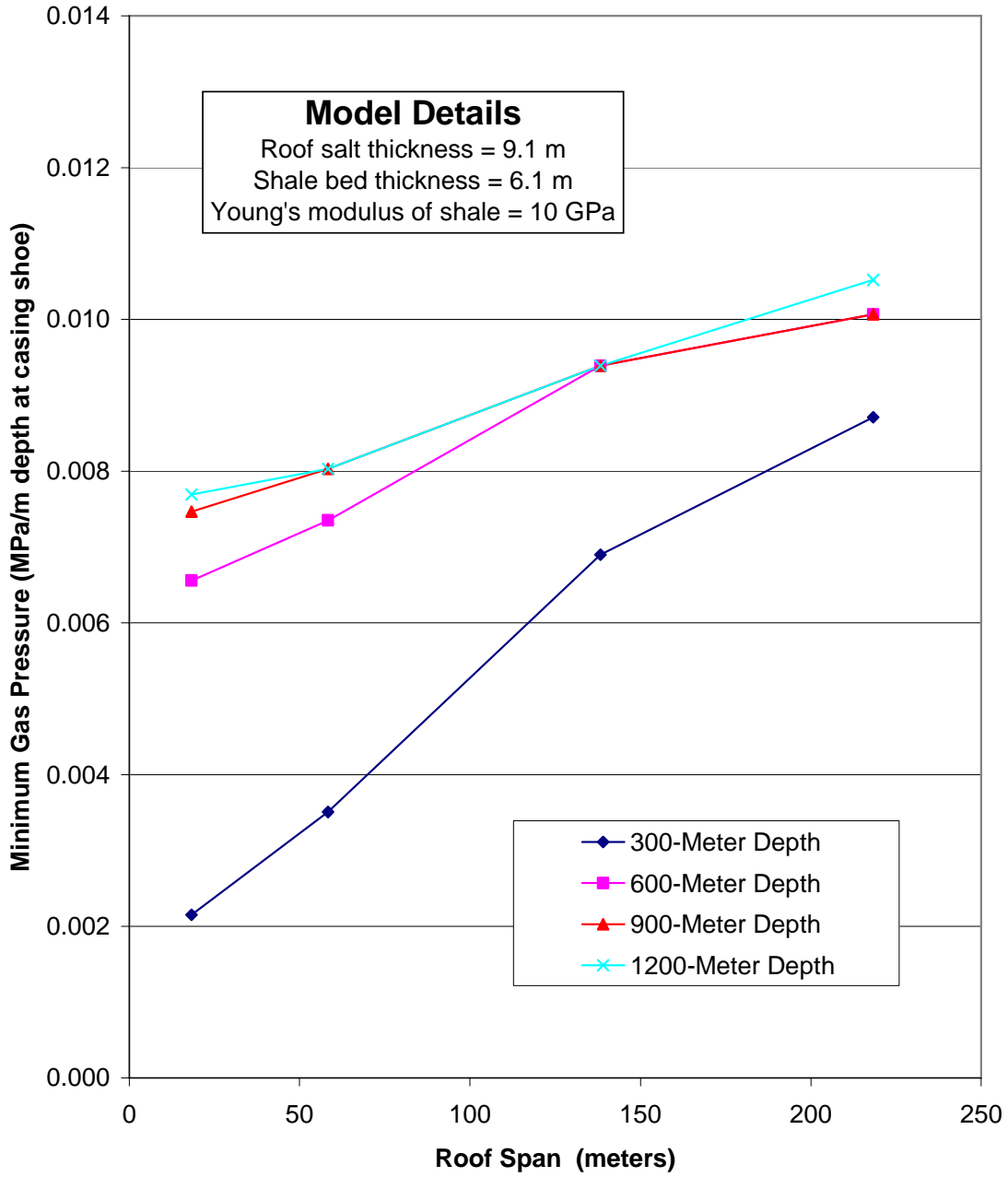
Figure 6-1. Minimum Gas Pressure Versus Cavern Roof Span Determined by the RD Criterion for Caverns Located at Depths of 300, 600, 900, and 1,200 Meters.

pressure gradients, the cavern pressures vary considerably with depth. The lowest gas pressure gradients are predicted for the caverns at a depth of 300 meters with successively higher gradients determined for the caverns at 600- and 900-meter depths. The minimum pressure gradient is not as sensitive to depth for the caverns at depths between 600 and 1,200 meters. As illustrated in Figure 6-1, the minimum pressure gradient determined for the caverns at a depth of 900 meters is essentially the same as those for caverns at a depth of 1,200 meters.

Figure 6-2 is similar to Figure 6-1 except that the DP criterion was used to determine the minimum gas pressure gradients. The results presented in Figure 6-2 indicate that the minimum gas pressure gradient decreases with cavern depth. This result contradicts that of the RD criterion. This finding can be explained by the dependency of the dilatancy limit on mean stress predicted by the two criteria. For the DP criterion, each 1 MPa incremental increase for I_1 results in a 0.18 MPa increase in the $\sqrt{J_2}$ stress measure. However, the nonlinear mean stress dependency of the RD criterion predicts that the ratio of $\sqrt{J_2}/I_1$ becomes less as the mean stress increases. The result is the depth dependency shown graphically in Figure 6-3. In addition to identifying the RD and DP dilation boundaries, Figure 6-3 illustrates the stress path histories of a point on the roof of a cavern near the axis of symmetry. The results presented are from the analyses that simulate an 18.3-meter cavern roof span at depths of 300, 600, 900, and 1,200 meters during the 10th year of the Cycle 2 gas service cycle (see Figure 5-7). The gas service cycle assumes that the cavern pressure varies between 0.019 and 0.00678 MPa/m of depth at the casing shoe for each of the four cavern depths. When the cavern pressure is at a minimum, the stress in the roof of the cavern nears the dilation boundaries; however, the predicted stresses at this point do not exceed either the RD or DP dilation limit for any of the analyses presented in Figure 6-3.

To further illustrate the differences between the DP and RD dilatancy criteria, the propensity for salt to dilate can be expressed using factor-of-safety values. Factor of safety is defined as the ratio of the $\sqrt{J_2}$ stress that will produce dilation according to Equations 4-19 and 4-3 to the calculated $\sqrt{J_2}$ stress state at the calculated I_1 stress state. A factor of safety of 1.0 is the limit stress state for dilation to occur. Dilation is expected to increase with decreasing factor-of-safety values.

Figure 6-4a compares the factor-of-safety values using the DP and RD criteria at a depth of 300 meters when the caverns are at a pressure of 0.0068 MPa/m depth at the casing shoe (1.9 MPa). The results of the two criteria are quite similar over the upper portion of the cavern but are slightly different below the cavern midheight. In general, the salt is predicted to be less safe below the cavern midheight using the DP criteria than the RD criteria. This finding is illustrated in Figure 6-4a where a zone of salt near the surface of the cavern between the two shale interbeds is shown to have a factor of safety less than 1.0 based on the DP criteria. Failure was not predicted by the RD criteria at this location.

94
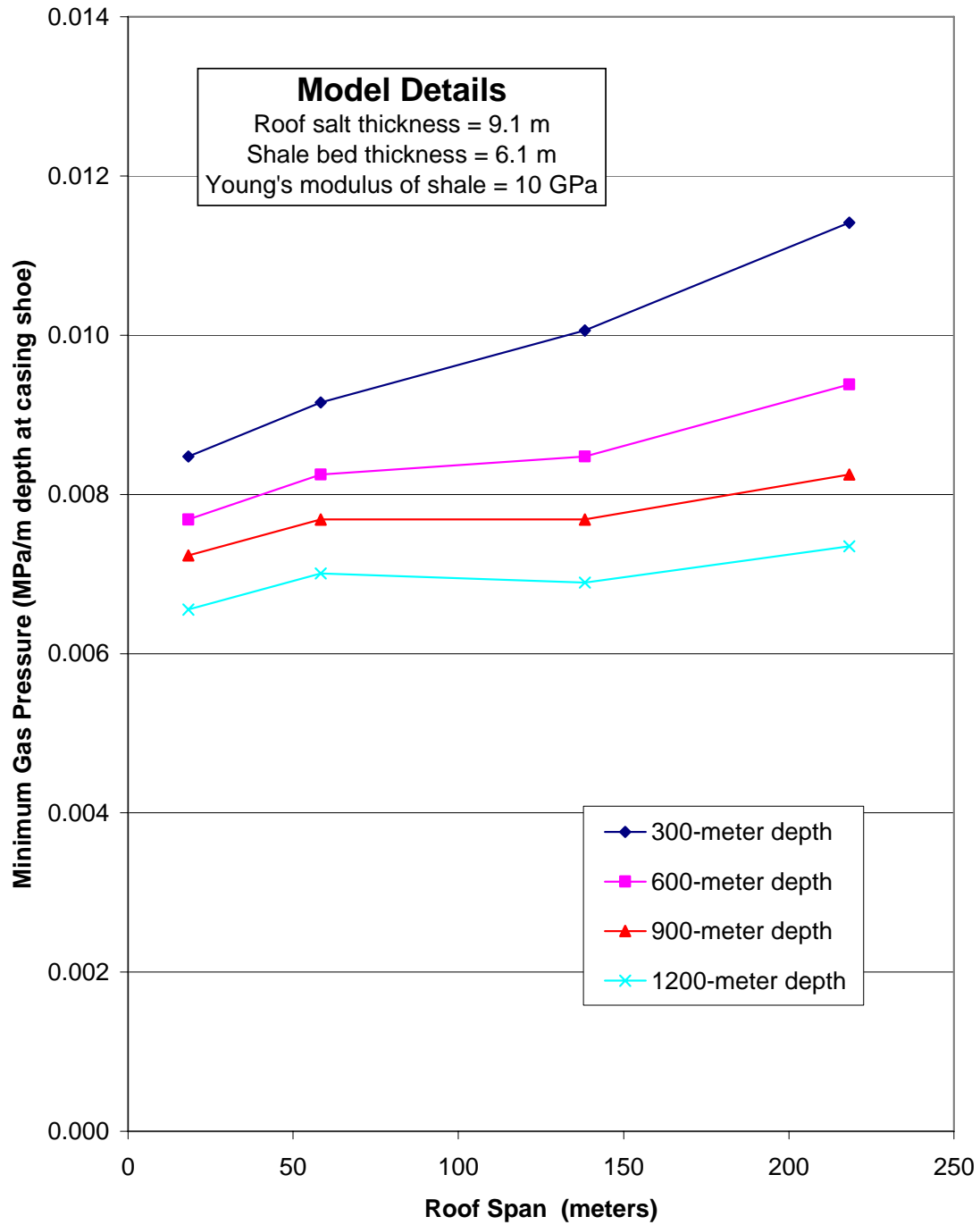
Figure 6-2. Minimum Gas Pressure Versus Cavern Roof Span Determined by the DP Criterion for Caverns Located at Depths of 300, 600, 900, and 1,200 Meters.
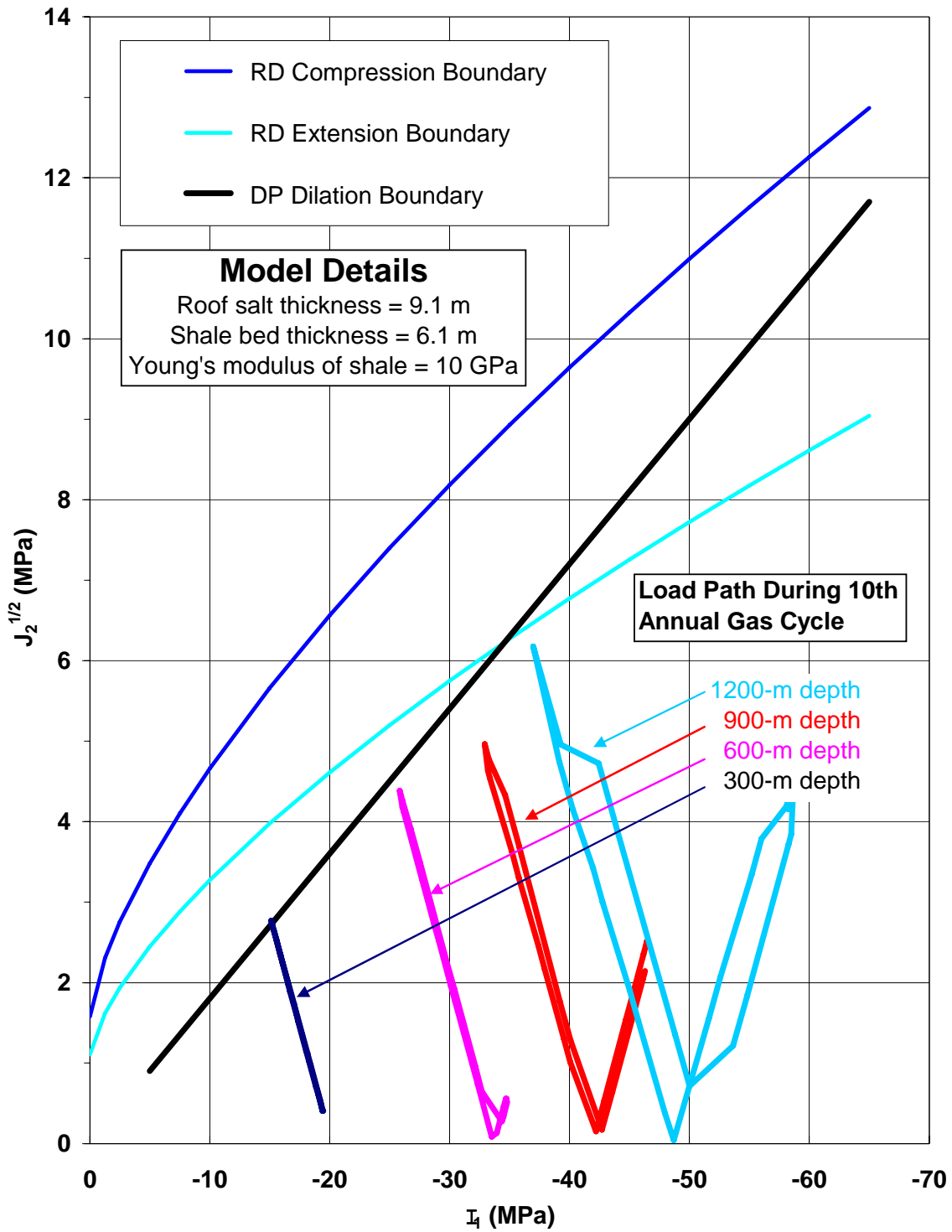
Figure 6-3. Illustration of Stress History at a Point on the Surface of Caverns Located at Depths of 300, 600, 900, and 1,200 Meters During the 10th Annual Gas Service Cycle.
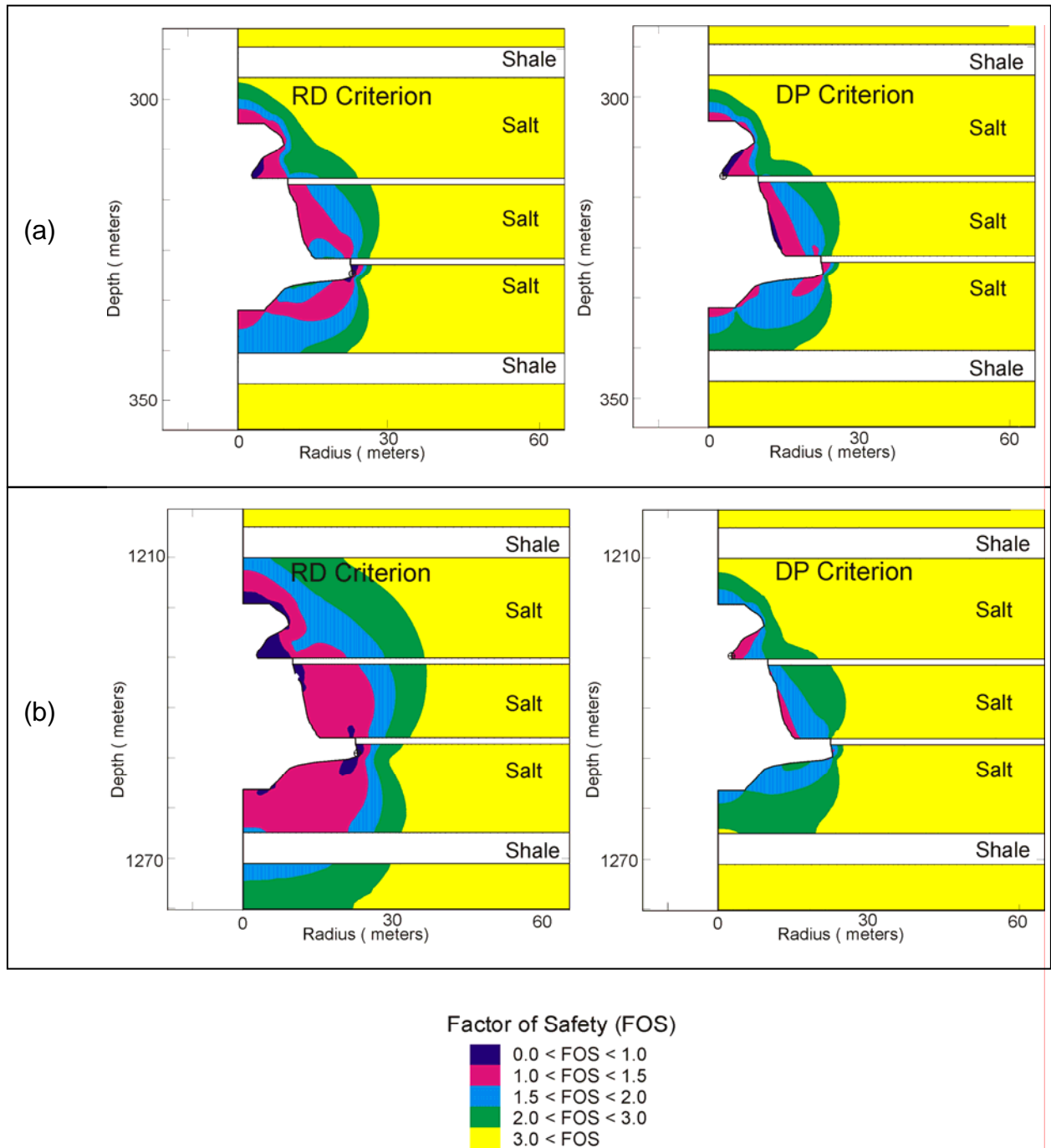
Figure 6-4. Comparison of Factor-of-Safety Contours Using the RD and DP Criterion for Caverns at a Depth of (a) 300 Meters and (b) 1,200 Meters (Gas Pressure Gradient of 0.0068 MPa/m Depth at the Casing Shoe).

97

Figure 6-4b is similar to Figure 6-4a but provides factor-of-safety contours determined from the analyses simulating caverns at a depth of 1,200 meters below ground surface. The results presented in Figure 6-4b were also predicted when the pressure in the caverns was 0.0068 MPa/m depth at the casing shoe (8.1 MPa). The predicted factor-of-safety results are significantly different for the two criteria at a depth of 1,200 meters. The RD criterion predicts that a significant amount of salt above the cavern midheight will fail; whereas, the DP criteria does not predict failure of the salt at this gas pressure. This difference is attributable to the nonlinear mean stress dependency of the RD criteria. The dilation limit predicted by the RD criterion for triaxial extension states of stress is greater than that predicted by the DP criterion at low mean stress (see Figure 6-3). As the cavern depth becomes progressively deeper, the mean stress in the salt increases because of the additional overburden. As shown in Figure 6-3, the dilation limit predicted by the DP criterion becomes greater than that predicted by the RD criterion for triaxial extension states of stress at a mean stress of about -11 MPa ($I_1 = -33$ MPa).

Based on the laboratory testing, the RD criterion more accurately describes the behavior of salt, and the DP criterion does not produce conservative results for caverns at great depth. This finding will have an impact on the minimum allowable gas pressure recommended for natural gas caverns, particularly for those caverns at greater depth. *Based on the RD criterion, the minimum gas pressure gradient necessary to prevent salt damage must be increased for progressively deeper cavern depths.*

6.1.2 Cavern Roof Span

Oval-shaped caverns, or ones with an arc-shaped roof with a maximum diameter to height ratio close to one, are the most stable when the far-field stress components are nearly equivalent. As the cavern diameter becomes larger, the vertical component of stress is reduced at the roof of the cavern. Additionally, the horizontal components of stress in the salt are influenced by roof span, cavern height, and salt creep. The resulting increase in shear stress and decrease in mean stress can lead to shear failure of the salt. Ultimately, the vertical components of stress may become positive, which means that the rock above the cavern is then subjected to vertical tensions that may endanger the stability of the cavern. This situation may occur over large caverns with extended flat roofs and weak caprock. Numerous geologic features or anomalous zones may exist within the underground setting. While it is impossible to include all of the known features in a model or to know all of the anomalous zones that exist, the chances of encountering or intersecting these features or zones increases as the cavern size increases.

The effects of cavern roof span on the minimum allowable gas pressure were investigated in this study. Numerical simulations were performed of caverns having maximum roof spans of about 18.3, 58.3, 128.3, and 218.3 meters. The correlation between minimum gas pressure and cavern roof span is apparent for every analysis performed in this study. Caverns with larger

roof spans require higher minimum gas pressures to maintain cavern stability using either the RD or the DP criteria.

Figures 6-1 and 6-2 illustrate the effects of cavern roof span on the minimum gas pressure gradient for caverns at depths of 300, 600, 900, and 1,200 meters using the RD and DP criteria, respectively. In general, the RD criterion predicts that the minimum pressure gradient must be greater than 0.0084 MPa/m depth at the casing shoe for caverns modeled with roof spans greater than 60 meters (see Table 5-4). Two conditions were determined that would allow the minimum gas pressure gradients to be less than 0.0084 MPa/m for cavern roof spans greater than 60 meters in bedded salt using the RD criterion. The first and most important feature is an extremely strong nonsalt bed must exist above the cavern. As shown in Table 5-4, those analyses performed with a high stiffness (Young's modulus of 70 GPa) for the overlying shale bed can sustain pressure gradients less than 0.0084 MPa/m without causing damage in the salt.

Gas pressure gradients less than 0.0084 MPa/m were also determined for a few of the analyses of a cavern having a 138.5-meter roof span. The conditions that allowed the pressure gradient to be less than 0.0084 MPa/m were shallow depth (300 meters) and reasonable stiffness for the overlying shale bed (Young's modulus = 10 GPa). A pressure gradient greater than 0.0084 MPa/m was determined necessary for all of the analyses performed with a roof span of 60 meters are greater and Young's modulus of 1.5 GPa for the overlying shale. *Thus cavern depth and stiffness of the nonsalt beds are extremely important factors that limit the roof span of a cavern. Also, the minimum allowable gas pressure necessary to prevent damage to the salt must be increased for caverns with progressively larger roof spans.*

6.1.3 Roof Salt Thickness

A total of 48 analyses were performed to assess the effects of roof salt thickness on the minimum allowable gas pressure necessary to maintain stability. The analyses were performed for four depths (300, 600, 900, and 1,200 meters) and three different roof salt thicknesses (3, 9.1, and 27.4 meters). A constant thickness and stiffness was specified for the shale bed overlying the cavern for the 48 analyses used in this assessment. The shale bed immediately above the caverns were assigned a value for Young's modulus of 10 GPa and were 6.1 meters thick.

Figures 6-5 and 6-6 provide example illustrations of the effects of roof salt thickness on the minimum allowable pressure necessary to prevent salt dilation using the RD and DP criteria, respectively. Figures 6-5 and 6-6 show results for a cavern roof span of 18.3 meters. The change in the minimum allowable gas pressure with roof span is given in Figures 6-1 and 6-2 for the RD and DP criteria, respectively, for a roof salt thickness of 9.1 meters. However, Figures 6-1 and 6-2 would look basically the same regardless of the roof salt thickness selected, which can be confirmed from Tables 5-3 and 5-4. Based on the results provided in Tables 5-3
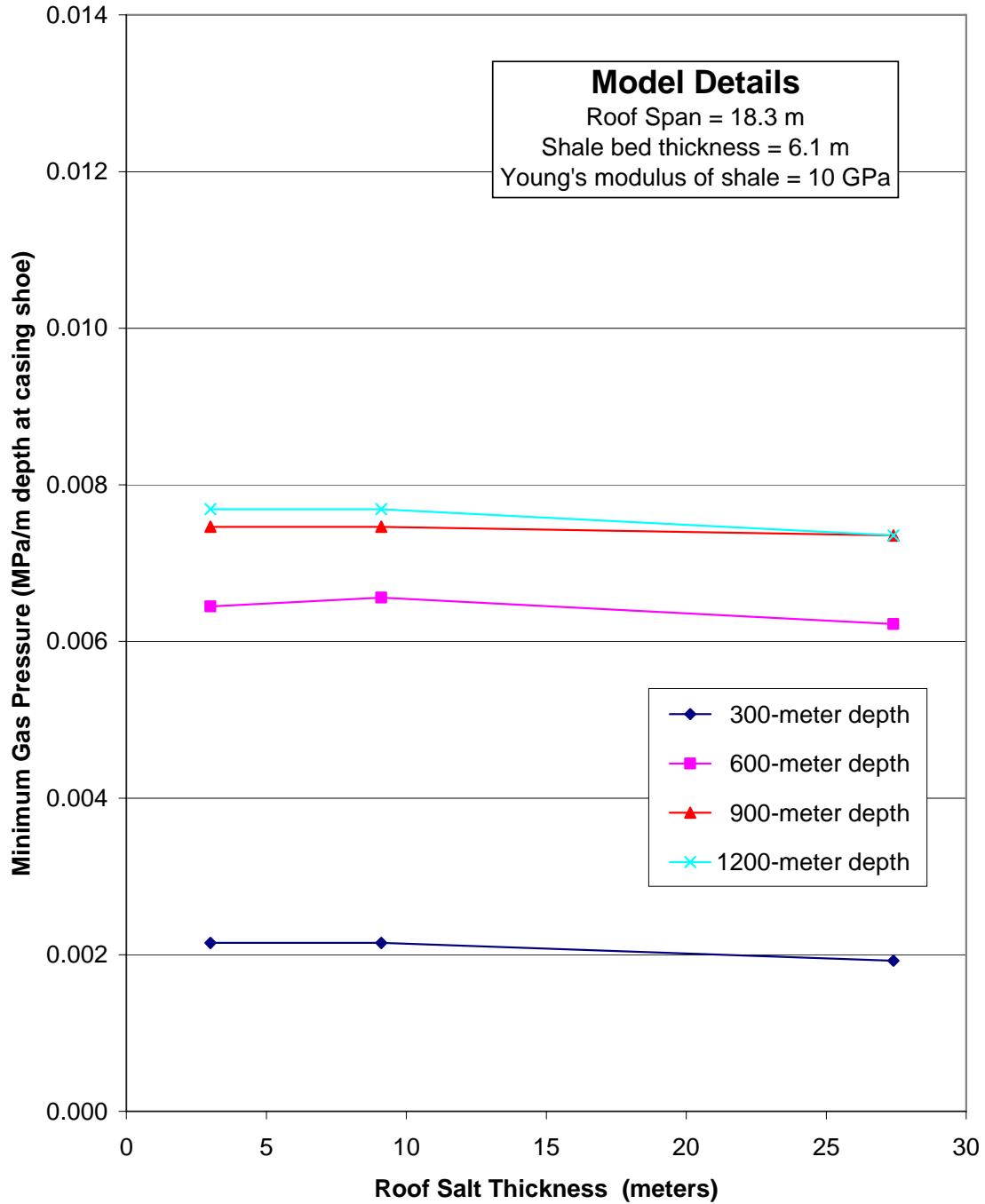
Figure 6-5. Minimum Gas Pressure Versus Roof Salt Thickness Determined by the RD Criterion for Caverns Located at Depths of 300, 600, 900, and 1,200 Meters.
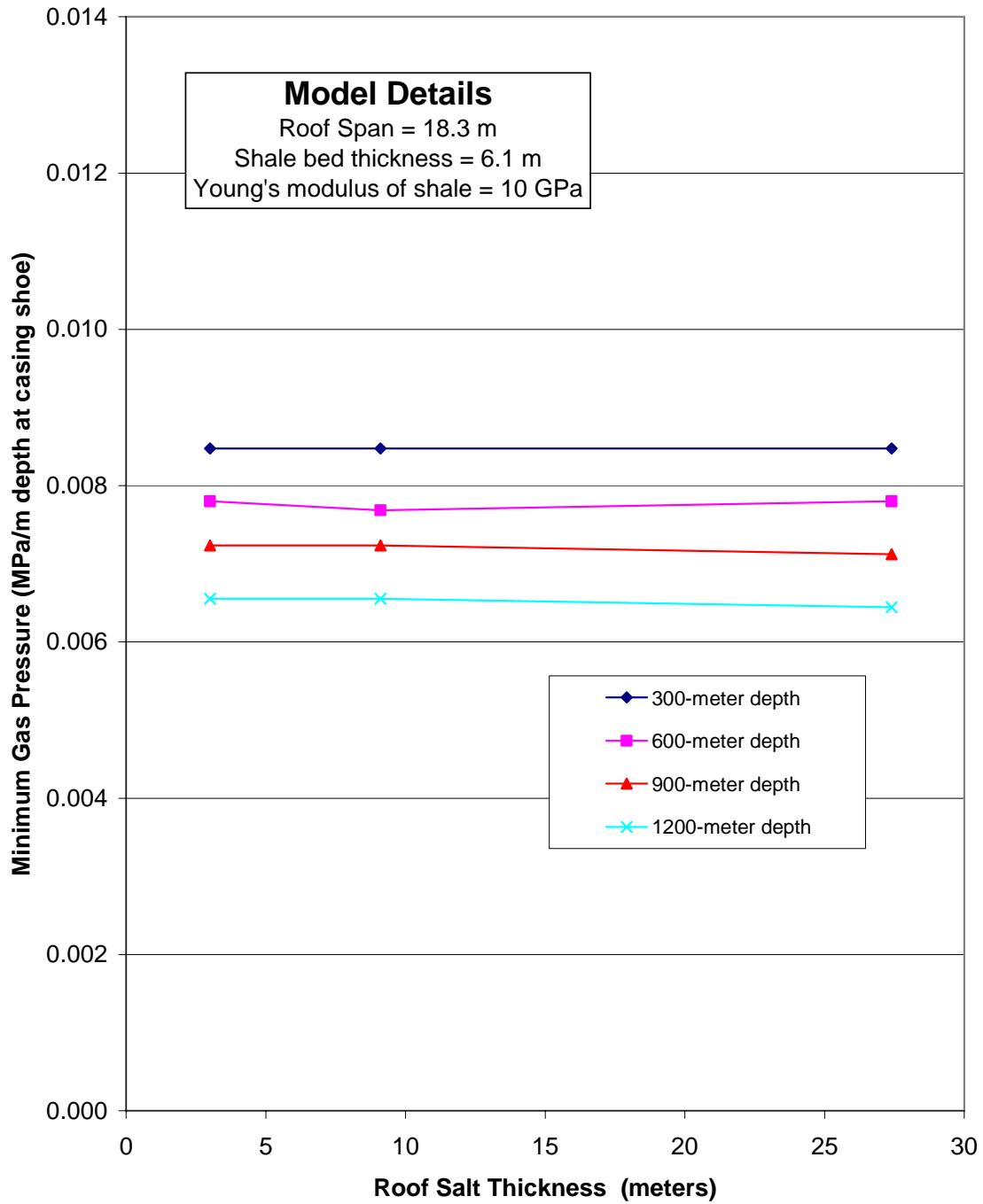
Figure 6-6. Minimum Gas Pressure Versus Roof Salt Thickness Determined by the DP Criterion for Caverns Located at Depths of 300, 600, 900, and 1,200 Meters.

101

and 5-4 and illustrated in Figures 6-5 and 6-6, *roof salt thickness has little or no influence on the minimum allowable gas pressure necessary to prevent damage to the salt surrounding the cavern*. However, the importance of maintaining a competent layer of salt above the cavern roof cannot be underestimated. The roof salt provides a barrier of rock having a low permeability necessary to prevent the upward migration of gas. Isolation of the nonsalt stratigraphic layers from the potentially degrading environmental effects of the stored gas is an important role for a competent roof salt member. Additionally, the salt in formations comprised of very weak nonsalt beds must provide the structural support to prevent cavern collapse. Analyses were not performed in this study to investigate the response of roof salt thickness in a formation having extremely weak nonsalt units.

6.1.4 Overlying Shale Bed Thickness

The thickness of the shale beds can very significantly in a bedded salt formation. In this study, numerical analyses were performed assuming that the shale bed immediately above the cavern had thicknesses of 3.0, 6.1, or 12.2 meters. The minimum pressure necessary to prevent salt dilation around the cavern were evaluated for caverns having four different roof spans (18.3, 58.3, 128.3, and 218.3 meters) located at four different depths (300, 600, 900, and 1,200 meters). For these comparative analyses, a single roof salt thickness of 9.1 meters was assumed and a constant value for Young's modulus of 10 GPa was specified for the shale.

The results of the modeling effort showed that the potential for salt dilation around the cavern was not influenced by the thickness of the shale bed above the cavern over the range of thicknesses evaluated (3.0 to 12.2 meters). This finding is based on both the RD and DP dilation criteria predictions. Although the two dilation criteria predict different minimum gas pressures, the minimum allowable pressure is the same regardless of the thickness of the overlying shale bed. The effect of the overlying shale bed thickness on the minimum gas pressure gradient predicted by the RD criterion is provided in Table 5-4. Similar results predicted by the DP criterion are presented in Table 5-3.

Figure 6-7 illustrates the minimum gas pressure gradient predicted by the RD criterion versus shale bed thickness for caverns at depths of 300, 600, 900, and 1,200 meters. The results presented in Figure 6-7 are for a cavern having a roof span of 18.3 meters. As shown in this figure, the thickness of the overlying shale bed had no affect on the minimum gas pressure for the conditions modeled.

6.1.5 Shale Bed Stiffness

The stiffness of the overlying shale beds modeled was found to have a significant affect on the predicted minimum allowable gas pressure necessary to prevent dilation of the salt surrounding the caverns. The effects of the overlying shale stiffness on the minimum gas pressure predicted by the DP and RD criterion are given in Tables 5-3 and 5-4, respectively. Results are reported
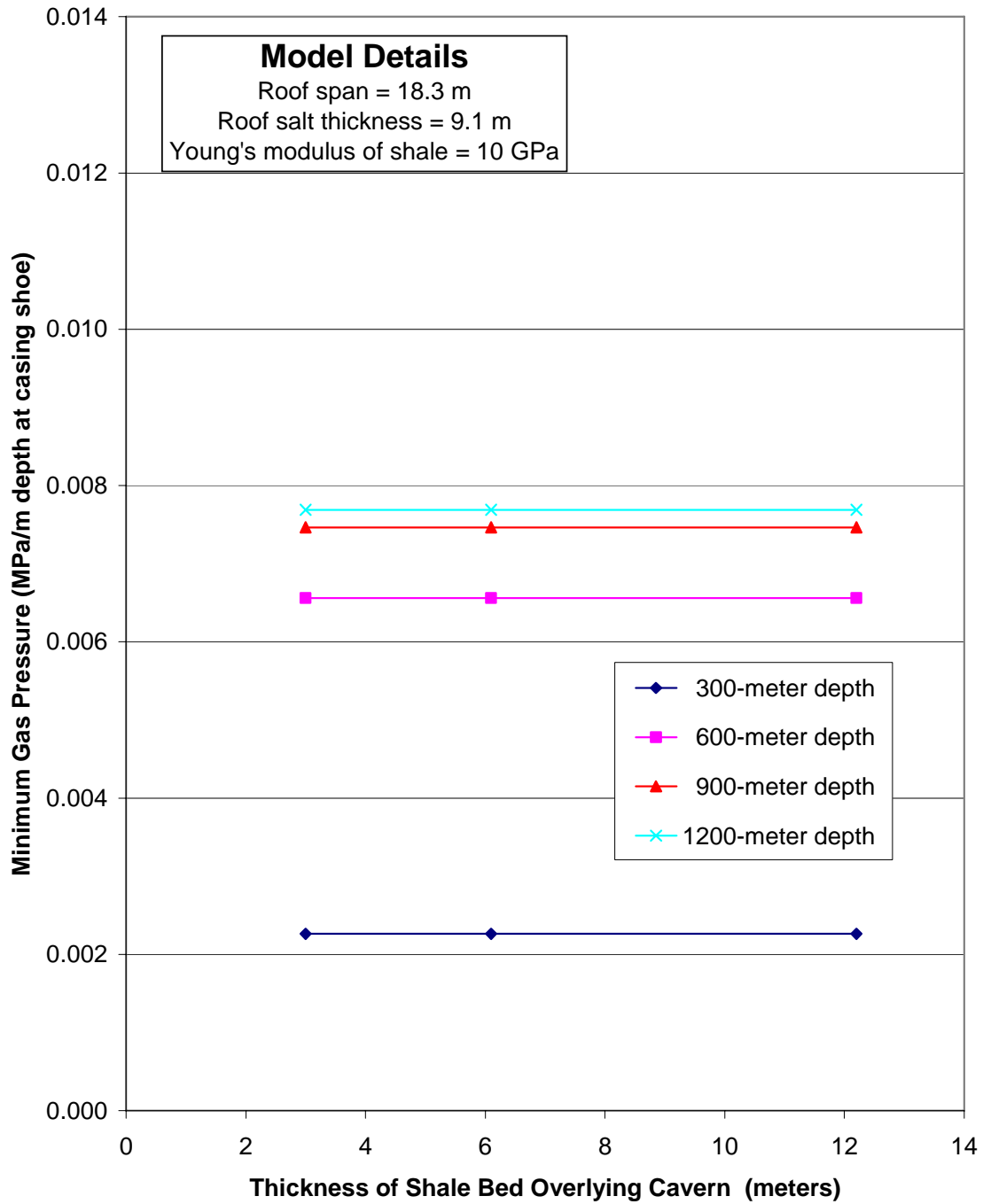
Figure 6-7. Minimum Gas Pressure Versus Shale Bed Thickness Determined by the RD Criterion for Caverns Located at Depths of 300, 600, 900, and 1,200 Meters.

for analyses using three different material stiffnesses for the shale beds (Young's modulus of 1.5, 10 and 70 GPa). The results were determined for the four cavern depths and four cavern roof spans investigated. The results show that lower minimum gas pressures are predicted by the RD and DP criteria for increasingly greater shale bed stiffness (higher values for Young's modulus).

Figure 6-8 provides an example illustration of the influence of shale bed stiffness on the minimum gas pressure gradient predicted by the RD criterion for a cavern having a roof span of about 58.3 meters at depths of 300, 600, 900, and 1,200 meters. The results presented in Figure 6-8 show a significant decrease in the minimum gas pressure for increasingly higher shale stiffness. Figure 6-8 also shows that the relative change in the minimum gas pressure as a function of Young's modulus in the shale is highly nonlinear.

Figure 6-9 is similar to Figure 6-8 except that the minimum pressure gradients determined using the DP criterion are presented. Comparison of Figures 6-8 and 6-9 shows that the results predicted by the DP criterion are less sensitive to the overlying shale bed stiffness than those predicted by the RD criterion.

Although not shown, the DP criterion results are more sensitive to the shale bed stiffness as the cavern roof span becomes larger. As shown in Table 5-3, the minimum gas pressure predicted by the DP criterion for the cavern having a roof span of 218.3 meters at a depth of 600 meters decreases by 0.0065 MPa/m when Young's modulus of the shale bed is varied from 1,500 to 70,000 MPa (the predicted minimum pressures are 0.0141 and 0.0076 MPa/m for Young's modulus of 1,500 and 70,000 MPa, respectively). This decrease for the minimum pressure is more than double that of the cavern with a roof span of 58.3 meters at the same depth (0.0025 MPa/m). Thus the stiffness of the shale bed becomes increasingly more important and a greater design issue as the cavern roof span increases when using the DP criterion.

The sensitivity of the RD criterion predictions to the shale bed stiffness as the cavern roof span becomes larger are difficult to summarize (see Table 5-4). However, it is undeniable that the stiffness of the shale bed has a major impact on the minimum gas pressure predicted by the RD criterion regardless of cavern roof span.

6.1.6 <u>Cavern Operating Scenario</u>

Analyses were performed using two different cavern operating scenarios. The first operating scenario (Cycle 1) simulated a single rapid withdrawal of gas from the cavern following dewatering of the cavern at an operating pressure gradient equal to 0.0204 MPa/m of depth to the casing shoe. During this operating scenario, the gas was completely removed from the cavern at a constant depressurization rate over 3 days (see Figure 5-7). The second cycle (Cycle 2) used in this study is an annual gas cycle that varied between 0.0204 and
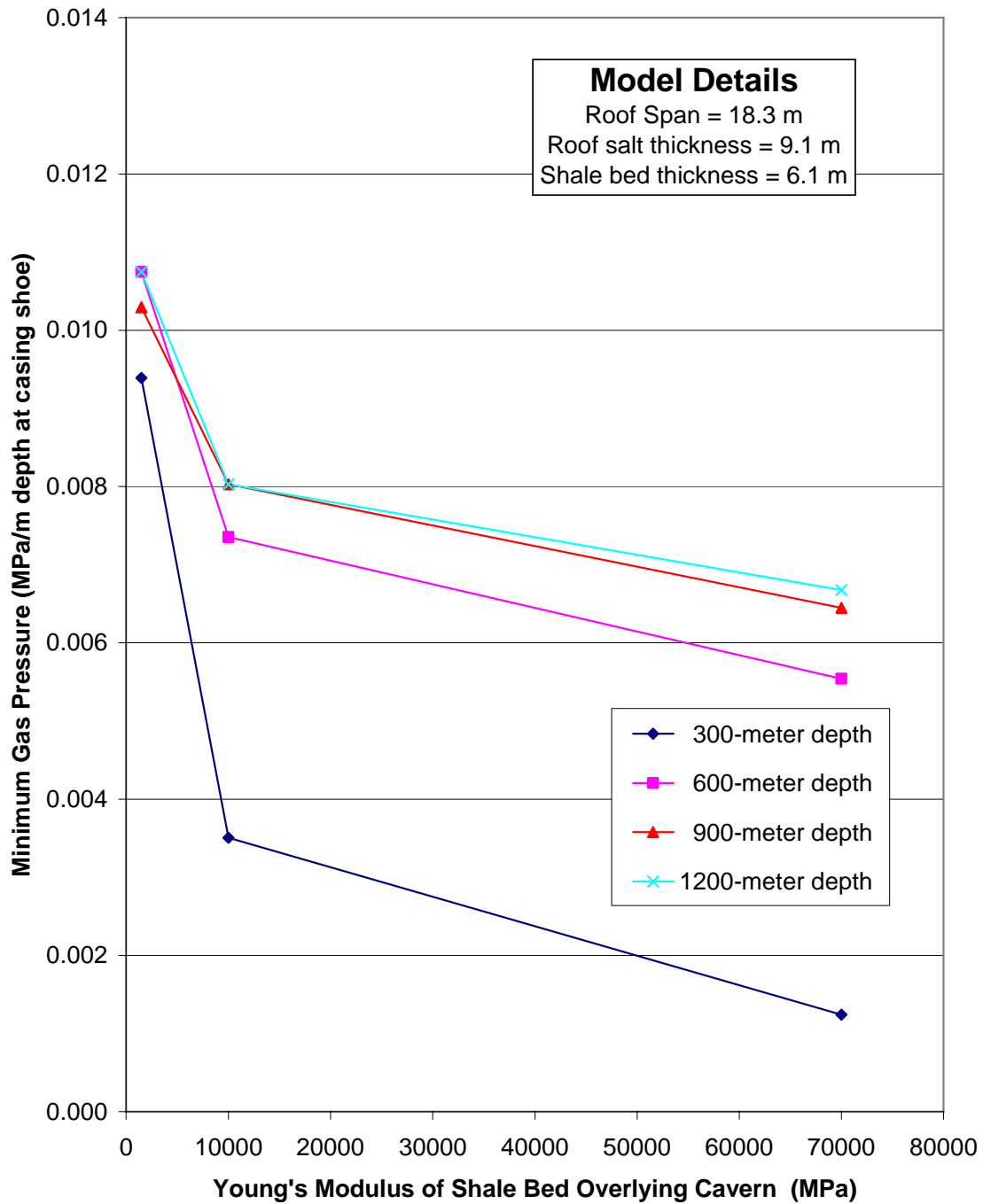
Figure 6-8. Minimum Gas Pressure Versus Overlying Shale Bed Stiffness Determined by the RD Criterion for Caverns Located at Depths of 300, 600, 900, and 1,200 Meters.

105
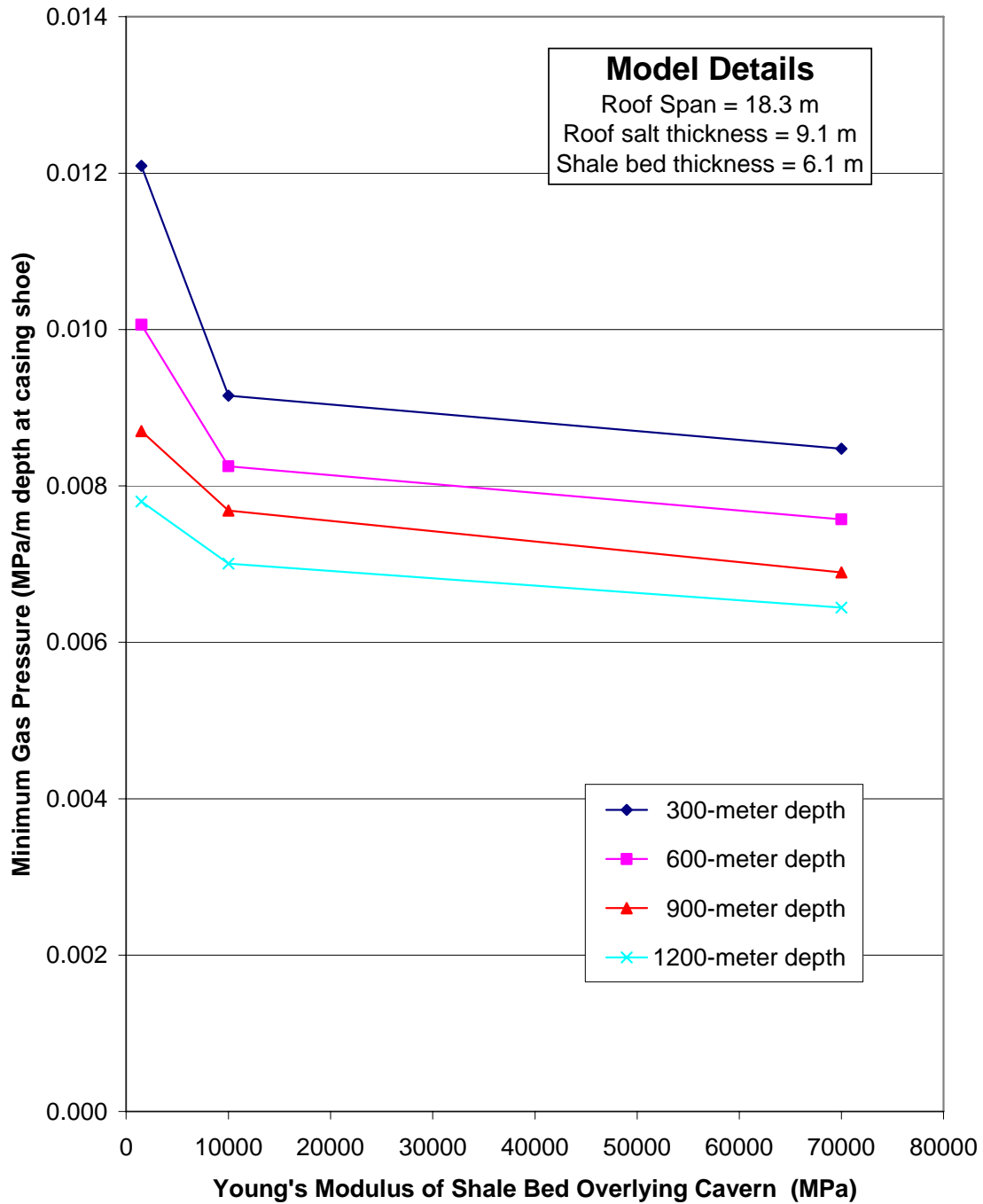
Figure 6-9. Minimum Gas Pressure Versus Overlying Shale Bed Stiffness Determined by the DP Criterion for Caverns Located at Depths of 300, 600, 900, and 1,200 Meters.

106

0.0057 MPa/m depth at the casing shoe. This cycle was repeated 10 times to provide estimates for the potential for salt dilation and failure of the shale beds over a 10-year period (see Figure 5-7). All of the simulations using Cycle 2 included a 6.1-meter-thick shale bed overlying caverns having a roof salt thickness of 9.1 meters.

A total of 112 numerical analyses were performed using the Cycle 1 gas service cycle. A total of 48 numerical simulations were performed using the second gas service cycle (Cycle 2). Early in the process of performing the 48 simulations using Cycle 2, the results showed that the state of stress in the salt surrounding the caverns was not deteriorating toward a condition that promotes the dilation of salt. However, the results did suggest that the factor of safety of the shale bed had decreased between the first and last annual cycle. Thus all minimum gas pressures reported using the RD and DP criteria thus far in this report are based on the Cycle 1 pressure history. Cycle 1 represents an extreme case and maintains a conservative approach for evaluating the minimum allowable gas pressure necessary to prevent dilation of the salt. Simulations using Cycle 2 were carried out to evaluate the potential for longer-term failure of the shale bed overlying the cavern. The 48 numerical simulations using Cycle 2 differ in the stiffness of the shale, cavern roof span, and cavern depth modeled.

Figure 6-10 plots the factor of safety of the salt at a point on the surface of the cavern at the centerline of the roof using the Cycle 2 gas pressure history. Figure 6-10 was generated from the analysis that included the following parameters: (1) cavern depth of 600 meters, (2) cavern roof span of 58.3 meters, and (3) Young's modulus of the overlying shale bed of 10 GPa. This figure provides an example illustration of the potential for salt dilation using both the RD and DP criteria for the 10-year gas service cycle. The factor of safety plotted varies with time and pressure. The pressure response is apparent by the cyclic response having a 1-year frequency. The time response can be identified as the change in the factor of safety predicted at the peaks and troughs of the history response. Although difficult to see because of the scale used in Figure 6-10, the minimum factor of safety for the salt occurs at the end of the first withdrawal cycle on Day 152. Subsequent cycles do not result in the prediction of lower factor-of-safety values for this point on the surface of the cavern. In general, this is also true for the salt at other locations around the cavern. This result is reasonable considering the fact that no deterioration of rock properties or cyclic fatigue was included in the analyses. Figure 6-10 clearly shows the increase in cavern stability that can be obtained by maintaining higher cavern pressures.

A significant difference between the RD and DP criteria is the inclusion of Lode angle effects in the RD model. A plot of the Lode angle in the salt surrounding the cavern at a depth of 600 meters with a roof span of 58.3 meters is provided in Figure 6-11. This figure shows contours of the Lode angle during the simulation using Cycle 2 at: (a) maximum pressure after filling the cavern with gas, (b) minimum pressure during the first cycle, (c) maximum pressure during the 10th cycle, and (d) minimum pressure during the 10th cycle. This figure clearly shows
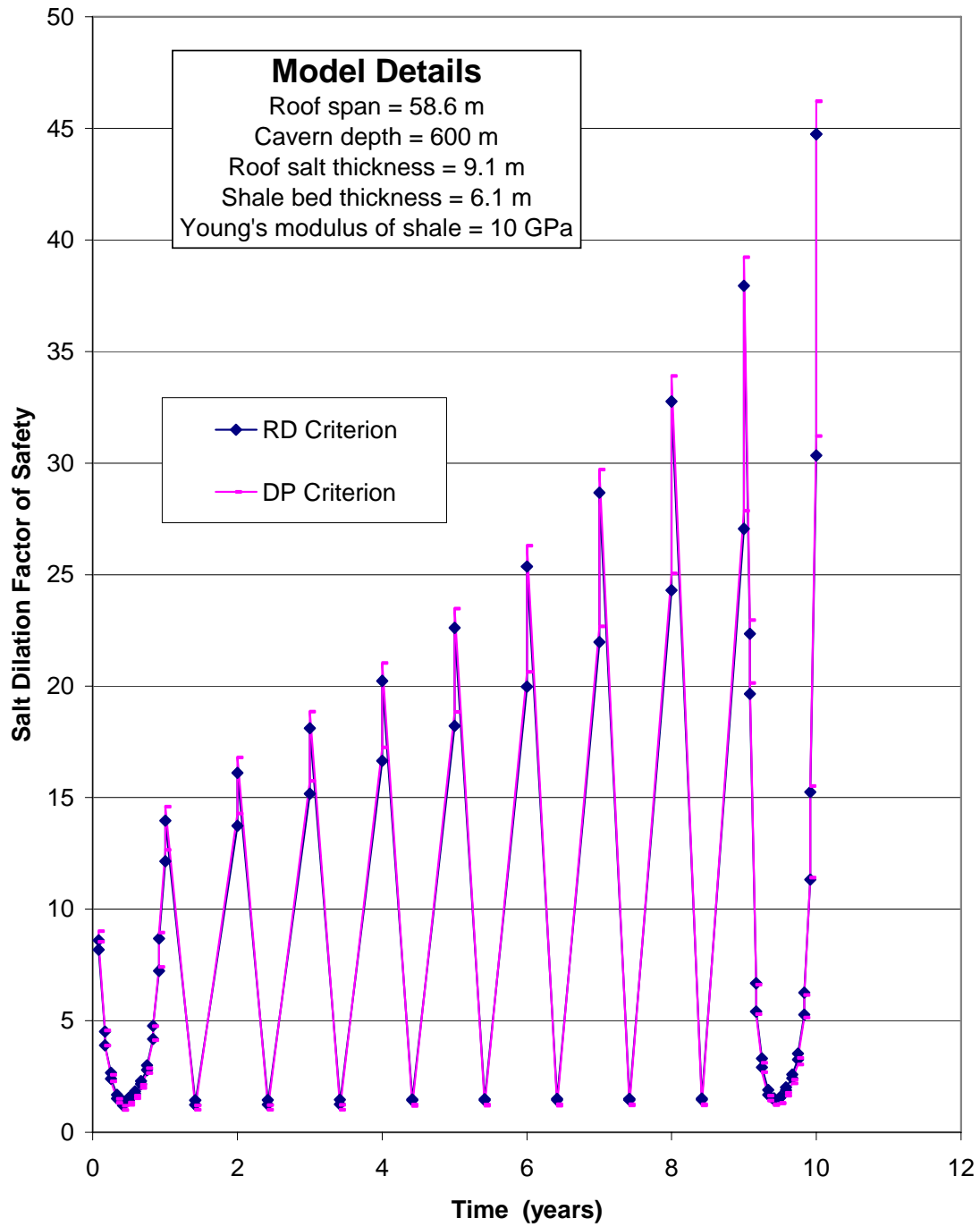
Figure 6-10. RD and DP Salt Damage Factor-of-Safety Histories at a Point on the Surface of a Cavern During 10 Years of Service.
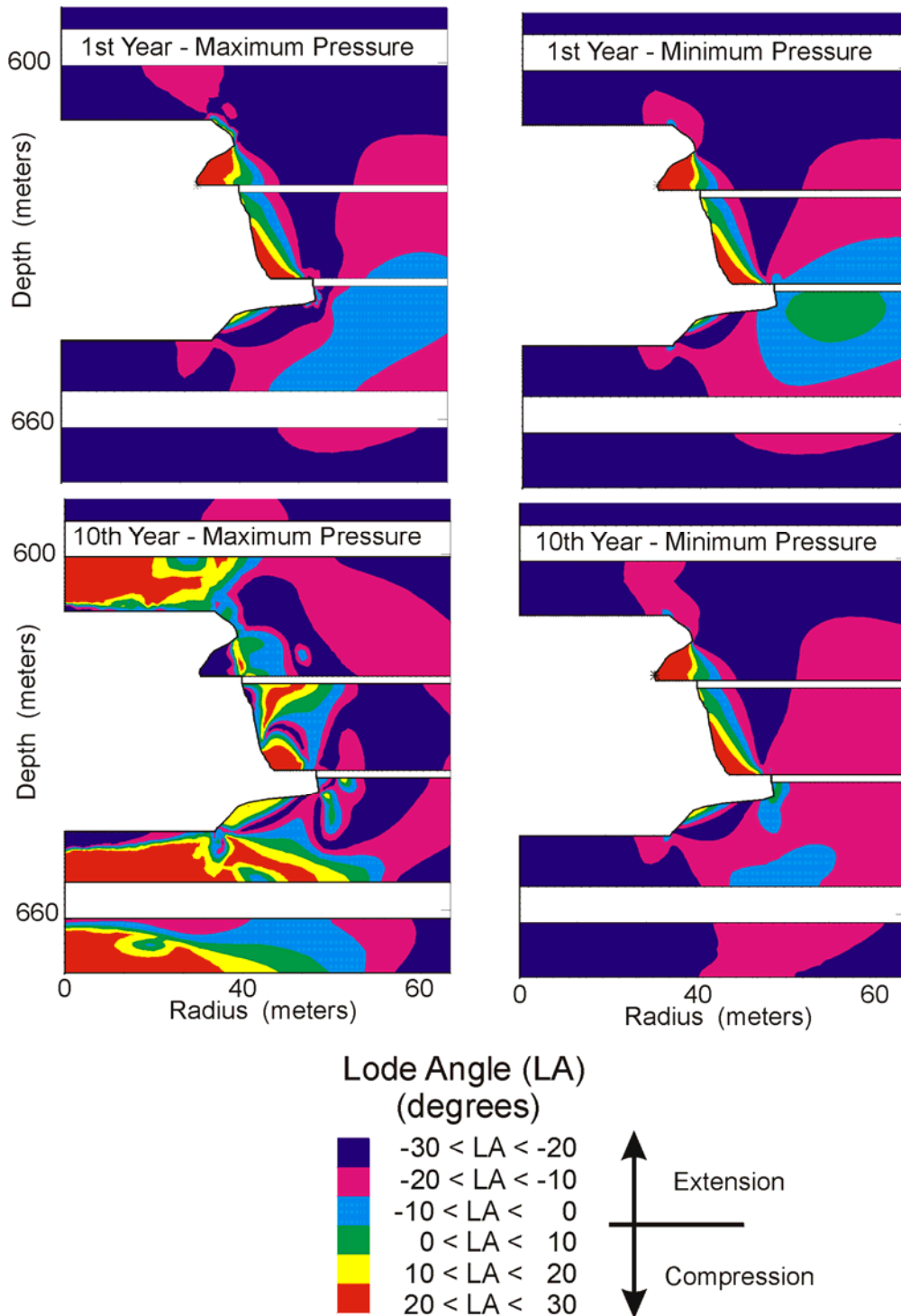
Figure 6-11. Predicted Lode Angle Around a 58.3-Meter Cavern Roof Span at a Depth of 600 Meters at Minimum and Maximum Pressure During the First and Tenth Cycle.

109

that the roof salt is near a state of triaxial extension (Lode angle of –30 degrees) when the cavern is at minimum pressure. This is significant because the laboratory testing clearly shows a reduced salt strength under triaxial extension states of stress (see Figure 3-3).

Because the potential for salt dilation was determined to be greatest during the first withdrawal of gas from the cavern, the major emphasis of the analyses using Cycle 2 was directed toward assessing the likelihood of failure of the shale as a function of time. A detailed discussion of Mohr-Coulomb factor-of-safety results of the shale bed immediately above the cavern is given in Section 5.4.3. The results indicate that the factor of safety for the shale bed above the cavern reduces slightly with each gas service cycle. However, the reduction in the Mohr-Coulomb factors of safety is most likely controlled by bed deformation. The deformation is not only a function of the gas pressure in the cavern but how that pressure is cycled. Gas cycles that result in increased cavern closure will undoubtedly produce lower factors of safety in the shale because increased shale deformation is likely to accompany an increase in cavern closure.

7.0 CONCLUSIONS

Three major work efforts were included in this project: (1) laboratory testing, (2) constitutive model development, and (3) numerical analyses. Laboratory testing was performed to characterize the strength and deformation behavior of bedded salt formations in the northeastern United States for evaluating cavern performance and predicting cavern stability. A new salt dilation criterion was developed based on the results of the laboratory tests. The new criterion includes Lode angle dependency to account for the lower strength exhibited by rock salt under triaxial extension states of stress compared to triaxial compression states of stress. This feature is not included in many of the existing dilation criteria and is an important aspect in evaluating the potential for salt damage. Finite element analyses were performed of hypothetical natural gas storage caverns that illustrate the use of the new criterion under a wide range of conditions that are expected to exist in the Appalachian Basin. A summary of the work effort is provided below.

7.1 LABORATORY TESTING

The purpose of the laboratory testing task was (1) to investigate the behavior of salt under load paths and states of stress that simulate those found in the field and (2) to acquire data that can be used to define the constitutive models used to assess accurately the stability of the roof salt. All testing was performed on Cayuta salt recovered from the Bale No. 1 Well, located approximately 1 mile southwest of Cayuta in Schuyler County, New York. The following general conclusions were determined from the laboratory testing of Cayuta salt:

1. The dilation limit is about 30 percent lower in extension than in compression.

2. The steady-state creep strain rates are equal in extension and compression.

3. Cycling between compression and extension produces a transient strain response each time the load is cycled under constant shear stress conditions.

4. Fluid pressure effects do not have a significant affect on the dilation limit.

5. A nonlinear relationship exists between mean stress and the dilation limit.

7.2 DILATION CRITERION DEVELOPMENT

A salt dilation criterion based on a Mohr-Coulomb-type model was developed using experimental evidence obtained from testing of Cayuta salt under triaxial compression and triaxial extension states of stress. The new criterion, which is named the RD criterion, assumes that the dilation limit of salt is a function of three stress invariants: (1) the first invariant of the Cauchy stress tensor (I_1), (2) the second invariant of the deviatoric stress

tensor (J_2), and (3) the Lode angle (ψ). The RD criterion provides a nonlinear relationship between dilation strength and mean stress and includes a nonzero value when mean stress is zero. Based on a comparison of measured strength results obtained in this and other studies, pore or fluid pressure and temperature were not found to have a significant impact on the dilation limit of salt. Although bedding plane orientation is expected to have a significant impact on the dilation limit, oriented salt core was not available for constitutive model development. However, the triaxial extension tests performed should provide the lowest possible dilation limit for bedded salt because the maximum compressive stress in these tests was oriented parallel to the bedding plane (internal shear planes).

7.3 NUMERICAL ANALYSES

Finite element analyses of a hypothetical cavern were performed to assess the stability of natural gas storage in a bedded salt formation. The analyses were performed to assess the effects of various cavern design parameters on the stability of the cavern using the newly developed RD criterion for predicting the potential for salt dilation. The following findings were determined from the numerical analyses and application of the RD criterion:

1. The thickness of the cavern roof salt does not have a significant affect on the minimum allowable gas pressure necessary to prevent salt surrounding the cavern from dilating.

2. The thickness of the first nonsalt bed overlying the cavern has very little affect on the potential for salt surrounding the cavern to dilate provided failure does not occur in the nonsalt bed.

3. The stiffness of the first nonsalt bed overlying the cavern is an important factor controlling the minimum gas pressure for the caverns investigated. Lower minimum gas pressures were predicted for increasingly greater values specified for Young's modulus of the shale bed above the cavern. This finding is based on analyses having a roof salt thickness of 10 meters. The influence of the nonsalt material stiffness is expected to be a function of distance from the cavern.

4. Based on the RD criterion, the percentage of overburden that must be supported by cushion gas to maintain cavern stability increases with depth (i.e., the minimum gas pressure gradient increases with depth).

5. Although lower minimum gas pressures can be realized for caverns that have extremely stiff overlying nonsalt beds, the stiffer beds modeled were more likely to fail than softer nonsalt beds.

7.4 SUMMARY

The Michigan and Appalachian Basins contain salt beds suitable for natural gas storage. Development of caverns within these basins will require that rock mechanic issues be addressed to ensure containment of the gas, cavern stability, and safe operation of the storage cavern. These issues limit cavern size, spacing, and operating pressure range. Geomechanical studies that use stress-based salt dilation criteria are typically used to identify the operating pressure range that prevents damage to the salt surrounding the cavern. A new dilation criterion was developed by this project that addresses some of the shortcomings of existing dilation criteria. The new RD criterion provides an improved method for evaluating cavern designs and avoiding dilatant states of stress that would be detrimental to the long-term stability of the cavern. Although the criterion was applied to the assessment of natural gas storage caverns in bedded salt, it is also applicable to caverns in domal salt.

8.0 REFERENCES

Aubertin, M., J. Sgaoula, and D. E. Gill, 1993. "A Damage Model for Rocksalt: Application to Tertiary Creep," *Proceedings, 7th Symposium on Salt*, Kyoto International Conference Hall, April 6–9, Kyoto, Japan, H. K Kakihana; H. R. Hardy, Jr.; T. Hoshi; and K. Toyokura (eds.), Elsevier Science Publishers B.V., Amsterdam, The Netherlands, Vol. 1, pp. 117–125.

Callahan, G. D., A. F. Fossum, and D. K. Svalstad, 1989. *Documentation of SPECTROM-32: A Finite Element Thermomechanical Stress Analysis Program*, DOE/CH/10378-2, prepared by RE/SPEC Inc., Rapid City, SD, for the U.S. Department of Energy, Chicago Operations Office, Argonne, IL, Vols. I and II.

Chabannes, C. C, J. G. Durup, and P. Lanham, 1999. "Geomechanical Evaluation of Sabine Gas Transmission Company's Cavern No. 2 at Spindel Top Salt Dome," *Solution Mining Research Institute Spring Meeting*, Las Vegas, NV, April 11–14.

Chan, K. S., 1993. *Further Development of Fracture Constitutive Model for Rock Salt,* Monthly Technical Report No. FY '93–8, prepared by Southwest Research Institute, San Antonio, TX, for Sandia National Laboratories, Albuquerque, NM, February.

Chan, K. S., 1996. *Final Development of the Multimechanism Deformation Coupled Fracture (MDCF) Constitutive Model*, Monthly Technical Report No. FY '96–2, Monthly Progress Report for Southwest Research Institute, Contract AQ-1458 with Sandia National Laboratories, February.

Chan, K. S., S. R. Bodner, A. F. Fossum, and D. E. Munson, 1992. "A Constitutive Model for Inelastic Flow and Damage Evolution in Solids Under Triaxial Compression," *Mechanics of Materials*, Vol. 14, pp. 1–14.

Chan, K. S., S. R. Bodner, A. F. Fossum, and D. E. Munson, 1995a. "Constitutive Representation of Damage Healing in WIPP Salt," *Proceedings, 35th U.S. Symposium on Rock Mechanics*, University of Nevada, Reno, NV, June 5–7, J. J. K. Daemen and R. A. Schultz (eds.), A. A. Balkema, Rotterdam, pp. 485–490.

Chan, K. S., K. L. DeVries, S. R. Bodner, A. F. Fossum, and D. E. Munson, 1995b. "A Damage Mechanics Approach to Life Prediction for a Salt Structure," *Computational Mechanics '95*, S. N. Atluri, G. Yagawa, and T. A. Cruse (eds.), Vol. 1, pp. 1140–1145.

Chan, K. S., S. R. Bodner, D. E. Munson, and A. F. Fossum, 1996a. "Inelastic Flow Behavior of Argillaceous Salt," *International Journal of Damage Mechanics*, Vol. 5, No. 3, pp. 292–314, July.

Chan, K. S., D. E. Munson, A. F. Fossum, and S. R. Bodner, 1996b. "A Constitutive Model for Representing Coupled Creep Fracture, and Healing in Rock Salt," *Proceedings, Fourth Conference of the Mechanical Behavior of Salt,* École Polytechnique de Montréal, Mineral Engineering Department, Québec, Canada, June 17 and 18, M. Aubertin and H. R. Hardy Jr. (eds.), Penn State University, Trans Tech Publications, Clausthal, Germany, 1998, pp. 221-234

Chen, W. F. and D. J. Han, 1988. *Plasticity for Structural Engineers,* Springer-Verlag, New York, NY.

Clark, S. P., 1966. *Handbook of Physical Constants*, 2nd Ed., The Geological Society of America, Inc., New York, NY, pp. 488–489.

Clifford, M. J., 1973. *Silurian Rock Salt of Ohio*, Ohio Geological Survey, Report of Investigations No. 90.

Coker, A. K., 1993. "Program Calculates Z-Factor for Natural Gas," O*il and Gas Journal,* pp. 74–75, February 15.

Cosenza, Ph. and M. Ghoreychi, 1998. "Effect of Added Fluids on Mechanical Behavior of Rock Salt," *Proceedings, 1998 Euroconference on Pore Pressure, Scale Effects and the Deformation of Rocks,* Aussois, France.

DeVries, K. L., K. D. Mellegard, and G. D. Callahan, 2002. *Salt Damage Criterion Proof-of-Concept Research*, RSI-1675, prepared by RESPEC, Rapid City, SD, for United States Department of Energy, National Energy Technology Laboratory, Pittsburgh, PA.

DeVries, K. L., K. D. Mellegard, and G. D. Callahan, 2003. "Laboratory Testing in Support of a Bedded Salt Failure Criterion," *Solution Mining Research Institute Fall Meeting*, Chester, United Kingdom, October 5–8.

Ehgartner B. and S. Sobolik, 2002. "3-D Cavern Enlargement Analyses," *Solution Mining Research Institute Spring Meeting*, Banff, Alberta, Canada, April 29–May 1.

Energy Information Administration, 2001. *Natural Gas Storage in the United States in 2001: A Current Assessment and Near-Term Outlook,* Washington, DC, March.

Fokker, P. A., C. J. Kenter, and H. P. Rogaar, 1993. "The Effect of Fluid Pressures on the Mechanical Stability of (Rock) Salt," *Proceedings, 7th Symposium on Salt*, Kyoto International Conference Hall, April 6–9, Kyoto, Japan, H. K Kakihana; H. R. Hardy, Jr.; T. Hoshi; and K. Toyokura (eds.), Elsevier Science Publishers B.V., Amsterdam, The Netherlands, Vol. 1, pp. 75–82.

Goodman, W. M. and C. E. Brett, 1994. "Roles of Eustasy and Tectonics in Development of Silurian Stratigraphic Architecture of the Appalachian Foreland Basin," *SEPM Concepts in Sedimentology and Paleontology*, Vol. 4, p. 147–169.

Goodman, W. M. and D. B. Plumeau, 2004. "Appalachian Basin Salt in the Silurian Salina Group: The View From the Mines," *Solution Mining Research Institute Spring Meeting*, Wichita, KS, pp. 88–119.

Hatzor, Y. H. and E. P. Heyman, 1997. "Dilation of Anisotropic Rock Salt: Evidence From Mount Sedom Diapir," *Journal of Geophysical Research*, Vol. 102, No. B7, July 10, pp. 14,853–14,868.

Hunsche, U. E., 1993. "Failure Behaviour of Rock Around Underground Cavities," *Proceedings, 7th Symposium on Salt*, Kyoto International Conference Hall, April 6–9, Kyoto, Japan, H. K Kakihana; H. R. Hardy, Jr.; T. Hoshi; and K. Toyokura (eds.), Elsevier Science Publishers B.V., Amsterdam, The Netherlands, Vol. 1, pp. 59–65.

Jacoby, C. H., 1969. "Correlation, Faulting and Metamorphism of Michigan and Appalachian Basin Salt*," The American Association of Petroleum Geologists Bulletin*, Vol. 53, No. 1, pp. 136–154.

Johnson, K. S. and S. Gonzales, 1978. *Salt Deposits in the United States and Regional Geological Characteristics Important for Storage of Radioactive Waste,* Y/OWI/SUB-7414-1, prepared by Earth Resource Associates, Inc., Athens, Georgia, for Office of Waste Isolation, Union Carbide Corp., Nuclear Division, U.S. Department of Energy.

Landes, K. K., 1945. *The Salina and Bass Island Rocks in the Michigan Basin,* U.S. Geological Survey Oil and Gas Investigations, Preliminary Map 40.

Lux, K. H., Z. Hou, and U. Düsterloh, 1998. "Some New Aspects in Modelling of Cavern Behaviour and Safety Analysis," *Solution Mining Research Institute Fall Meeting*, Rome, Italy, October 4–7.

Mesolella, K. J., 1978. "Paleogeography of Some Silurian and Devonian Reef Trends, Central Appalachian Basin," *AAPG Bulletin*, Vol. 62, pp. 1607–1644.

Munson, D. E., A. F. Fossum, and P. E. Senseny, 1989. *Advances in Resolution of Discrepancies Between Predicted and Measured In Situ WIPP Room Closures,* SAND88-2948, Sandia National Laboratories, Albuquerque, NM.

Nieland, J. D., K. L. DeVries, and K. D. Mellegard, 1999. *Phase II Feasibility Study for Lowering the Minimum Gas Pressure in Solution-Mined Caverns Based on Geomechanical Analyses of Creep-Induced Damage and Healing*, RSI-1165, prepared by RESPEC, Rapid City, SD, for U.S. Department of Energy, Morgantown, WV.

Nieland, J. D., K. D. Mellegard, R. S. Schalge, and H. D. Kaiser, 2001. *Storage of Chilled Natural Gas in Bedded Salt Storage Caverns*, RSI-1354, prepared by RESPEC, Rapid City, SD, for U.S. Department of Energy, Morgantown, WV.

Popp, T., H. Kern, and O. Schulze, 1999. "Permeation and Development of Dilatancy in Rock Salt," *Proceedings, Fifth Conference on The Mechanical Behavior of Salt*, University of Bucharest, Bucharest, Romania, August 9–11, N. D. Cristescu; J. R. Hardy, Jr.; and R. O. Simionescu (eds.), A. A. Balkema, Netherlands, 2002, pp. 95–124.

Ratigan, J. L., L. L. Van Sambeek, K. L. DeVries, and J. D. Nieland, 1991. *The Influence of Seal Design on the Development of the Disturbed Rock Zone in the WIPP Alcove Seal Tests*, RSI-0400, prepared by RE/SPEC Inc., Rapid City, SD, for Sandia National Laboratories, Albuquerque, NM.

Rickard, L. V., 1969. *Stratigraphy of the Upper Silurian Salina Group, New York, Pennsylvania, Ohio, Ontario,* Map and Chart Series, No. 12, New York State Museum and Science Service.

Sanford, B. V., F. J. Thompson, and G. H. McFall, 1985. "Plate Tectonics–A Possible Controlling Mechanism in the Development of Hydrocarbon Traps in Southwestern Ontario," *Bulletin of Canadian Petroleum Geology*, Vol. 33, pp. 52–71.

Schmidt, U. and K. Staudtmeister, 1989. *Determining Minimum Permissible Operating Pressure for a Cavern Using the Finite Element Method,* Storage of Gases in Rock Caverns, Nilsen & Olsen (eds.), Balkema, Rotterdam, pp. 103–113.

Schulz, R., H. Denzau, and K. Benke, 1998. "Introduction of a Continuum Damage Method (CDM) for FEM Calculations of Fracture Mechanisms in Salt," *Solution Mining Research Institute Fall Meeting*, Rome, Italy, October 4–7, pp. 489–502.

Spiers, C. J., C. J. Peach, R. H. Brzesowsky, P. M. T. M. Schutjens, J. L. Liezenberg, and H. J. Zwart, 1988. *Long Term Rheological and Transport Properties of Dry and Wet Salt Rocks*, EUR 11848, prepared for Commission of the European Communities, by University of Utrecht, Utrecht, The Netherlands.

Stormont, J. C., J. J. K. Daemen, and C. S. Desai, 1992. "Prediction of Dilation and Permeability Changes in Rock Salt," *International Journal for Numerical and Analytical Methods in Geomechanics*, Vol. 16, pp. 545–569.

Thoms, R. L., R. M. Gehle, and C. L. Brassow, 1999. "Analyses of Salt Caverns With Granular Wastes," *Solution Mining Research Institute Spring Meeting*, Las Vegas, NV, April 11–14.

Thorel, L., M. Ghoreychi, Ph. Cosenza, and S. Chanchole, 1996. *Rocksalt Damage & Failure Under Dry or Wet Conditions*, École Polytechnique de Montréal, Mineral Engineering Department, Québec, Canada, June 17 and 18, M. Aubertin and H. R. Hardy Jr. (eds.), Penn State University, Trans Tech Publications, Clausthal, Germany, 1998, pp. 189–202.

Ulteig, J. R., 1964. *Upper Niagaran and Cayugan Stratigraphy*, Ohio State Geological Survey Report of Investigations No. 51, 48 p.

Van Sambeek, L. L., J. L. Ratigan, and F. D. Hansen, 1993. "Dilatancy of Rock Salt in Laboratory Test," *Proceedings, 34th U.S. Symposium on Rock Mechanics*, University of Wisconsin-Madison, Madison, WI, June 27–30, B. C. Haimson (ed.), International Journal of Rock Mechanics and Mining Sciences & Geomechanics Abstracts, Pergamon Press, Vol. 30, No. 7, pp. 735–738.

APPENDIX A

LABORATORY TESTING PROCEDURES

APPENDIX A
LABORATORY TESTING PROCEDURES

A.1 TEST SPECIMEN PREPARATION

The test specimens used in the rock mechanics testing were prepared from 100-millimeter-diameter field core samples. The field core was machined to produce right-circular cylindrical specimens for mechanical testing. The machining operation was performed in two steps. In the first step, the field cores were dry-cut to approximate length using an ordinary band saw. The sawed ends were then finished flat and parallel in a lathe using carbide tooling. In the second step, the diameters of the cores were turned down in a lathe to remove irregularities and pits that may have resulted from the field coring operation. Final specimen dimensions for the triaxial compression tests were approximately 100 millimeters in diameter and 200 millimeters in length. All of the specimens were given a unique identification number for tracking within the RESPEC laboratory. A typical specimen identification number is:

BAL1/87/1

where:

BAL1 = Bale Well No. 1 near Cayuta, New York

87 = Core piece number

1 = RESPEC identification number.

A.2 MECHANICAL PROPERTIES TEST PROCEDURES

RESPEC personnel performed all the mechanical properties testing of the Cayuta salt specimens using the laboratory facility located in Rapid City, South Dakota. The strength tests and the dilation tests were performed on a servohydraulic test system, shown in Figure A-1, where the prominent test system components are labeled. One notable feature of the test system shown in Figure A-1 is the capability to mount the strain-measuring instrumentation directly on the specimen. This capability ensures that the specimen strain response is measured within a uniform stress field within the specimen. Additionally, the strain measurements are unaffected by the compliance of the reaction frame or the interfaces between the specimen and the load frame components. This test system was used to perform confined constant strain rate and constant mean stress tests.

The creep tests were performed on computerized static loading test systems designed for maintaining stable loads over long periods of time. A typical static load frame is shown in Figure A-2. Creep tests are performed at a constant confining pressure and constant total axial stress. Because the area of the specimen changes during a creep test, the computer control uses
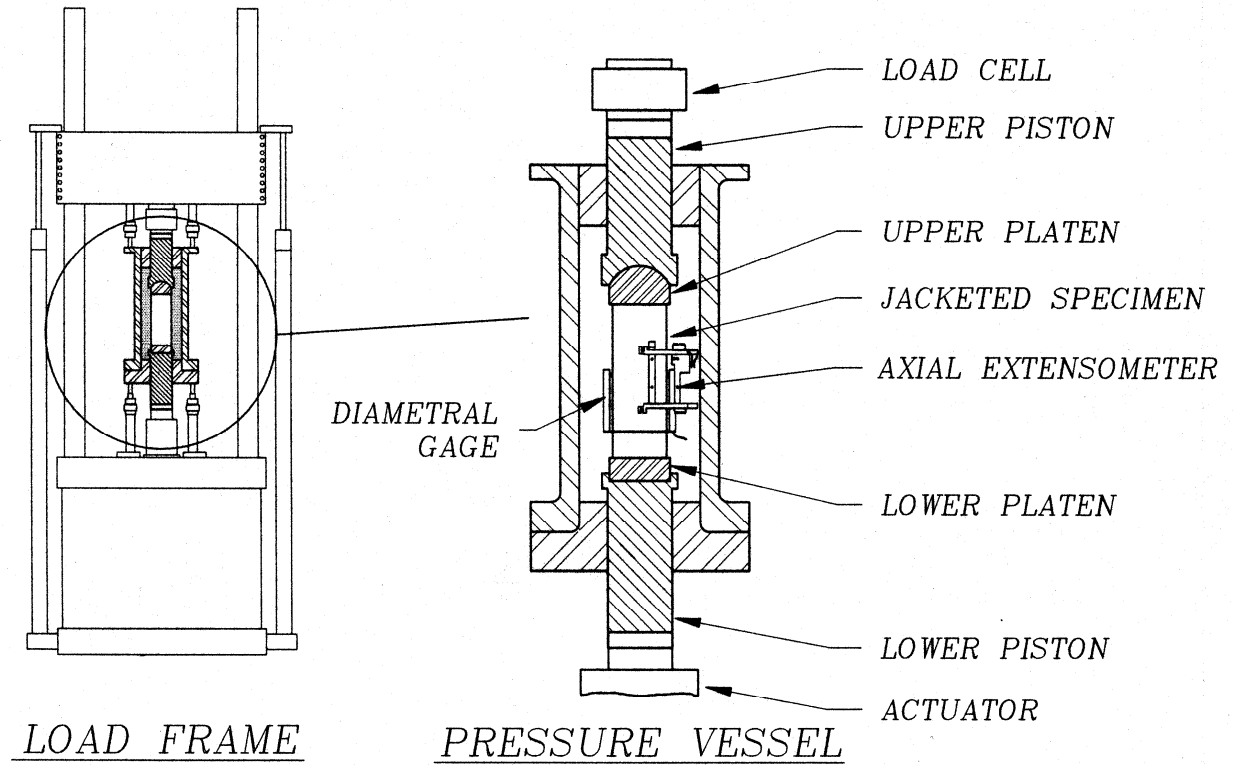
Figure A-1. Schematic of UTS2 Load Frame and Pressure Vessel.
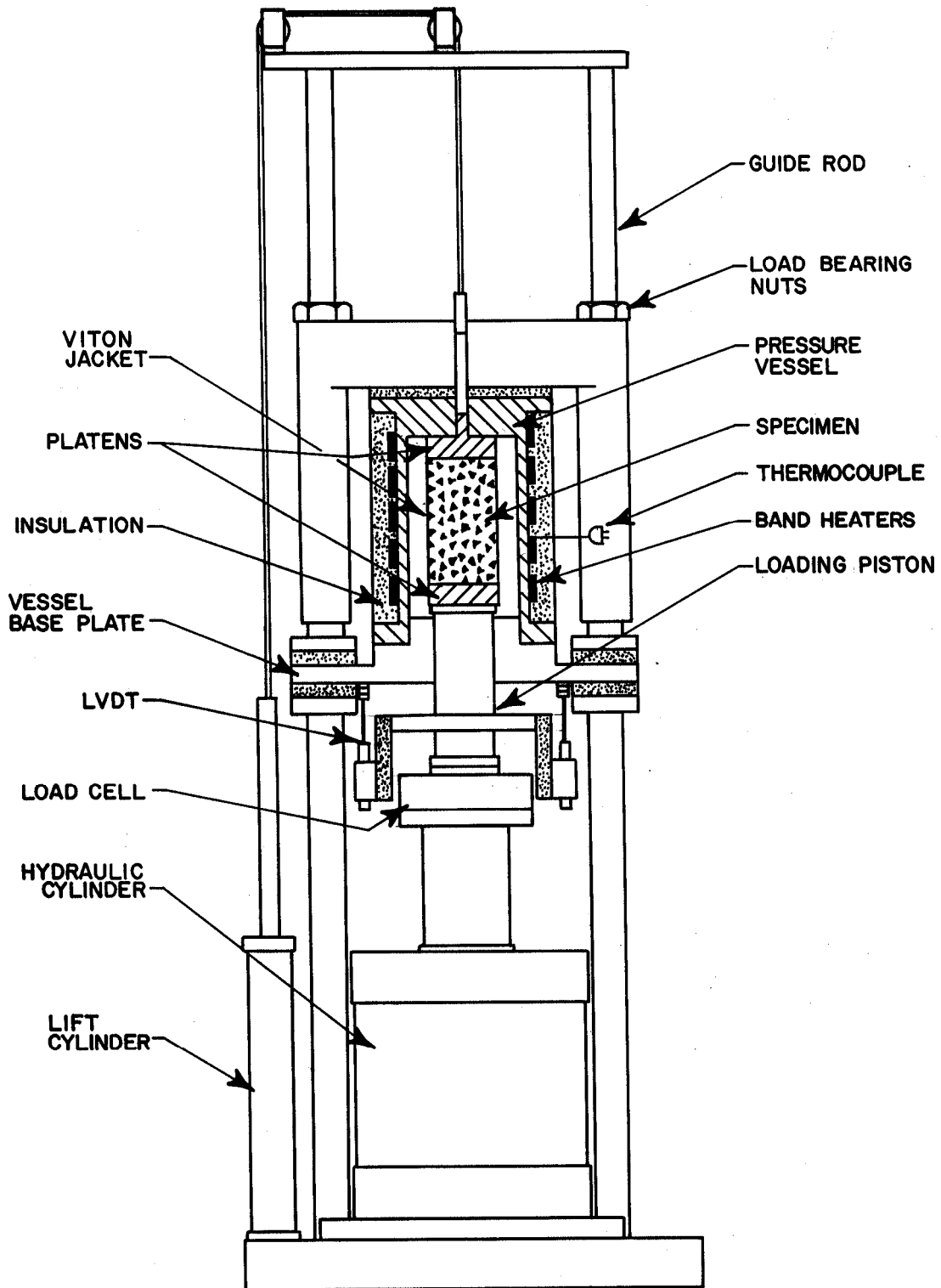
Figure A-2. Schematic of Static Creep Test System.

the measured radial strain of the specimen to continually adjust the applied axial force to maintain a constant axial stress.

A brief description of each type of mechanical properties test is given in separate sections that follow.

A.2.1 <u>Confined Constant Strain Rate</u>

In the confined constant strain rate (CSR) tests, the axial stress, σ_a, is increased and the confining pressure, σ_c , is held constant. A special case of the CSR test is generally known as the unconfined compression test (UCC), which is simply a CSR test performed at a confining pressure of zero. The primary objective of CSR and UCC tests is to determine the elastic and strength characteristics of the salt.

In the CSR test, the test specimen is first loaded hydrostatically by applying radial stress (or confining pressure) and axial stress in equal increments until the mean stress specified for the test has been reached. Then a stress difference (difference between the axial stress and the radial stress) is applied by increasing the axial stress while holding the radial stress constant. The application of the stress difference is controlled to maintain a constant axial strain rate. Tests are terminated when the specimen fails or a machine limit is reached. Machine limits include the rated force capacity of the reaction frame and the displacement range of the extensometers used to measure strain.

A typical stress-strain curve for a constant strain rate compression test would show that the stress-strain response during loading is quite nonlinear, particularly at higher stress difference levels. Initially, the stress difference increases rapidly with strain; however, the stress difference eventually reaches a peak and then decreases as the specimen continues to strain. This peak stress difference is defined as the ultimate compressive strength.

The load path may include an unload/reload cycle characterized by a decrease in stress followed by a comparable increase in stress at an axial strain level of approximately 0.25 to 0.50 percent. The data acquired during the cycle are used to calculate two elastic constants, Young's modulus, E, and Poisson's ratio, ν , using two mathematical equations as follows:

$$E = \frac{\Delta\sigma}{\Delta\varepsilon_1} \tag{A-1}$$

$$\nu = -\frac{E}{\dfrac{\Delta\sigma}{\Delta\varepsilon_3}} \tag{A-2}$$

where $\Delta\sigma$ is the change in stress and $\Delta\varepsilon_1$ and $\Delta\varepsilon_3$ are the changes in axial and radial strain, respectively. Equation A-2 and the denominator of Equation A-3 represent the slopes of the

stress versus axial strain and stress versus radial strain curves, respectively, generated during the unload/reload portion of the load path.

A.2.2 Confined Constant Mean Stress Dilation Tests

The constant mean stress (CMS) test described by Mellegard and Pfeifle [1998] is used to characterize the dilational behavior of the salt. In this test, a hydrostatic stress or uniform pressure is applied to all surfaces of the specimen. The axial stress (σ_a) and the confining pressure (σ_c) are then simultaneously changed in a manner that maintains the mean stress $(\sigma_m = (\sigma_a + 2\sigma_c)/3)$ constant. The volumetric strain is monitored during the test and is used to determine the stress state that induces salt dilation (volume expansion caused by micro-fracturing).

In a constant mean stress test, the test specimen is first loaded hydrostatically by applying radial stress (or confining pressure) and axial stress in equal increments until the mean stress specified for the test has been reached. Then a stress difference (difference between the axial stress and the radial stress) is applied by simultaneously changing the axial stress at twice the rate the radial stress is changed (with opposite algebraic sign) to maintain a state of constant mean stress. Tests are terminated either when the specimen fails or when either of the principal stresses has been completely removed.

Conventionally, the stress difference is applied by increasing the axial stress while simultaneously decreasing the confining pressure. The stress state in the conventional CMS test is generally termed triaxial *compression* (CMC). Alternatively, a state of stress termed triaxial *extension* (CMX) can be imposed by simultaneously decreasing the axial stress and increasing the confining pressure. Both the CMC and CMX tests impose the same difference between the maximum and minimum compressive principal stresses, but the intermediate principal stress is different between the two tests. In the CMC test, the intermediate principal stress equals the minimum compressive principal stress, while in the CMX test; the intermediate principal stress equals the maximum compressive principal stress. Dilational strength observed in CMX tests are generally lower than the dilational strength observed in the more conventional CMC tests.

A stress difference versus strain plot for a typical CMC test is shown in Figure A-3. Because the mean stress is not changing during the CMC tests, the volumetric strain remains virtually unchanged or indicates a small level of compaction at low to moderate stress differences. This behavior is consistent with a material that is not dilating. However, at some elevated stress difference $(\Delta\sigma_{\text{dil}})$, the slope of the volumetric strain curve changes as the volumetric strain starts becoming more negative[1], which implies that the specimen is being damaged through

---

[1] Compressive stresses and strains are signed positive so negative volumetric strains imply a volume expansion.
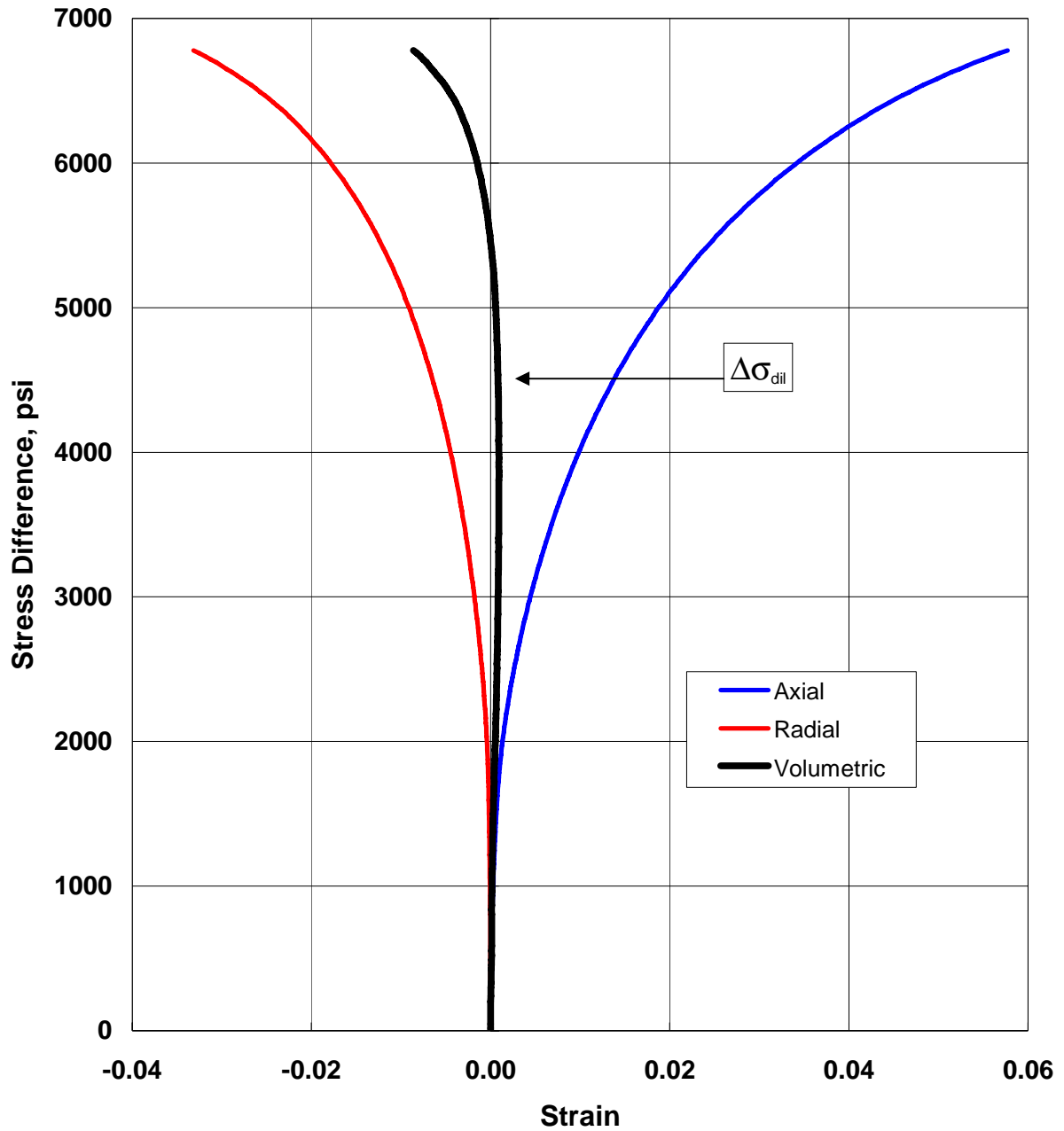
Figure A-3. Stress Versus Strain Curves From a Typical Constant Mean Stress Test in Compression.

microfracturing (creation of voids). As shown by the remainder of the stress-strain curve, the specimen can sustain even larger stress differences beyond the point where dilation begins; however, it also experiences higher levels of damage (dilatant volumetric strain) at these stress conditions.

The data obtained from the constant mean stress tests can be used to develop a relationship between mean stress and the stress difference that produces salt dilation. A common method used to develop such a relationship is to: (1) redefine the mean stress and stress difference levels which induce dilation in terms of stress invariants, and then (2) develop a mathematical model which relates the stress invariants in a manner consistent with the experimental data. The stress invariants typically used to develop these models are the first invariant of the Cauchy stress tensor, I_1, the second invariant of the deviatoric stress tensor, J_2, and the Lode angle, ψ, which describes the ordering of the applied principal stresses. When constant mean stress data are available, the stress invariants can be defined as follows:

$$I_1 = 3\sigma_m = \sigma_a + 2\sigma_c \tag{A-3}$$

$$\sqrt{J_2} = \frac{\Delta\sigma_{dil}}{\sqrt{3}} = \frac{|\sigma_a - \sigma_c|_{dil}}{\sqrt{3}} \tag{A-4}$$

$$\psi = \begin{cases} +\pi/6, & \sigma_a > \sigma_c \quad \text{(CMC)} \\ -\pi/6, & \sigma_a < \sigma_c \quad \text{(CMX)} \end{cases} \tag{A-5}$$

If just CMC data ($\psi = +\pi/6$) are plotted in a $\sqrt{J_2}$ - versus - I_1 stress space, the data will generally define a trend that will divide the stress space into two distinct regions, as shown in Figure A-4. The region above and to the left of the trend line represents stress states where dilation will occur, while the region below and to the right of the trend line represents stress states where dilation will not occur. If CMX data ($\psi = -\pi/6$) were also plotted on Figure A-4, a second trend line would appear below the CMC trend line because salt is weaker in extension than in compression.

A.2.3 Confined Creep Tests

Confined creep tests are performed to evaluate the time-dependent behavior of materials (e.g., salt). A creep test is initiated by applying confining pressure to all exterior surfaces of a specimen that has been jacketed in a flexible membrane to protect it from the pressurizing medium and then heating the jacketed specimen to the prescribed test temperature. Once the confining pressure and temperature are stable, axial stress is quickly applied to the ends of the specimen until the target stress difference is reached; at which time, the confining pressure and stress difference are maintained at their specified levels for the duration of the test or until a subsequent stage is initiated by changing the level of applied axial stress.
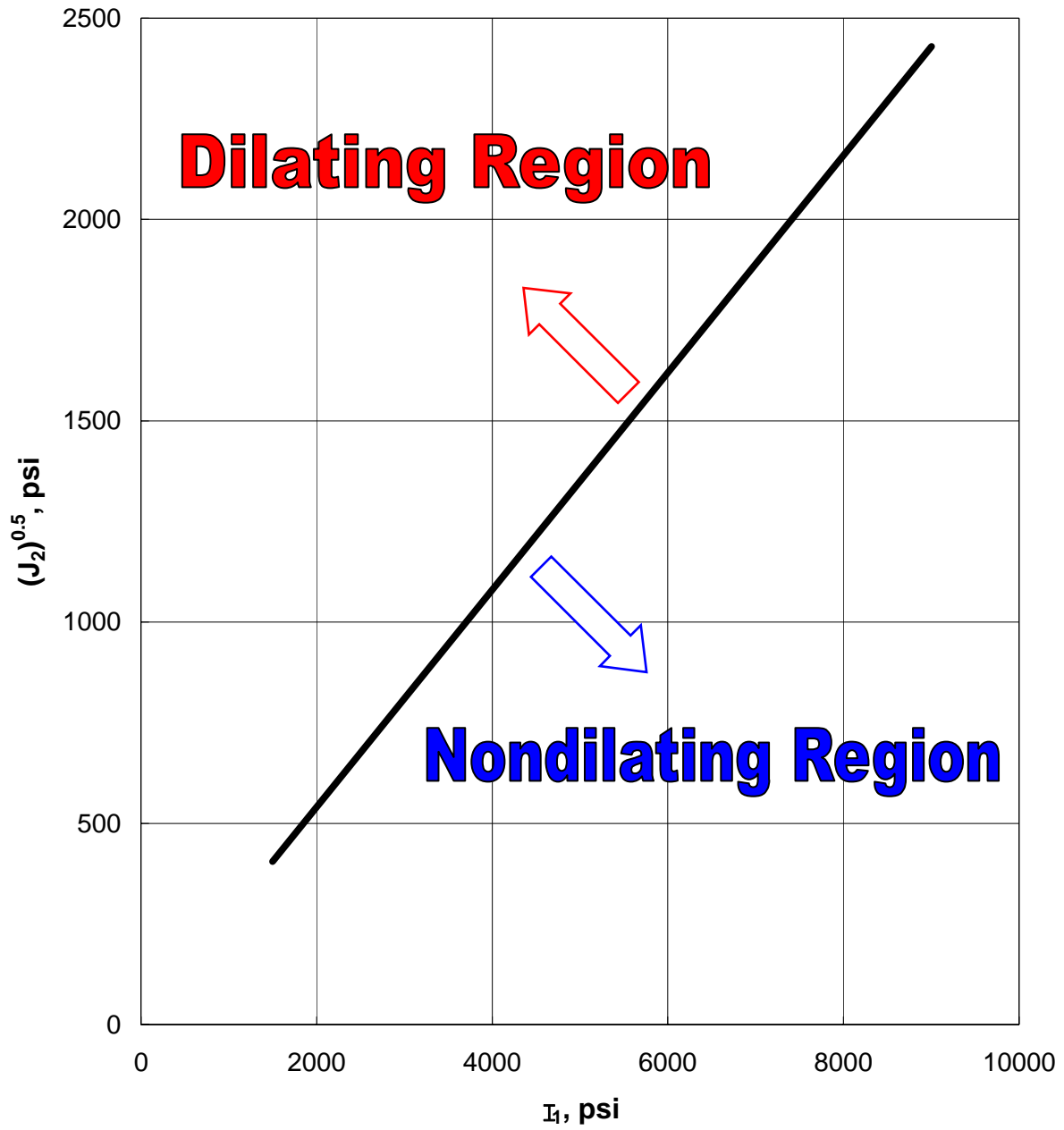
Figure A-4. $\sqrt{J_2}$ -Versus-I_1 Dilation Criterion.

During the test, axial force, confining pressure, axial displacement, lateral displacement, and temperature are recorded. Axial and lateral true (logarithmic) strains are calculated from the axial and lateral displacements and the specimen dimensions as:

$$\varepsilon_a = -\ln\left(\frac{L}{L_o}\right)$$

$$\varepsilon_l = -\ln\left(\frac{D}{D_o}\right)$$

(A-6)

where:

ε_a = axial strain

ε_l = lateral strain

D, D_o = current and original specimen diameter, respectively

L, L_o = current and original specimen length, respectively.

Axial and lateral stresses are calculated from the confining pressure, axial force, and the current cross-sectional area of the specimen as:

$$\sigma_a = \frac{F}{A}$$

$$\sigma_l = P$$

(A-7)

where:

σ_a = axial stress

σ_l = lateral stress

F = axial force on the specimen

A = current area of the specimen

P = confining pressure.

A typical strain-versus-time response from a creep test would show that at early times, the strain rates are high immediately after the change in axial stress but then decrease with time as they approach nearly constant values. Steady-state strain rates can be estimated from the linear portion of the strain-time curve, which is typically the last few days of a test that continued for a month or longer.

In a manner somewhat similar to the CMS tests, a creep test can be performed in either a compressive or extensile state of stress. In both types of tests the specimen is first brought to a hydrostatic state of stress equivalent to the desired confining pressure, which will be held

constant while the axial stress is changed to initiate creep. If the test is to be performed in compression, the axial stress is increased, which results in a shortening of the specimen. If the test is to be performed in extension, the axial stress is decreased, which results in a lengthening of the specimen.

A.3 TEST SYSTEM CALIBRATION PROCEDURES

The testing requires use of sophisticated, computer-controlled test systems equipped with electronic transducers used to measure force, pressure, displacement, and temperature. The transducers are calibrated at regular intervals using certified in-house standards that are traceable to the National Institute of Standards and Technology (NIST).

Verification procedures indicate that the transducer readings are accurate within 1 percent for load and pressure measurements and 2 percent for deformation and volume measurements. Also, temperature measurements are accurate within 1°C (2°F). The testing systems, including the electronics, are housed in an environmentally controlled facility in which the temperature is maintained at $20 \pm 1^\circ$C ($68 \pm 2^\circ$F).

A.4 REFERENCE

Mellegard, K. D. and T. W. Pfeifle, 1998. "Laboratory Evaluation of Mechanical Properties of Rock Using an Automated Triaxial Compression Test With a Constant Mean Stress Criterion," *Nondestructive and Automated Testing for Soil and Rock Properties*, ASTM STP 1350, W. A. Marr and C. E. Fairhurst (eds.), American Society for Testing and Materials, West Conshohocken, PA.

APPENDIX B

**LABORATORY RESULTS OF
CONSTANT MEAN STRESS TESTS
FOR CAYUTA SALT**
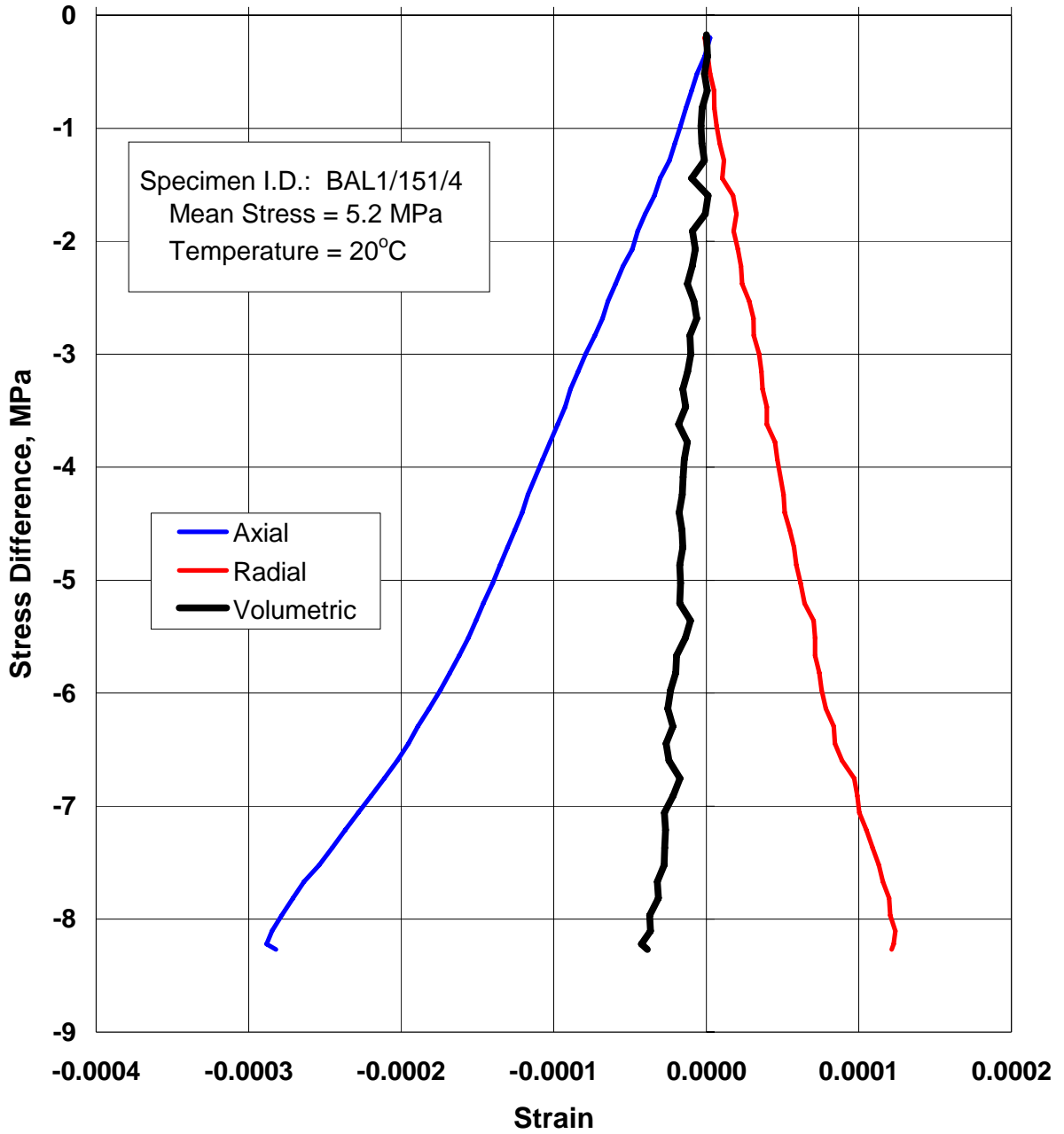
Figure B-1. Stress-Strain Plot of CMX Test on Specimen BAL1/151/4.
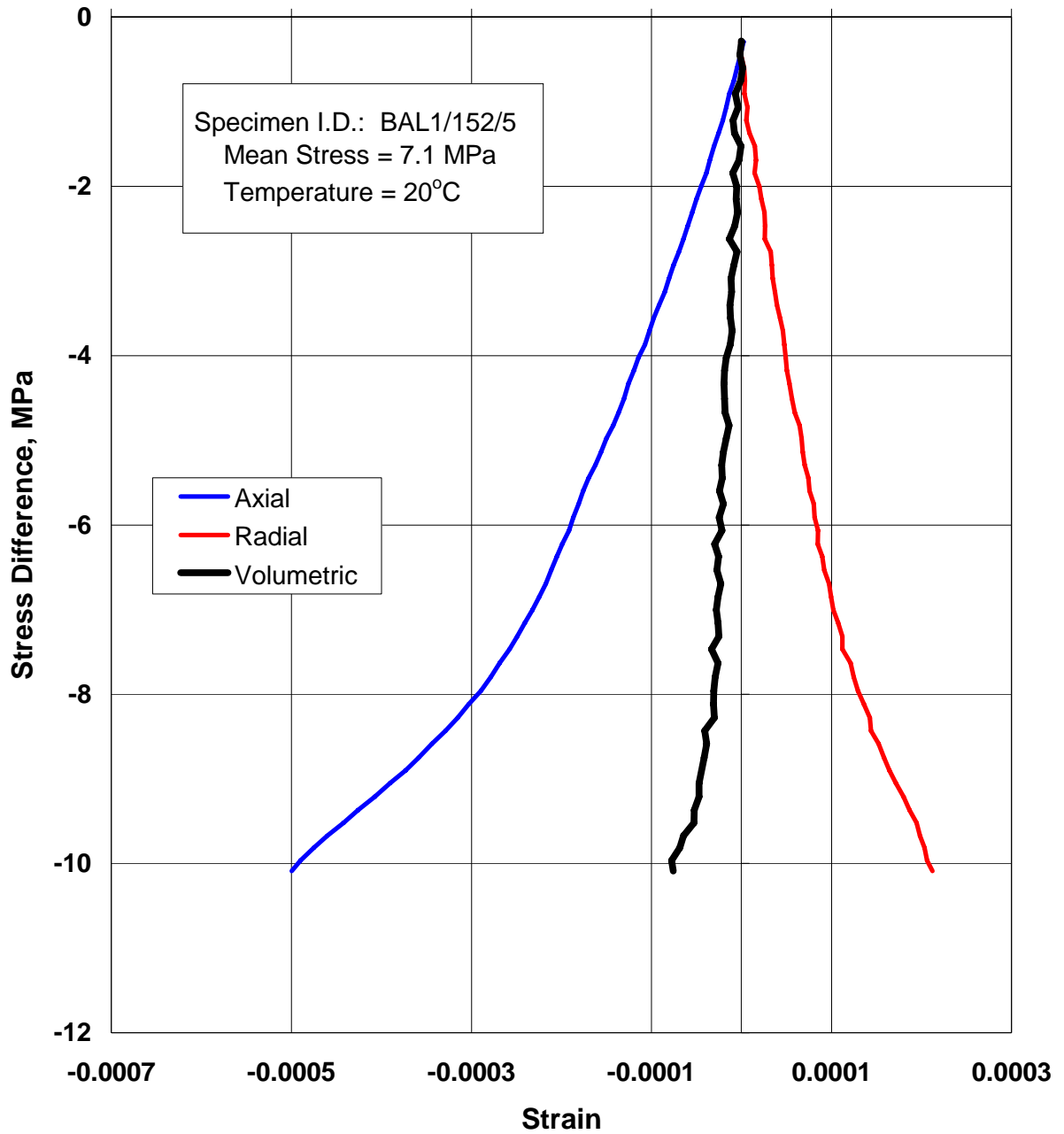
Figure B-2. Stress-Strain Plot of CMX Test on Specimen BAL1/152/5.
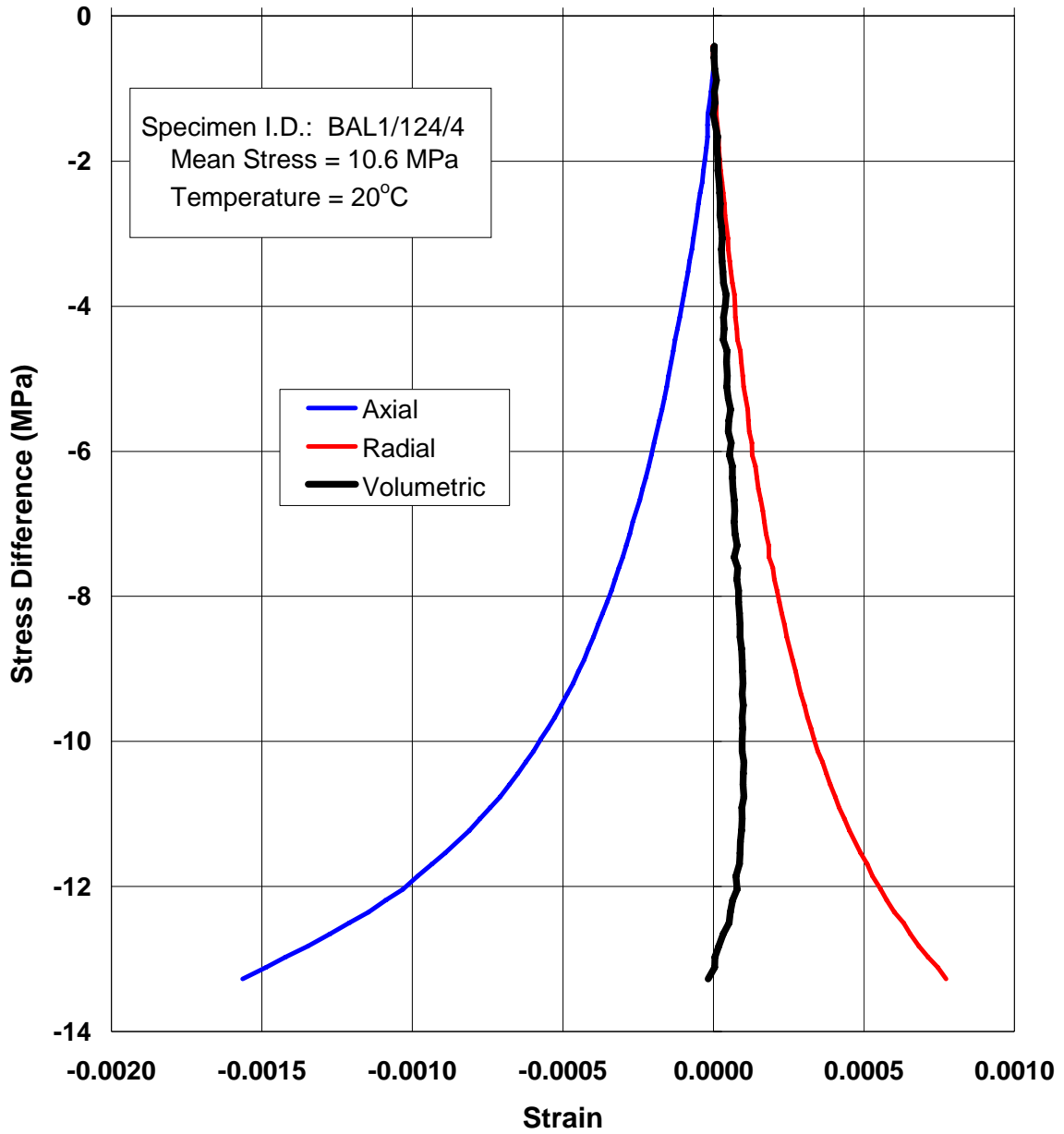
Figure B-3. Stress-Strain Plot of CMX Test on Specimen BAL1/124/4.
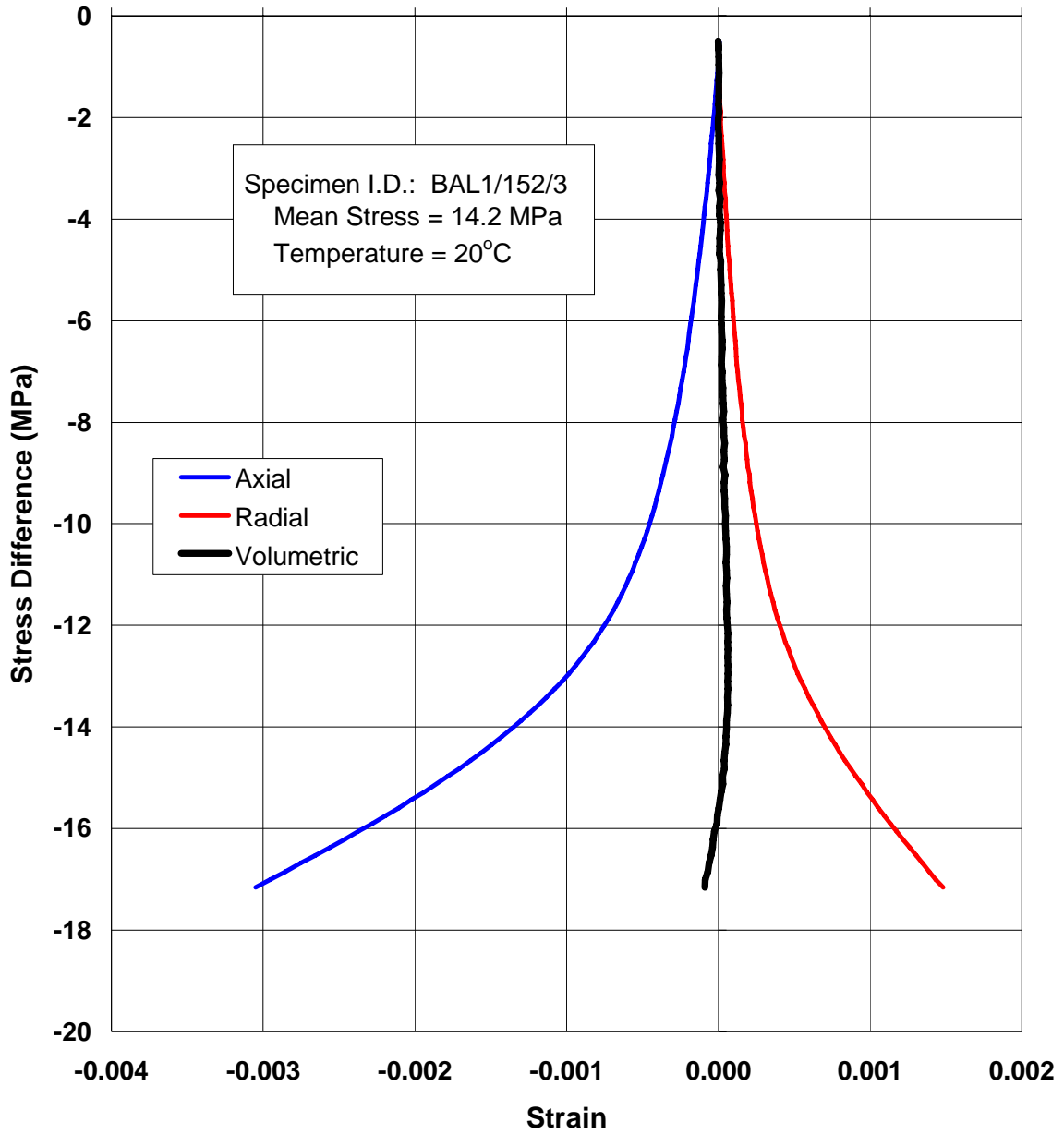
Figure B-4. Stress-Strain Plot of CMX Test on Specimen BAL1/152/3.
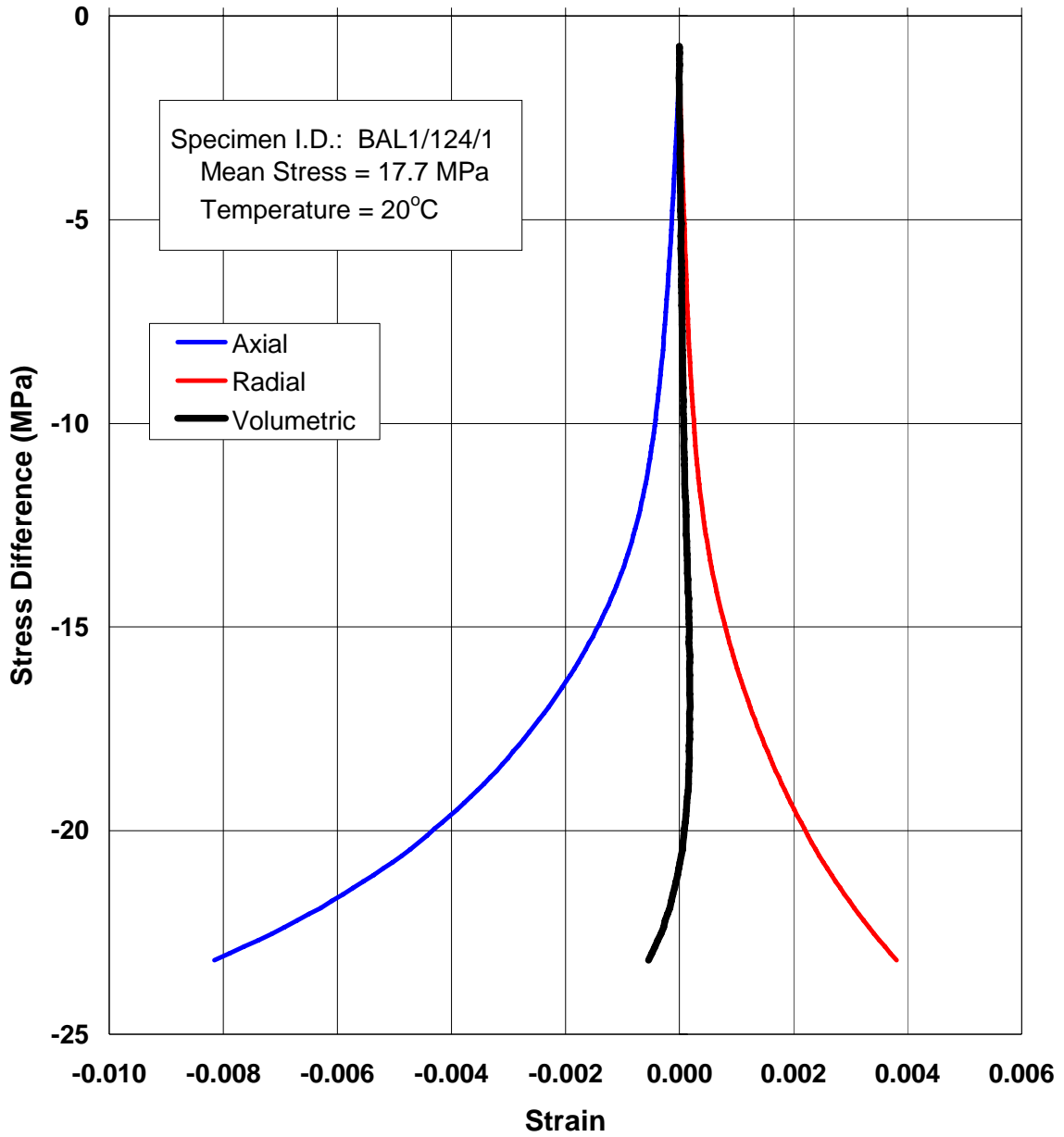
Figure B-5. Stress-Strain Plot of CMX Test on Specimen BAL1/124/1.
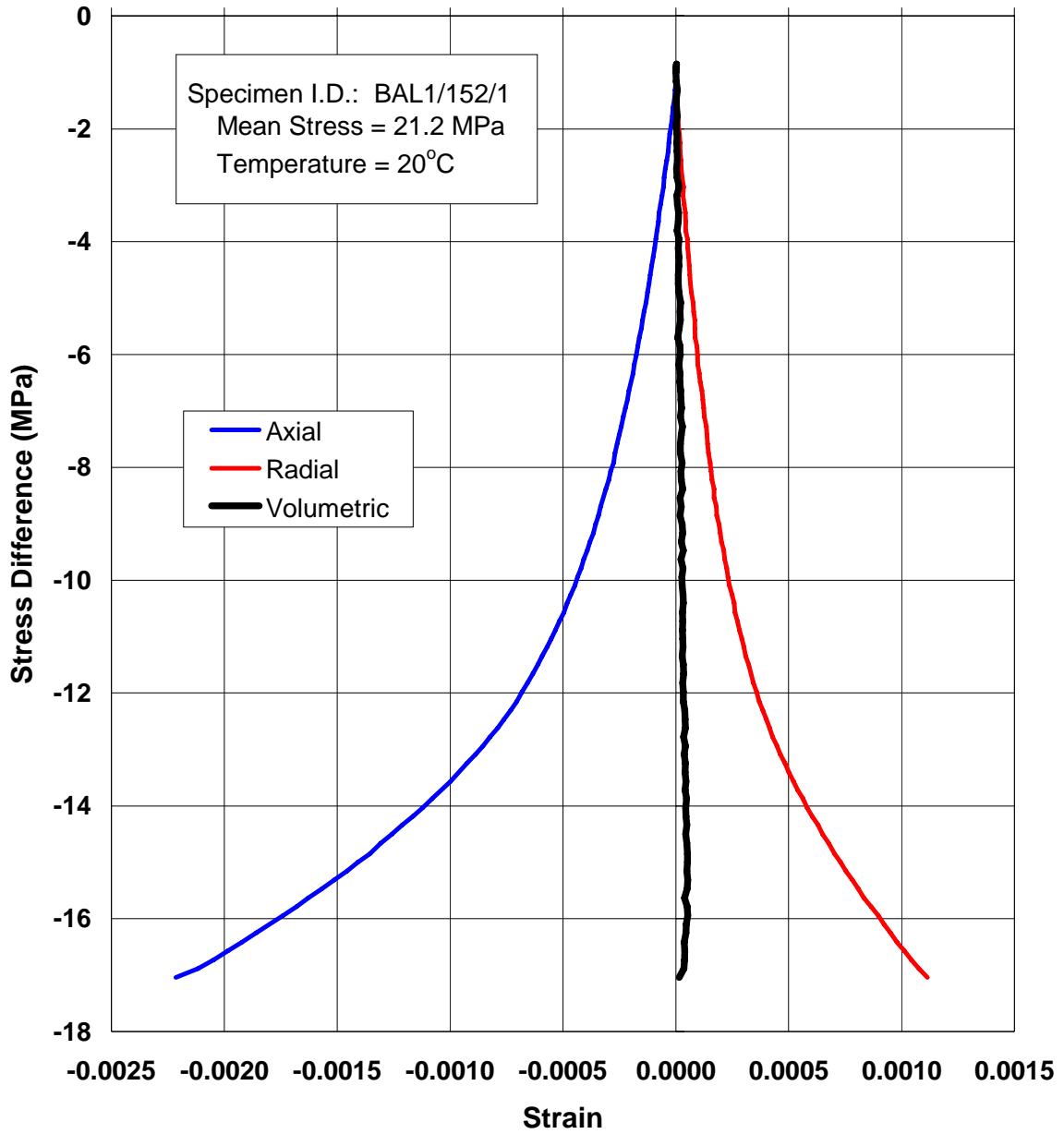
Figure B-6. Stress-Strain Plot of CMX Test on Specimen BAL1/152/1.
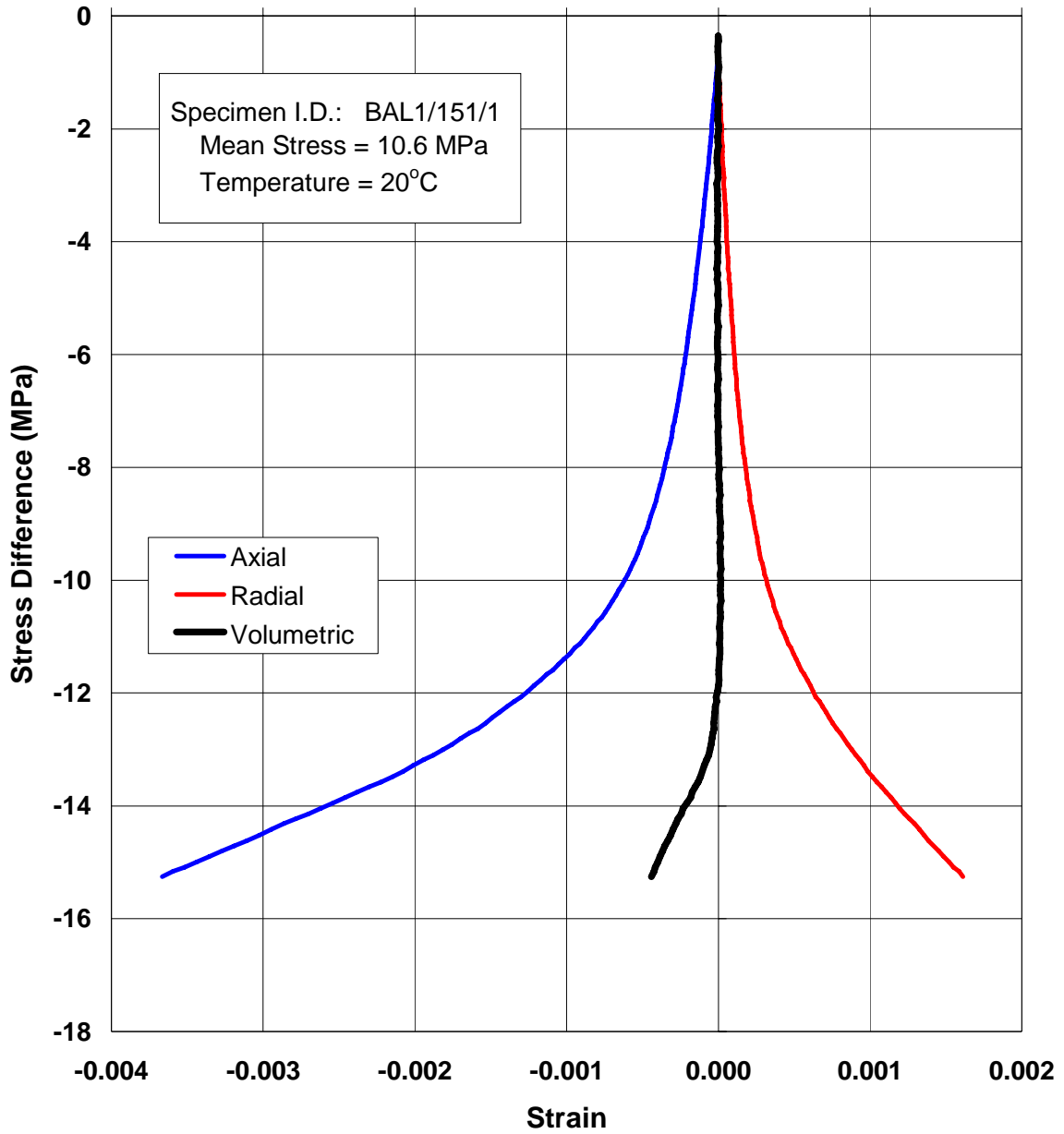
Figure B-7. Stress-Strain Plot of CMX Test on Specimen BAL1/151/1.
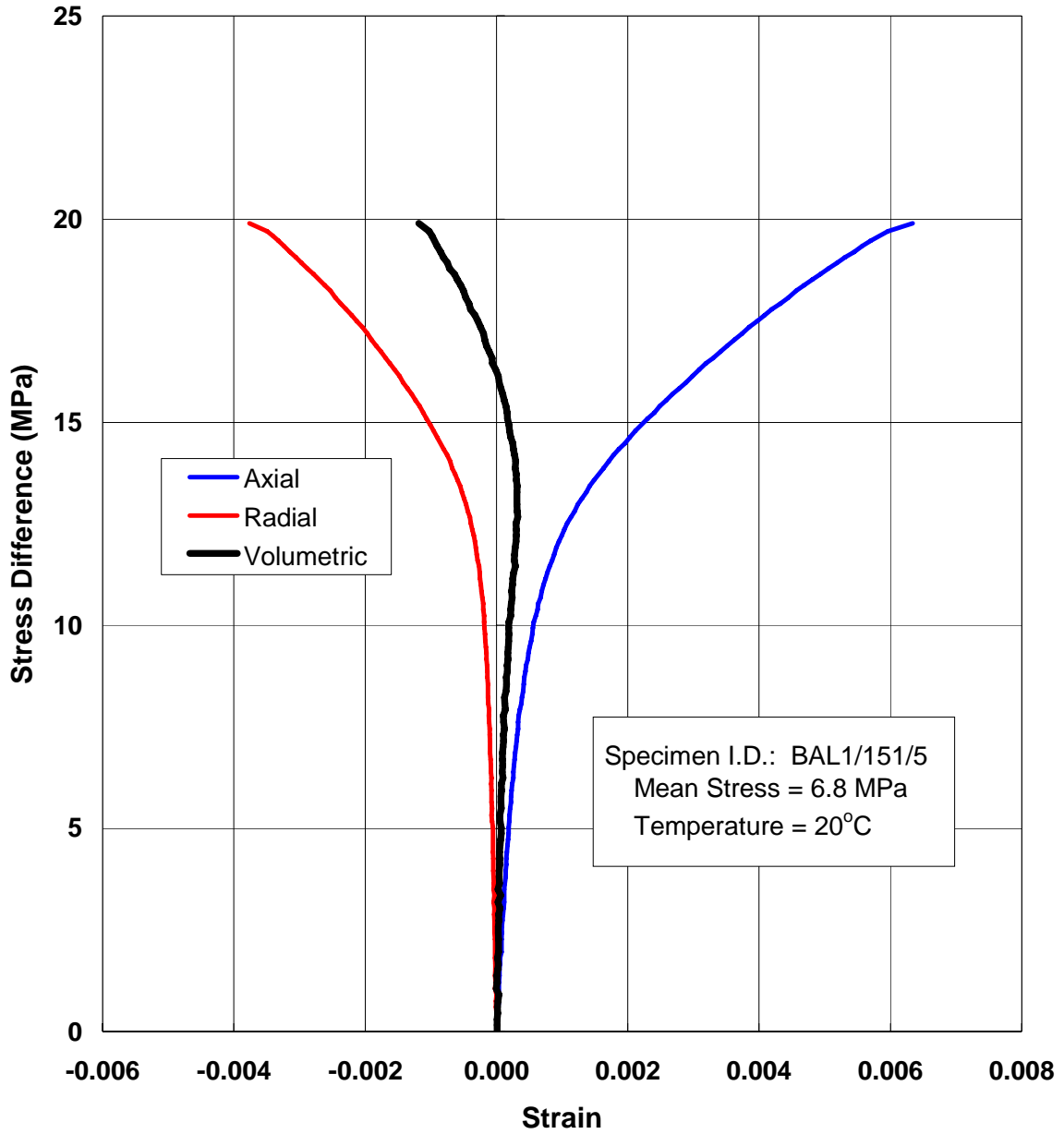
Figure B-8. Stress-Strain Plot of CMC Test on Specimen BAL1/151/5.
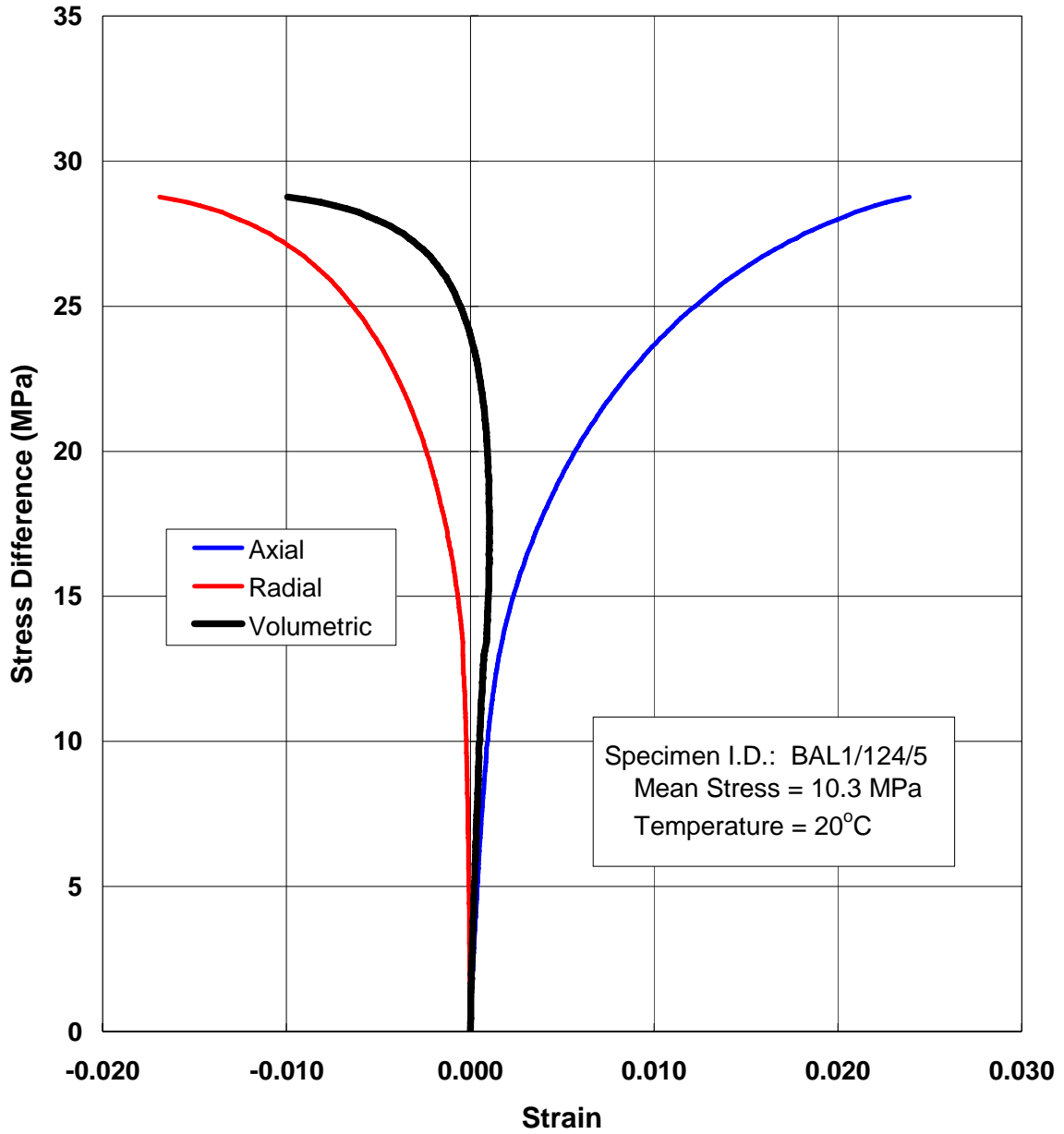
Figure B-9. Stress-Strain Plot of CMC Test on Specimen BAL1/124/5.
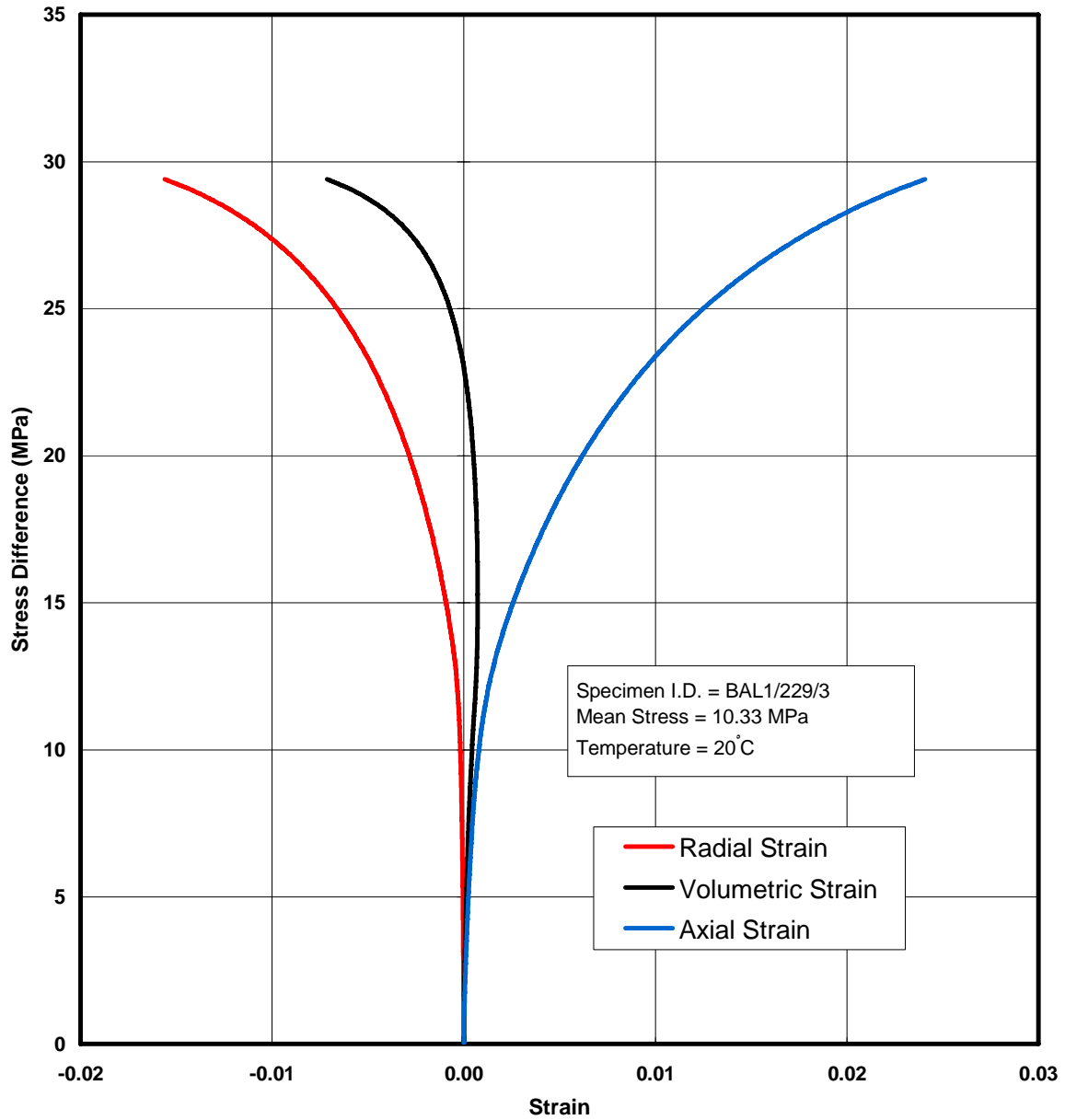
Figure B-10. Stress-Strain Plot of CMC Test on Specimen BAL1/229/3.
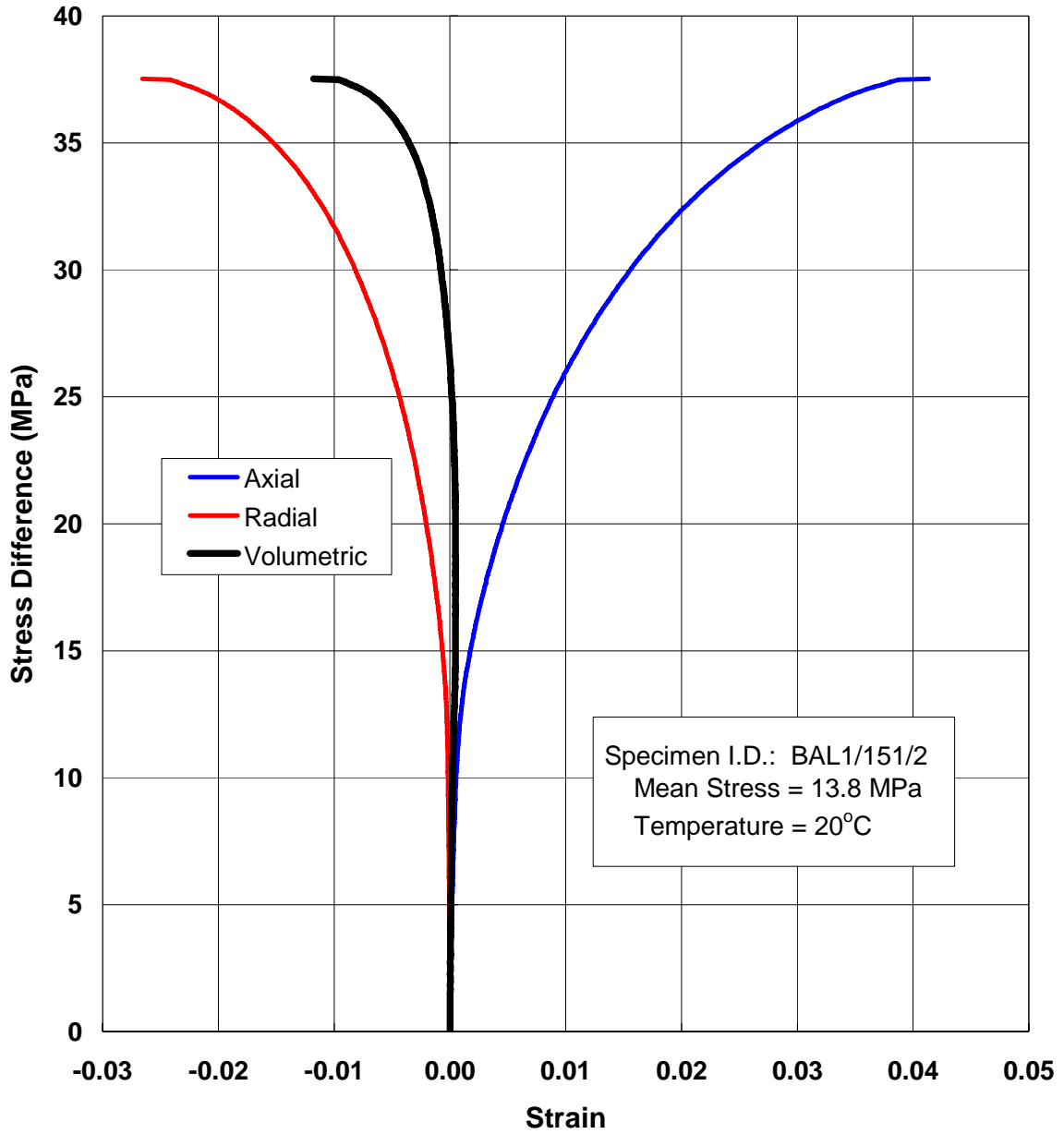
Figure B-11. Stress-Strain Plot of CMC Test on Specimen BAL1/151/2.
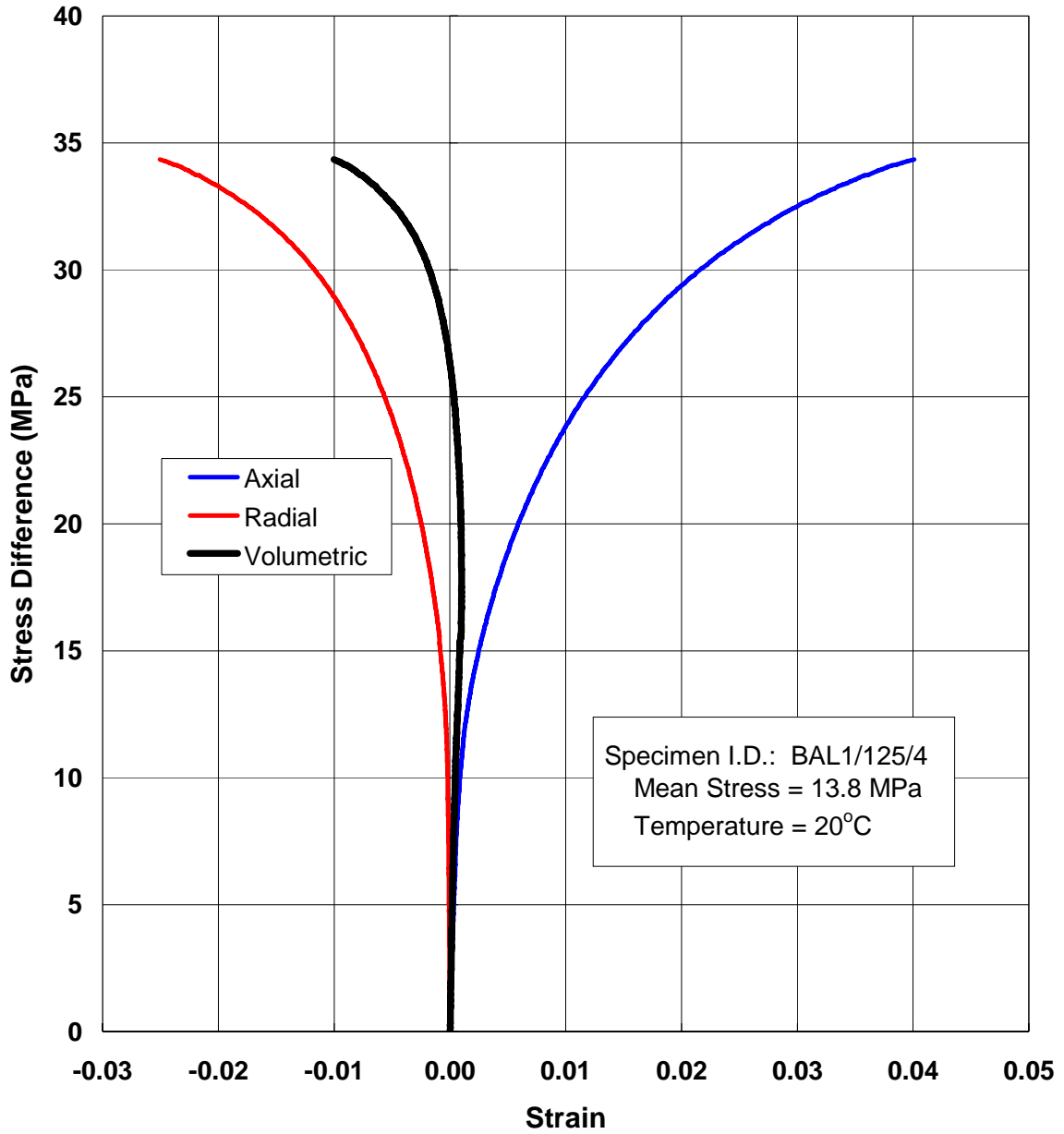
Figure B-12. Stress-Strain Plot of CMC Test on Specimen BAL1/125/4.
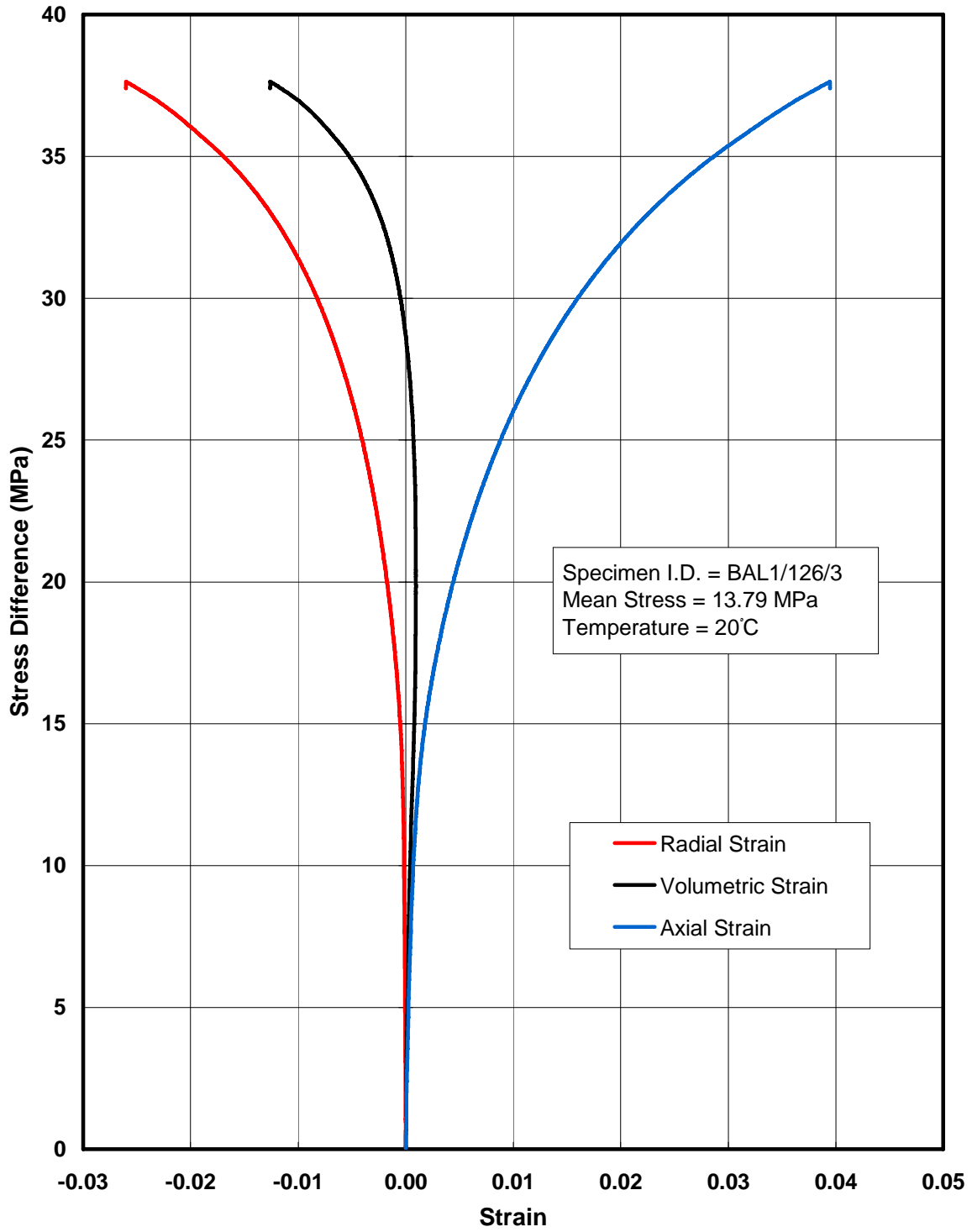
Figure B-13. Stress-Strain Plot of CMC Test on Specimen BAL1/126/3.
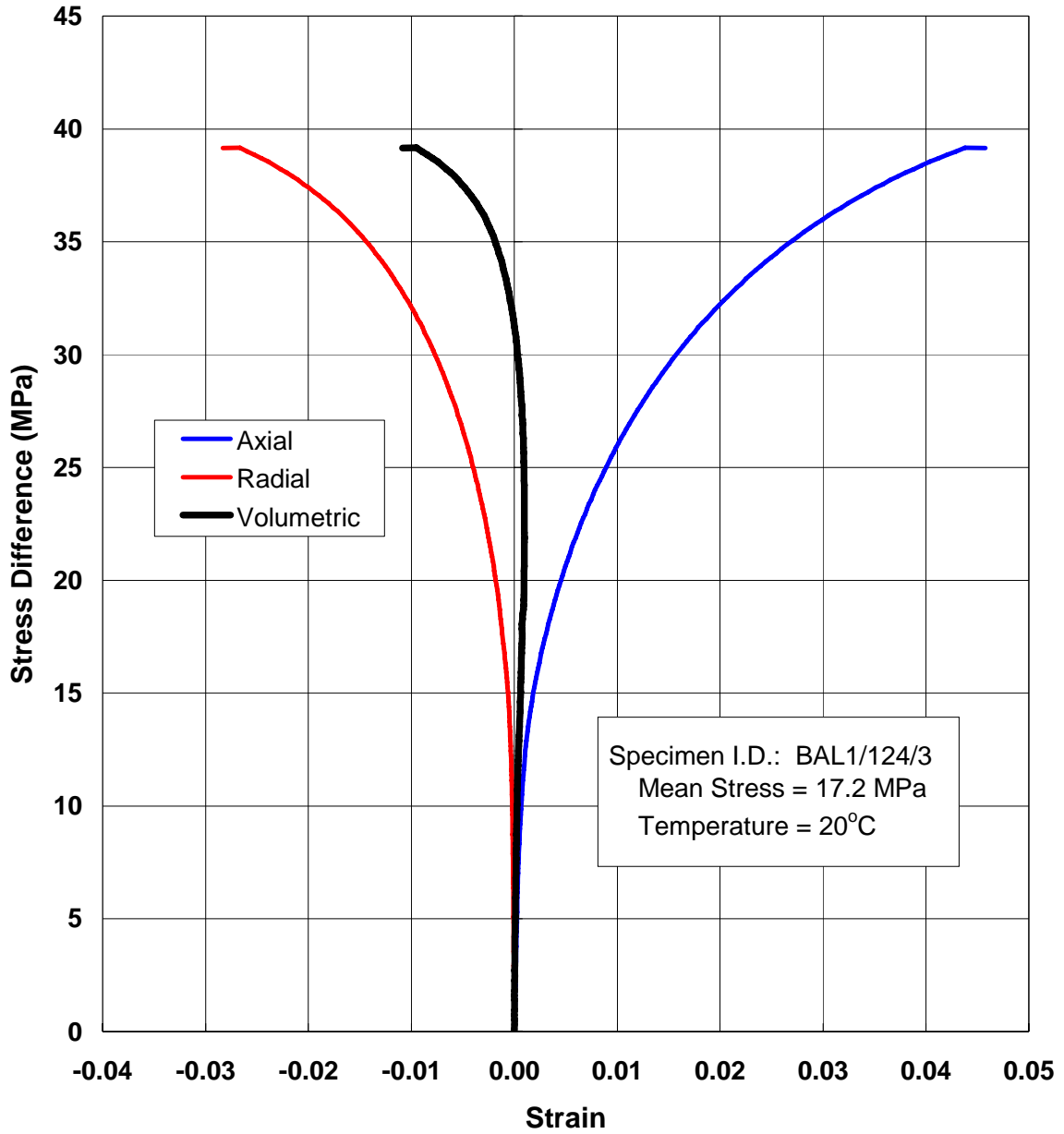
Figure B-14. Stress-Strain Plot of CMC Test on Specimen BAL1/124/3.
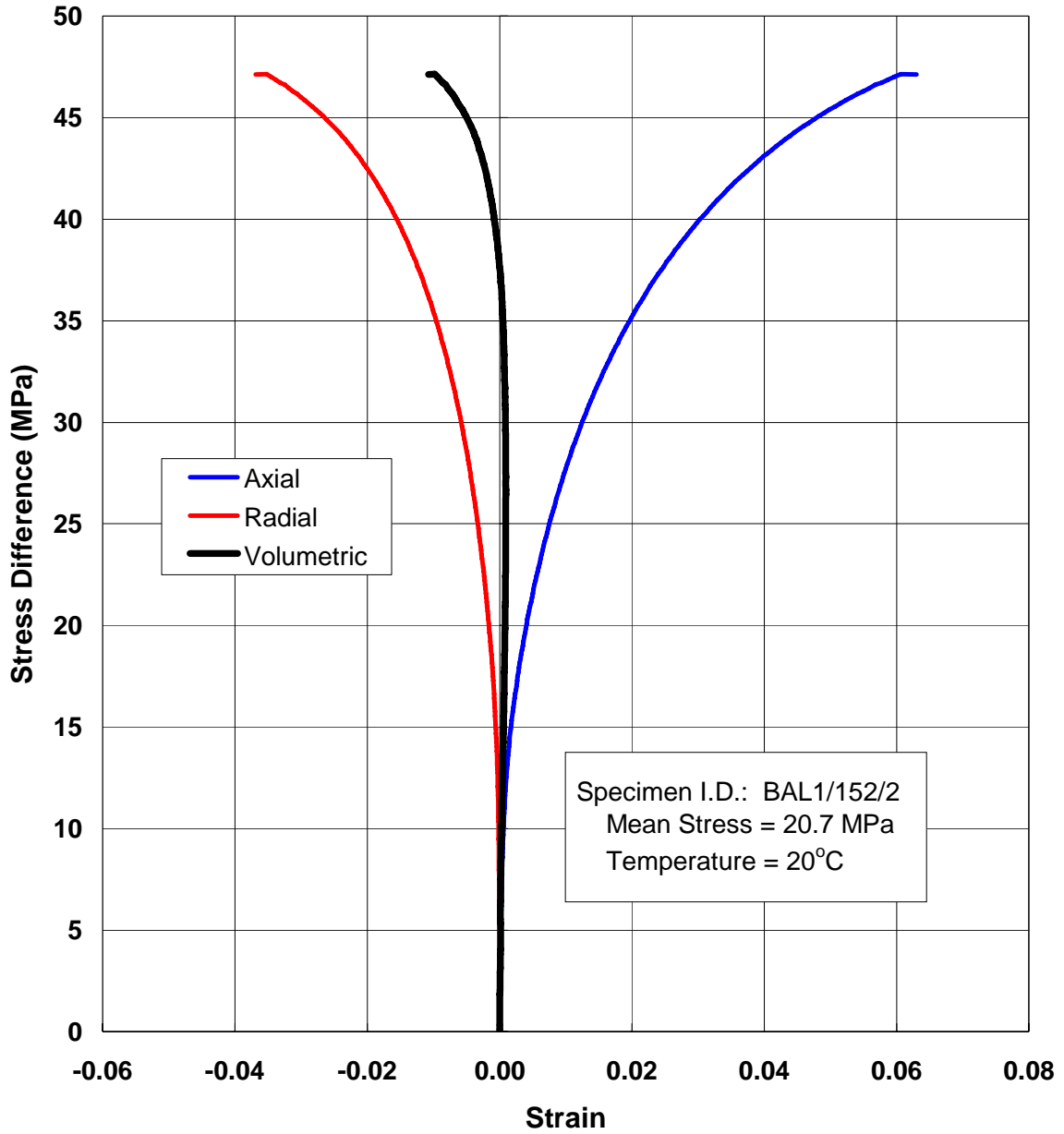
Figure B-15. Stress-Strain Plot of CMC Test on Specimen BAL1/152/2.
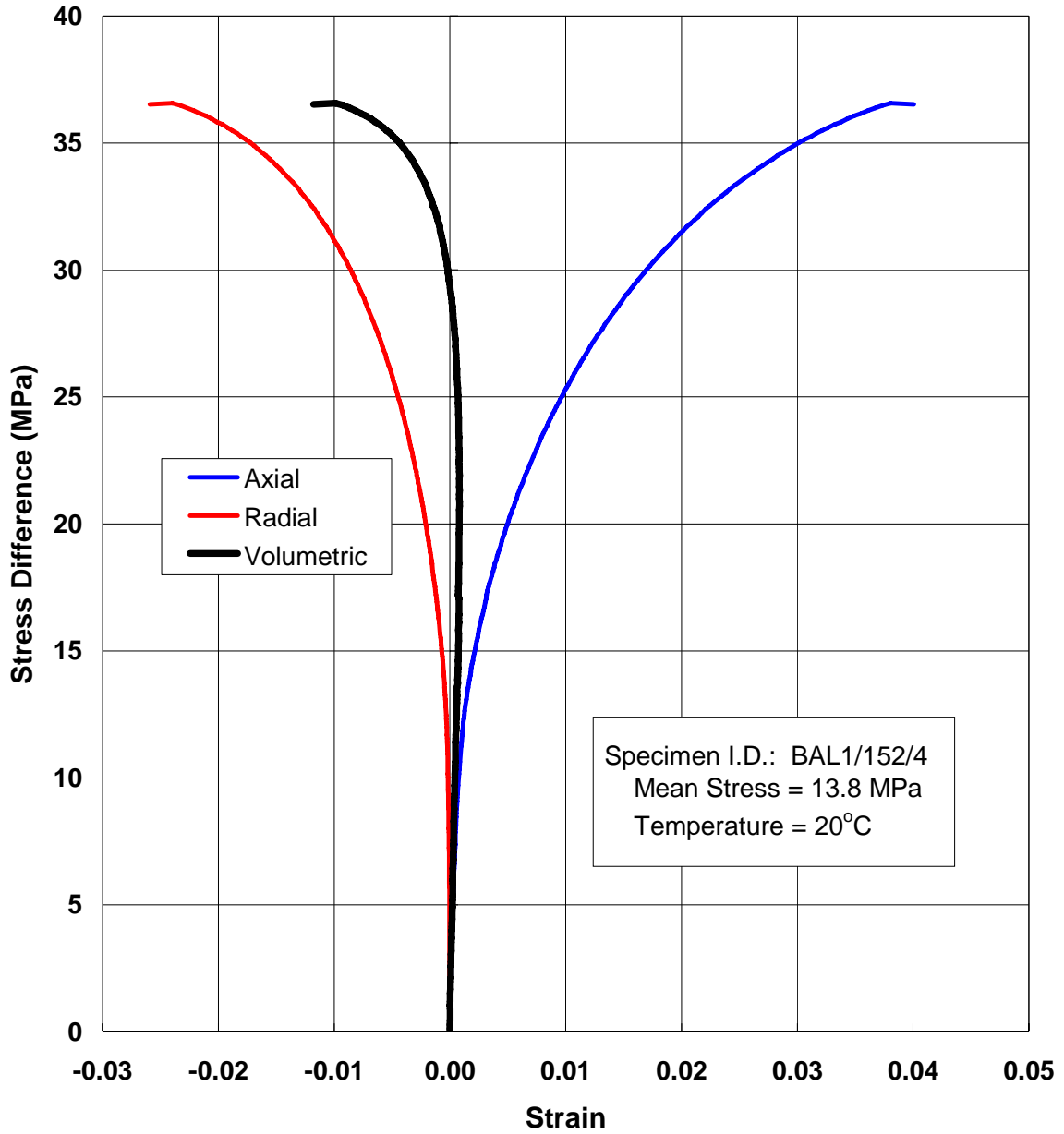
Figure B-16. Stress-Strain Plot of CMC Test on Specimen BAL1/152/4.
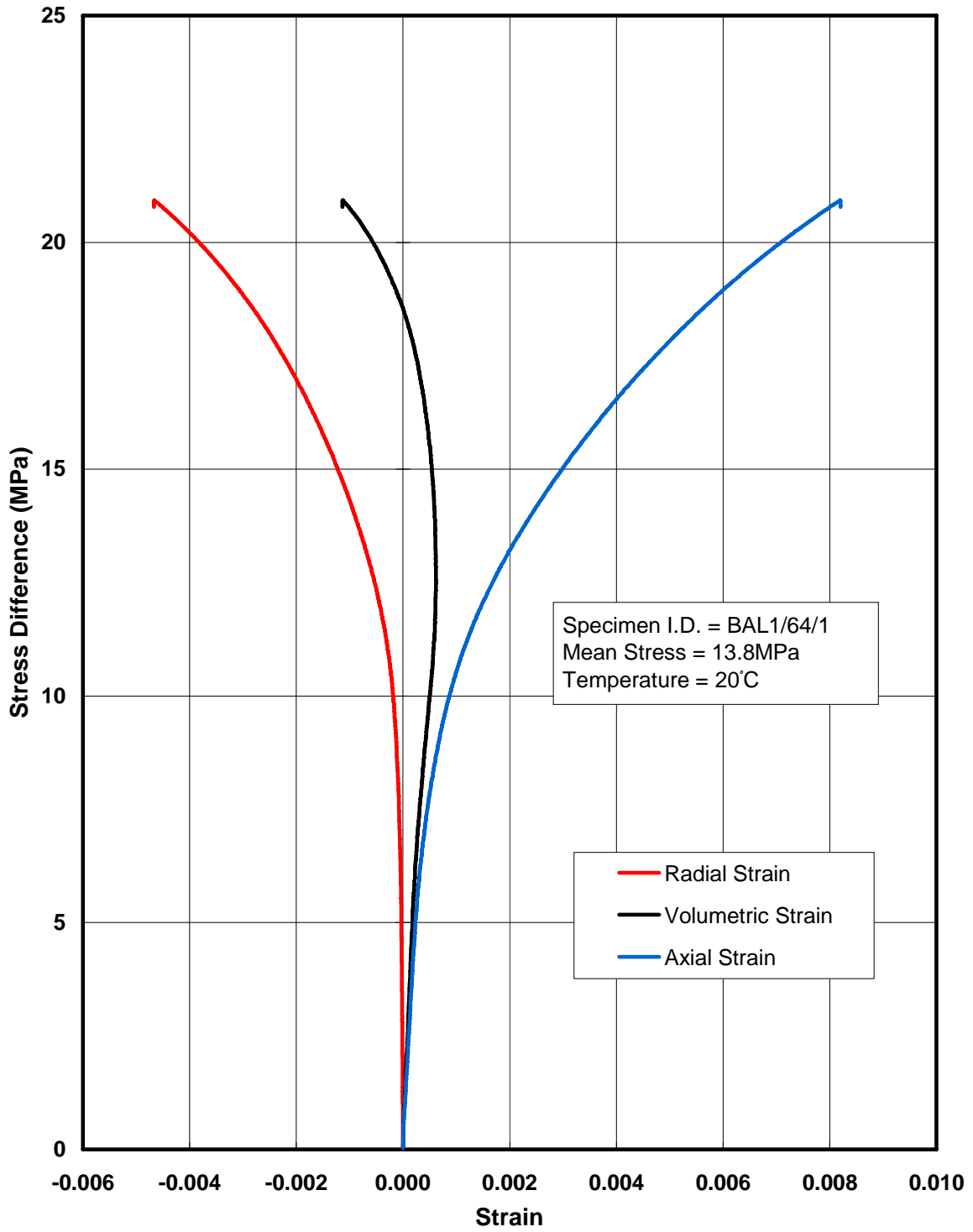
Figure B-17. Stress-Strain Plot of CMC Test on Specimen BAL1/64/1.
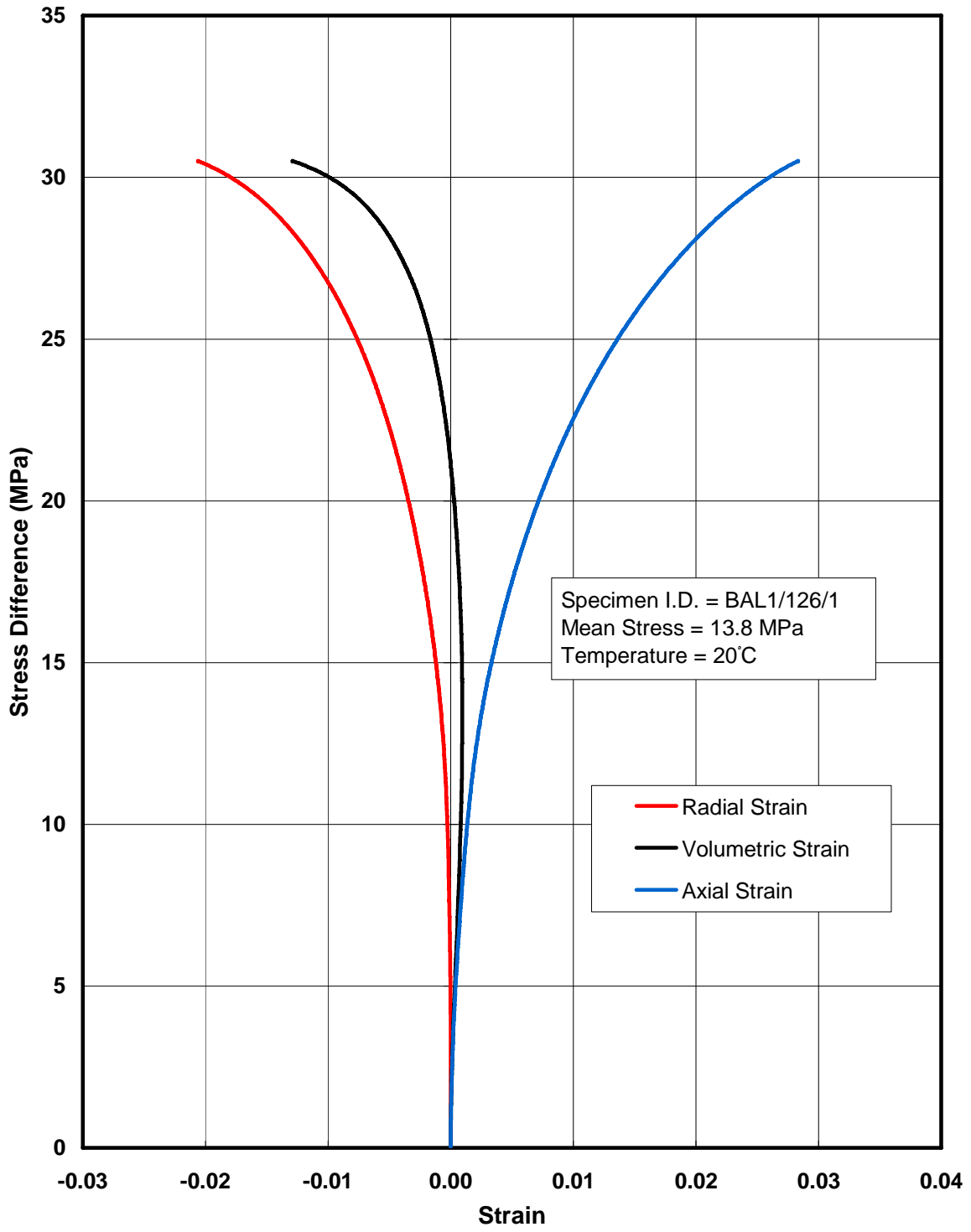
Figure B-18. Stress-Strain Plot of CMC Test on Specimen BAL1/126/1.
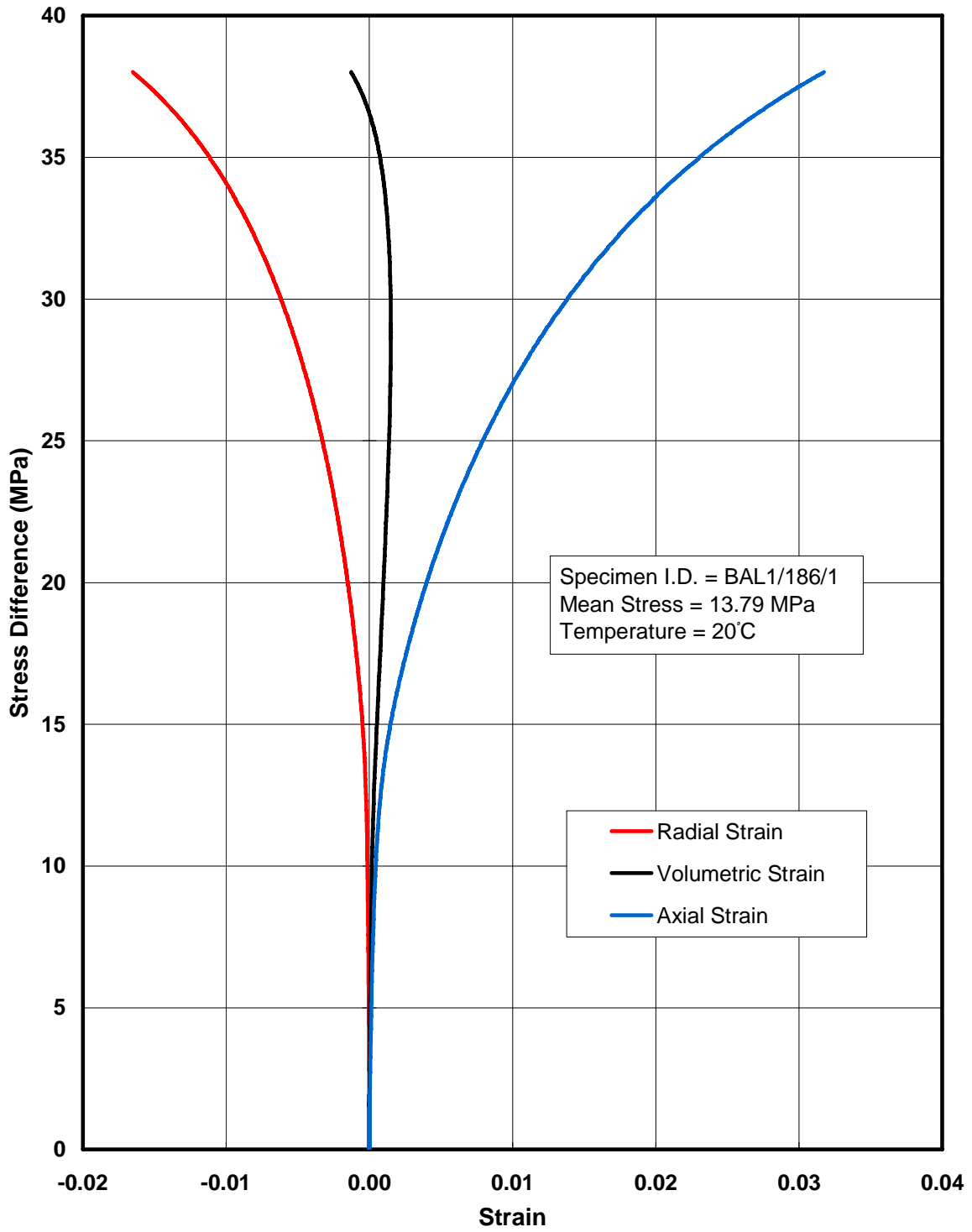
Figure B-19. Stress-Strain Plot of CMC Test on Specimen BAL1/186/1.
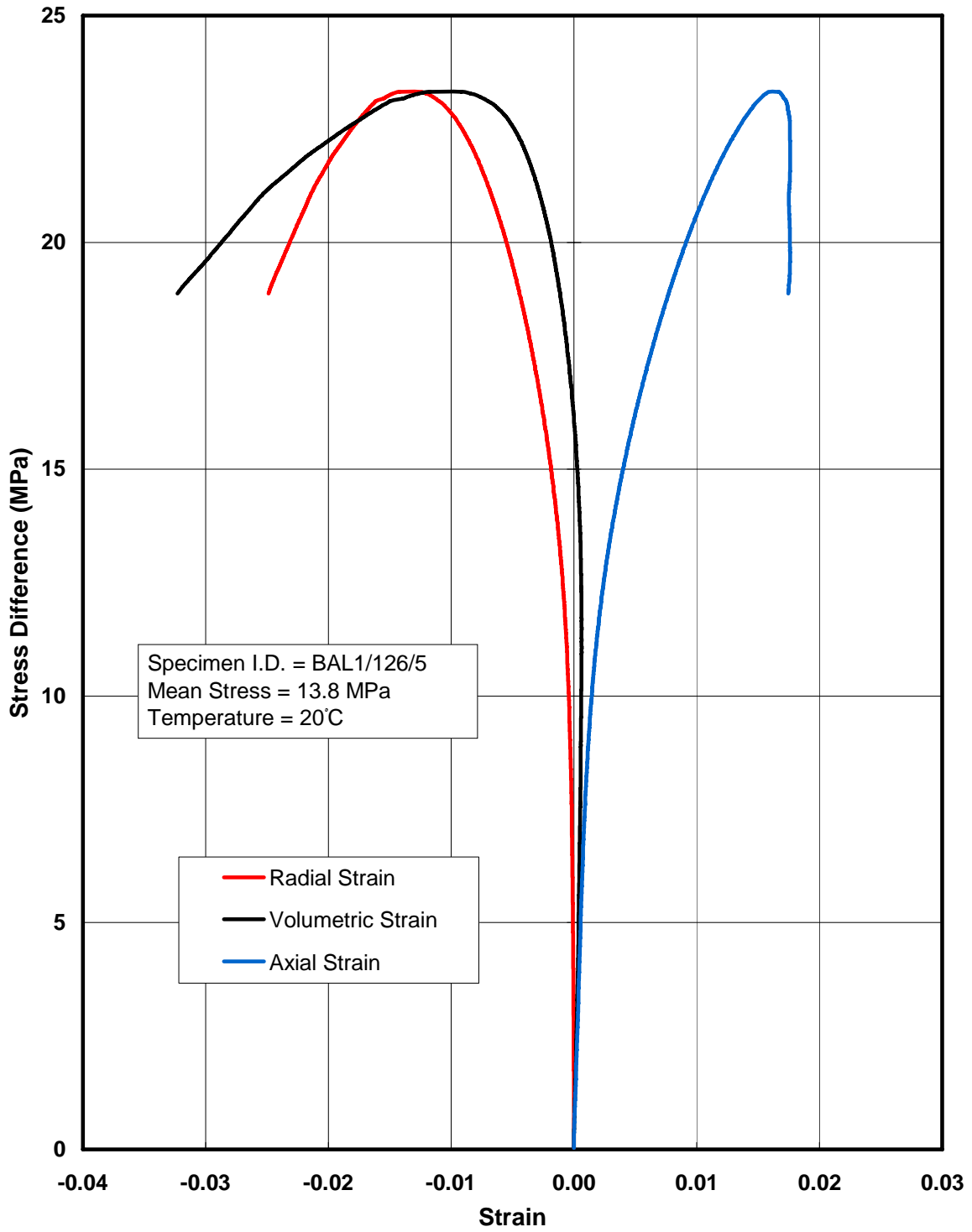
Figure B-20. Stress-Strain Plot of CMC Test on Specimen BAL1/126/5.
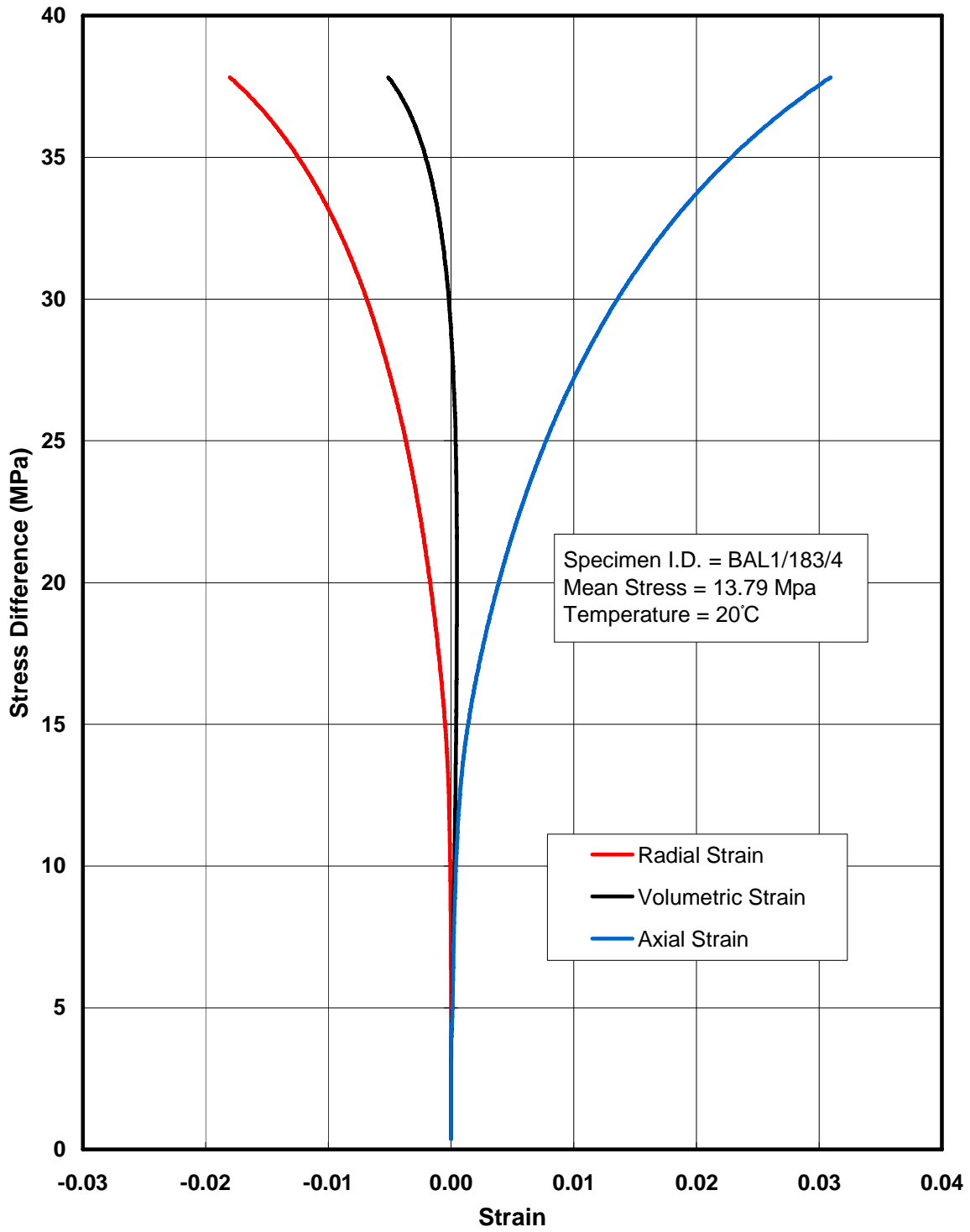
Figure B-21. Stress-Strain Plot of CMC Test on Specimen BAL1/183/4.
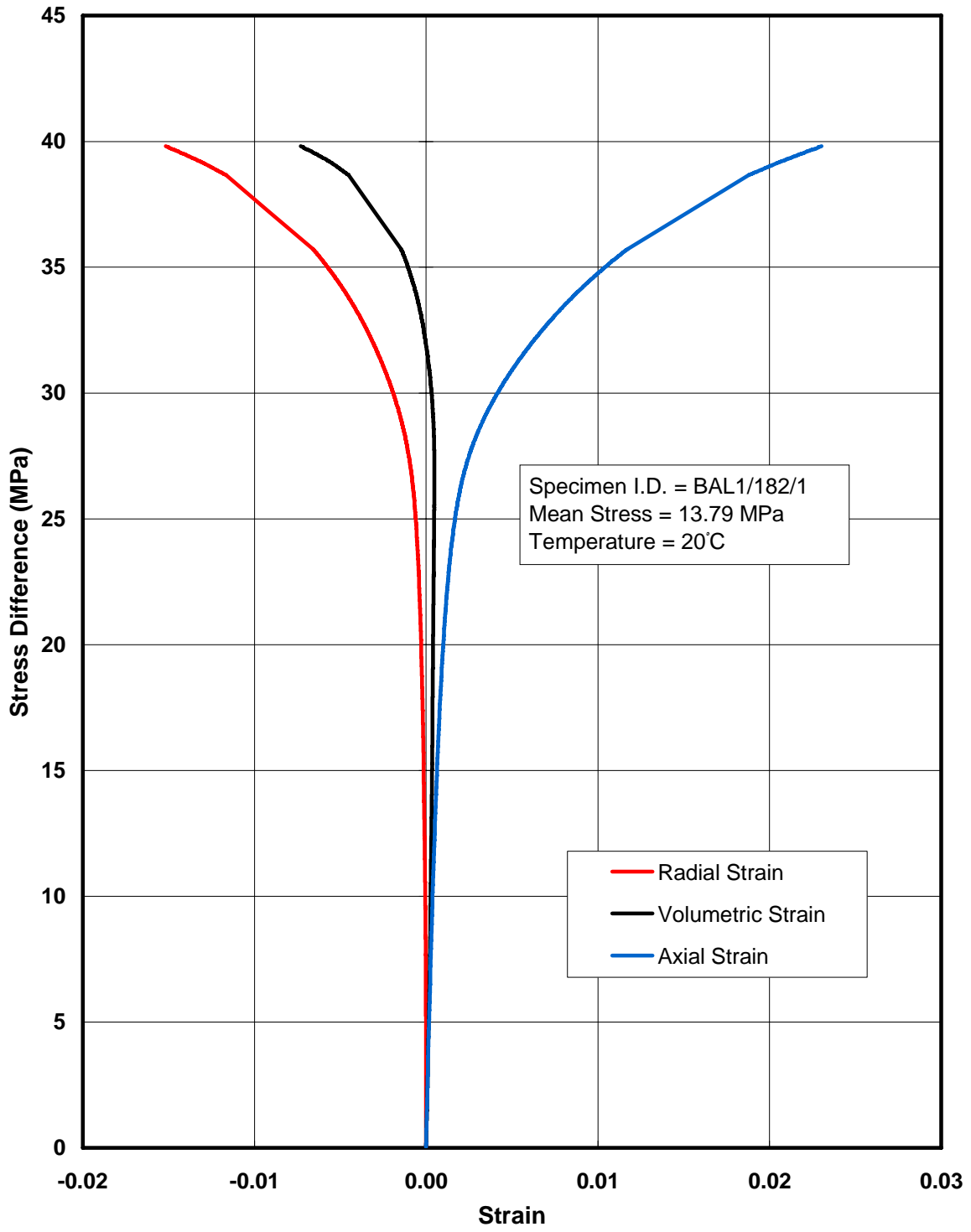
Figure B-22. Stress-Strain Plot of CMC Test on Specimen BAL1/182/1.
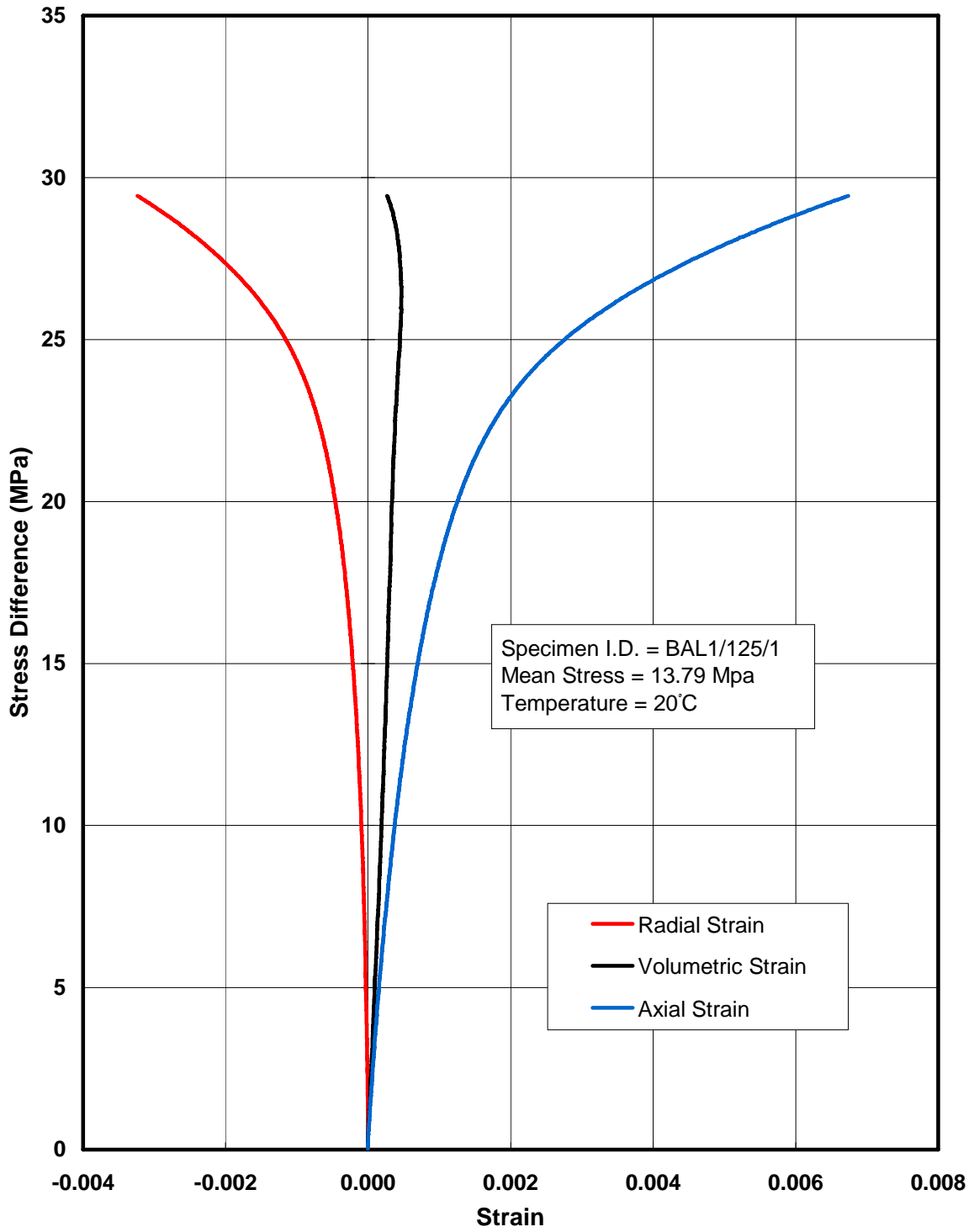
Figure B-23. Stress-Strain Plot of CMC Test on Specimen BAL1/125/1.

APPENDIX C

LABORATORY RESULTS OF
CONSTANT STRAIN RATE TESTS
FOR CAYUTA SALT
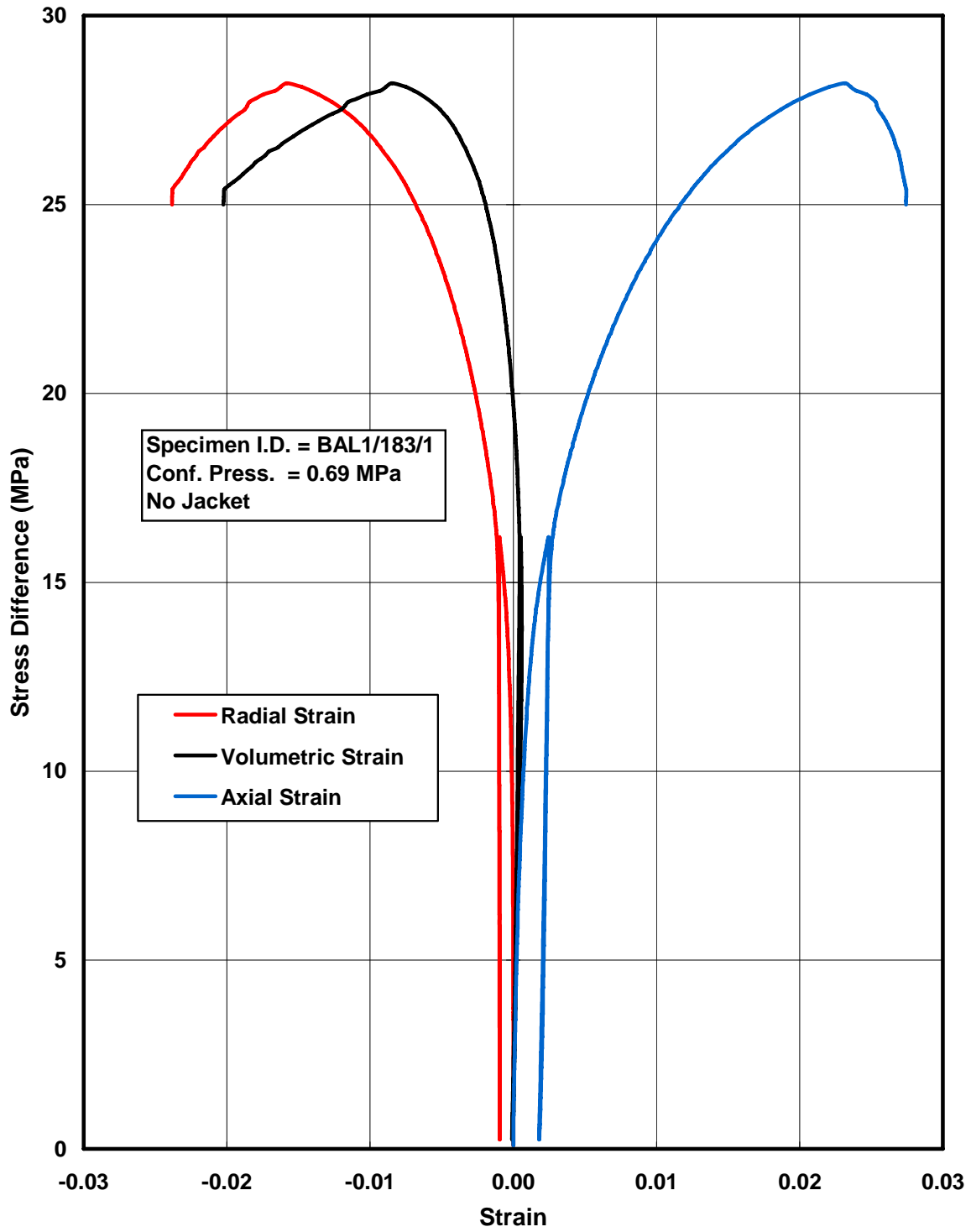
Figure C-1. Stress-Strain Plot of Triaxial Compression Test on Specimen BAL1/183/1.
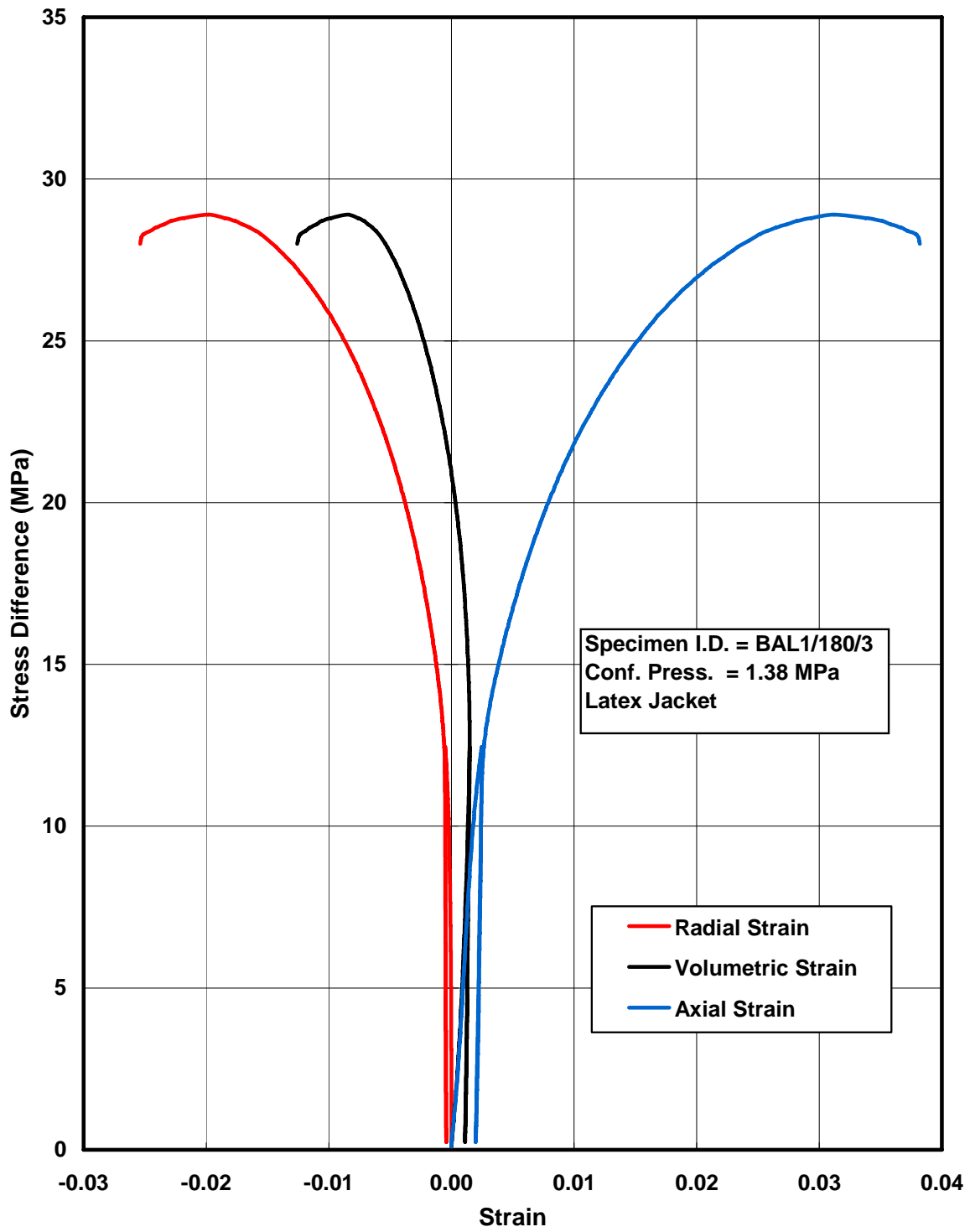
Figure C-2. Stress-Strain Plot of Triaxial Compression Test on Specimen BAL1/180/3.
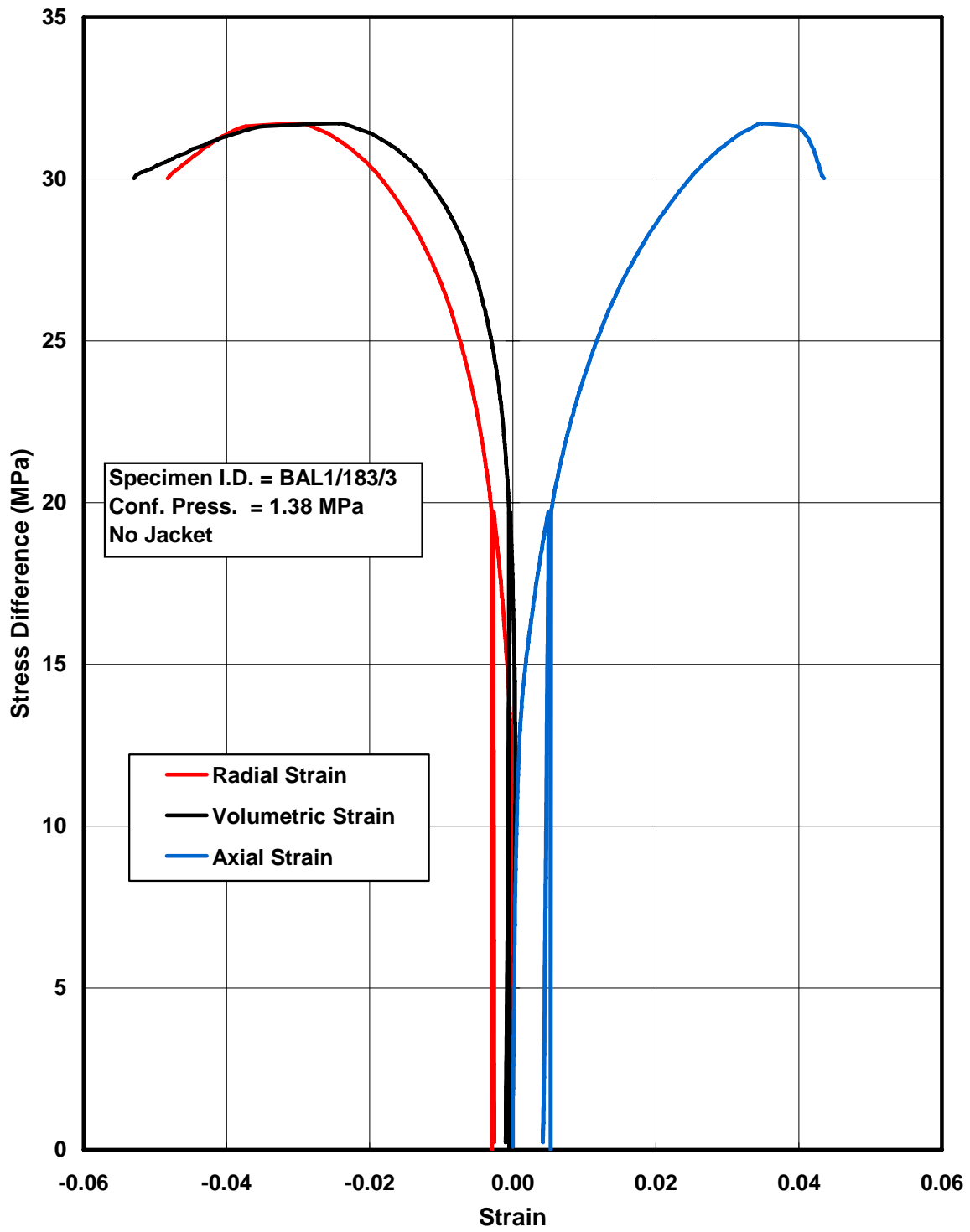
Figure C-3. Stress-Strain Plot of Triaxial Compression Test on Specimen BAL1/183/3.

C-4
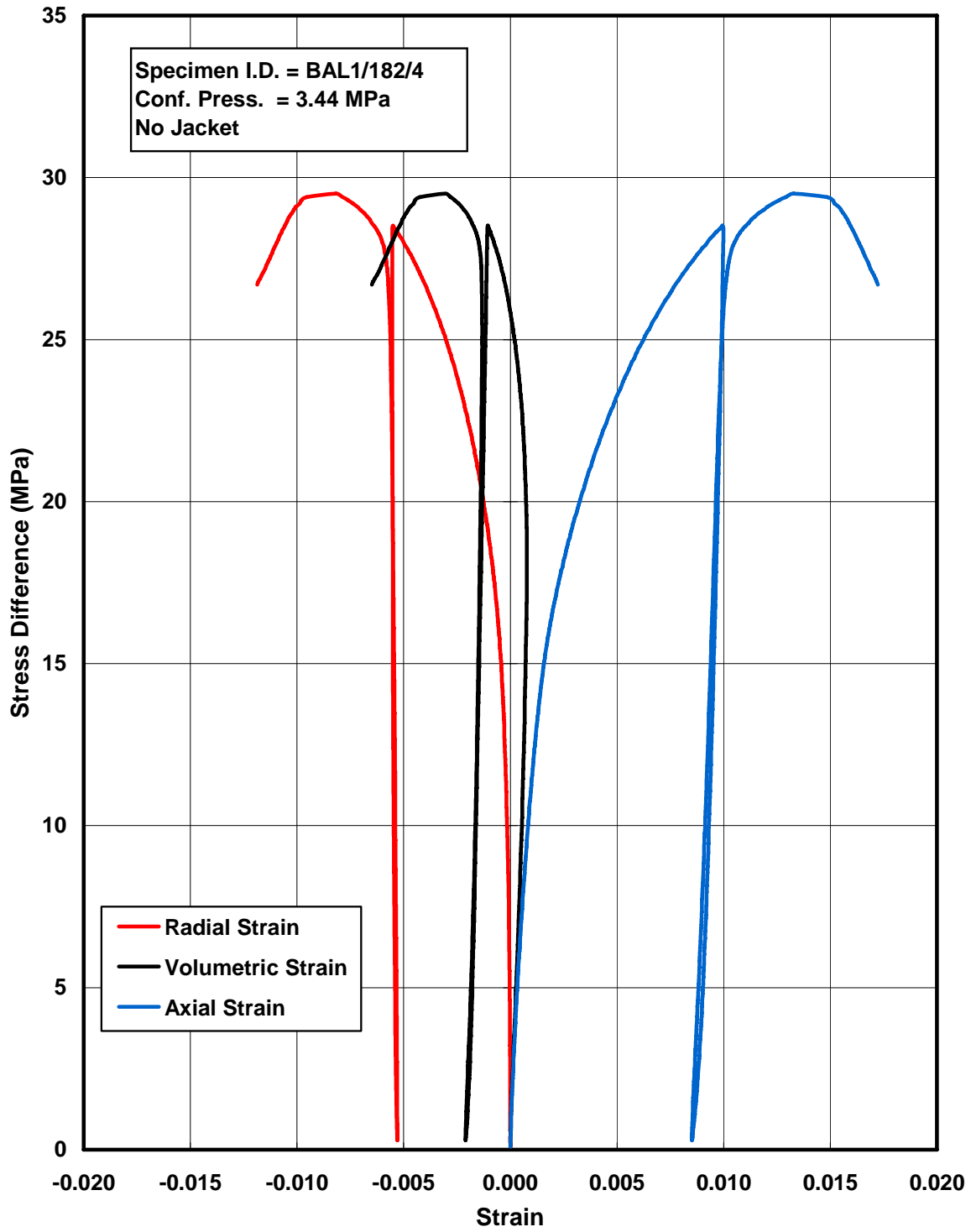
Figure C-4. Stress-Strain Plot of Triaxial Compression Test on Specimen BAL1/182/4.

APPENDIX D

**LABORATORY RESULTS OF
CONSTANT STRESS CREEP TESTS
FOR CAYUTA SALT**
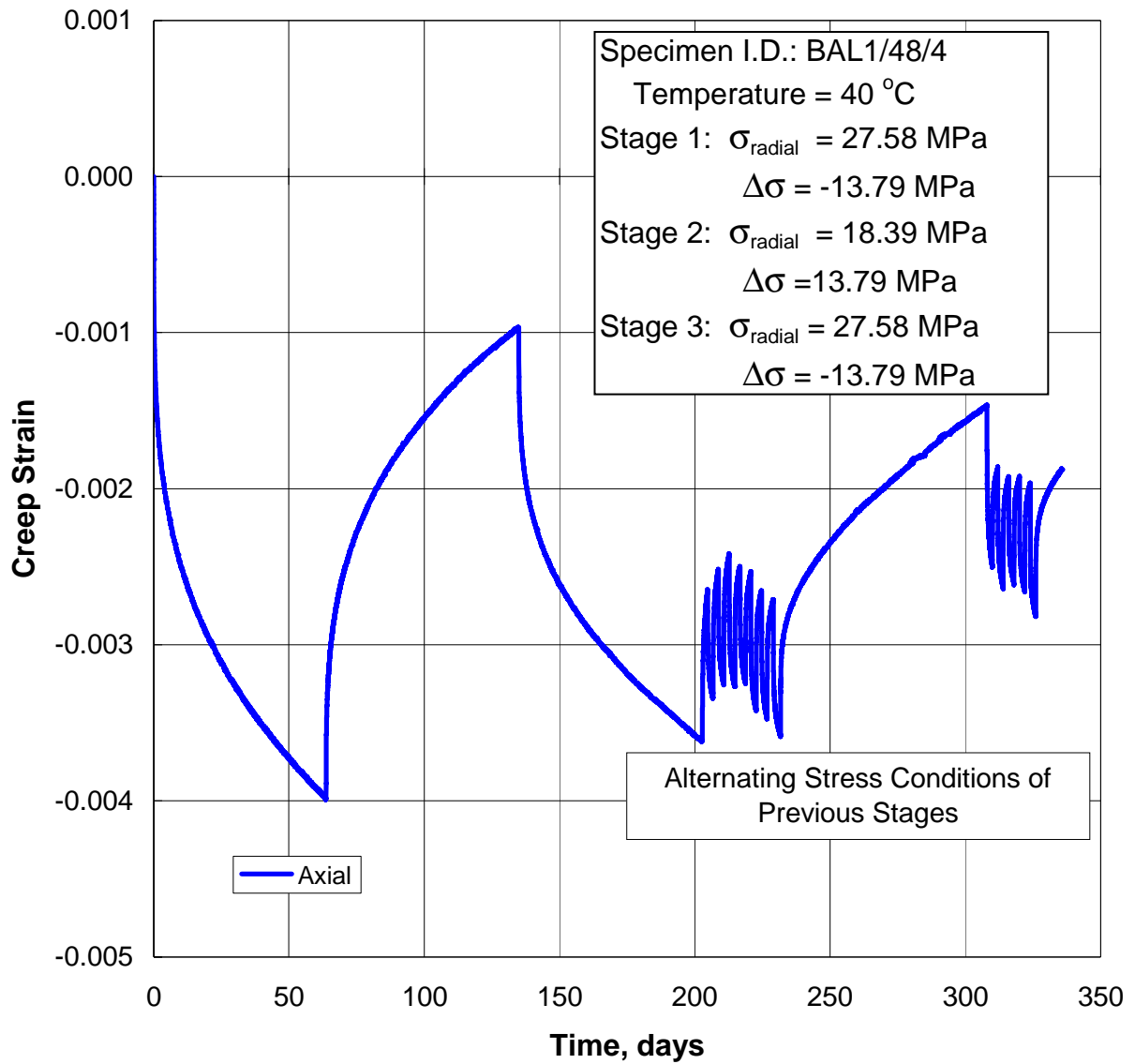
Figure D-1. Strain-Time Plot of Creep Test on Specimen BAL1/48/4.
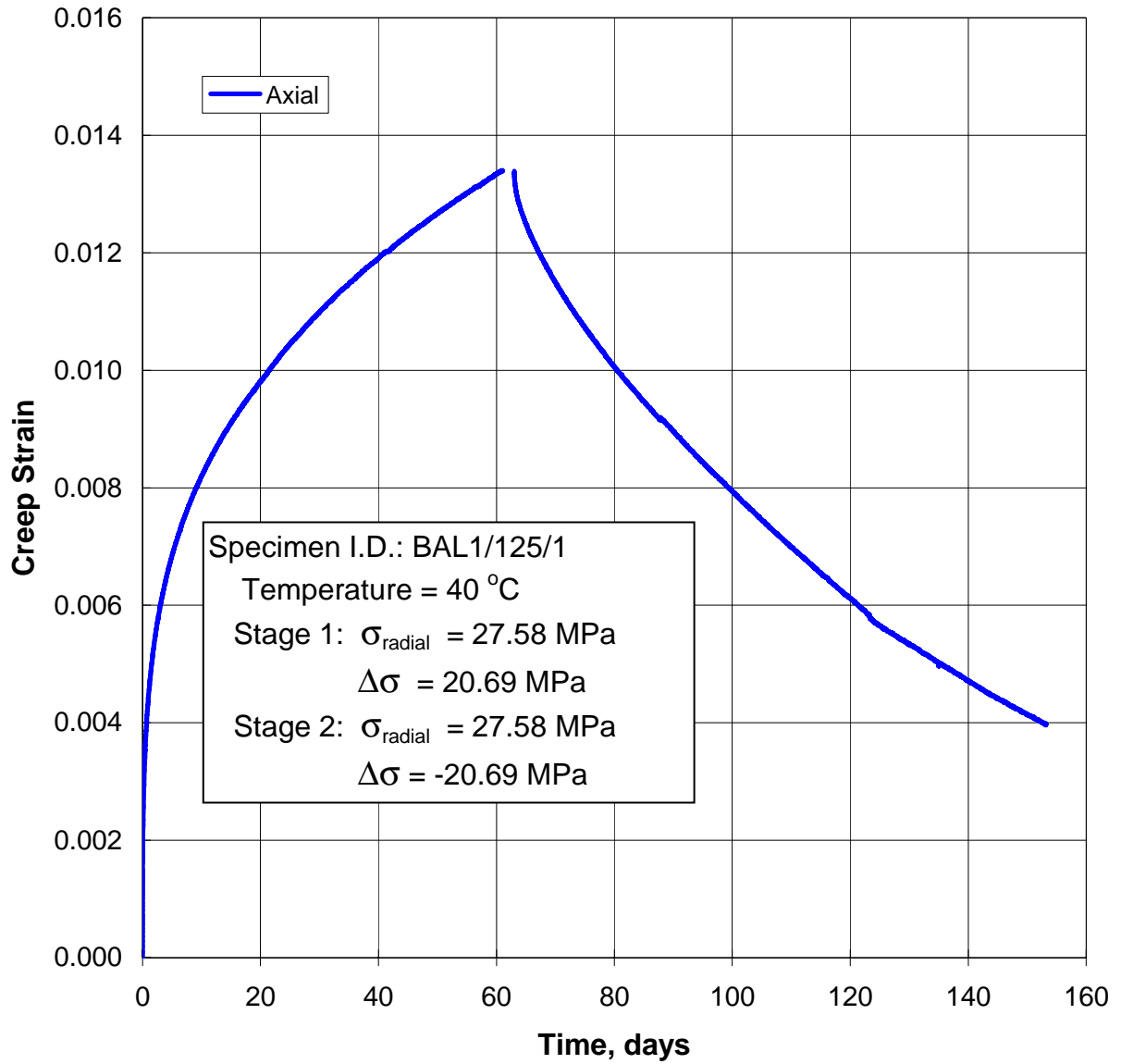
Figure D-2. Strain-Time Plot of Creep Test on Specimen BAL1/125/1.

D-3
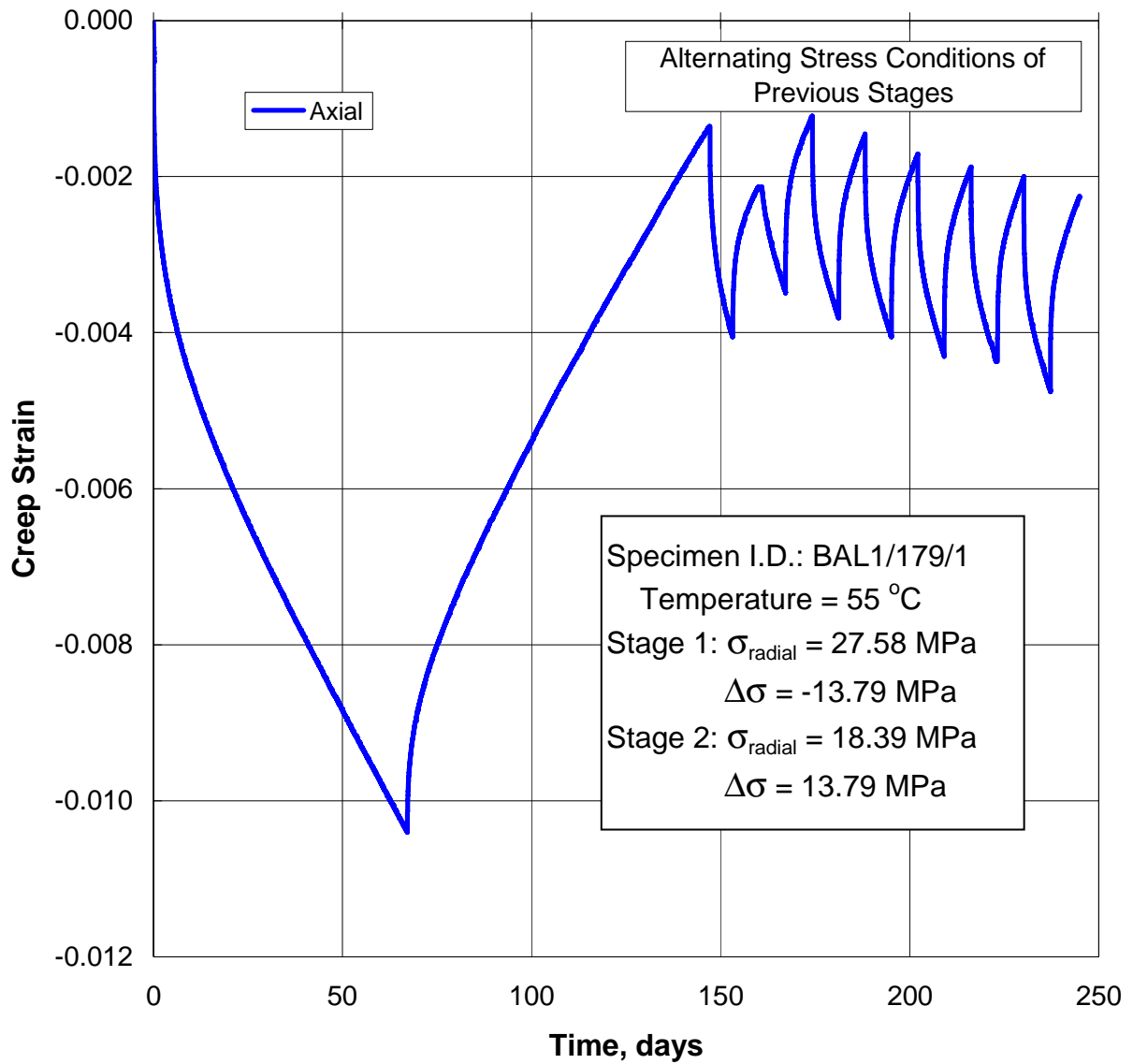
Figure D-3. Strain-Time Plot of Creep Test on Specimen BAL1/179/1.
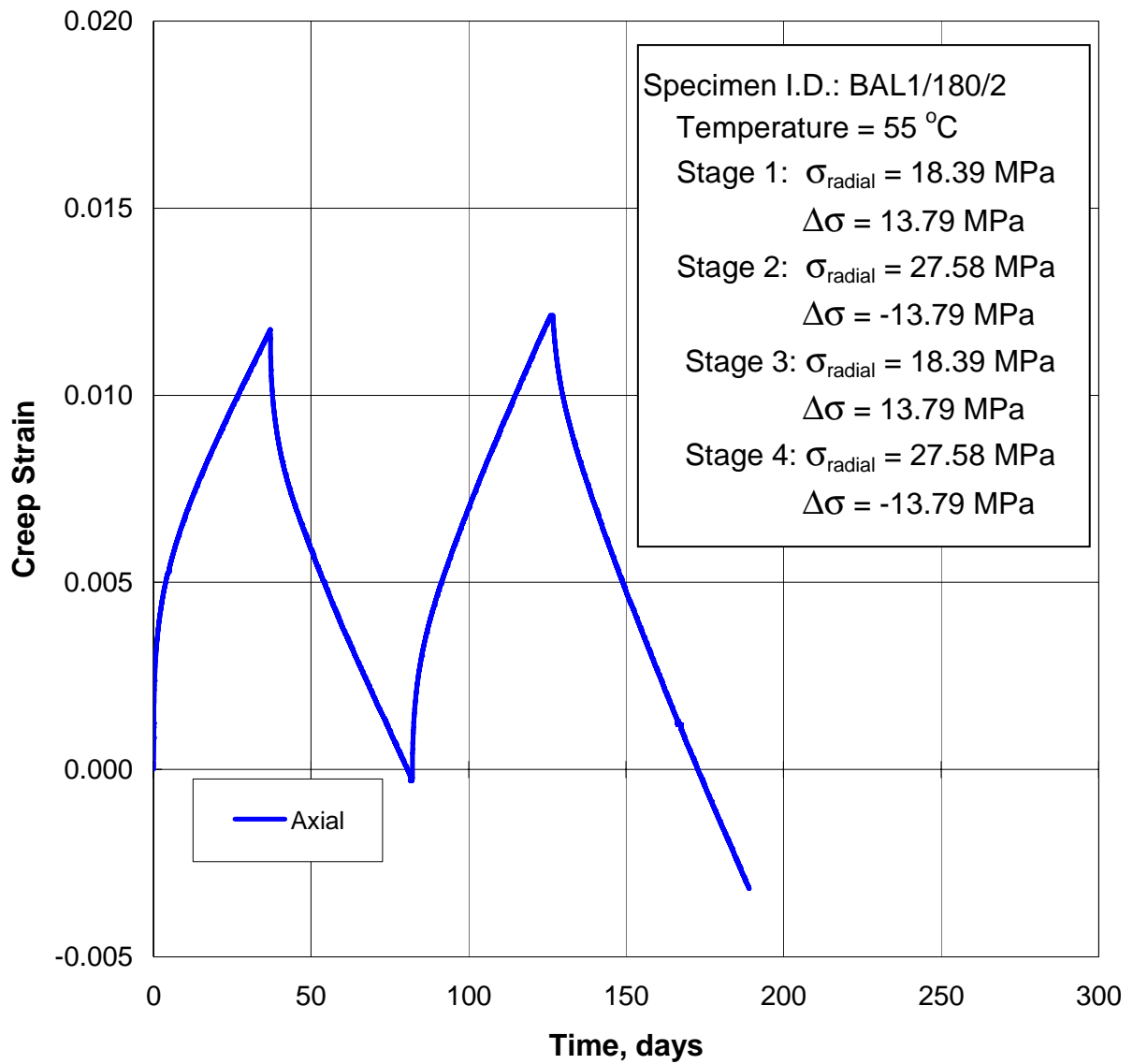
Figure D-4. Strain-Time Plot of Creep Test on Specimen BAL1/180/2.
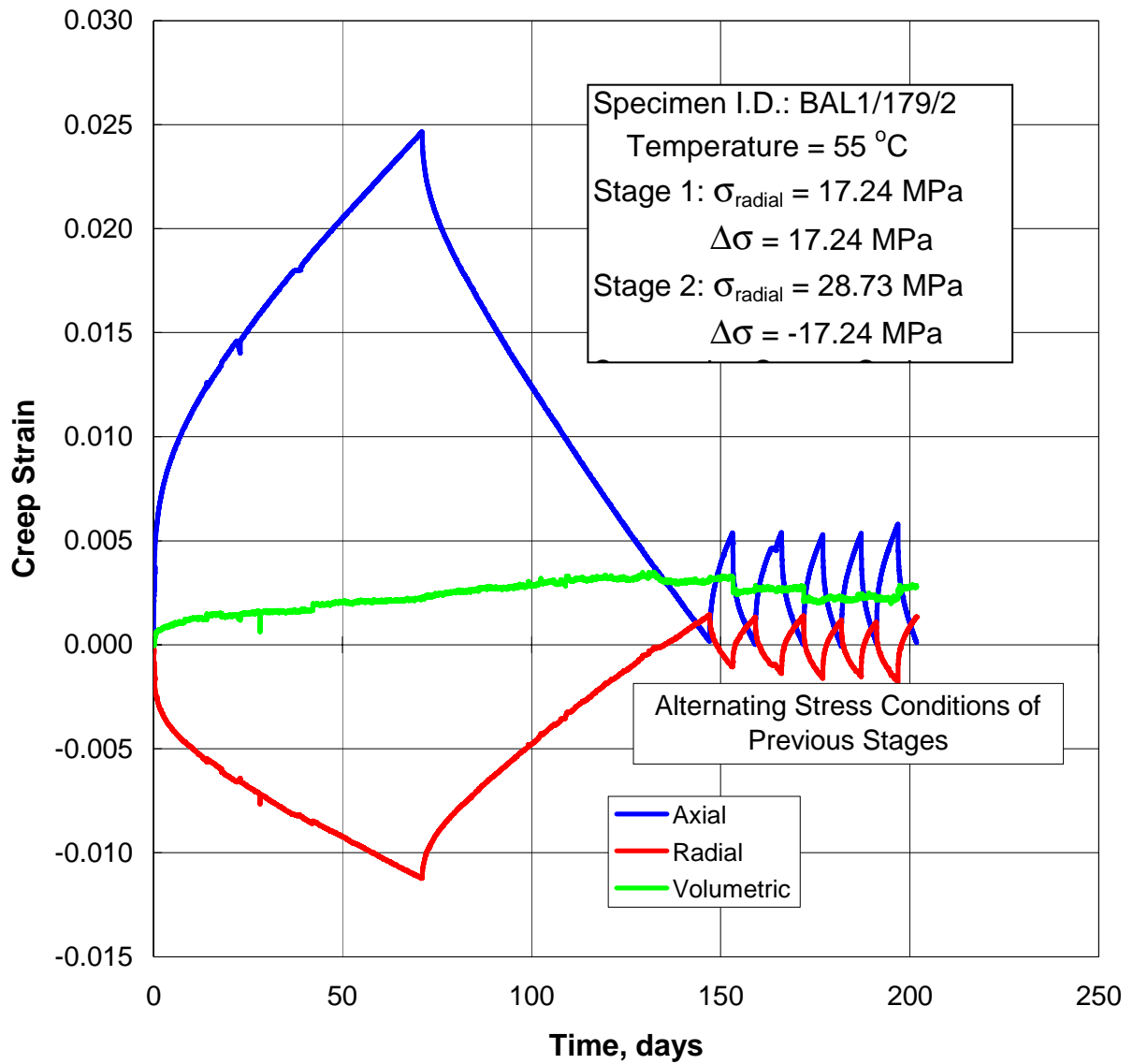
Figure D-5. Strain-Time Plot of Creep Test on Specimen BAL1/179/2.
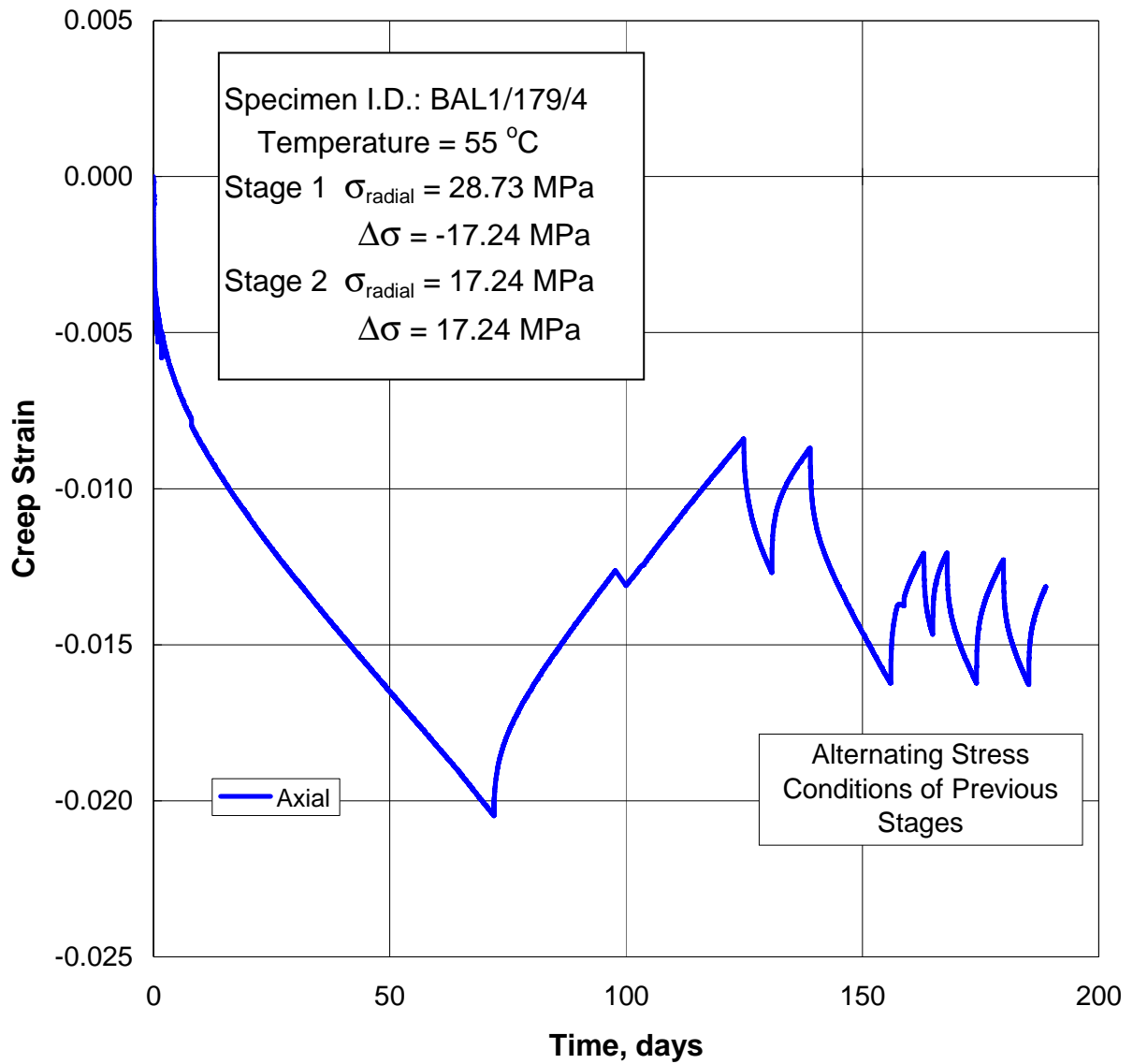
Figure D-6. Strain-Time Plot of Creep Test on Specimen BAL1/179/4.
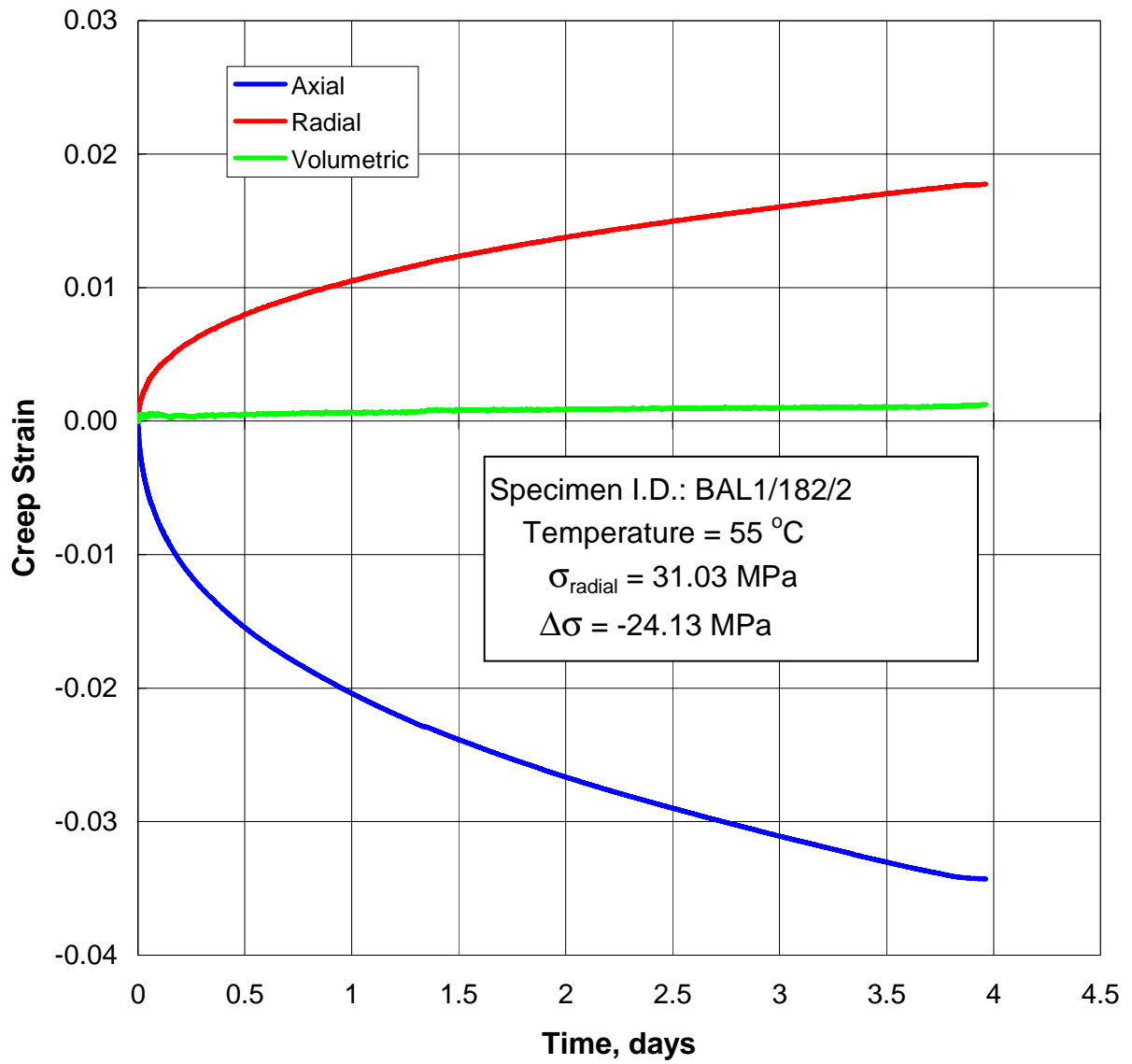
Figure D-7. Strain-Time Plot of Creep Test on Specimen BAL1/182/2.

APPENDIX E

M-D MODEL FOR CAYUTA SALT

APPENDIX E
M-D MODEL FOR CAYUTA SALT

The M-D model was originally developed to predict the behavior of salt for isolation of radioactive waste generated by the U.S. defense programs at the Waste Isolation Pilot Plant (WIPP) site in southeastern New Mexico. Two differential rate equations comprise the M-D model: (1) the strain-rate equation, which gives the viscoplastic strain rate (Equation E-1) and (2) the evolutionary equation, which gives the rate of change of an internal variable (Equation E-2). The three-dimensional form of the M-D model is given below.

$$\dot{\varepsilon}_{ij}^{vp} = \frac{\partial \sigma_e}{\partial \sigma_{ij}} F \dot{\varepsilon}_s \tag{E-1}$$

$$\dot{\zeta} = \text{sign}(\varepsilon_t^* - \zeta)(F_r - 1)\dot{\varepsilon}_s \tag{E-2}$$

where:

$$\dot{\varepsilon}_s = \sum_{i=1}^{3} \dot{\varepsilon}_{s_i} \tag{E-3}$$

$$\dot{\varepsilon}_{s_i} = \text{ steady-state strain rate for mechanism } i \tag{E-4}$$

$$\dot{\varepsilon}_{s_1} = A_1 \exp(-Q_1/RT)(\sigma_e/\mu)^{n_1} \tag{E-5}$$

$$\dot{\varepsilon}_{s_2} = A_2 \exp(-Q_2/RT)(\sigma_e/\mu)^{n_2} \tag{E-6}$$

$$\dot{\varepsilon}_{s_3} = \left[B_1 \exp(-Q_1/RT) + B_2 \exp(-Q_2/RT) \right] \cdot \sinh\left[q(\sigma_e - \sigma_o)/\mu \right] H(\sigma_e - \sigma_o) \tag{E-7}$$

$$F = \begin{cases} \exp\left[\Delta\left(1 - \dfrac{\varsigma}{\varepsilon_t^*}\right)^2 \right] & \text{for } \varsigma < \varepsilon_t^* \\[3mm] 1 & \text{for } \varsigma = \varepsilon_t^* \\[3mm] \exp\left[-\delta\left(1 - \dfrac{\varsigma}{\varepsilon_t^*}\right)^2 \right] & \text{for } \varsigma > \varepsilon_t^* \end{cases} \tag{E-8}$$

$$\dot{\zeta} = \text{sign}(\varepsilon_t^* - \zeta)(F_r - 1)\dot{\varepsilon}_s \tag{E-9}$$

$$
F_r = \begin{cases}
\exp\left[\Delta\left(1 - \dfrac{\varsigma}{\varepsilon_t^*}\right)^2\right] & \text{for } \varsigma < \varepsilon_t^* \\[4mm]
1 & \text{for } \varsigma = \varepsilon_t^* \\[4mm]
\exp\left[\Delta\left(1 - \dfrac{\varepsilon_t^*}{\varsigma}\right)\right] & \text{for } \varsigma > \varepsilon_t^*
\end{cases}
\tag{E-10}
$$

$$
\varepsilon_t^* = K_o \exp(cT)(\sigma_e/\mu)^m
\tag{E-11}
$$

$$
\Delta = \alpha_w + \beta_w \log\left(\frac{\sigma_e}{\mu}\right)
\tag{E-12}
$$

$$
\delta = \alpha_r + \beta_r \log\left(\frac{\sigma_e}{\mu}\right)
\tag{E-13}
$$

and

$$
\begin{aligned}
\dot{\varepsilon}_{ij}^{vp} &= \text{viscoplastic strain-rate tensor} \\
\sigma_e &= \sqrt{3J_2} \ \text{(effective stress)} \\
J_2 &= \frac{1}{2} s_{ij} s_{ji} \\
s_{ij} &= \sigma_{ij} - \delta_{ij}\sigma_m \ \text{(deviatoric stress tensor)} \\
\sigma_m &= \frac{1}{3}\sigma_{kk} \ \text{(mean stress)} \\
\sigma_{ij} &= \text{stress tensor} \\
\delta_{ij} &= \text{Kronecker delta} \\
\varsigma &= \text{internal variable} \\
R &= \text{universal gas constant} \\
T &= \text{absolute temperature} \\
H(x) &= \text{Heaviside function} \\
\mu &= 9{,}620 \text{ MPa (a normalizing constant)}
\end{aligned}
$$

A_1, A_2, B_1, B_2, Q_1, Q_2, n_1, n_2,
q, σ_o, K_o, c, m, α_w, β_w, α_r, $\beta_r = $ experimentally determined parameters.

As indicated by Equation E-3, the steady-state creep rate $(\dot{\varepsilon}_s)$ based on the M-D model is composed of three terms. Each term is associated with a different creep mechanism. The first and third mechanisms $(\dot{\varepsilon}_{s_1}$ and $\dot{\varepsilon}_{s_3})$ are dislocation climb and dislocation glide, respectively, and

E-3

the second mechanism $\left(\dot{\varepsilon}_{s_2}\right)$ is referred to as the undefined mechanism. The relative contribution of each mechanism to the steady-state creep rate strongly depends on the effective stress and temperature.

When pressure conditions in a storage cavern are changed, the transient nature of the M-D model can be an important factor in the response of the cavern. According to Equation E-1, the steady-state creep rate is multiplied by a transient factor (F) to obtain the viscoplastic strain rate. The value of the transient factor depends on whether the internal variable (ς) is less than, equal to, or greater than the transient strain limit $\left(\varepsilon_t^*\right)$, which is a function of the effective stress and temperature. When $\varsigma < \varepsilon_t^*$, the viscoplastic strain rate is greater than the steady-state creep rate ($F > 1$). This is the work-hardening branch of the M-D model. The work-hardening branch is commonly associated with an increase in loading, such as when the cavern pressure is decreased. When $\varsigma > \varepsilon_t^*$, the viscoplastic strain rate is less than the steady-state creep rate ($F < 1$). This is the recovery branch of the M-D law. This branch is commonly associated with a decrease in loading, such as when the cavern pressure is increased. Through the evolutionary equation, the value of the internal variable is always approaching the transient strain limit. In turn, the viscoplastic strain rate is always approaching the steady-state creep rate (i.e., F approaches unity as ς approaches ε_t^*).

APPENDIX F

**REPRESENTATION OF STRESSES
IN PRINCIPAL STRESS SPACE**

APPENDIX F
REPRESENTATION OF STRESSES
IN PRINCIPAL STRESS SPACE

The representation of states of stress in principal stress space is considered to help facilitate the discussion of states of stress around underground caverns and as a means to visualize those states of stress. Consider the state of stress at a point (Q) in a body represented by the principal stresses σ_i (i = 1, 2, 3) at that point as shown in Figure F-1. If the principal stresses are taken as the Cartesian coordinates in a three-dimensional space, an isotropic yield (or potential) surface may be mapped in the coordinate system. A vivid two-dimensional illustration of the bounding states of stress is achieved by projecting these stresses into the π-plane or Haigh-Westergaard stress space (e.g., Chen and Han [1988][1]). The π-plane is a plane perpendicular to the hydrostatic axis $\left(\sigma_1 = \sigma_2 = \sigma_3\right)$ where the mean stress $\left(\sigma_m = (\sigma_1 + \sigma_2 + \sigma_3)/3\right)$ is zero, and Haigh-Westergaard stress space is similar to the π-plane but includes those planes where the mean stress is a nonzero constant. For simplicity, these representations will be referred to as the π-plane, recognizing the shortcomings in nomenclature as stated above. Local two-dimensional Cartesian and polar coordinate systems embedded in the π-plane are convenient for representing yield or potential surfaces. This fact exists because a unique state of stress can also be uniquely defined by three stress invariants, and yield and potential functions are typically written in terms of stress invariants. Of particular interest are the invariants of the deviatoric stress tensor, $s_{ij}\left(s_{ij} = \sigma_{ij} - \sigma_m\delta_{ij}\right)$, which are:

$$J_1 = 0$$

$$J_2 = \frac{1}{2}s_{ij}\,s_{ji} \tag{F-1}$$

$$J_3 = \frac{1}{3}s_{ij}\,s_{jk}\,s_{ki}$$

Now consider the principal stress space of Figure F-2. Figure F-2 is a view looking directly down the hydrostatic axis. In this orientation, the principal stress coordinate axes appear to be 120° apart. Cartesian coordinates x and y are defined, as shown in Figure F-2 (the choice is arbitrary). The x and y axes selected originate at point O on the hydrostatic axis. The x-axis is located 30° counterclockwise from the σ_1 axis and the y axis lies along (but not parallel to) the σ_2 axis. In terms of the principal stresses, the coordinates are:

---

[1] **Chen, W. F. and D. J. Han, 1988.** *Plasticity for Structural Engineers,* Springer-Verlag, New York, NY.
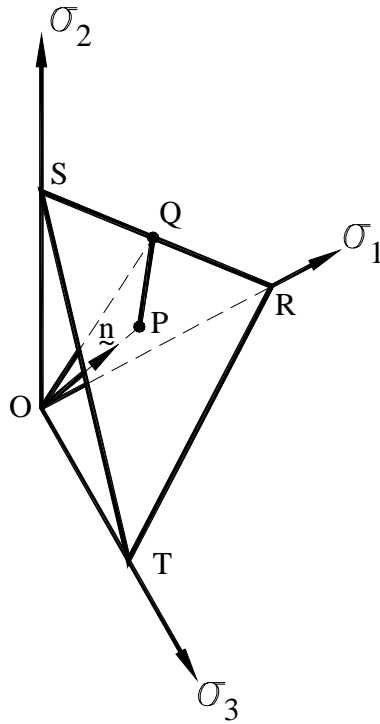
Figure F-1. Stress Points in Principal Stress Space.
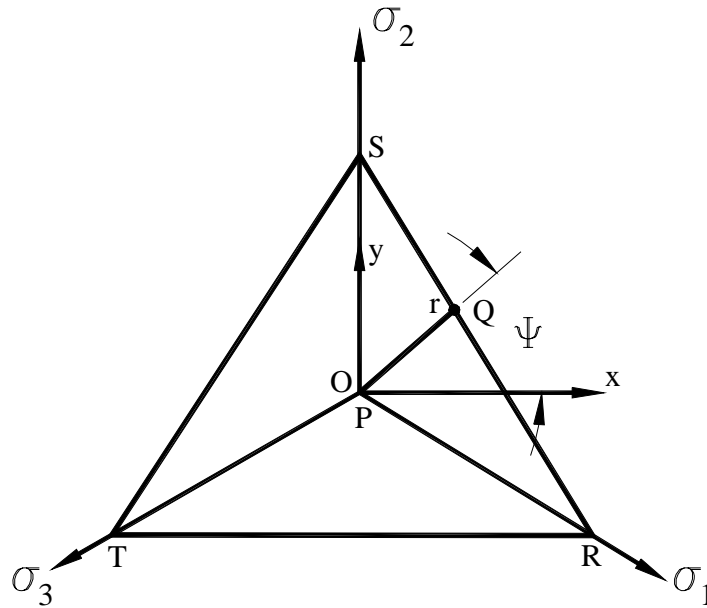
Figure F-2. Stress Points in Principal Stress Space Viewed Down the Hydrostatic Axis.

$$X = \frac{\sigma_1 - \sigma_3}{\sqrt{2}} \tag{F-2}$$

$$y = \frac{2\sigma_2 - \sigma_1 - \sigma_3}{\sqrt{6}} \tag{F-3}$$

Equations F-2 and F-3 may be used to obtain a polar coordinate (r, ψ) system, *viz*:

$$r = \sqrt{x^2 + y^2} = \frac{1}{\sqrt{3}}\sqrt{\left(\sigma_1 - \sigma_2\right)^2 + \left(\sigma_2 - \sigma_3\right)^2 + \left(\sigma_3 - \sigma_1\right)^2} \tag{F-4}$$

$$\psi = \tan^{-1}\left(\frac{y}{x}\right) = \tan^{-1}\frac{1}{\sqrt{3}}\left[\frac{2\sigma_2 - \sigma_1 - \sigma_3}{\sigma_1 - \sigma_3}\right] \tag{F-5}$$

The angle ψ is referred to as the Lode angle (e.g., Hill [1950][2]). The Lode angle may be expressed in terms of the invariants J_2 and J_3 as [Nayak and Zienkiewicz, 1972][3]:

$$\psi = \frac{1}{3}\sin^{-1}\left[\frac{-3\sqrt{3}\,J_3}{2\,J_2^{3/2}}\right] \tag{F-6}$$

However, when the Lode angle is defined in this manner, it is restricted to $-30° \leq \psi \leq 30°$. This restriction requires symmetry of the yield condition in all $60°$ sextants in the π-plane. When J_2 is expressed in terms of the principal stresses, it becomes:

$$J_2 = \frac{1}{6}\left\{\left(\sigma_1 - \sigma_2\right)^2 + \left(\sigma_2 - \sigma_3\right)^2 + \left(\sigma_1 - \sigma_3\right)^2\right\} \tag{F-7}$$

From Equations F-4 and F-7, one readily sees that the distance from the hydrostatic axes to a stress point is equivalent to $\sqrt{2\,J_2}$ when lying in the π-plane. Yield or potential functions expressed in terms of these coordinate systems may be plotted in the π-plane easily.

---

[2] **Hill, R, 1950.** *The Mathematical Theory of Plasticity,* Clarendon Press, Oxford, UK.

[3] **Nayak, G. C. and O. C. Zienkiewicz, 1972.** "A Convenient Form of Invariants and its Application in Plasticity," *Journal of the Structural Division*, ASCE, Vol. 98, pp. 949–954.